Electrochemical Transformation of Alkanes,

Carbon Dioxide and Protons at Iron-Porphyrins

and Iron-Sulfur Clusters

A thesis submitted to the University of East Anglia

For the degree of Doctor of Philosophy

Submitted December 2013

Khalaf Msalam Alenezi

Energy Materials Laboratory

School of Chemistry, UEA

Norwich

THIS THESIS IS DEDICATED TO THE MEMORY OF MY

FATHER

Contents

Chapter 1

Chapter 2

Chapter 3

Chapter 4

Abstract

The work contained in this thesis focuses on (i) chemical and electrochemical alkane oxidation using Fe-porphyrin complexes as catalysts (ii) electrochemical and photoelectrochemical CO_2 reduction using Fe-porphyrin complexes (iii) electrochemical and photoelectrochemical generation of hydrogen using iron-sulfur cluster.

Chapter 1 gives a general overview of the electrochemical techniques which underpin the work presenedt in this thesis.

Chapter 2 reports the chemical and electrocatalytic oxidation of hydrocarbons to alcohols and epoxides by using iron (III) porphyrins as catalysts. A series of new basket-handle thiolate Fe (III) porphyrins have been used to mediate anodic oxidation of hydrocarbons, specifically adamantane hydroxylation and cyclooctene epoxidation. The electrocatalytic and chemical catalytic activity oxidation of the thiolate porphyrins are benchmarked against Fe (III) tetraphenyl porphyrin chloride and its tetrapentafluorophenyl analogue.

Chapter 3 describes the electrochemical and photoelectrochemical reduction of carbon dioxide to carbon monoxide. This chapter shows that iron (III) porphyrin complexes are capable of carrying out electrocatalytic reduction of carbon dioxide at both vitreous carbon and illuminated p-type silicon surfaces, with reasonable current efficiencies. At illuminated p-type silicon photovoltages of ca 500mV are obtained.

Chapter 4 describes the electrochemical and photoelectrochemical reduction of proton to H_2 using $[Fe_4S_4 (SPh)_4]^{2-}$ as an electrocatalyst at both vitreous carbon and at illuminated p-type Si electrodes.

Acknowledgements

First I would like to thank my supervisor, Prof. Chris Pickett, for his enthusiastic and friendly supervision during my PhD research, and I am greatly indebted to him for the knowledge he has generously imparted to me during my studies.

My sincere acknowledgment to the people in the School of Chemistry at UEA that assisted me during this work: Dr. Saad Ibrahim and Dr. Joseph Wright for their lab skills in electrochemistry and for help, as well as their continued friendship, with particular thanks to Dr. Saad Ibrahim for supporting help during my research work and writing. My thanks also goes to Dr Peiyi Li for the synthesis of the new thiolate Fe(III) porphyrins which were used in this research.

I wish also to thank past and present colleagues in the Energy Materials Laboratory, Lee, Ahmed, Amanda and Ausra for their friendship and general support during my studies.

My deepest and heartfelt thanks are given to my darling wife Faydhah and my kids Fawz, Emad, Layal and Wael, for their support and love during my studying. I would also like to thank other family members, my uncle, mum, and all my brothers and sisters.

The University of Hail, Saudi Arabia, is thanked for providing a Scholarship.

Abbreviations

A	Electrode area
A^0	Angstrom
D	Diffusion coefficient
P	Products
fc^+/fc	Ferrocenium /Ferrocene
V	Volt
N	Number of electrons
C	Concentration
k	Rate constant
F	Faraday constan
µA,mA	Microampere, Milliampere
v	Scan rate
E^o	Potential of formal reduction
ΔE	The peak potential separation
E_p	Peak potential
$E_{1/2}$	Mid-potential between the two peak potential of a reversible cyclic voltammogram
i_p	Peak current
i_p^{red}	Cathodic peak current
i_p^{ox}	Anodic peak current
I	Current density
CV	Cyclic voltammetry
WE	working electrode
RE	Reference electrode
SE	Recondary (auxillary) electrode
c_0^{bulk}	Bulk concentration
C.P.E	Controlled potential electrolysis
E.C	Electron- transfer followed by a chemical reaction
ECE	Electron- transfer chemical reaction electron- transfer
Q	Charge passed
O	Oxidation
R	Reduction
η	The overpotential

MMO	Methane monooxygenase
TTP	Tetraphenylporphyrin
PFTPP	Tetrakis(pentaflourophenyl)porphyrin
TON	Turnover number
RT	Room temperature
DMF	Dimethylformamide
AN	Acetonitrile
GC	Gas chromatography
R	The gas constant

Chapter 1

1 Electrochemistry techniques

1.1 Overall scope of the thesis

This thesis covers three areas of research which are concerned with the general area of electrocatalysis of substrate conversion by certain metal complexes and, in two of these areas, approaches to photoelectrocatalysis of the reactions on p – type Si. These areas are:

(i) electrocatalysis of alkane oxidation by iron porphyrin systems

(ii) electrocatalysis and photoelectrocatalysis of carbon dioxide reduction by iron porphyrin systems

(iii) electrocatalysis and photoelectrocatalysis of dihydrogen formation by iron-sulfur clusters

The areas are linked by a general relevance to energy conversion. Area (i) is specifically concerned with electocatalysis of hydrocarbon oxidation to oxygenates such as alcohols or epoxides. The second area (ii) is concerned with electrochemical and photoelectrochemical production of CO from CO_2, the latter concerning an approach to the generation of a solar fuel. The third area (iii) is concerned with electrocatalysis and photoelectrocatalysis of H_2 production by 'simple' 4Fe-4S iron-sulfur clusters and has relevance to the potential role of ferredoxins as primitive hydrogenases. These three research areas are described in self-contained chapters (Chapters 2, 3 and 4) which provide an introduction and background to earlier work, results and discussion, an experimental section and references. The following sections in this chapter provide a description of the more general techniques which underpin the research carried out. Finally, Chapter 5 provides a short summary of the achievements of this thesis, general conclusions and possible avenues of further research.

1.2 Background to experimental techniques

1.2.1 Overview of electrochemistry

Electrochemistry plays an important role in many areas of science and technology, examples include electroanalytical processes such as measuring devices derived from electrochemical principles in areas of medicine and biology, electrochemical methods for the synthesis of bulk chemicals such as chlorine and sodium hydroxide in the major chlor-alkali industries, electrosynthesis of fine chemicals for the pharmaceutical industry, and is increasingly seen as having the potential to contribute to the solution of the energy and environmental problems now facing mankind, in particular the development of hydrogen fuel and producer cells which underpin progress towards a hydrogen economy and photoelectrochemical devices for solar fuel production – water splitting and artificial photosynthesis [1-3].

Electrochemistry is the part of chemistry which is concerned with study of charge separation at an electrode material which can be driven by application of a potential across a solution – electrode interface or which may involve adsorption of redox active molecules at the electrode surface [4]. In the following sections fundamentals of charge –transfer at a solution/electrode interface are described in more detail with a particular emphasis on methods such as cyclic voltammetry which constitute a major part of the work described in this thesis.

1.2.3 Electrode reactions

An electrode reaction is a heterogeneous chemical process which involves the transfer of electrons to or from a molecule at the surface of electrode. This reaction can take place in the interfacial region between electrode and solution or *via* adsorption of the electroactive species at the electrode surface. The electrode

acts as a source (cathode, reduction) or sink (anode, oxidation) of electrons, the energy of which can be infinitely tuned between the limits set by the electrochemical decomposition of the solvent and the electrolyte employed. In a conventional non-aqueous solvent such as MeCN containing $[NBu_4][BF_4]$ this is *ca* -2.5 to +2.5V *versus* the saturated calomel electrode (SCE) [1,5].

Equation 1.1 represents a generalised electrode reaction in which a species in the oxidised form O receives n electrons from the electrode to form its reduced counterpart R. For a solution redox couple with the electrode held at a fixed potential E, the system will attain equilibrium as defined by the Nernst equation 1.2. Charge will flow to or from the electrode at held at a potential E until the bulk concentration of O and R attain their equilibrium values.

$$O \ + \ ne^- \ \rightleftharpoons \ R \qquad 1.1$$
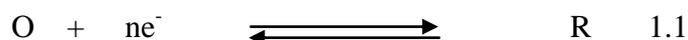
$$E = E^{0/} + \frac{RT}{nF} \log \frac{c_O}{c_R} \qquad\qquad 1.2$$

Where O and R are the oxidation and reduction of components in solution, respectively, $E^{0/}$ is the formal potential, *n* is the number of electrons transfered, c_O and c_R are the concentrations of O and R respectively, *R* is the gas constant, *F* the faraday constant, and *T* the temperature. At $T = 298 \ ^{o}A$ the pre-logarithmic term is 0.0591V.

The process of attaining of such equilibrium is represented by Figure 1.1. The steps involved can be broken down as follows. Here we can consider starting with 100% O and choosing an applied potential E which would drive the conversion to essentially 100% R *ie* the equilibrium is driven far to the right hand side.

1. *The reactant O moves from solution to surface of electrode by mass transfer.*

This will take place in an unstirred (quiet) solution by diffusion. As the electrode removes O by reduction (or R by oxidation) then a concentration gradient will be set up and O will migrate from the bulk solution towards the electrode. If the electrode is rotated or the solution stirred (forced convection) then the concentration gradient will be steeper, O will diffuse more rapidly to the electrode surface, there will be a higher current flow and the conversion of O to R will take place more rapidly than in a quiet solution.

2. *The electron transfer occurs in a region which is close to the surface of the electrode.*

The rate at which this occurs is dependent on the electrode potential and is described by the Butler-Volmer equation which relates the driving-force (the overpotential) for the electron-transfer reaction to the current density, I. The overpotential (η) is the difference between the equilibrium potential and the applied potential, Equation 1.3

$$I = I_0 \left[\exp\left(\frac{\alpha_A nF}{RT}\eta\right) - \exp\left(-\frac{\alpha_C nF}{RT}\eta\right) \right] \qquad 1.3$$

α_A and α_C are constants known as the transfer coefficients for the anodic and cathodic reaction respectively (between 0 and 1 and generally 0.5). I_0 is the exchange current density and corresponds to the situation at zero overpotential when the forward current flow equals the back current flow and $I = 0$.

3. *The product R moves away from electrode surface.*

This is the reverse of migration of O to the electrode. The electrode reaction may not necessarily involve simple electron – transfer. Following chemistry may well

15

occur, for example when R is unstable and converts to another product, which in turn may be electroactive at the applied E. This is where time-dependent techniques such as cyclic voltammetry (see below) can be powerful aids to unravelling the mechanisms of more complex reactions [1,4]
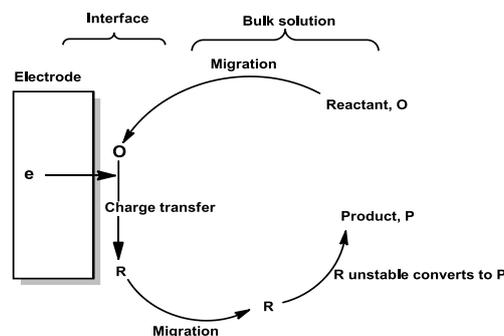
Figure 1.1   Schematic representation of an electrode process.

1.2.3 Cyclic voltammetry

In 1938 Randles provided the first theoretical description for the cyclic voltammetry technique [6,7] and over several decades cyclic voltammetry has been applied as powerful technique to study a very wide range of solution and surface redox processes at the thermodynamic and mechanistic levels [3]. The theory of cyclic voltammetry is highly developed and over the last thirty or so years and in combination with digital simulation methods provides a powerful means of analysing complex electrode reactions. In the following sections the general experimental set up and the underlying principles of cyclic voltammetry are described.

1.2.3.1 Basic experimental conditions

The redox active species of interest is dissolved in solution which contains a suitable redox <u>inactive</u> electrolyte to make the system conducting. Typically

concentrations of the redox active species and that of the electrolyte salt are 1mM and 0.1M respectively. For non-aqueous work in solvents such as MeCN or tetrahydrofuran tetraalkylammonium BF_4 or PF_6 salts are commonly used. This solution is contained in an electrochemical cell which has three electrodes: an <u>inert</u> working electrode (WE), a reference electrode (RE) and a secondary (auxillary) electrode SE. The configuration of these electrodes is shown schematically by Figure 1.2. The working electrode is normally a small microelectrode, typically 0.1 cm^2. Useful WE materials are vitreous carbon, platinum, gold and amalgamated gold. The secondary electrode is larger, normally 10 times that of the WE and is commonly platinum. In non-aqueous solutions the resistance of the solution can be high and the actual potential at the working electrode solution interface will be less that the applied potential by an amount iR where R is the solution resistance and i is the measured current flowing between the WE and the SE, Equation 1.4.

$$E_{applied} = E_{actual} \pm iR \qquad\qquad 1.4$$

In order to minimise this iR drop (uncompensated resistance) which distorts the cyclic voltammogram the i component can be diminished by (i) working with a low concentration of the redox active species (ii) using a WE with small surface area (iii) using low potential scan –rates (see below). In addition, the solution resistance can be minimised by placing the RE as close to the WE electrode as possible without screening it from the SE. Often this best achieved using a Luggin capillary probe as illustrated by the cell diagram in Figure 1.2 [1,3,6,7].

This three – electrode arrangement completes the circuit of a potentiostatic device which controls the applied potential between the reference electrode and the working electrode by adjusting the voltage between the WE and SE.
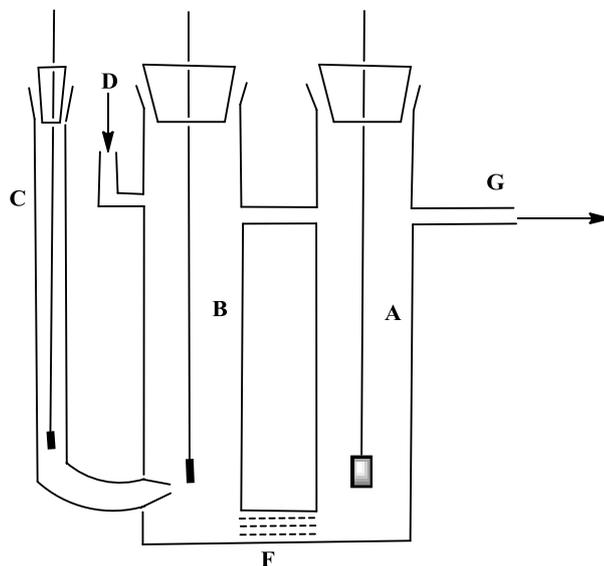
Figure 1.2 Electrochemical cell A counter electrode, B working electrode, C reference electrode, D, G inlet and outlet taps for purging gas, F a frit for ion exchange.

1.2.3.2 Experimental measurements

The potentiostatic instrumentation allows superposition of a potential waveform at the WE electrode - solution interface and the simultaneous monitoring of the current flowing between the WE and SE as a consequence of the perturbation of the potential and redox chemistry of the electroactive species. Specifically, in a cyclic voltammetry experiment a <u>triangular</u> waveform is superimposed as shown in Figure 1.3 with the applied potential varied linearly with time. Thus the potential is scanned from an initial value $E_{initial}$ to the 'switching' potential E_{switch} at, for example, $100 mVs^{-1}$. The scan is then reversed at E_{switch} and the potential is (usually) changed at the same rate as in the forward scan until it reaches $E_{initial}$ at which point the scan is stopped. The initial potential is set at a value at which no electrode reaction occurs, the switching potential is set at or beyond a value at

which the oxidation or reduction reaction of the electroactive species takes place. Simultaneously with the potential scan current data is collected and it is the analysis of the $i - V$ response which gives much information on the nature of the electrode process [1, 3,7].
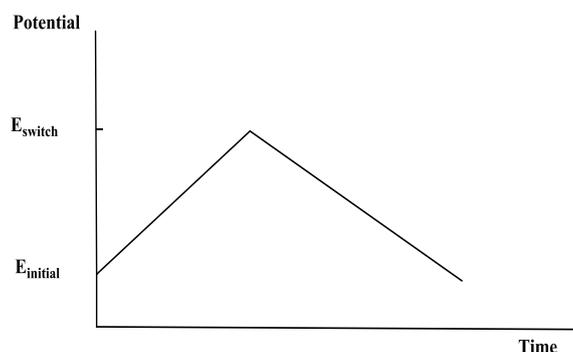
Figure 1.3 The triangular waveform used in cyclic voltammetry

1.2.3.3 The i – V response for an electrochemically reversible system

Figure1.4 shows the cyclic voltammetric response for a typical electrochemically reversible system the ferrocene (Fc) couple in which both redox partners Fc and Fc^+ are stable on the time – scale of the experiment (seconds). This experimental voltammogram was recorded at a vitreous carbon electrode at 22 ^{o}C in MeCN – 0.1M [NBu$_4$][BF$_4$]. The key experimental parameters which can be obtained from the voltammogram are as flows.

The potentials $E_{1/2}$, E_p^{ox} and E_p^{red}

The location of the peak potentials E_p^{ox} and E_p^{red} are shown in Figure1.4 where superscripts *ox* and *red* refer to the oxidation and reduction peaks respectively. $E_{1/2}$ is also located in the figure and has the value ½ [E_p^{ox} + E_p^{red}]. These parameters are expressed in volts, V relative to the chosen reference electrode, in this case the Ag/AgCl electrode. (Importantly, absolute redox potentials cannot be

determined, only relative potentials). $E_{1/2}$ is not a strictly thermodynamic quantity but its value can be consider to be very close to the formal potential $E^{0/}$ which itself is close to the standard potential E^0. These potentials are related by Equations 1.4 to 1.5 .The approximation that $E_{1/2} \simeq E^0$ for most molecular systems is based on the assumption that the activity coefficients of the oxidised O and reduced forms R of the couple are nearly identical in Equations 1.6 and 1.7, and that the diffusion coefficients for these same couples are also nearly equal, Equation 1.8 [1].

$$E = E^0 + \frac{RT}{nF} \ln \frac{\gamma^{ox} \, c^{ox}}{\gamma^{red} \, c^{red}} \qquad\qquad 1.4$$

$$E = E^0 + \frac{RT}{nF} \ln \frac{c^{ox}}{c^{red}} + \frac{RT}{nF} \ln \frac{\gamma^{ox}}{\gamma^{red}} \qquad\qquad 1.5$$

Defining the formal potential as:

$$E^{0/} = E^0 + \frac{RT}{nF} \ln \frac{\gamma^{ox}}{\gamma^{red}} \qquad\qquad 1.6$$

Gives the modified Nernst equation:

$$E = E^{0/} + \frac{RT}{nF} \ln \frac{c^{ox}}{c^{red}} \qquad\qquad 1.7$$

$E^{0/}$ is directly related to $E_{1/2}$ by the relationship [2] :

$$E_{1/2} = E^{0/} + \frac{RT}{nF} \ln \left(\frac{D_{ox}}{D_{red}} \right)^{1/2} \qquad\qquad 1.8$$

The magnitude of the peak potential separation $|E_p^{ox} - E_p^{red}|$ is directly related to the value of n the number of electrons involved in the primary electron-transfer step by the relationship given in Equation 1.9. Thus for the ferrocene couple shown in the Figure 1.4, the experimental value of ΔE_p is found to be $71 \pm 5\text{mV}$ at 25mV s^{-1} which is close to the theoretical value of 59mV for the expected $n = 1$ process.

$$\Delta E_p = |E_p^{ox} - E_p^{red}| = \frac{59}{n} \; mV \qquad\qquad 1.9$$

This relationship pertains to a solution couple. If the redox couple is attached to an electrode surface or is confined in a thin layer, then ΔE_p is close to zero.
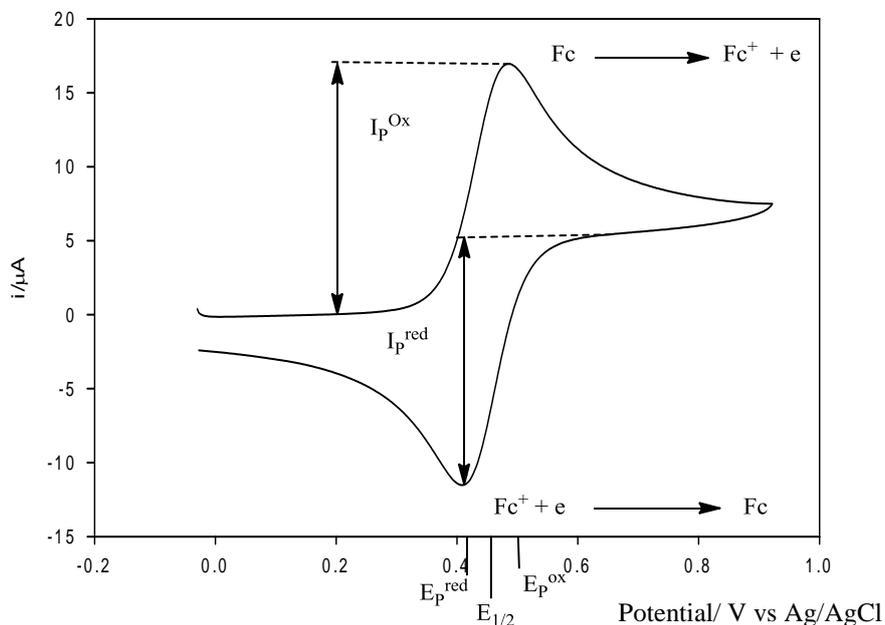
Figure 1.4 Cyclic voltammogram of a solution of ferrocene in 1.5 mM CH_3CN/ $[NBu_4][BF_4]$ at carbon electrode , scan rate $v = 0.025$ Vs^{-1}.

The peak currents I_p^{ox} and I_p^{red} and the ratio I_p^{red} / I_p^{ox}.

The peak current density I_p^{ox} for a reversible oxidation process (or I_p^{red} for a reduction) is given at 25^oC by the Randles – Sevcik Equation, 1.10, where c_0^{bulk} is the bulk concentration in mol/cm^3, D is the diffusion coefficient in cm^2 s^{-1} , v is the potential scan – rate in V s^{-1} and I is the current density in A. If the oxidation involves a solution redox couple then the peak current is controlled by mass-transport, that is the process is diffusion controlled. Consequently a plot of I_p *versus* $v^{1/2}$ will be linear. The relationship contains information on D and n, if either is known independently then the other can be determined provided the surface area of the electrode and concentration of the redox active species are also

known. In the experimental example shown in Figure 1.4, I_p is 8.17×10^{-5} A cm^{-2} at 25 mVs^{-1} thus with n = 1 then D is calculated to 1.6×10^{-6} cm^2 s^{-1}.

$$I_p = - (2.69 \times 10^5) \, n^{3/2} \, c_0^{bulk} D^{1/2} \, v^{1/2} \qquad 1.10$$

If the redox couple is attached to an electrode surface then I_p is proportional to the scan-rate rather than to the square root of scan-rate, thus solution and surface processes can generally be readily distinguished. In addition, the shape of the voltammogram of a surface confined species is quite different from that for a solution process [1,3].

The ratio $I_p^{\,red} / I_p^{\,ox}$ gives valuable information on the reversibility of the system on an experimental time-scale determined by the scan-rate. Figure 1.5 shows diagramatically how these current parameters are measured. For a fully reversible oxidation system where the primary product O is stable then $I_p^{\,red} / I_p^{\,ox} = 1$. If however O is removed from the diffusion layer adjacent to the WE by following chemistry then this ratio will be less than one. The scan-rate is important in defining the reversibility and the dependence of the $I_p^{\,red} / I_p^{\,ox}$ ratio on v can give kinetic information as discussed below.
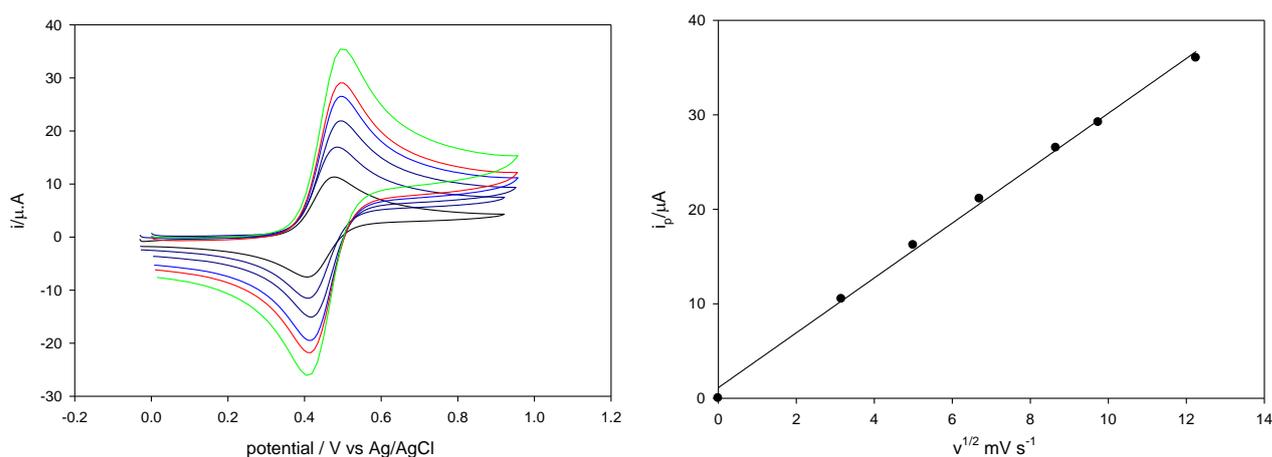
Figure 1.5 Cyclic voltammograms obtained for 1.5 mM ferrocene in CH$_3$CN at a glassy carbon electrode (0.072 cm^2) at scan rates of : 0.01 , 0.025 , 0.045 , 0.075, 0.095, and 0.15 V/s. (b) The dependence of square root of the scan-rate ($v^{1/2}$) on the peak current for oxidation of ferrocene.

The origin of the shape of the cyclic voltammogram for a reversible couple.

For the ferrocene couple illustrated above the Nernst equilibrium is rapidly maintained by electron flow across the electrode – solution interface as the applied potential is scanned towards $E_{1/2}$. At potentials approaching E_p^{ox} the electron-transfer rate becomes controlled by diffusion of ferrocene to the electrode surface because the concentration at the electrode approaches zero. Diffusion of ferrocene to the electrode is driven by the concentration gradient in the diffusion layer. Initially this is steep but as consumption of ferrocene occurs the diffusion layer thickness expands and the concentration gradient falls (relaxes) and consequently the current also falls, Figure1.6. This explains the shape of the voltammogram for ferrocene beyond E_p^{ox}. In the reverse scan the electrode 'sees' a concentration of ferrocinium close to that of the initial bulk concentration of ferrocene and essentially mirrors the response for the forward process with current flowing in an opposite sense.

Distance from electrode surface, x
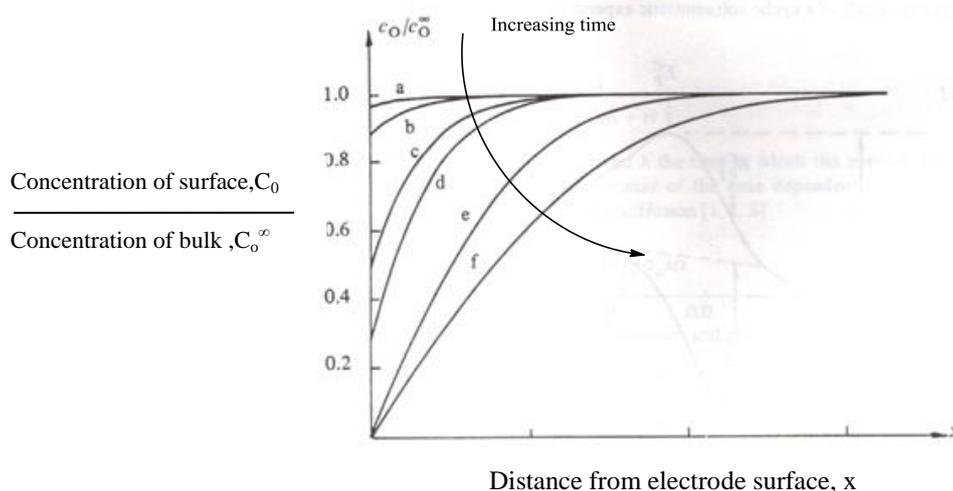
Figure 1.6 Concentration-distance profiles for the electroactive species with increasing time   a ⟶ f [1].

23

1.2.3.4 Heterogenous electron-transfer kinetics : quasi-reversible systems

In the above discussion of the cyclic voltammetry of a reversible one-electron transfer couple, ferrocene, the heterogenous electron transfer step across the electrode solution interface is not rate limiting at conventional scan-rates. The Nernst equilibrium is always rapidly maintained by electron flow across the interface as the applied potential is scanned and, at sufficiently positive potentials the current flow becomes controlled by diffusion of ferrocene from the bulk to the electrode surface. This 'fast' reversible electrochemistry occurs because the heterogenous rate constant for electron transfer is greater than about 10^{-2} cm s^{-1} and, at modest scan-rates of *ca* 100 mVs^{-1} this step is not rate (current) limiting. However, there are systems in which it is the heterogenous step which is rate limiting and this leads to quasi-reversible electron transfer. The cyclic voltammograms take on a different form in which ΔE is no longer independent of scan-rate but increases as ν is increased. At a specific scan-rate the smaller the heterogenous electron transfer rate constant, the greater is ΔE, as shown by Figure 1.7.
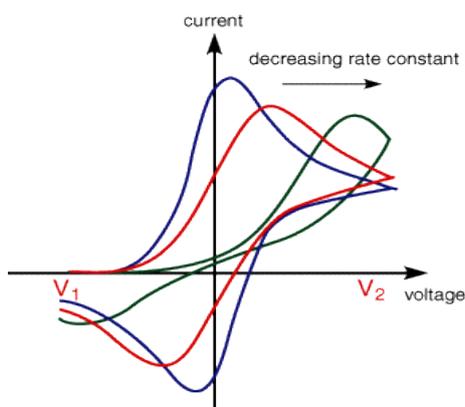
Figure 1.7 Schematic representation of a quasi-reversible system

The dependence of electron-transfer rate on potential is explicity described by the Butler-Volmer equation, Equation 1.3. I_0 in this equation can be written in terms of a standard heterogenous rate constant k_0, Equation 1.11 :

$$I_0 = k_0 \, nF(c_O^{bulk})^{\alpha_A}(c_R^{bulk})^{\alpha_C} \qquad\qquad 1.11$$

The electron $-$ transfer coefficients α_A and α_C are related by $\alpha_A + \alpha_C = 1$. Generally they are approximately equal with $\alpha_A = \alpha_C = 0.5$. The coefficient α relates to the geometry to the intersection of the potential energy surfaces for the electrode and the redox active molecule.

In the case of quasi-reversible systems the wave shape of cyclic voltammogram varies with different scan-rates, which provides a probe of quasi-reversible systems in which electron-transfer across the electrode-solution interface is slow. A reversible cyclic voltammogram is obtained at slow scan rates because the rate of electron transfer is greater than of mass transport. However, at higher scan rates the rate of mass transport becomes high compared to the rate of electron transfer and this result in the peak potential shifting to more negative values for the reduction process and to more positive potentials on the reverse scan for the re-oxidation. Figure 1.7 schematically shows the behaviour of a quasi-reversible system for decreasing electron-transfer rate constants.

If k_0 is very small then the value of $k_{forward}$ is only significant for large overpotentials and in this potential regime the potential dependent rate constant for the back reaction, k_{back} approaches zero. Where $k_{back} = 0$ the system can be described as <u>totally irreversible</u>. The peak current density for a totally irreversible system is given by Equation 1.12 at 25^0C [1.10].

$$I_p = -(2.69 \times 10^5)n(\alpha_C n_\alpha)^{1/2} c_0^{Bulk} D^{1/2} v^{1/2} \qquad 1.12$$

Where, I_p the peak current density A cm^{-2}, D in cm^{2}s^{-1}, v is in Vs^{-1}, c_0^{Bulk} is in mol cm^{-3}and n_α is the number of electrons transferred in the rate controlling step.

In a cyclic voltammetric experiment reversibility, quasi-reversibility and irreversibility are related by the scan-rate. The change from reversible to totally irreversible behaviour can be viewed as having an intermediate quasi-reversible regime where the relationship between the current density I_p as function of $v^{1/2}$ is not directly proportional. Figure 1.8 shows the transition from reversible to irreversible behaviour with increasing of scan rate through the quasi-reversible regime [1,3-9].
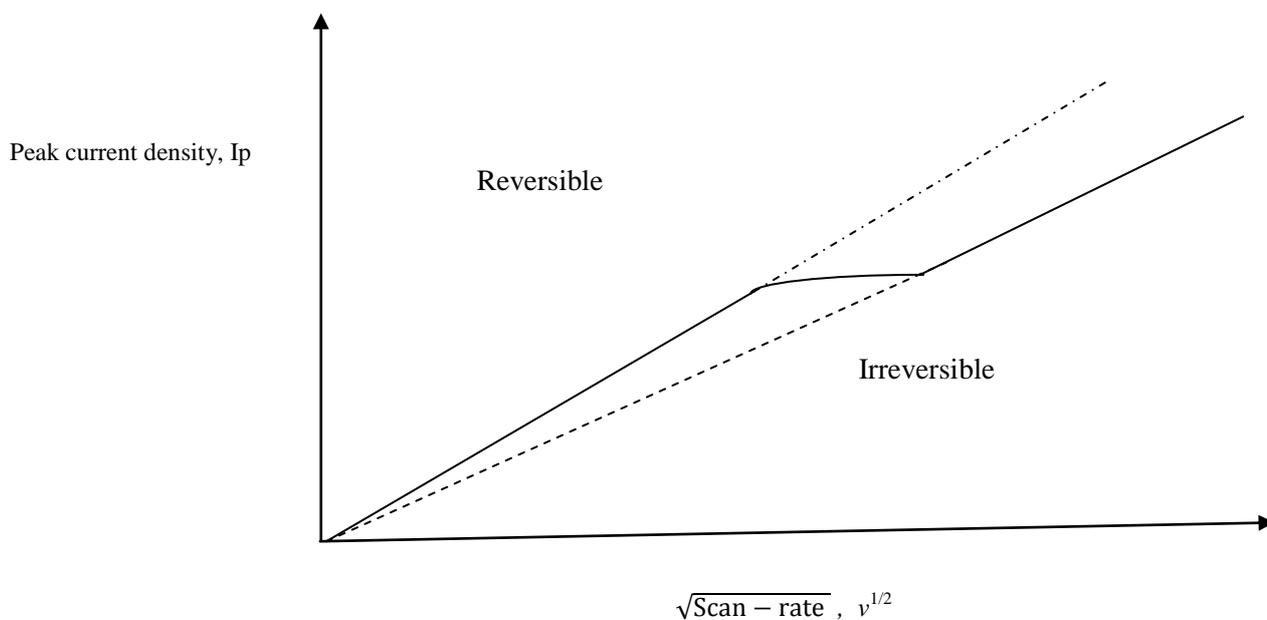
Figure 1.8 The transition of system from reversible to irreversible case with increasing of $v^{1/2}$.

1.2.3.5 The EC reaction

A process in which an electron-transfer step (E) at an electrode surface is followed by a homogenous chemical step (C) in solution is referred to as an EC mechanism. It is a frequently encountered mechanism in electrochemistry and can be represented by the two steps E and C in Scheme 1.2 below.

$$O \; + \; ne^- \; \rightleftharpoons \; R \qquad E$$

$$R \; \xrightarrow{\;k\;} \; Y \qquad C$$
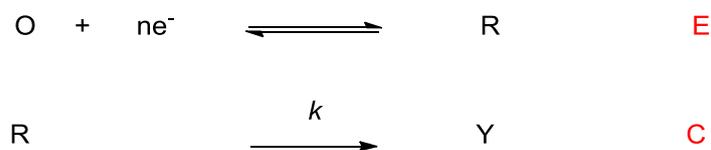
Scheme 1.2

The cyclic voltammetry of this process depends on the relative rate of the two reaction steps. The first step is simple electron transfer, if the electron transfer is fast and the rate constant of chemical reaction has k = 0 then no chemical reactions occur and the R species is oxidised back to O hence the cyclic

voltammetry will be fully reversible ($I_{pa} = I_{pc}$). If the chemical reaction is fast (k is large) then R will be converted to Y thus the wave will be irreversible.

At intermediate values of k, when the chemical reaction is relatively slow, reversibility of wave will depends upon the scan rate with the ratio of the anodic to cathodic peak current increasing with increasing of scan rate until full reversibility is observed. Figures 1.9a and 1.9b show the cyclic voltammetry of EC reaction if the chemical reaction is slow.
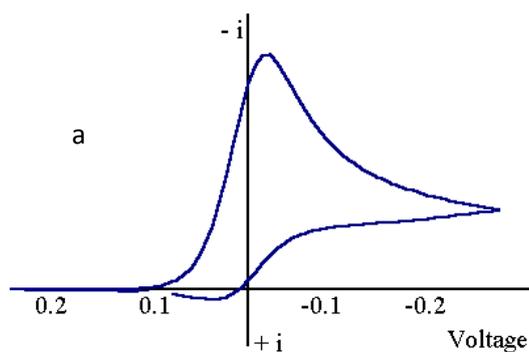
Figure 1.9 a   The cyclic voltammetry of EC reaction if the chemical reaction is slow. At a low scan rate there is sufficient time for a significant conversion of R to the product and the peak current ratio $I_p^{back}/ I_p^{forward}$ is < 1.
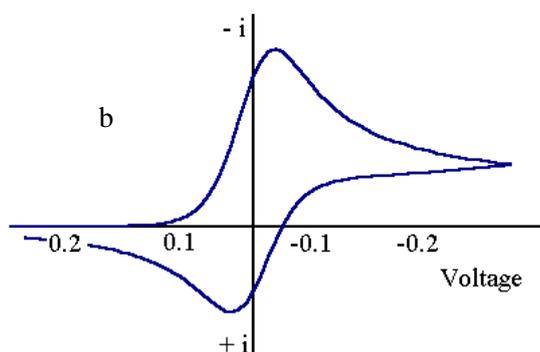
Figure 1.9 b   At fast scan-rates the time 'window' is sufficiently small so that there is little conversion of R to Y and the peak current ratio $I_p^{back}/ I_p^{forward}$ is close to 1.

28

In the case where the chemical reaction is very fast the system will be totally irreversible and no kinetic imformation can be derived. [1,3, 4, 7].

1.2.3.6 The ECE reaction

In an ECE processes we have a situation where a chemical step is interposed between two electron transfer steps as shown in Scheme1.3 below. In the first E step, electron transfer to O occurs to generate R. In the second C step, R reacts chemically to yield Y. In the third step Y produced by is reduced by electron to produce the product H. This reaction sequence is common in multi- electrons transfer processes in organic electrochemistry.

$$O \; + \; ne^- \; \rightleftharpoons \; R \qquad E$$

$$R \; \xrightarrow{k} \; Y \qquad C$$

$$Y \; + \; ne^- \; \rightleftharpoons \; H \qquad E$$
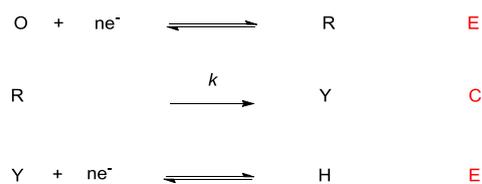
Scheme 1.3

If k is large then R will convert chemically to Y which reduces further to generate H. This means the reaction will behave as an (n_1+n_2) electron transfer. However, when k is small no significant amount of Y is generated and the reaction will behave as a reversible n_1 electron transfer.
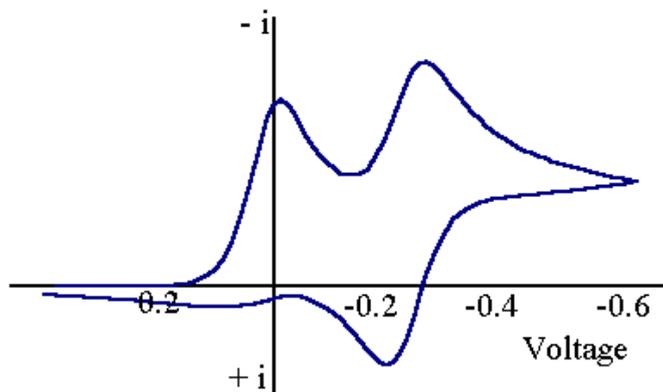
Figure 1.10 The cyclic voltammetry of ECE reaction. In this illustration the chemical step is fast and two waves are observed for the two E processes

There are many examples where the reduction potential for the second step is positive of the first potential in an ECE process involving single electron transfers. In such cases the observed cyclic voltammogram may show a single forward peak which at fast scans appears as a reversible one-electron system but at slow scans tends towards an irreversible two-electron process, [1,3,4,8].

1.2.4 Controlled potential electrolysis and coulometry

1.2.4.1. Introduction

In a controlled potential electrolysis experiment the electrode is held at a fixed value which drives the oxidation or reduction reaction and the decay of the current is monitored as a function of time. Controlled potential electrolysis is used to determine the number of electrons which are involved in the overall electrochemical reaction process as well as providing a means of identifying electrolysis products by standard analytical techniques [1,7]. A divided cell is used in a controlled electrolysis experiment with the working electrode separated from the secondary electrode and the reference electrode by glass frits. This stops products generated in the secondary electrode compartment from interfering with

the system under study. The working electrode is located in a known volume of solution which contains a known concentration of electroactive species. The solution is stirred continuously and evenly during the electrolysis at constant applied potential.

The charge passed Q at any time t can be calculated from the i-t decay curve. In most modern instrumentation the Q is automatically calculated and a plot of i *versus* Q provides a useful method of estimating the overall stochiometry of an electrolysis (see below).

1.2.4.2 Relationships between current, time and charged passed in the course of a controlled potential electrolysis experiment

For an uncomplicated reaction where O is reduced:

$$O \quad + \quad n e \quad \xrightarrow{\quad E_{applied} \quad} \quad R$$

The charge passed as a function of time is given by

$$i(t) = \frac{Q(t)}{t} \qquad \text{or} \qquad Q(t) = i(t) \times t \qquad 1.12$$

Where *i(t)* is the instantaneous current at time *t* and *Q(t)* is charge-passed at time *t*.

$$Q(t) = \int_0^t i(t)dt \qquad \text{where } i \text{ is the instantaneous current}$$

The relationship between the log $\left| i \right|$ and time should be linear and any deviation from linear behaviour that implies the reaction is more complicated.
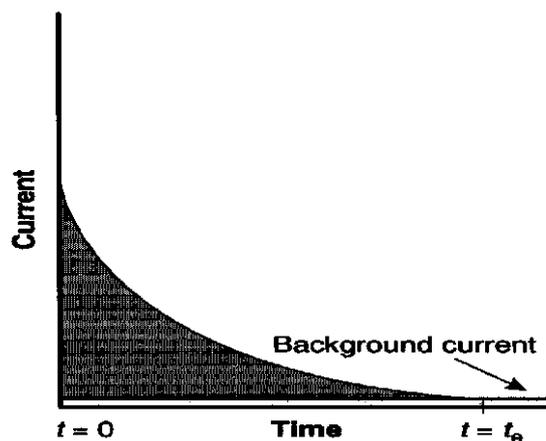
Figure 1.11 The current change during electrolysis at constant applied potential as the starting material is consumed.

Figure 1.11 shows that charge- passed as a function of the electrolysis time. The integration of the i-t curve gives charge passed Q_{total} during the course of the electrolysis and corresponds to the area under the curve. Q_{total} is reached when all of the substrate O is consumed substance and provides a measure of the number of electrons (n) involved in the overall reduction (or oxidation) from the Faraday equation:

$$Q = nNF \qquad\qquad 1.13$$

Where Q is number of coulombs passed, n is number of electrons involved, N represents the number of moles of complex, and *F* is the faraday constant (96485 C). The rate of electrolysis depends on two factors, the area of working electrode surface and the rate of stirring of the electrolyte solution [7-10].

In an uncomplicated electrolysis the current measured at time *t* is proportional to the concentration of the starting material in solution at that time. The amount of starting material present is of course proportional to the charge passed at that time. Thus a plot of *i(t) versus Q(t)/F* will be linear with the intercept at *i* = 0 corresponding to the number of electrons consumed.

1.2.5 Electrocatalysis

1.2.5.1 Introduction

Electrocatalaysis (**EC′ reaction**) can be defined as the catalytic production of a substrate by a chemical species, derived from an electrochemical reduction or oxidation of a starting material. Similar to chemical reactions, many electrochemical reactions in the absence of catalyst require overpotential to achieve the catalysis at a fast rate. Therefore, it is necessary to find catalyst to perform the reduction or oxidation at lower potential and high current density also to drive the reaction for favourable products. To catalyse the electrode reactions, the catalyst is attached to electrode surface or dissolved in electrolyte solution, in some cases the catalyst is the electrode material itself [11]. When the electrocatalyst is attached to the electrode surface or the electrode itself is the electrocatalytic material then this is referred to as heterogenous electrocatalysis. When the catalyst is molecular and freely diffusing in solution then the process is referred to as homogenous electrocatalysis. **Table 1.1** shows the comparison between homogeneous and heterogeneous electrocatalysis [12, 13]. This thesis is concerned with homogeneous electrocatalysis.

1.1. Comparison between Homogeneous and Heterogeneous electrocatalysis.

Comparison	Homogeneous	Heterogeneous
Selectivity	High	Low
Mass Transfer Limitations	Very rare	Can be severe
Structure/Mechanism	Defined	Undefined
Applicability	Limited	Wide
Catalyst Separation	Difficult	Easy
Cost of Catalyst Losses	High	Low

1.2.5.2 Heterogeneous electrocatalysis

In the process of heterogeneous electrocatalysis, the catalyst is attached at the electrode surface or is itself the electrode surface (eg platinum for proton reduction) . The processes occur by three steps as shown in Figure 1.13. These are diffusion of substrate from the bulk to the interface, electron-transfer and diffusion of the product to the bulk solution, [11, 12].
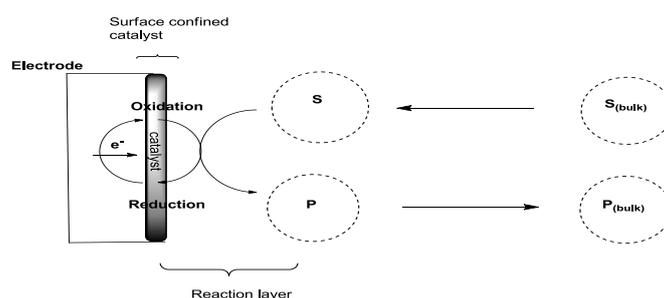
Figure 1.13 The heterogeneous electrocatalysis processes [11].

1.2.5.3 Homogeneous electrocatalysis

In homogeneous electrocatalysis, the electrons exchange take place in the bulk solution between the substrate and catalyst, it is not between the substrate and the electrode directly [13, 14] as illustrated in Figure1.14.
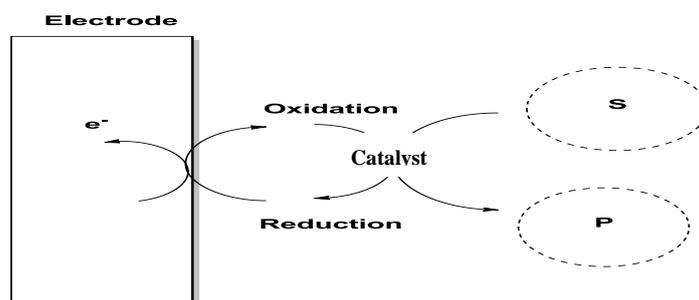
Figure 1.14 The homogeneous electrocatalysis processes [11].

The mechanism for electrocatalysis reaction is described as **an EC′ reaction**, in which E is a heterogeneous electron transfer and C is a homogenous chemical

reaction with the prime (′) commonly used to distinguish between a simple

chemical step and a catalytic process.

 The catalytic mechanism can be described by following Scheme1.4:

$$O \ + \ ne^- \ \rightleftharpoons \ R$$

$$R \ + \ X \ \xrightarrow{\ k\ } \ O \ + \ Y$$
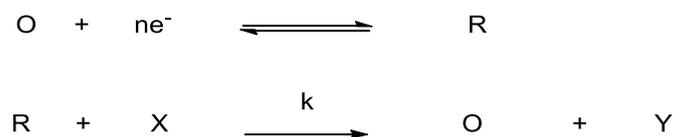
Scheme1.4

Scheme 1.4 shows in the first step, the reduction of catalyst by n electrons to

generate R then in the second step R reacts chemically with X to yield Y and the

catalyst O. If the rate of reaction is small or the scan rate is fast then the chemical

reaction will have no effect on cyclic voltammetry of starting material and a

reversible process will be observed. On the other hand, if k is large or the scan

rate is slow, the current will be increased as X reacts with R and the process

becomes irreversible. However, the value of the catalytic current response is

dependent on the rate of reaction between R and X as well as in concentration of

substrates X. Figure 1.15 shows the cyclic voltammetry for the EC′ process

[1,4,15].
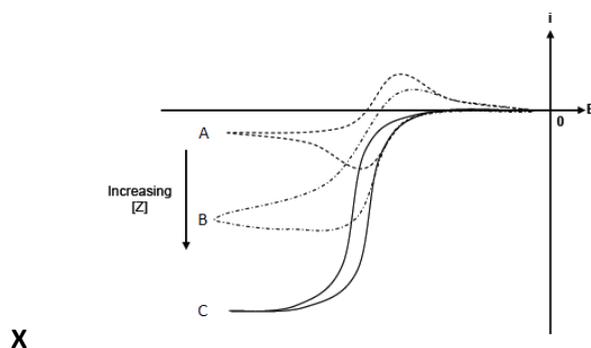
Figure 1.15 Cyclic voltammogram for the EC′ process, (A) in the absence of substrate X, (B) in

the presence of xM of substrate X, (C) in the presence of nxM of substrate X [15]

35

The rate constant of the reaction (k_{cat}) can be calculated at 25 ^{0}C using the relationships below. The value of the peak current i_o in the absence of substrate is given by the Randles – Sevcik equation (1.13) :

$$i_o = (2.69 \times 10^5)\, n^{3/2} A D_0^{1/2} C_0 v^{1/2} \qquad\qquad 1.13$$

The magnitude of i_{cat}, the plateau current, is given by Equation 1.14 [16].

$$i_{cat} = nFA\, [C_0](D_0 k_{obs})^{1/2} \qquad\qquad 1.14$$

Where A is the electrode area and C_0 and D_0 are the concentration of the catalyst and its diffusion coefficient respectively. Dividing equation 1.14 by equation1.13 provides a simple relationship between the ratio $i_{cat}\,/\,i_o$ and k_{obs} which conveniently eliminates C_0, A and D_0 , Equation 1.15, [17]. Note $n^{3/2}$ is usually 1 and *n* is not the same as n.

$$i_{cat}/i_0 = \frac{n}{0.4463}\sqrt{\frac{RTk_{obs}}{Fv}} \qquad\qquad (1.15)$$

Where, n is the number of electrons involved in the catalysis, T is the temperature in K (298K), R is the gas constant , F is the Faraday constant , v is the scan rate in V/s and k_{obs} is the observed rate constant. The catalytic rate constant k_{cat} can be calculated from k_{obs} using the relationship in equation (1.16) where [S] is the concentration of the substrate in a first-order reaction. [When the catalytic current has a second-order dependence on substrate concentration, for example in hydrogen evolution, then [S] is replaced by [S]^2 in equation 1.16].

$$k_{cat} = \frac{k_{obs}}{[S]} \qquad\qquad 1.16$$

1.2.6 Photoelectrochemistry and photoelectrocatalysis at semiconductor electrodes

1.2.6.1 Introduction

Interest among scientists worldwide has surged in the field of photoelectrochemistry in particular its application in solar energy conversion into both electrical energy and chemical energy. Fossil fuels are currently the main source of energy. However, their long term consequences are unacceptable, and this has led scientists to look for alternative renewable energy sources. The sun supplies the earth with approximately 3×10^{24} joules a year which about 10,000 times more than human activity requires for energy use so research to exploit sunlight to generate solar fuels is now a major area of investigation [18 - 21].

In 1839 Becquerel originated the field of photoelectrochemistry when he produced a voltage and an electric current from immersed silver chloride electrode which is illuminated in an electrolytic solution and connected this electrode with a counter electrode; this was the first photoelectrochemical experiment. However, this phenomenon was not understood until 1954, when Brattain and Garrett classified the factors which could be affected on the chemical reactions occurring at the surface of germanium semiconductor electrodes [19]. Photoelectrochemistry to generate a 'solar fuel' using a semiconductor electrode was first reported over forty years ago when H_2 was produced by water splitting using an n-type TiO_2 electrode with a platinum electrocatalyst 1972 [20].

1.2.6.2 Semiconductor electrodes

Semiconductor electrodes are classified on the basis of the difference energy gap between the level of energy which is occupied by electrons and the empty level.

In case of metal electrode there is no gap between these levels, but in a semiconductor there are two levels, the valence and the conduction band, Figure 1.17.

Conduction band, CB ═══════ edge

Band Gap

Valence band, VB ═══════ edge
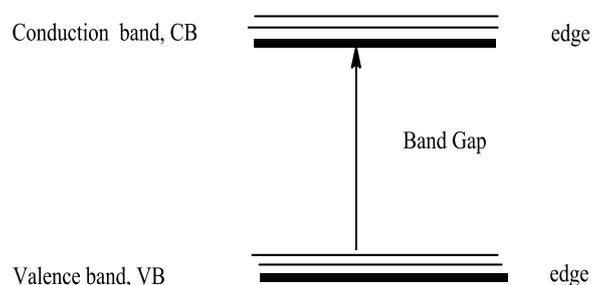
Figure 1.17 The valence and the conduction band in semiconductor

As with molecular orbitals the energy bands of interest are the highest occupied (valence band) and the lowest unoccupied (conduction band). The energy gap (band gap) between these bands determines the properties of material. **Table 1.2** summarises the band gaps of some common semiconductor materials [21, 22].

Material	Band gap (eV)
Si	1.12
Ge	0.66
GaAs	1.43
InP	1.43
CdTe	1.44
$Cd_{0.9}Zn_{0.1}Te$	1.57
PbI_2	2.3-2.5
HgI_2	2.13
TlBr	2.68

Table 1.2 The band gaps of some common semiconductor materials [22].

Semiconductor electrodes are considered as the attractive materials for photoelectrochemical energy conversion by light because the band gap allows charge separation and charge transfer [18]**.** This is illustrated by Figure 1.18 which schematically shows how a photocathode might function on illumination in the presence of a molecular electrocatalyst. When a semiconductor electrode is

illuminated with light which has energy higher than or equal to the band gap energy of the semiconductor the light is absorbed resulting in an electron promotion from valence band to conduction band. The consequence of this movement is to generate a positive charged vacancy in the valence band (which is called a hole). These holes are mobile and can be moved through space by transfer of an electron to the vacancy [18, 19, 20], importantly when the semiconductor is connected to a metallic contact the holes can be quenched by an electron − source. This leaves 'high energy' electrons populating the CB which can be transfer directly to a substrate or to an electrocatalyst for indirect reduction. The efficiency of the photoelectrochemical conversion depends upon various factors [23,24,25]. A key factor is the extent to which recombination processes within the semiconductor provide pathways for anihilating the electrons and holes.
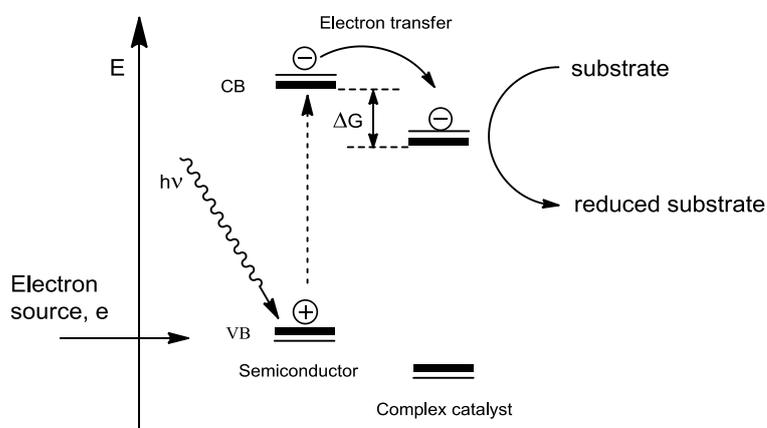
Figure 1.18 Illustration of reduction process on a semiconductor electrode under illumination by light.

The magnitude of the band gap is not the only consideration in a photoelectrochemical process. Where the energies of the VB and CB lie relative to the free electron in vacuum is represented by Figure1.19. A useful convention is the energy of the Fermi level (E_F) which corresponds to the energy at which an

electron in the semi-conductor has a 50% probability of occupying the VB and CB. For an undoped semiconductor this lies midway between the VB and CB. The value of E_F for various semiconductor materials can be related to standard electrochemical reference couples such as the normal hydrogen electrode NHE, SCE or ferrocene and Table 1.1 lists some values.

The conductivity of a semiconductor can be dramatically enhanced by doping. This involves the addition of donor or acceptor atoms in the semiconductor lattice. Doping with donor atoms, for example As in Si, gives a n-type semiconductor in which the charge carriers are predominately the electrons in the CB, Figure 1.19. Conversely doping with acceptor atoms, for example B in Si gives a p-type semiconductor in which the majority charge carriers are the holes in the VB, Figure 1.19. In a moderately to heavily doped semi-conductor the position of E_F lies close to the CB for a n-type material whereas it lies close to the VB in a p-type material.
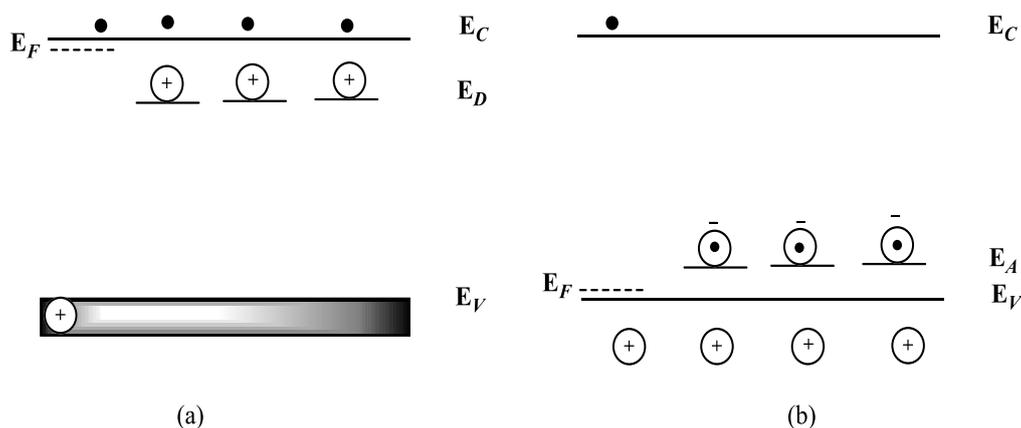
Figure1.19 Energy band gaps of semiconductor lattices. (a) n-type. (b) p-type.[4]

There are other important aspects of semiconductor electrochemistry and photoelectrochemistry which are important to the understanding of electron – transfer at the semiconductor/photoelectrode – solution interface in the presence

of a redox active material. The concepts of band bending and Fermi level pinning as described in early work by Bard, Wrighton and others has been extensively reviewed. Figure1.20 illustrates how the application of a potential across the interface at a p-type semiconductor can be viewed in terms of CB and VB bending at potentials positive or negative of the flat-band potential of the Fermi level in a p-type semiconductor [4, 26, 27].
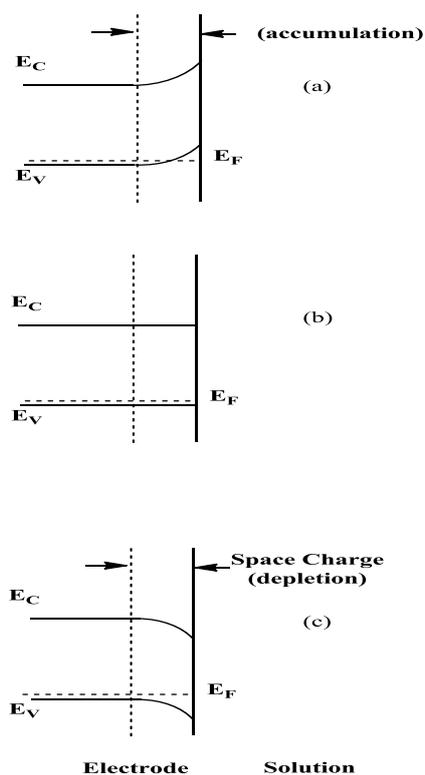
Figure 1.20 Effect of varying the applied potential (E) on the band edges in the interior of a p-type semiconductor. a) $E > E_{fb}$ b) $E = E_{fb}$ c) $E < E_{fb}$

1.3 References

1. R. Greef, R. Peat, L. M. Peter, D. Pletcher, J. Robinson. " Instrumental Methods in Electrochemistry". Woodhead Publishing Limited. Cambridge . **2011**.

2. A. Bard, M. Fox. Acc. Chem. Res. **1995**, 28, 141-145.

3. D. Sawyer, J. Beebe, W. Heineman. "Chemistry Experiments for instrumental Methods". John Wiley & Sons. New York. **1984**.

4. J. A. Bard, L. R. Faulkner. "Electrochemical Methods Fundamentals and Application" John Wiley & Sons. New York. **2001**.

5. J. Wang. "Analytical electrochemistry" John Wiley& Sons. New York . **2006**.

6. B. Vassos, G. Ewing."Electroanalytical chemistry". John Wiley, New York.**1983**.

7. R. Compton, C. Banks. "Understanding voltammetry" .World scientific publishing Co. Pte. Ltd. London. **2011**.

8. A. Brett, C. Brett. "Electrochemistry Principles, Methods and Applications". Oxford University Press Inc. **1993**.

9. V. Mirceski**,** J. Electroanal. Chem. **2001**, 508, 138-149.

10. G. Mabbott, J. Chem. Educ. **1983**, 60, 697-701.

11. K. Cheung, W. Wong, D. Ma, T. Lai, K. Wong. Coord. Chem. Rev. **2007**, 251, 2367-2385.

12. L. Bhangun, D. Lexa, J-M. Saveant, J. Am. Chem. Soc. **1996**, 118, 1769-1776.

13. J. Hagen, Industrial Catalysis: a Practical Approach, 2nd ed. Wiley–VCH, Weinheim. **2006**.

14. C. P. Andrieux, J. D. Bouchiat, J-M. Saveant. J. Electroanal. Chem. **1978**, 39, 11-87.

15. C. Tard, D. Phil.Thesis, University of East Anglia. **2005**.

16. D. Pool, M. Stewart, M. Hagan, W. Shaw, J. Roberts, R. Bullock, D. DuBois. PNAS. **2012**, 109, 15634-15639.

17. T. Liu, D. DuBois, R. Bullock. Nature Chem. **2013**, 5, 228-233.

18. M. Gratzel. Nature. **2001**, 414, 338-344.

19. J. Nozik, Ann. Rev. Phys. Chern. **1978**, 29 , 189-222.

20. H. Lewerenz ,C. Heine, K, Skorupska, N. Szabo, T. Hannappel, T. Vo-Dinh, S. A. Campbell, H. Klemm , A. G. Munoz. Energy Environ. Sci. **2010**, 3, 748-760.

21. A. Owens, A. Peacock, M. Bavdaz. Proc. of SPIE. **2003**, 4851, 1059-1070.

22. D. Tryk, A. Fujishima, K. Honda. J. Electrochim. Acta .**2000**, 45 , 2363-2376.

23. F. Osterloh. Chem. Mater. **2008**, 20, 35-54.

24. A. J. Bard. J. Phys. Chem. **1982**, 86, 177-181.

25. M. A. Butler, D. S. Ginley. J. Mater. Sci. **1980**, 15, 1-19

26. D. Wei, G.Amaratunga. Int. J. Electrochem. Sci. **2007**, 2, 897 - 912

Chapter 2

1 Hydrocarbon Oxidation Catalysed by Iron Porphyrins

2.1 Background and Objectives

2.1.1 Alkane and Alkene Oxidation in Biology

A common and important process in biochemical systems is conversion of an inactive C-H bond into an alcohol, by insertion of an oxygen atom from dioxygen [1]. In biological systems, there are two classes of enzymatic hydroxylation: methane monooxygenase and cytochrome P-450 [1]. How to achieve these transformations efficiently and selectively at room temperature by synthetic catalysts is still a formidable challenge, particularly when specificity is desired with regard to reactants and products, as in a biochemical context. There is a great interest in hydroxylation of C-H bonds and alkene epoxidation by enzymatic reactions or synthetic systems, as is evident from the wide number of metal complexes that have been developed and employed as catalysts for this purpose [1-4]. In the last few decades, mimics of cytochrome P-450 and methane monoxygenase, have been developed to test for their effectiveness toward hydrocarbon oxidation [2,3].

2.1.2 Methane monooxygenase (MMO)

Methane monooxygenase (MMO), catalyses the conversion of methane (C H bond energy, 104 kcal mol^{-1}), NADH and dioxygen to methanol and water. An equation for methane oxidation by MMO, was first proposed by Foster and Leadbetter in 1959 [4] Equation 2.1.

$$CH_4 + O_2 + NADH + H^+ \xrightarrow{\quad MMO \quad} CH_3OH + H_2O + NAD^+ \quad 2.1$$

This reaction is the first step in the metabolic pathway of methanotrophic bacteria, which utilize methane as their sole source of carbon and energy [5].
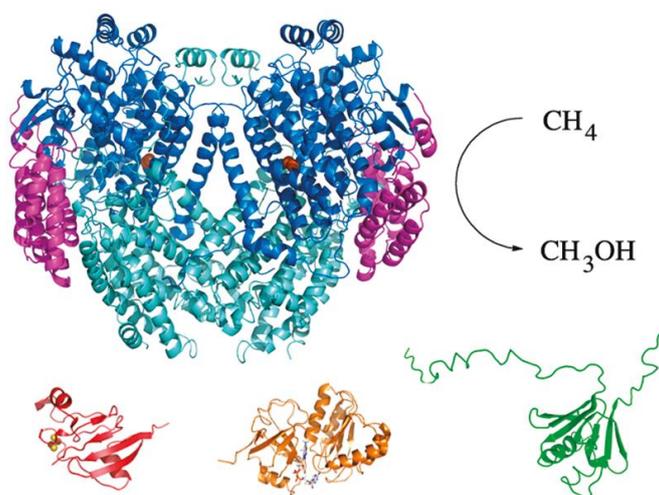
Figure 2.1 Dioxygen activation in soluble methane monooxygenase

There are two types of MMO systems, a soluble, cytoplasmic complex (sMMO) and a membrane-bound, particulate system (pMMO). Both MMOs utilize a metal centre to activate atmospheric dioxygen, which then attacks a strong C-H bond of methane [3, 4].

Due to the importance of methane as an energy vector, there is significant interest to develop processes that allow us to generate alternative fuels, in a sustainable manner, for use as sources of renewable energy. Methane gas is an abundant precursor of liquid fuels, but current approaches for conversion of methane to methanol are uneconomical as well as unsustainable [4,6].

2.1.3 Cytochrome P450 enzyme

Alkane hydroxylation and alkene epoxidation are important industrial processes, but achieving these transformations efficiently and selectively is still a formidable challenge. It is well known that cytochrome P450 enzymes catalyse a wide range of hydrocarbon oxidations under mild condition [7]. Cytochrome P450 enzymes are present in all forms of life (plants, bacteria, and mammals), and play important roles in their biological system, with their major role being the detoxification of foreign compounds within the liver. Due to this importance, the P450s have been studied to determine the mechanism of catalysis with substrates (hydrocarbons) , and there is therefore a great interest in the preparation of synthetic metalloporphyrins which mimic the structure of P450 [2,3]. The reaction of cytochrome P450 is shown in equation.2.2 [7].

$$RH + O_2 + NADPH + H^+ \longrightarrow ROH + H_2O + NADP^+ \qquad 2.2$$

In recent years, there has been significant progress in understanding the catalytic cycle of the P450 enzyme, which was first proposed in 1968 (scheme 2.1) [8].
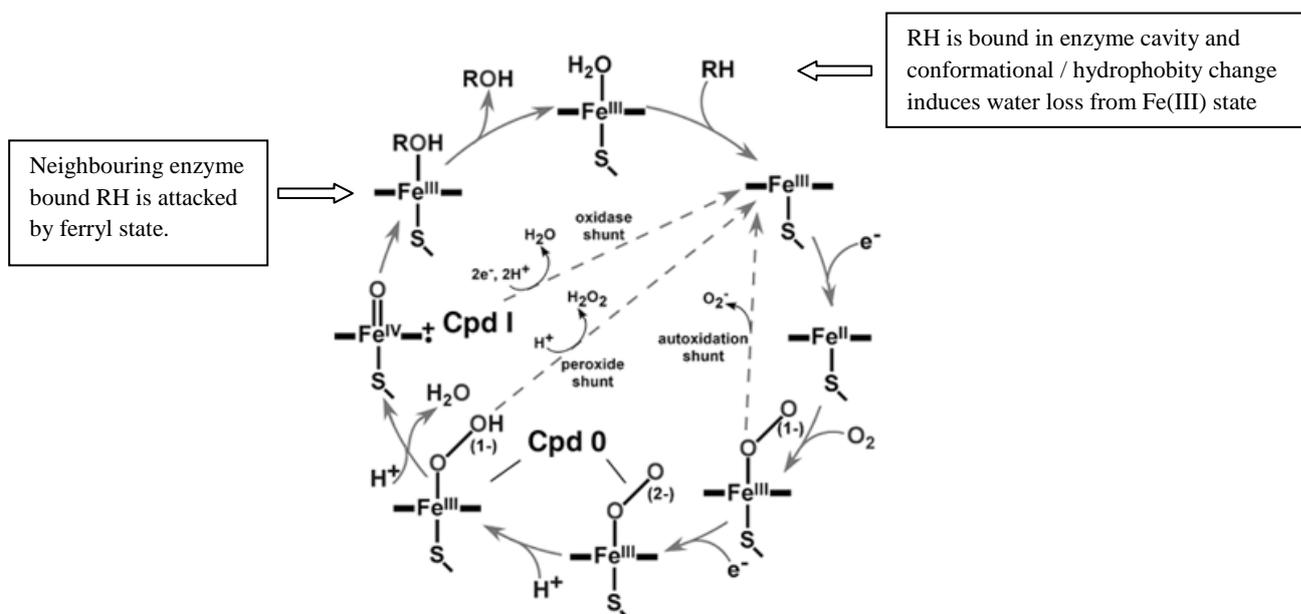
Scheme 2.1 The P450 catalytic cycle. Modified from reference [8].

The catalytic process starts with a ferric –enzyme that is in the low-spin state. Typically, the distal position of the ferric enzyme is coordinated by a water molecule as the sixth ligand, coordinated to iron, which then changes to a high spin state. A substrate (RH) binds near the Fe centre and induces the displacement of the water ligand, which serves to shift the redox potential to a more positive value. The transfer of the first electron in the presence of oxygen leads to a ferrous dioxy complex. Following this, the ferric peroxy intermediate is generated by a second electron transfer. This species is then protonated to produce the ferric hydroperoxo intermediate which is unstable. The oxygen-oxygen bond breaks directly to give water and an oxo-ferryl intermediate which is a highly reactive complex. Ultimately, the oxo-ferric complex reacts with the neighbouring protein bound substrate (RH) to produce an alcohol and turn the enzyme to a ferric state. This catalytic cycle does however suffer from three major problems that lead to undesired products [8]:

(1)- Oxidation of the oxy-ferrous enzyme leads to a return to the initial state.

(2)- Dissociation of the peroxide or hydroperoxide anions from the complex, which generates hydrogen peroxide.

(3)-The oxo ferryl radical cation is reduced to water and thus loses its role in substrate oxidation.

2.1.4 Porphyrins

Ever since the discovery of the P450 enzymes, much effort has been focused on the development of novel model porphyrin mimics [9, 10]. Tetraphenylporphyrin (TTP) was the first such complex reported, prepared from pyrrole and a benzaldehyde by Rothmund in 1936 [10]. Since then, this area of research has grown rapidly [7-11], with the preparation of many new complexes achieved and these model systems have been utilised to probe the effects that substitution onto the porphyrin ring, and variation of the axial ligands coordinated to the metal centre (such as thiolates and chloride ligands) has on that impact of alkane and alkene oxidation [7, 9,10].

2.1.4.1 Porphyrin structure.

 The porphyrin structure includes four pyrrole rings, linked by methane bridges, with a metal centre coordinated by the four central nitrogen atoms.   This coordination leads to the loss of the protons from two of the nitrogen atoms, and the metal centre has two remaining, axial coordination sites Figure 2.2 [12].
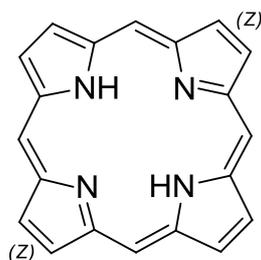
Figure 2.2 Porphyrin ring

In recent years, synthetic iron porphyrins have been used as catalysts in hydrocarbon oxidations [2,3]. It has been established that the hydroxylation of inactive alkanes, and the epoxidation of alkenes, catalysed by iron porphyrins, depends on the generation of an oxo ferryl radical cation, which reacts with alkanes and alkenes to produce alcohols and epoxides respectively, under mild conditions [1]. According to previous studies, alkane oxidation occurs by hydrogen abstraction from an alkane, whilst alkene epoxidation occurs by a one electron transfer [13]. There are numerous ways to generate oxo ferryl radical cations. The most common method is to employ an oxygen transfer reagent, such as iodosylbenzene (PhIO), meta-chloroperoxybenzoic acid (m-CPBA) or H_2O_2. Iodosylbenzene was the first reported oxidant used to generate the oxo ferryl radical, and is still widely used as a single oxygen atom donor [14]. Where reactive oxo species have been generated by electrochemical reduction of dioxygen, the obvious alternative, the generation of the oxo ferryl radical cation by electrochemically oxidation of bound water is a relatively unexplored area.

2.1.4.2 The effect of substitution on the porphyrin ring

Previous studies indicate that substitution of porphyrin rings plays a major role in their catalytic properties. The most efficient Fe-porphyrin rings bear electron-withdrawing groups such as penta-fluoro, which decreases electron density at the

iron centre. This facilitates generation of the oxo ferryl radical cation, whilst shifting the redox potentials to more positive values. The inverse is true when attaching electro-donating groups such as methoxy, with the increase in electron density at iron centre making it more difficult to generate the oxo ferryl radical cation, as well as generating a negative shift in the oxidation potential [14a]. The ligands introduced to provided steric effects to avoid the formation of catalytically inactive complexes or to enhance the electrophilicity of the metal-oxo entity by withdrawing groups, eg the stability of iron-TPP catalyst is enhanced by pentafluorophenyl occupying the meso position of the porphyrin ring [14b].

2.1.4.3 Chemical hydrocarbon oxidation using porphyrins

Groves and co-workers [15] were the first to report the hydroxylation of saturated C-H bonds catalysed by metal porphyrins. In their study they used the meso-tetraphenylporphyrin chloride complex [Fe(TPP)Cl] to catalyse the oxidation of cyclohexane and adamantane with iodosylbenzene(PhIO) as an oxidant. This to give their alcohol derivatives (cyclohexanol, 1-adamantanol, 2- adamantanol) with yields of 8 % and 13% , 1% , respectively (based on iodosobenzene). By altering the solvent from dichloromethane to benzene in the presence of excess cyclohexane, Mansuy and co-work managed to increase the yield of cyclohexanol to 19% [16]. Groves used iron tetrakis(2-methyl-phenyl)porphyrin to increase the yield of cyclohexanol marginally to 20% [17].

The importance of introducing electron withdrawing groups was neatly highlighted by Chang, by employing an iron tetrakis(pentaflourophenyl)porphyrin to give a 71% yield of cyclohexanol [18]. This was followed by Traylor *et al*. who

similarly obtained yields of 73% using iron tetrakis(2,6-dichlorophenyl)porphyrin with pentafluoroiodosobenzene as an oxidant [19].

Mario *et al*. [20] used iron-tetraphenylporphyrin to study the mechanism of the catalytic oxidation of cyclohexane using iodosobenezene as the oxidant. This study was carried out in CH_2Cl_2 and they described the mechanism of the reaction by four steps, which involved a competitive oxidation of iodosobenzene to give iodoxybenzene:

$$PhIO + \text{Fe-porphyrin} \xrightarrow{k_1} PhI + \text{OFe-porphyrin} \qquad 2.3$$

$$\text{OFe-porphyrin} + Cy\text{-}H \xrightarrow{k_2} \text{Fe-porphyrin} + CyOH \qquad 2.4$$

$$\text{OFe-porphyrin} + PhIO \xrightarrow{k_3} \text{Fe-porphyrin} + PhIO_2 \qquad 2.5$$

$$\text{OFe-porphyrin} + Fe \xrightarrow{k_4} \text{Fe-porphyrin} + \text{degradation} \qquad 2.6$$
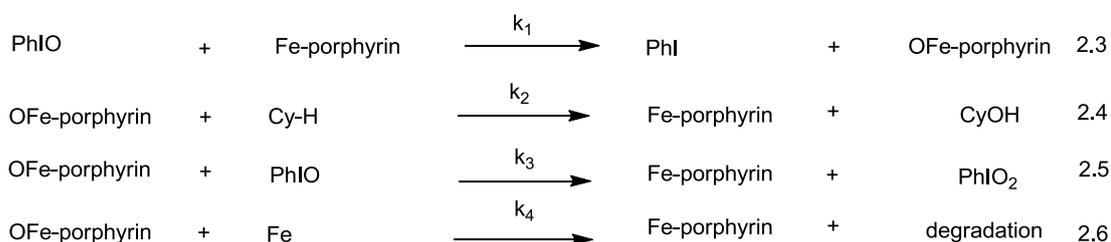
The first step (reaction 2.3) involves oxygen transfer from oxidant to iron porphyrin, to generate the active oxo-ferryl intermediate, and the second step (reaction 2.4) is insertion of the oxygen atom into the inactive alkane bond (C-H) to generate alcohol (cyclohexanol). The following steps show the competitive reactions among the oxo- ferryl intermediates firstly with iodosobenzene to produce iodoxybenzene, and secondly degradation of the iron-porphyrin, reactions (2.5) and (2.6).

In 2001, Nam and co-workers [21] studied cyclohexane and adamantane oxidation with meta-chloroperoxybenzoic acid (m-CPBA), catalysed by $[Co(III)(F_2OTPP)]CF_3SO_3$. They reported the conversion of cyclohexane to cyclohexanol in 39 % yield, and cyclohexanone in 8 % yield, based on PhIO. The oxidation of adamantane resulted in the isolation of 1-adamantanol in 53 % yield, and 2-adamantanol in 9% yield.

In a subsequent study, Nam *et al.* [22] investigated the ability of [bis(acetoxy)iodo]benzene PhI(OAC)$_2$, in the presence of water as an oxygen source, to catalyse the hydroxylation of cyclooctane and cyclohexane, as well as the epoxidation of cyclooctene and cyclohexene by Fe(TPFPP)Cl. The major products were found to be cyclooctanol and cyclohexanol in 47 % and 37 % yields respectively, with small proportions of ketone (6-7 %), based on PhI(OAC)$_2$. The epoxidation of cyclohexene and cyclooctene gave large yields of cyclohexene oxide and cyclooctene oxide, 90% and 98% respectively.

Chun *et al.* [23] have used the meso-tetrakis (pentafluorophenyl) porphinato manganese(III) chloride, for the epoxide of alkenes with Ph(OAc)$_2$ in ionic liquid at room temperature. This study has shown high yields for conversion, e.g., cyclohexene is converted into cyclohexene epoxidation by 98% as conversion and yield 74% .

The mechanisms of hydrocarbon oxidation catalysed by metalloporphyrins were widely studied during the period of 1979-1999 [10, 25]. All of these studies agreed that the mechanism is based on the transfer of an oxygen atom [e.g. PhIO, H_2O_2, m-(CPBA), etc.). Oxygen transfer from oxidant to metal–porphyrin, leads to generation of the reactive M=O intermediate, which is able to insert the oxygen atom into the saturated C-H bond, by abstraction of a hydrogen atom [14].

2.1.4.4 Electrochemical hydrocarbon oxidation using porphyrins

There is a large interest in using electrochemistry to study the behaviour of porphyrin complexes, used to catalyse the hydrocarbon oxidation [26].

Of the first studies of electrochemistry, Mellor et al. reported the electrochemical oxidation of adamantane and substituted derivatives in the absence of catalyst,

with cyclic voltammetry of adamantane in acetonitrile showing two oxidation waves at 2.38 V and 2.88V vs Ag/AgNO$_3$, the anodic oxidation leads to removal of two electrons in the first oxidation and a further two in second oxidation [27].

To investigate the electrochemical behaviour of the porphyrin, Groves *et al.* [28] reported the cyclic voltammograms of iron[(III)] tetramesityl porphyrins [(TMP) Fe[(III)]Cl] under various conditions. Firstly, cyclic voltammetry of [(TMP) Fe[(III)]Cl] was carried out in CH$_2$Cl$_2$ in the presence of 0.1M tetrabutylammonium perchlorate (TBAP) in the range of 0.00 to +1.8 V, resulting in the appearance of two quasi-reversible waves at 1.15 V and 1.5 V. Secondly, cyclic voltammetry was performed in a mixture of 9:1 acetonitrile and water containing 0.1 M HClO$_4$, which revealed a reversible one electron oxidation at + 1.01 V and a reversible two electron oxidation at +1.34V. Thirdly, oxidation of the hydroxide complex (TMP) Fe[(III)]OH in DCM, in the presence of TBAP, showed three waves , one reversible wave at +1.00 V , one broad, irreversible wave, and a third wave at +1.55V (all potentials *vs.* Hg/HgO). [See *Appendix*]

Murray *et al.* [29] performed an electrochemical reductive epoxidation of alkenes, in the presence of a manganese porphyrin and (C$_6$H$_5$CO)$_2$O, to yield epoxides

$$\text{alkene} + O_2 + (C_6H_5CO)_2O + 2e^- \xrightarrow{\text{Mn(TPP)Cl}} \text{epoxide} + 2\ C_6H_5COO^- \qquad 2.7$$
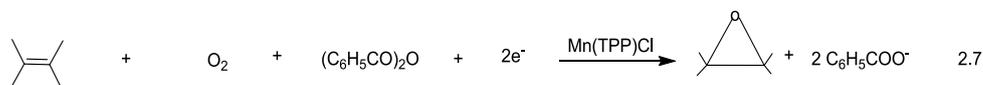
Murray and co-workers described the mechanism for electrocatalytic epoxidation of olefins, which involved the initial binding of O$_2$ to the Mn(III) porphyrin, followed by a one–electron reduction to generate the Mn(III)-peroxo porphyrin. Subsequently, dioxygen cleavage by an electrophilic activator such as benzoic

anhydride, leads to formation of Mn(II)-oxo, concluding with oxygen transfer to the olefin to produce an epoxide species.

Oliver *et al.* [30] have reported that electrocatalytic oxidation of styrene by a high valent ruthenium porphyrin cation radical. Electrolysis was carried out at a potential of 1.37 V, with resulting products analysed by gas chromatography. The major product is phenylacetaldehyde (96 %), and the minor product benzaldehyde (4 %.) equation 2.8 and scheme 2.2.
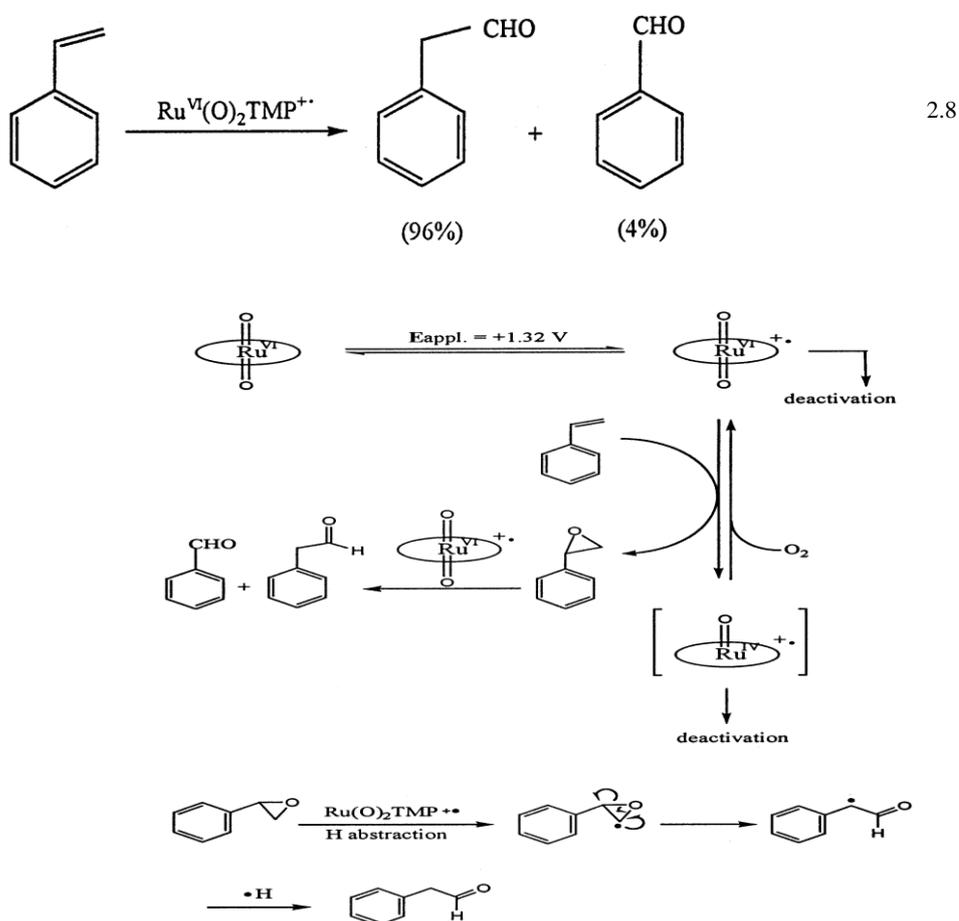
Scheme 2.2 The reaction mechanism proposed of electrocatalytic oxidation of styrene by a high valent ruthenium porphyrin cation radical [30].

Haber *et al.* [31] have studied manganese porphyrins as catalysts for oxidation of cyclooctane in a 'Lyons' system. Manganese meso-tetraphenyl porphyrins

(Mn(III) TTP) with varying axial ligands (F⁻, Cl⁻, Br⁻⁾ were used for a comparative cyclooctane oxidation study, to compare the effects of these axial ligands. They reported the products of cyclooctane oxidation to be cyclooctanone and cyclooctanol, suggesting a shift in the order of activity as following..

F⁻ > CH₃COO⁻ > Cl⁻ ≥ OH⁻ > Br ⁻ > I⁻

2.1.5 Summary of background chemistry

In summary, high valent ferryl porphyrin generated by chemical oxygen atom transfer, using reagents such as iodosobenzene have been widely utilised for studies of cytochrome P450 analogues [1-4, 7, 13, 14-25]. Generation of ferryl intermediates and oxomanganese species by electrochemical reduction in the presence of dioxygen has also received some attention [26-32]. However generation of high valent oxo intermediates by electrochemical oxidation in the presence of water as the oxygen source has received little attention [28] and the use of iron porphyrin electrocatalysts for oxidation of hydrocarbons by such a pathway is very limited. There is only a single report on the oxidation of an alkane by electrochemical oxidation of an iron porphyrin [30] and this gives very little detail. Similarly, studies on electrochemical alkene oxidation are confined to a single report [29] with the source of [O] for the oxygenation not clear beyond a single turnover.

2.1.6 Scope of this work

The scope of this research is to develop a methodology for chemical and electrochemical catalysis of alkane oxidation and alkene epoxidation by thiolate iron (III) porphyrins, as cytochrome P450 mimics.

This chapter will describe the electrocatalytic oxidation of hydrocarbons, using conventional and novel iron porphyrin electrocatalyst which possess an axial thiolate ligand as is seen in the cytochrome P450 enzymes [33-38]. These synthetic iron porphyrins possess structurally robust axial thiolate coordination, which is provided by a basket-handle arrangement in the systems described herein, with the rigid basket-handle possibly providing steric protection of the S-ligand from oxidative degradation. These thiolate iron(III) porphyrins were designed and synthesised in our lab [39] and their structures are shown in Figure 2.3.
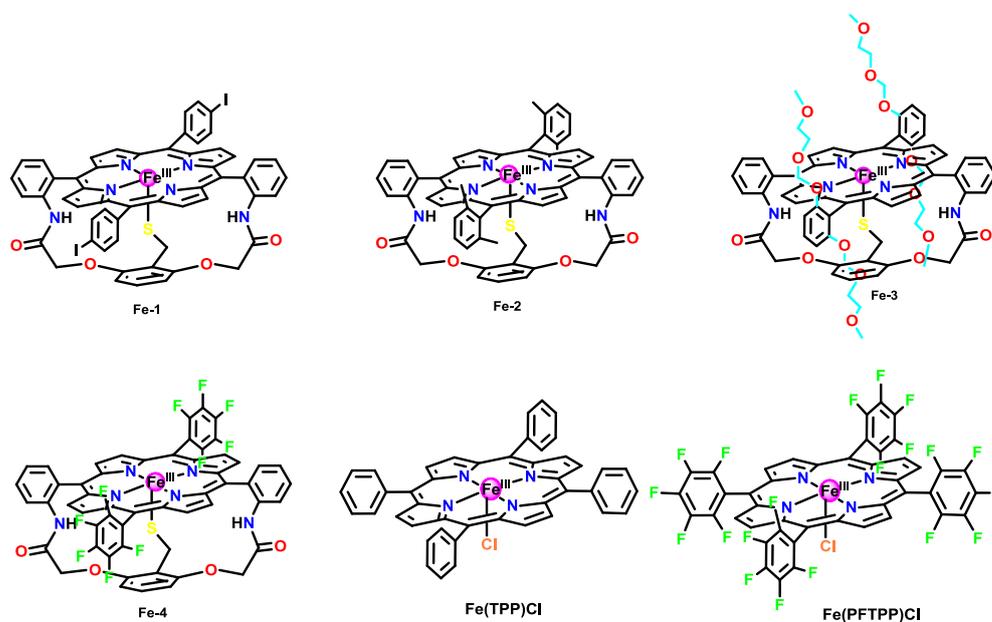
Figure 2:3   Molecular structures **of Fe(TPP)Cl**, **Fe(PFTPP)Cl** and basket-handle iron(III) porphrins [39]

The natural and synthetic catalyst systems are understood to operate *via* the formation of an oxo ferryl porphyrin radical cation which abstracts a hydrogen atom from hydrocarbon C—H bond [1, 36]. It would appear that there are two principal indicators of the reactivity of the active species, the oxidation potential E_o necessary to access the oxo ferryl porphyrin radical cation species, and the pKa of the Fe(IV)-OH intermediate formed by H-atom abstraction [9]. Electron-withdrawing groups on the porphyrin ring increase the oxidising power of the ferryl porphyrin radical cation and this is reflected by a more positive E_o. On the other hand, a more electron-donating group in the axial position will increase the O—H bond strength by increasing the pKa. We have explored this balance by synthesising a range of Fe porphyrin precursors shown in Figure 2.3 which possess electron-donating or -withdrawing substituent groups. The aim of this study was to find the optimum conditions for catalysing adamantane hydroxylation and cyclooctene epoxidation both electrochemically and chemically using conventional and basket handle thiolate iron(III) porphyrin catalysts. The catalytic activities of the thiolate systems are benchmarked against the activity of **Fe(PFTPP)Cl** (meso-tetrakis(pentafluorophenyl)porphyriniron(III) chloride), one of the most robust and efficient iron porphyrin catalysts, and **Fe(TPP)Cl** (meso-tetraphenylporphyriniron(III) chloride), to probe the effect of the thiolate ligand and other substituents on the catalytic activity.

The products of both chemical and electrochemical oxidation were analysed by gas chromatography to determine their identity, final yield and catalytic efficiency.

2.2 Results and discussion

2.2.1 Chemical oxidation

Chemical oxidation of adamantane and cyclooctene using iodosylbenzene (PhIO) as an oxygen source catalysed by the various iron prophyrin complexes were carried out in CH_2Cl_2 at 20 °C under N_2 for 1 hour. The analyte solution was filtered by a short pad of dry celite and the yield of products were analysised by gas chromatography (GC-FID) and quantified with bromobenzene (PhBr) and decane respectively as internal standards. Under our reaction conditions, we found that all the new iron porphyrins **Fe-1** to **Fe-4** catalysed the oxidation of adamantane and cyclooctene to 1-adamantanol and cyclooctene oxide respectively, with minimal formation of other hydrocarbon oxidation products Table 2.1.

2.2.1.1 Illustrative results: adamantane oxidation with iodosobenzene catalysed by porphyrins

As an example of adamantane oxidation we show the comparative results for the complex **Fe(PFPP)Cl** and **Fe-4**. GC analysis of adamantane oxidation catalysed by **Fe (PFPP)Cl** showed a 60.8% yield of 1-adamantanol, retention time 4.88 m, Figure(2.4)a. Under the same conditions, complex **Fe-4** showed a 43.4 % yield of 1-adamantanol. The other peaks correspond to PhBr at 2.58min, PhI at 3.12 m, and adamantane at 3.48 m, Figure (2.4)a,b. The minor peak at 5.56 minutes is assigned to 2-adamantanol as observed in previous studies which show this as a product from reaction of adamantane hydroxylation catalysed by porphyrins [1,12].
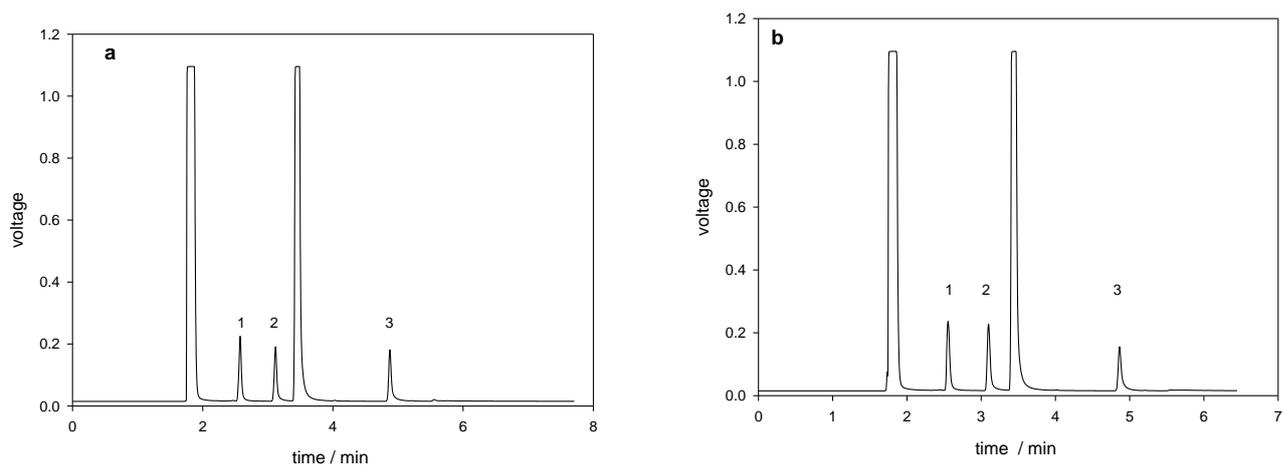
Figure 2.4 Gas chromatography of adamantane oxidation with PhIO catalysed by (a) **Fe (PFPP)Cl**,(b) **Fe-4.** 1 is PhBr, 2 is PhI , 3 is 1-adamantanol.

2.2.1.2 The relationship between yield of adamantanol and the ratio of iodosobenzene to catalyst.

Figure 2.5 shows the effect of the ratio of PhIO to catalyst on the conversion of adamantane to 1-adamantanol in the presence of **Fe(TPFPP)Cl**. (1×10^{-3} M , 1×10^{-6} moles)
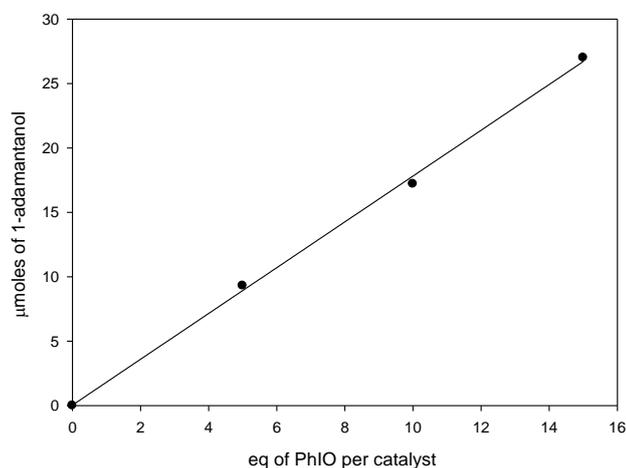
Figure 2.5 Effect of PhIO concentration on 1-adamantonol products

It is clear that increasing of oxidant/catalyst ratio led to an increase in the number of moles of 1-adamantanol. In the presence of (5, 10, 15 eq) of PhIO the reaction products were 9.3, 17.3 and 27.2 μmoles of 1-adamantanol respectively.

60

2.2.1.3 Illustrative results: cyclooctene epoxidation with iodosobenzene catalysed by iron porphyrins

In this section we have chosen the catalyst **Fe-1** as an example of basket-handle porphyrins to show the result cyclooctene epoxidation and for comparison show results obtained with **Fe(PFPP)Cl**. Typical results for cyclooctene epoxidation by **Fe-1** are shown in Figure 2.6. The peak for cyclooctene oxide appears at retention time 7.2 min and the four other peaks correspond to dichloromethane at 1.86 min, cyclooctene (starting material) at 3.49 min, decane as reference at 4.27 min and PhI at 5.79.

The GC analysis of cyclooctene epoxidation catalysed by **Fe(PFPP)Cl** showed 86.2% yield of cyclooctene oxide based on PhIO consumed Figure (2.6)a. Under the same condition, the cyclooctene epoxidation catalysed by complex **Fe-1** gave a chemical yield 70.4% based on PhIO Figure (2.6)b. The yields of cyclooctene oxide by other catalysts are summarised in Table 2.1.
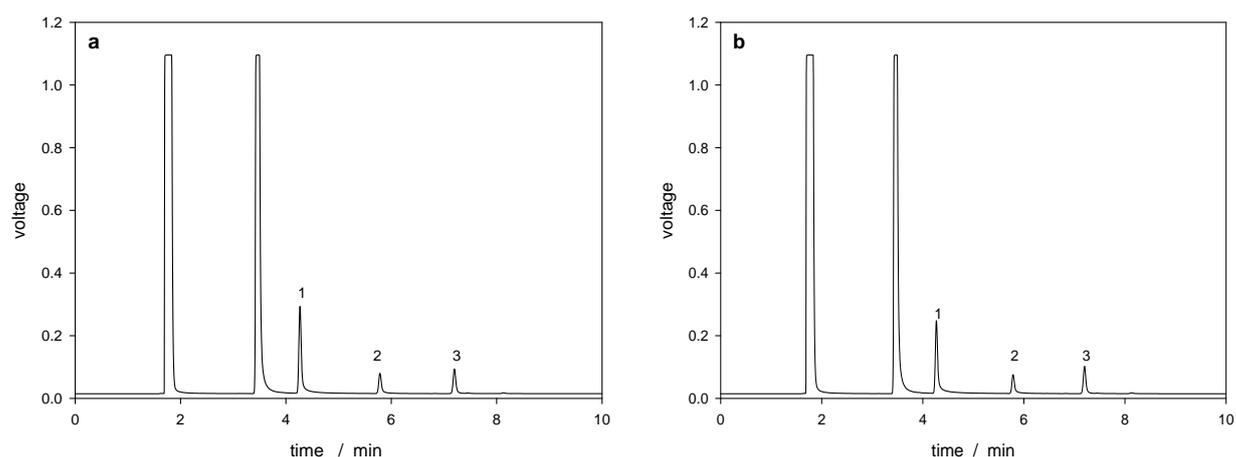
Figure 2.6 Gas chromatography of cyclooctene epoxidation with PhIO catalysed by (a) **Fe (PTPP) Cl**, (b) **Fe-1.** 1 is decane, 2 is PhI, 3 is cyclooctene oxide.

Table 2.1 Yields of Fe (III) porphyrin-catalysed adamantane/cyclooctene oxidations by PhIO[a].

Catalyst	1-Adamantanol		Cyclooctene oxide	
	Yield/%[b]	TON[c]	Yield/%[b]	TON[c]
Fe-1	22.5	3	70.4	5.2
Fe-2	34.7	2	69.7	5.5
Fe-3	10.5	0.53	66.4	4
Fe-4	43.4	3.2	86.1	6
Fe(TPPF$_{20}$)Cl	60.8	3.7	86.2	7
Fe(TPP)Cl	11.3	0.5	74.7	5.2

[a] Reactions were carried out in CH_2Cl_2 at 20 °C under N_2 for 1 hour. [Fe^{III} porphyrin]:1.0 mM; [PhIO]: 10 mM; [Adamantane or Cyclooctene]: 0.1 M. [b] Average value of two experiments based on PhIO consumed. [c] TON = moles of product/moles of catalyst. [Catalyst bleaches after 1 hour].

The first and simplest iron porphyrin catalyst **Fe(TPP)Cl** provides a benchmark [1,16] against which we can compare hydrocarbon oxidation by the thiolate porphyrins. Table 2.1 shows that all of the thiolate complexes except **Fe-3** have higher activity than **Fe(TPP)Cl**, both in terms of turnover number (TON) and yield of 1-adamantanol. The least electron-rich complex, **Fe-4** is the best thiolate based catalyst, the most electron-rich complex; **Fe-3** is the least active. This indicates that electron-withdrawing groups gives rise to the most reactive ferryl

unit[40,41]. This electronic effect must override the protection against Fe—O—Fe μ-oxo dimer formation (deactivation) that we might expect to be afforded by the oligoether chains of **Fe-3**. An earlier study of the pentafluorophenylporphyrin iron complex [16] showed notably high adamantane oxidation activity. In accord with this we find that **Fe(PFTPP)Cl** is the most active catalyst precursor under our conditions: it is correspondingly the hardest to oxidise electrochemically, Table 2.2. Other than electron density, the geometric arrangement around the thiolate sulfur may also play a role. The electron densities on **Fe-1** and **Fe-2** are very similar, yet the 1-adamantanol yield employing **Fe-2** (34.7%) is significantly higher than that for **Fe-1** (22.5%). The four *ortho*-methyl groups in **Fe-2** may shield the thiolate ligand from oxidative destruction and/or prevent the formation of the inactive μ-oxo dimer Scheme 2.3. Where there is no significant electronic perturbation of the porphyrin ring, as in the cases of **Fe-1** and **Fe(TPP)Cl**, then the sulfur axial ligand must favour hydrogen abstraction from the substrate, as demonstrated by the yield of 1-adamantanol (22.5% for **Fe-1** *vs* 11.3% for **Fe(TPP)Cl**). In an earlier study Higuchi *et al.*[42] were also able to show that a ring anchored benzyl thiolate had substantially better activity than **Fe(TPP)Cl** using a peroxy acid as the oxygen atom source.

In cyclooctene epoxidation, we found that all complexes exhibit a good yield but the complex **Fe-4** (86.%, TON 6) is the best catalyst while complex **Fe-3** gave the lower yield (66.4 %, TON 4) due to the reasons discussed above. If we compare the yield to each of the complexes with **Fe (PFPP)Cl** and **Fe(TPP)Cl**, it is noted that the yields of all complexes located in an area between the yield of **Fe(PFPP)Cl** and **Fe(TPP)**. With respect to epoxidation of the more reactive cyclooctene, the electronic and geometric effects of the iron porphyrins on the

catalytic activity are levelled out, regardless of the axial ligand, be it a chloride or a thiolate , the two most electron deficient iron porphrins gave the highest yields of ca. 85%, with the other complexes giving yields of ca. 70% , Table 2.1

Scheme 2.3 shows a possible mechanism for the catalytic cycle of adamantane and cyclooctene oxidation catalysed by iron (III) porphyrin. As suggested by [20].

inactive -oxo dimer
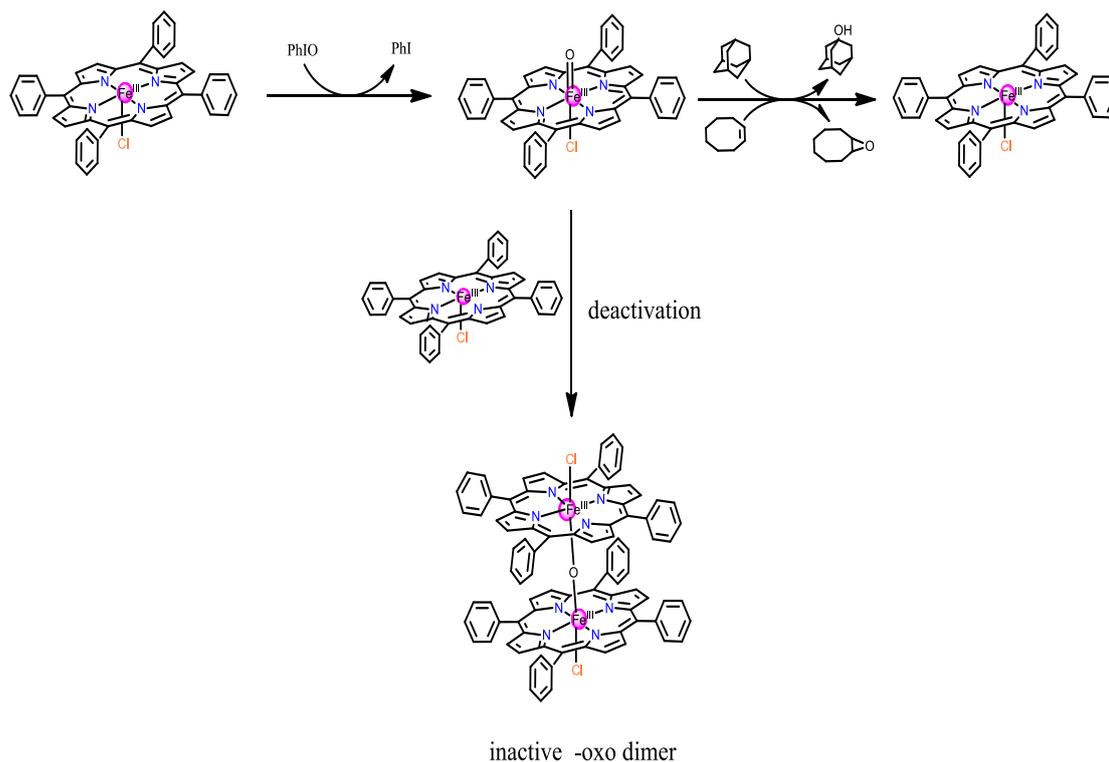
Scheme 2.3 Mechanism of catalytic cycle of adamantane and cyclooctene oxidation catalysed by iron (III) porphyrin

2.2.2 Electrochemical Oxidation of Hydrocarbons

An investigation of the electrochemical oxidation of adamantane and cyclooctene was carried out using cyclic voltammetry and controlled potential electrolysis techniques. Cyclic voltammetry studies were used to determine the appropriate potential for the oxidation of the catalyst used in the preparative scale the

electrolyses. The electrocatalysis was carried out for 1.5 h and the current was recorded as a function of the charge passed.

2.2.2.1 Cyclic voltammetry of iron(III) porphyrin complexes

The electrooxidation of the four new thiolate Fe(III) porphyrins and the known complexes **Fe(PFTPP)Cl** and **Fe(TPP)Cl** were studied by cyclic voltammetry in CH_2Cl_2 containing 0.2 M $[Bu_4N][BF_4]$ at a vitreous carbon electrode at room temperature, Figure 2.7. All potentials determined by cyclic voltammetry are given in Table 2.2 are quoted versus SCE .

Complexes **Fe-1**,**Fe-2**,**Fe-3**, and **Fe-4** exhibit a quasi-reversible oxidation coresponding to the Fe(III)/Fe(IV) couple with complex **Fe-4** having the more positive oxidation potential, $E^{ox}_{1/2} = 0.96V$. Further irreversible oxidation steps of the complexes are observed at more positive potentials nominally corresponding to metal centred Fe(IV)/Fe(V) and/or porphyrin centred processes, Table 2.2. The higher primary oxidation potential of complex **Fe-4** is expected, since it possesess two strongly electron withdrawing pentafluorophenyl groups which decrease the electron density at the metal centre. On the other hand, complex **Fe-3** exhibits the lowest oxidation potential due to the electron-donating alkoxy groups which increase the electron density at the metal centre. Both complexes **Fe-1** and **Fe-2** show somewhat similar potentials because the complex **Fe-1** weak electron withdrawing groups while complex **Fe-2** contains two weak electron-donating groups. The cyclic voltammetry of **Fe(PFPP)** does not exhibit a clear 1e quasi-reversible oxidation for Fe(III)/Fe(IV); instead a 2e quasi-reversible oxidation involving Fe(III)/Fe(IV) and Fe(V) or mixed porphyrin ligand oxidation steps are observed at $E_{1/2} = 1.58V$. Fe-(TPP) exhibits a quasi-reversible oxidation of

Fe(III)/Fe(IV) at $E_{1/2}$ = 1.12V and followed by a further reversible oxidation at 1.39V.
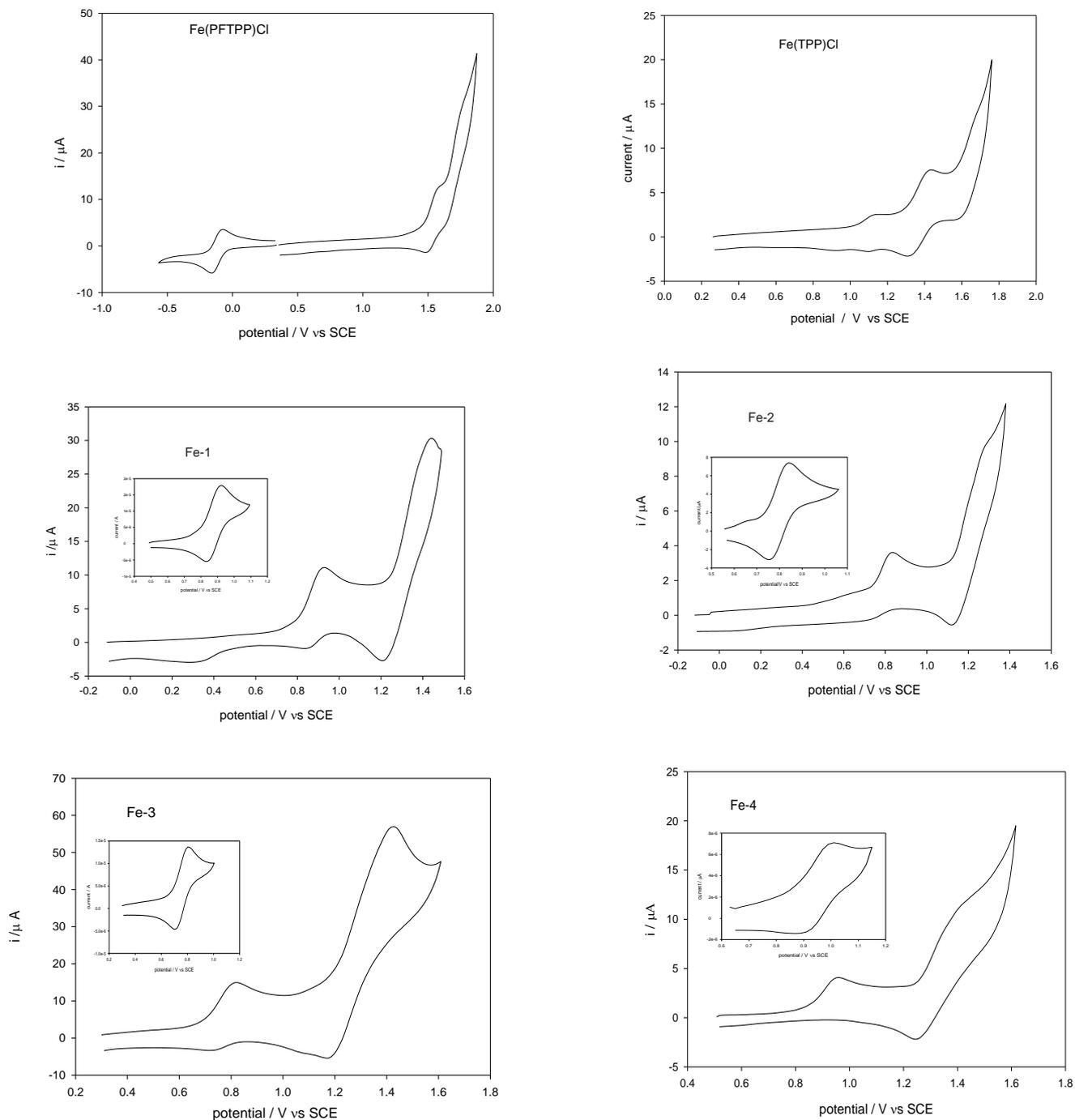
Figure 2.7 Cyclic voltammograms of **Fe-(1-4)**, **Fe(TPP)Cl** and **Fe(PFTPP)Cl** in CH$_2$Cl$_2$ containing 0.2M [Bu$_4$N[]BF$_4$] at RT. Scan rate = 0.1V/s. The inset figures are the quasi-reversible one-electron oxidations (peak 1).

Table 2.2 Oxidation potentials (V *vs* SCE) in CH_2Cl_2 containing 0.2 m [Bu_4NBF_4]

	Fe-1	Fe-2	Fe-3	Fe-4	Fe(PFTPP)Cl	Fe(TPP)Cl
$^{I}E_{1/2}$/V[a]	0.88	0.80	0.76	0.96	1.58[b]/1.48[c]	1.12
$^{II}E_p^{ox}$/V[d]	1.44	1.37	1.43	1.45	1.77	1.39[e]
$^{II}E_p^{red}$/V[d]	1.21	1.19	1.17	1.29	1.62	

[a] Reversible one-electron process. [b] E_p^{ox} for irreversible two-electron process. [c] E_p^{red} for irreversible one-electron process. [d] Irreversible multi-electron process [e] Reversible one-electron process, $^{II}E_{1/2}$.

2.2.2.2 Cyclic voltammetry of Fe-1
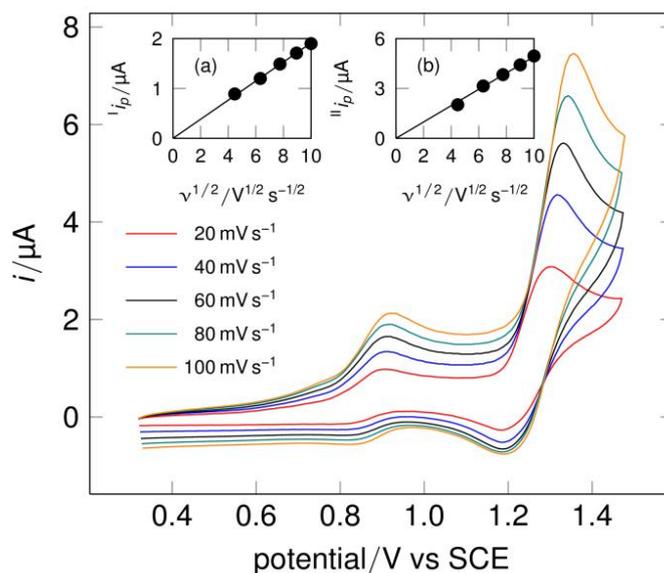
Figure 2.8 Cyclic voltammograms of **Fe-1** at various scan rate in CH_2Cl_2 containing 0.2 M [Bu_4N][BF_4]. The inset figures are the plots of i_p^{ox} *versus* $\nu^{1/2}$

Figure 2.8 shows a set of voltammograms recorded at various scan rates for complex **Fe-1**. The primary oxidation process is a diffusion controlled reversible one-electron step. Thus: (i) the plot of the peak current $^{I}i_p^{ox}$ *versus* $\nu^{1/2}$ is linear with an intercept close to zero [Figure 2.8, inset (a)] (ii) the magnitude of $^{I}i_p^{ox}$ at

each scan rate is, as expected, equal to those observed for the primary Fe(II)(/III) one-electron reduction process Figure 2.9. This first oxidation is probably a metal-centred $Fe^{(IV/III)}$ couple, rather than a ligand-based oxidation, as the potential is sensitive to the addition of water/hydroxide (see below). Each of the four thiolate complexes shows a similar primary oxidation step Figure 2.7. The $^{I}E_{1/2}$ values range from 0.76 V *versus* SCE for the most electron-rich porphyrin to 0.96 V *versus* SCE for the most electron-poor porphyrin Table 2.2. The primary oxidation potential for the **Fe(TPP)Cl** complex, 1.12 V *versus* SCE is some 240 mV more positive than that of **Fe-1**. This maybe a consequence of the better electron-donating ability of the thiolate group compared with Cl, or perhaps more likely a switch from a metal based oxidation in the case of **Fe-1** to a porphyrin based oxidation as has been established for **Fe(TPP)Cl** [43].
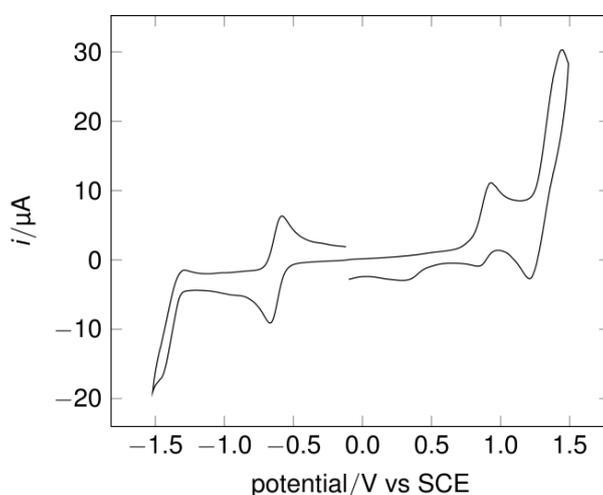
Figure 2.9 Electro-oxidation and reduction of **Fe-1** in CH_2Cl_2 containing 0.2M [Bu_4N][BF_4] at RT. Scan rate = 0.1V/s.

Following the primary one-electron oxidation step, a secondary process is observed at a more positive potential: the plot of $^{II}i_p^{ox}$ *versus* $v^{1/2}$ is linear, which is consistent with a diffusion controlled process, Figure 2.8, inset (b). The process

appears partially reversible and the plot of $^{II}i_p^{ox}$ *versus* i_p^{ox} is linear with a slope of

2.5 as shown in Figure 2.10.
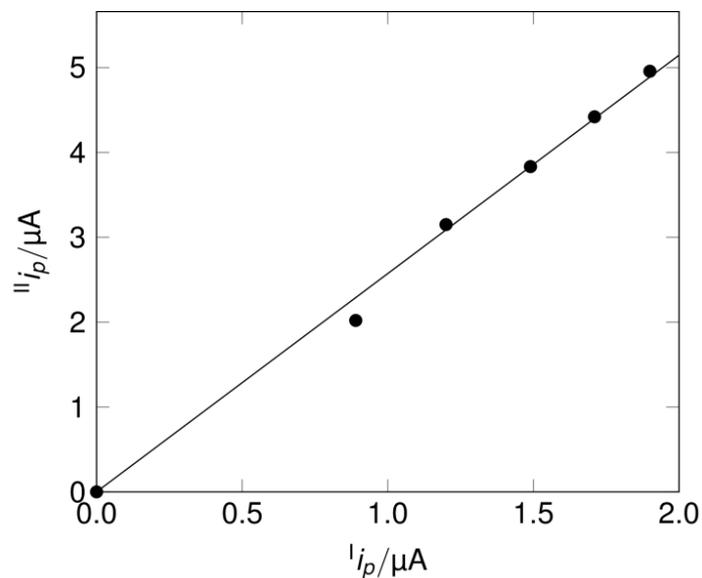
Figure 2.10 Plots of $^{II}i_p^{ox}$ *versus* $^{I}i_p^{ox}$. Scan rate = 0.1 V s^{-1}.

The expected ratio between fast reversible two-electron and one-electron systems

is $(^{II}n/^{I}n)^{3/2}$ = 2.83. The ratio we observe is 2.5

2.2.2.3 Effect of the base [NBu₄][OH]•30(H₂O) on cyclic voltammetry of Fe-1

In preparative electrolyses using the iron porphyrins as electrocatalysts we found that the presence of the strong base $[NBu_4][OH] \cdot 30(H_2O)$ was essential for hydrocarbon oxidation in all cases. We have therefore examined the effect of this reagent upon the cyclic voltammetry of the systems, focusing again on **Fe-1**. Figure 2.11(a) shows the effect of the base at low concentration (2.4 equivalents OH⁻) on the cyclic voltammetry. The key features are a negative shift in the potential for the primary oxidation by about 120 mV and a reduction in the magnitude of $^{II}i_{pox}$ by about 20%. Figure 2.11(b) shows the effect of increasing the reagent concentration from 2.4 to 32 equivalents. In this case, we see a new oxidation peak at a relatively low potential with $^{OH}E_p = 0.43$ V *vs* SCE, which is accompanied by suppression of the low base/zero base peaks at 0.7- 0.9 V versus SCE and a negative shift of the 'secondary' oxidation process by about 160 mV.
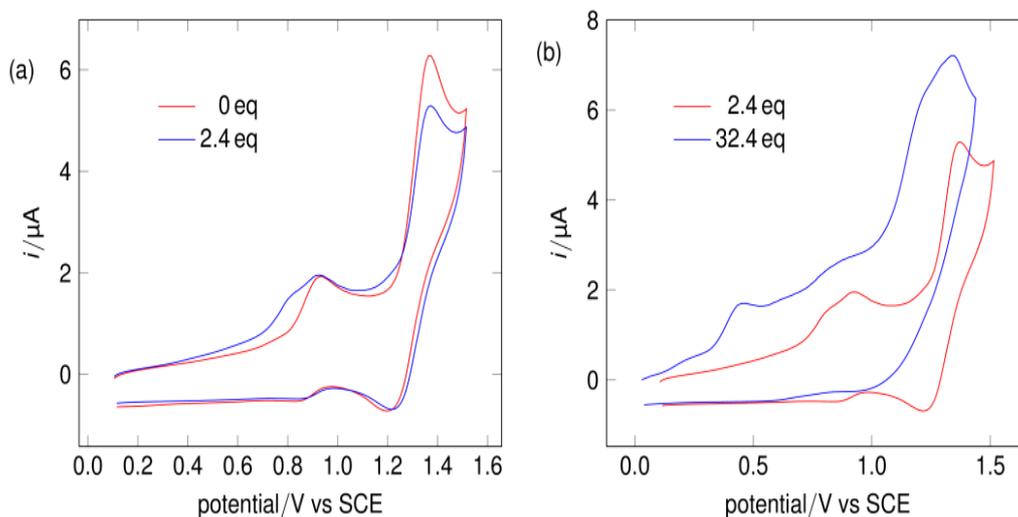
Figure 2.11   Cyclic voltammograms of **Fe-1** in CH_2Cl_2 containing 0.2 M $[Bu_4N][BF_4]$ at room temperature with added $[Bu_4N][OH]$. Scan rate = 0.1 V s^{-1}
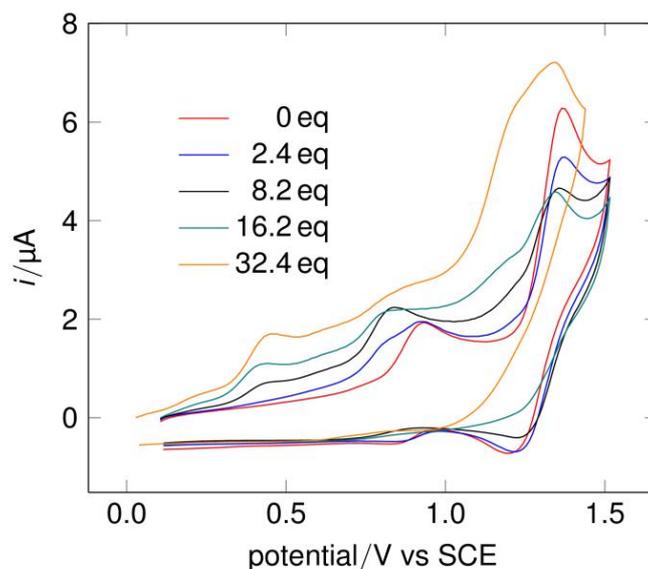
Figure 2.12 Cyclic voltammograms of **Fe-1** in CH_2Cl_2 containing 0.2 M $[Bu_4N][BF_4]$ at room temperature with increasing concentration of $[Bu_4N][OH]$. Scan rate = 0.1 V s^{-1}

The effect of increasing base concentration across the full range of base concentration is shown by Figure 2.12. We suggest that at low concentrations of the added base speciation is predominately water occupying the axial site and at higher base concentrations the majority species is the hydroxide ligated complex, scheme 2.4. This would be consistent with the new peak at E_p = 0.43 V *vs* SCE being associated with the hydroxide species whilst that at 0.79 V versus SCE being the aquo species. The irreversibility of the oxidation of the aquo species may be attributed to proton removal by base; similarly this may explain the irreversibility of the oxidation of the hydroxide species whereby a Fe (IV) oxo species is formed, Scheme 2.4. The lower peak current associated with secondary process in the presence of base maybe attributable to the formation of stable oxo species rather than destructive oxidation of the porphyrin.

Scheme 2.4 suggests how the observed electrochemistry might be related to speciation in the presence of base. In this scheme Fe(PorpS) is **Fe-1** or more generally the thiolate ligated porphyrins.
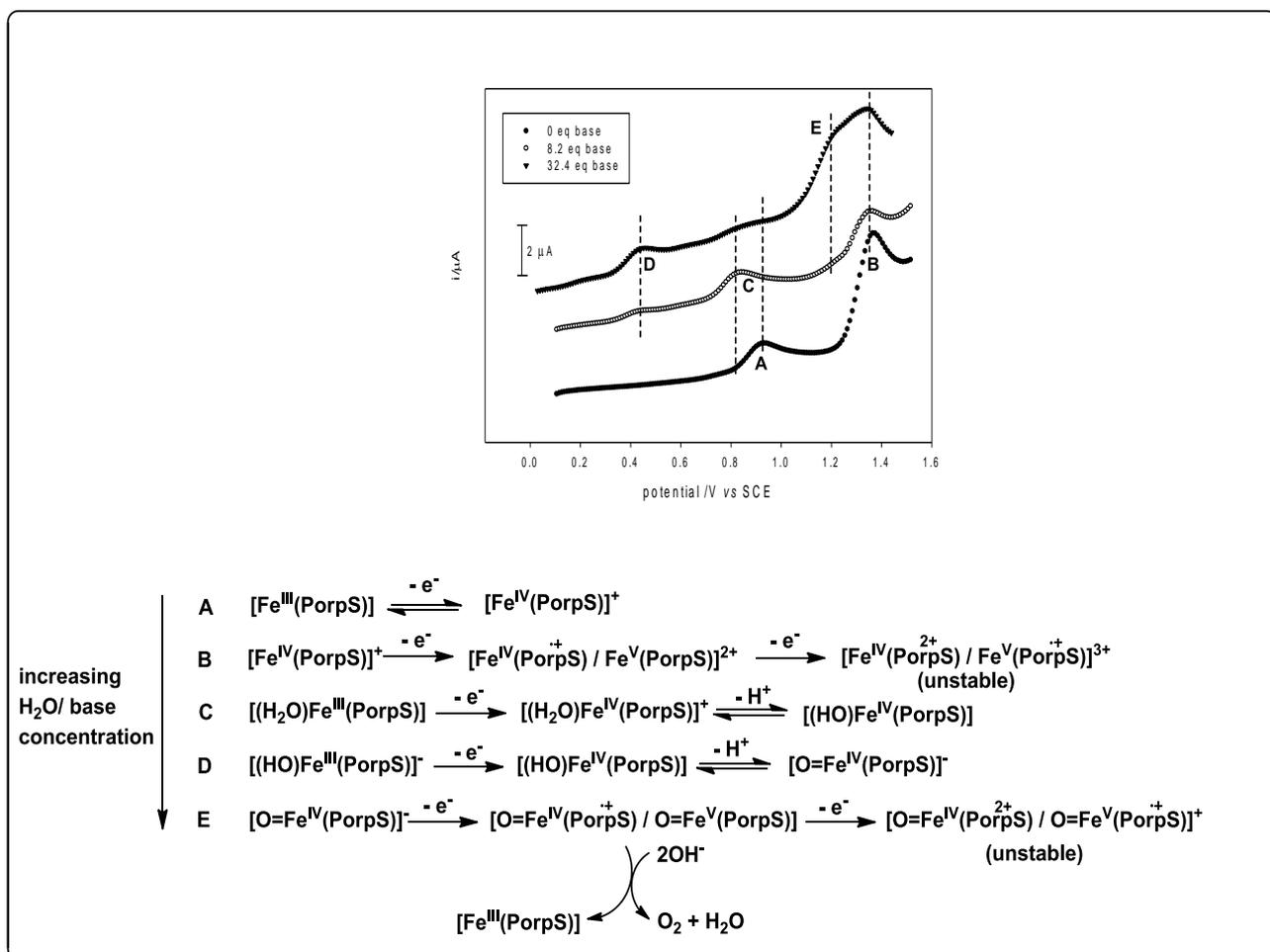
Scheme 2.4 Proposed oxidation steps of the thiolate ligated porphyrins in the absence and presence of base

2.2.2.4 The effect of adamantane on the cyclic voltammetry of Fe-1

We have examined the effect of adamantane upon the cyclic voltammetry of the porphyrin systems, focusing on **Fe-1**. Figure 2.13 shows the effect of increasing the concentrations of adamantane (16.3 eq – 174 eq). It is clear that there is no major effect on the peak potential nor significant effect on the magnitude of the $^I i_{pox}$ and $^{II} i_{pox}$. It is known, that direct adamantane oxidation is very positive, in MeCN at 2.38 V vs Ag/AgNO$_3$ [27]. This suggests that the hydrocarbon oxidation is slow on the C .V timescale.
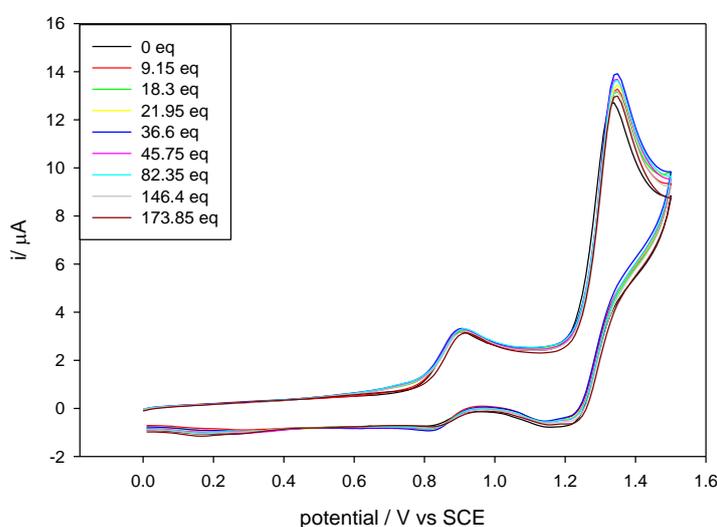
Figure 2.13 Cyclic voltammograms of **Fe-1** in CH$_2$Cl$_2$ containing 0.2 M [Bu$_4$N][BF$_4$] at room temperature with various adamantane concentrations. Scan rate = 0.1 V s^{-1}.

2.2.2.5 Electrocatalytic oxidation of adamantane and cyclooctene

Electrocatalytic oxidations of adamantane and cyclooctene were carried out in CH$_2$Cl$_2$ at room temperature under N$_2$ for 1.5 hours using 0.2 M [Bu$_4$N][BF$_4$] as the electrolyte and in the presence of tetrabutylammonium hydroxide. Based on the cyclic voltammograms of the four thiolate iron porphyrins, **Fe(PFTPP)Cl** and **Fe(TPP)Cl**, the applied potentials for **Fe-1**, **Fe-2**, **Fe-3**, **Fe-4**, **Fe(PFTPP)Cl** and **Fe(TPP)Cl** were set at 1.36 V, 1.27 V, 1.31 V, 1.42 V, 1.70 V and 1.49 V (V *vs* SCE) respectively. These are sufficiently positive to ensure accessing the two-electron oxidised state from the Fe^{III} complexes.

2.2.2.6 Controlled potential electrolysis: hydrocarbon oxidation

Preparative bulk electrolyses were performed at appropriate potentials at a vitreous carbon electrode and current and charge passed were monitored during the course of the experiments. The standard conditions chosen were: 0.45mM catalyst; 62mM hydroxide; 0.1M substrate at room temperature, 23°C. The working electrode compartment was stirred at a constant rate during electrolyses. Figure 2.14 shows the relationship between the current and charged passed (C) for **Fe(PFTPP)Cl** and **Fe-2** respectively in the presence of base and adamantane. Figure 2.15 shows the corresponding plots for the oxidation of cyclooctene by **Fe(PFTPP)Cl** and **Fe-4.** During the course of each oxidation the initial current rapidly decayed to a plateau of about 40% of the initial current before falling off towards the end of electrolysis.

Table 2.3 summarises the data for the electrochemical oxidation of adamantane and cyclooctene for all the Fe porphyrin catalysts. It was found that the presence of hydroxide is crucial. Without this base control experiments show that no adamantanol or cyclooctene oxide is formed. This is consistent with the proposed electrocatalytic mechanism shown in Scheme 2.5. The Fe^{III} hydroxide is oxidised by removal of two electrons and a proton, assisted by free base, which thus generates the highly reactive ferryl species. In the *absence* of an iron porphyrin catalyst, cyclooctene could be electrochemically oxidised to cyclooctene epoxide in the presence of OH^- with a current efficiency of 5.6% at an anode potential of 1.8 V (V *vs* SCE). This potential is positive enough to produce $OH^{\bullet}$ radicals [44] notably only a trace amount of 1-adamantanol was detected under the same experimental conditions. Generation of $OH^{\bullet}$ radicals could convert cyclooctene to cyclooctene oxide, presumably via peroxide or superoxide intermediates; however, none of these intermediates are powerful enough to oxidise adamantane to 1-adamantanol. Thus the presence of iron porphyrins lowers the activation barriers for adamantane hydroxylation and cyclooctene epoxidation, dramatically increasing the current efficiency for their formation and substantially lowering the anode potentials required (Table 2.

3). Notably, the cyclic voltammetry of **Fe-1** in the presence of adamantane at high concentration is only marginally perturbed by the substrate, consistent with no direct oxidation. In the presence of the base and the substrate the cyclic voltammogram is largely dominated by the effect of base consistent with slow hydrocarbon oxidation kinetics, some minor effects on peak currents are observed.
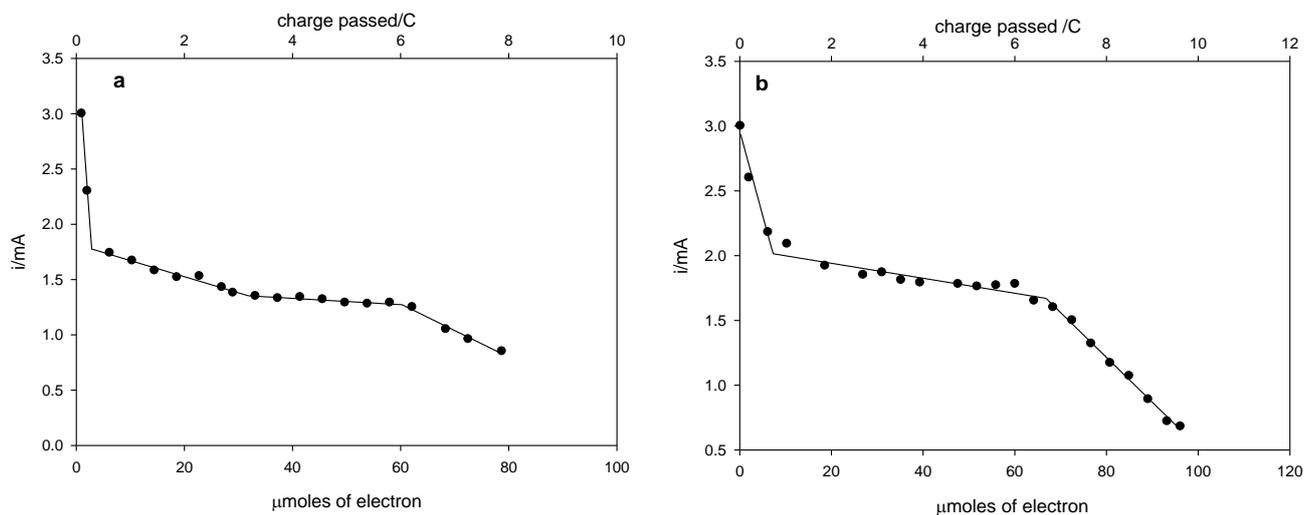
Figure 2.14 Coulometry of adamantane oxidation catalysed by (a). **Fe(PFPP)Cl**, (b) **Fe-2**
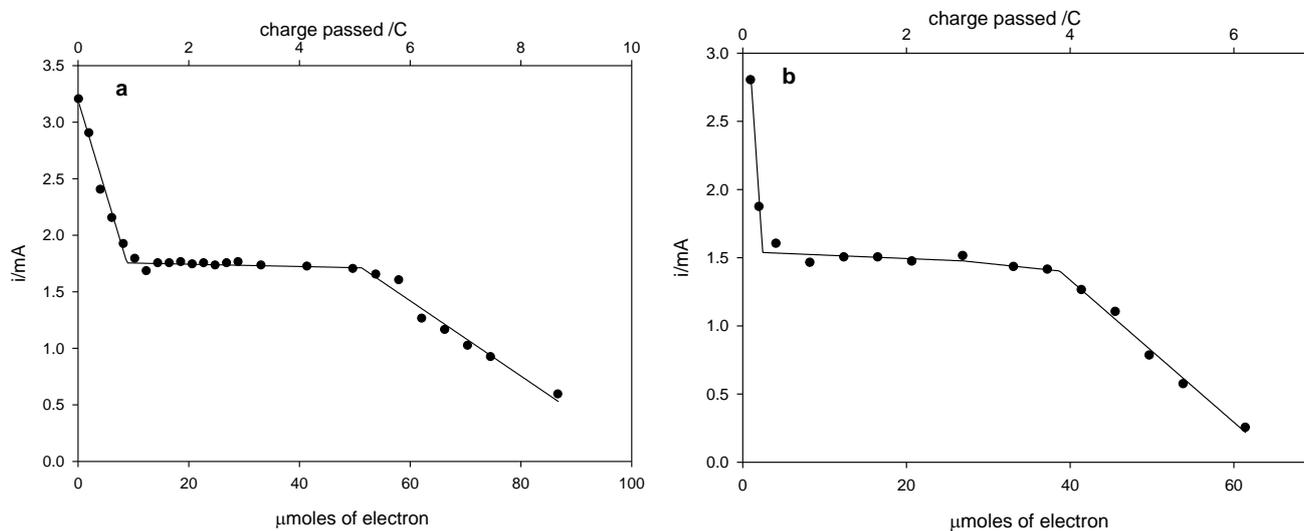
Figure 2.15 Coulometry of cyclooctene epoxidation catalysed by (a) **Fe (PFPP)Cl**,(b) **Fe-4**
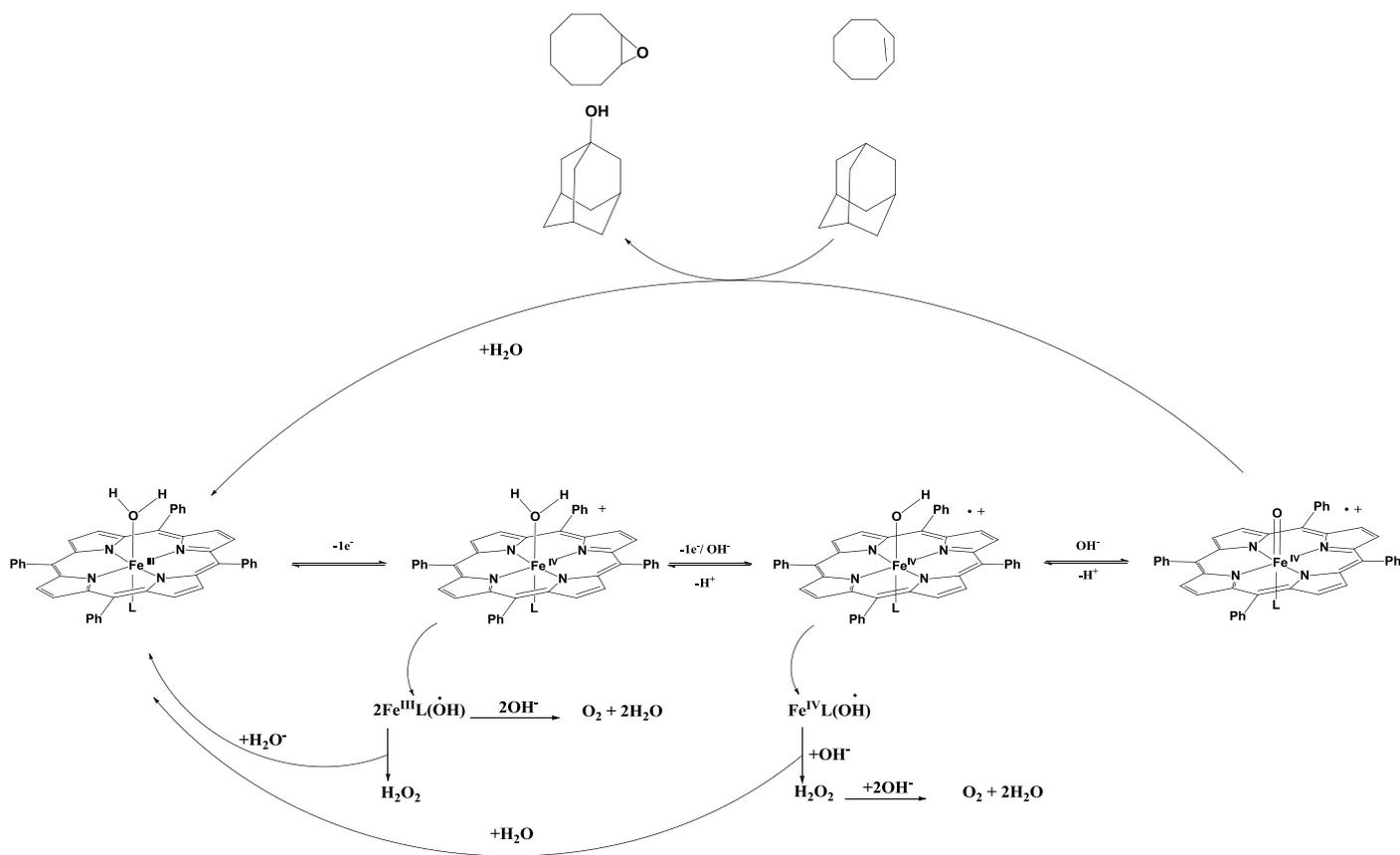
Scheme 2.5 Proposed mechanism of electrocatalytic oxidation of hydrocarbon.

Table 2.3 Current efficiencies and turnover numbers for electrocatalytic oxidations of adamantane/cyclooctene catalysed by Fe[III] porphyrins.[a]

Catalyst	Oxidation potential/V vs SCE	1-Adamantanol		Cyclooctene oxide	
		Yield/%[b]	TON[c]	Yield/%[b]	TON[c]
Fe-1	1.36	9.4	2.7(28.1)	16.1	4.6(28.7)
Fe-2	1.27	9.8	3.0(33.8)	20.9	5.1(24.5)
Fe-3	1.31	2.5	0.7(25.9)	12.5	3.4(27.6)
Fe-4	1.42	14.5	4.1(28.5)	28.2	6.4(22.7)
Fe(PFTPP)Cl	1.70	35.8	7.5(29.1)	38.9	12.3(31.4)
Fe(TPP)Cl	1.49	2.6	0.8(31.9)	17.4	5.2(24.5)

[a] Reactions were carried out in CH_2Cl_2 at RT under N_2 for 1.5 hours. [Fe[III] porphyrin]: 0.45 mM; [Bu$_4$NOH]: 62 mM; [adamantane or cyclooctene]: 0.1 M; [Bu$_4$NBF$_4$]: 0.2 M; [H$_2$O]: 1.8 M. [b] Average value of two experiments. [c] TON = moles of product/moles of catalyst; number in bracket is the theoretical TON. The theoretical maximum TNO is based upon the total charge passed (F)/ 2moles of catalyst

2.2.3 Comparison between chemical and electrochemical oxidation of hydrocarbons

In parallel with the chemical oxidation of adamantane, the electron density on the iron porphyrin appears to be the major factor that determines the current efficiency and turnover number: both increase as the electron density on the iron porphyrin decreases. Thus, among the four thiolate porphyrins, the most electron deficient **Fe-4** provides the highest current efficiency and the most electron rich **Fe-3** gives the lowest current efficiency. Again, **Fe(PFTPP)Cl** exhibits overall the highest current efficiency whilst **Fe(TPP)Cl** has the lowest. The effect of geometric arrangement around the thiolate sulfur on the current efficiency of electrocatalytic oxidation (9.4% for **Fe-1** vs 9.8% for **Fe-2**) is not as significant as for that observed for the chemical oxidation (22.5% for **Fe-1** vs 34.7% for **Fe-2**). This is understandable since the oxidative destruction of the thiolate ligand from a strong oxygen transfer reagent, such as PhIO, is no longer applicable in the case of electrocatalytic oxidation. The current efficiencies of cyclooctene epoxidation are also shown in Table 2.3. **Fe(PFTPP)Cl** is the best electrocatalyst in terms of current efficiency but it is also operates at the highest oxidation potential.

In general, the basket handle thiolate complexes are clearly superior to the prototypical **Fe(TPP)Cl** system both in terms of potential and current efficiency and further modification might increase current efficiency without significantly increasing the oxidation potential.

The Figure 2.16 shows that the comparative electrochemical and chemical of efficiency of porphyrins complexes to convert adamantane into 1-adamantanol and cyclooctene to the epoxide. These efficiencies are based upon the equivalents

of iodosobenzene or electron-pairs consumed for the chemical and electrochemical oxidations respectively. The lower efficiency of electrochemical oxidation with respect to chemical oxidation can be ascribed to competing generation of superoxide, peroxide or dioxygen (Scheme 2.5) which will unproductively consume charge.
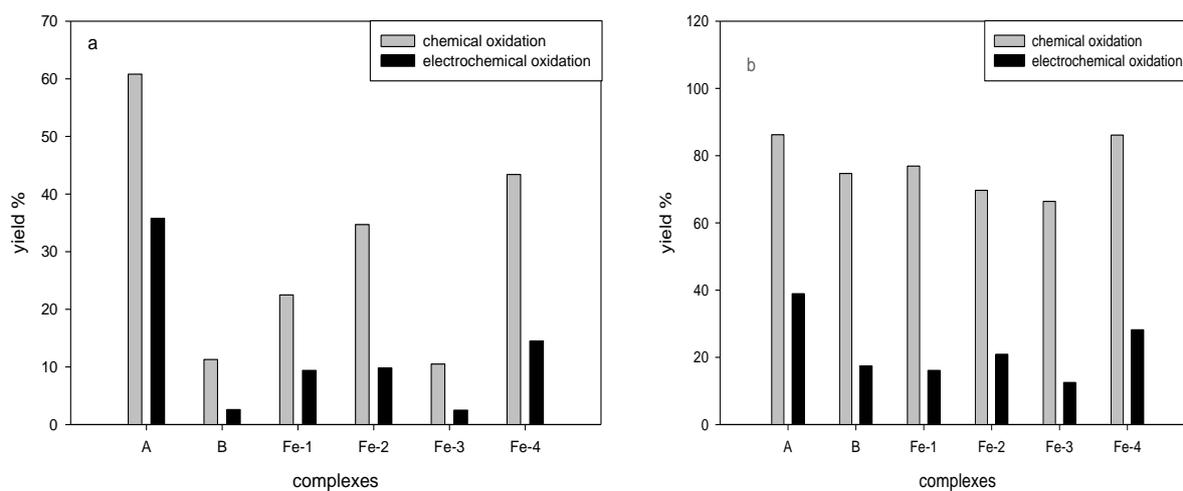
Figure 2.16 The comparing the yield of (a)1-adamantanol, (b) cyclooctene oxide for chemical and electrochemical oxidation. The yields are based upon iodosobenzene consumed for the chemical oxidation and number of two electron equivalents consumed in the electrochemical oxidation. A = **Fe(PFTPP)Cl**,   B = **Fe(TPP)Cl**

2.3 Conclusion

We have determined the activity of new basket-handle thiolate Fe(III) porphyrins as catalysts in chemical hydrocarbon oxidations and have bench marked them against iron tetraphenylporphyrin and its tetrapentafluorophenyl analogue.

Importantly, we show that in principle hydrocarbon oxidation can be driven anodically using these iron porphyrins. We report the first current efficiency data (yields) for this type of electrochemical oxidation. We show that a current efficiency of 36% can be achieved with an iron tetrapentafluorophenylporphyrin electrocatalyst in a dichloromethane electrolyte at +1.70 V versus SCE. Notably the operating potential can be reduced to *ca* +1.4 V versus SCE by using a thiolate ligated iron porphyrin, although at the cost of a lower current efficiency (14.5 %). This work goes some way towards establishing a proof of concept that alternatives to that of water oxidation might usefully be explored in solar fuel / feedstock generating systems. Lower oxidation potentials and faster kinetics are of course necessary targets.

The catalytic activities of new thiolate iron (III) porphyrins have been examined by electrochemical and chemical oxidation of adamantane and cyclooctene. The results showed that it was indeed possible to oxidise alkanes and alkenes by electrochemical means with water as the oxygen source, although the current efficiency and turnover number were not impressively high. In both electrochemical and chemical oxidations, **Fe (PFTPP)** gave the best yield and turnover number, followed by **Fe-4**, **Fe- 2, Fe-1, Fe(TPP)Cl ,Fe-3** respectively . Based on our limited observations here, the more electron deficient the porphyrin, the more reactive towards the chemical and electrochemical oxidation, regardless

of the axial ligand, be it a chloride or a thiolate. The role of thiolate in electrochemical and chemical catalysis is still elusive, but future investigation of a phenolate iron porphyrin could shed light on this. Compared to chemical oxidation, electrochemical oxidation is not so efficient, probably due to undesired reactions, such as water splitting, competing for charge during the electrolysis.

2.4 Experimental section

2.4.1 General aspects

All solvents were dried and degassed prior to being used. All commercial chemicals were used as received unless otherwise stated. All reactions were carried out under a dry N_2-atmosphere unless otherwise stated.

GC analyses were performed using a Hewlett-Packard 5890 II gas chromatograph equipped with a FID detector and a 25 m × 0.32 mm 5% phenyl-95% dimethylpolysiloxane capillary column (ID-BPX5 1.0). An injection volume of 1 μl was used in all GC analyses. The products were identified by comparing their retention times in GC with those of authentic samples. The yields of oxidation products were determined by comparison against standard curves (bromobenzene was used as an internal standard for adamantine hydroxylation and decane for epoxidation of cyclooctene). In adamantane oxidation, the operating conditions were, oven temperature 160 ^{0}C , injected volume 1 μml, analysis time 20 min and flow of gas rate 10 DEG/ min whilst in the case of cyclooctene oxidation, the operating conditions were oven temperature 120 ^{0}C, injected volume 1 μml, analysis time 20 min and flow of gas rate 4 DEG/ min as the best conditions.

2.4.2 Chemical oxidation of hydrocarbons

The chemical oxidations of adamantane and cyclooctene were carried out using iodosylbenzene (PhIO) as an oxygen source. Iodosylbenzene was prepared according to a published procedure by Saltzmann and Sharefkin [45] and its purity was checked by iodometric titration to be above 99%. All reactions were performed in dry dichloromethane at 20 ^{0}C in a dry small schlenk-tube fitted with

rubber septum under an atmosphere of N_2. Dichloromethane was refluxed over 50 g potassium carbonate and 25 g of P_2O_5 (b.p 39-40.5 ^{0}C).

The porphyrins (1×10^{-3} mmol) and admantane (0.014g, 0.1 mmol) or cyclooctene (0.011g, 0.1 mmol) were placed under an N_2 atmosphere in dichloromethane (1 ml). The mixture was bubbled with N_2 and subsequently PhIO $(2.2 \times 10^{-3}$g, 0.01 mmol),(10equiv) was added to reaction. The mixture was stirred for an hour at room temperature in the absence of light then PhBr $(7.5 \times 10^{-3}$ M) was added as internal standard and the mixture was stirred for 5 minutes. The reaction mixture was passed through a short pad of dry Celite to remove unreacted PhIO. The 1µl sample filtrate was injected directly to a gas chromatographer (GC-FID) for product analysis.

2.4.3 Electrochemical oxidation of hydrocarbons

2.4.3.1 Preparation of the electrolyte tetrabutylammonium tetrafluoroborate, [Bu$_4$N][BF$_4$]

Tetrabutylammonium hydrogen sulphate (169 g, 0.498 mol) was dissolved in 200 ml of distilled water and sodium tetrafluoroborate (54.65 g, 0.498 mol) was dissolved in 200 ml distilled water. The sodium tetrafluoroborate solution was filtered and added slowly to the tetrabutylammonium hydrogen sulphate solution which was stirred vigorously. The white solid product was filtered off and washed with distilled water. It was placed under vacuum pump to make it as dry as possible and dissolved in 50 ml of dry dichloromethane. The dichloromethane layer was separated from the water layer then dried overnight over anhydrous magnesium sulphate. The dichloromethane layer was filtered from anhydrous magnesium sulphate also; 25 ml of dry dichloromethane was added to wash the

anhydrous magnesium sulphate during filtration. The dichloromethane solution was added slowly to 1.5 L dry diethyl ether and stirred vigorously. The white product $[Bu_4N][BF_4]$ was filtered and dried overnight in a heated vacuum oven at $80\ ^0C$. The product $[Bu_4N][BF_4]$ was stored in a Schlenk flask under Ar [46,47].

2.4.3.2 Electrochemical procedures

Cyclic voltammetric measurements were carried out using an Autolab PGSTAT 30 potentiostat. A conventional three-electrode arrangement was employed, consisting of a vitreous carbon working electrode, a platinum wire as the auxiliary electrode, and SCE as a reference electrode. All measurements were done in dry CH_2Cl_2 in the presence of 0.2M tetrabutylammonium tetrafluoroborate as the supporting electrolyte at room temperature. All solutions were thoroughly degassed with nitrogen prior to being used, and during the measurements a nitrogen atmosphere was maintained. The electrocatalytic hydrocarbon oxidations were performed in a three-electrode and three-compartment cell where adjacent compartments were separated by a glass frit. A vitreous carbon working electrode was fitted into the central compartment with platinum wire auxiliary electrode and Ag/AgCl $(CH_2Cl_2$, 0.5 m $[Bu_4N]Cl$) reference electrode in the adjoining compartments. The Fe^{III} porphyrin catalyst($1.35x10^{-4}$ mmol), $[Bu_4N][OH]\cdot30H_2O$ base (0.143g, 0.18 mmol), hydrocarbon substrate,(0.3 mmol) and 0.2M $[Bu_4N][BF_4]$ electrolyte were added into the working electrode compartment and dissolved in 3 mL CH_2Cl_2. The auxiliary and reference compartments were charged with CH_2Cl_2 solution containing $[Bu_4N][BF_4]$ electrolyte. All the solution inside the cell was thoroughly degassed with nitrogen and sealed under N_2 prior to use. The mixture was left stirred for 20 min under N_2 atmosphere. Then the electrolysis was carried out by setting the potential of the cell 50-100 mV positive

of the secondary oxidation. After 1.5 h of electrolysis the experiment was terminated. To avoid damage to the capillary column we found it necessary to remove the supporting electrolyte. This was done in the following way. After each electrolysis CH_2Cl_2 was removed from the solution mixture under a controlled vacuum (320 mmHg) at room temperature. This was optimal for removal of the solvent whilst leaving the organic product intact. The residue was then treated with dry diethyl ether which extracted the product leaving insoluble $[Bu_4N][BF_4]$ which was removed by pipette filtration. The filtrate was evaporated under a controlled vacuum (320 mmHg) to remove diethyl ether. The residue was re-dissolved in 2 mL dry CH_2Cl_2 with an added internal reference. The resulting CH_2Cl_2 solution was then subjected to GC analysis. Control experiments established the efficacy of this extraction procedure.

2. 5 References

1.   J. T. Groves , T. E. Nemo. J. Am. Chem. Soc. **1983**,105, 6243-6248.

2.   C. M. Che, V. K. L. Lo, C. Y. Zhou, J. S. Huang. J. Chem. Soc. Rev. **2011**, 40, 1950-1975.

3.   D. Mansuy, C. R. Chimie. **2007**, 10, 392-413; b) B. Meunier. Chem. Rev. **1992**, 92, 1411-1456.

4.   C. E. Tinberg, S. J. Lippard. Acc. Chem. Res. **2011**, 44, 280-288.

5.   J. D. Lipscomb. Ann. Rev. Microbiol. **1994**, 48, 371-99.

6.   J. Murrell, B. Gilbert, I. McDonald. Arch. Microbiol. **2000**, 173, 325-332.

7.   F. P. Guengerich. Chem. Res. Toxicol.**2001**,14, 611-50.

8.   I. G . Denisov, T. M. Makris, S. G. Sligar, I. Schlichting. Chem. Rev. **2005**, 105, 2253-2277.

9.   T. Dohnoh, N. Suzuki, T. Dokoh, Y. Urano, K. Kikuchi, M. Hirobe, T. Higuchi, T. Nagano. J. Inorg. Biochem. **2000**, 82, 123-125.

10. J. W. Buchler. "The Porphyrins", D. Dolphin (Ed.), Academic, New York, Vol. 1, Part A, Structure and Synthesis .**1978**.

11. S. Shanmugathasan, C. Edwards, R. Boyle. Tetrahedron. **2000**, 56, 1025-1046.

12. M. Biesaga, K. Pyrzynska, M. Trojanowicz, Talanta. **2000**, 51, 209-224.

13. M. D. Assis, J. R. Smith. J. Chem.Soc, Perkin Tran. **1998**, 2, 2221-2226.

14. A) M. Autret, Z. Ou, A. Antonini, T. Bosch, P. Tagliatesta, K. Kadish. J. Chem. Soc, Dalton Trans. **1996**, 2793- 2797. B). C. K. Chang, F. Ebina. Chem. Comm. **1981**, 778-779.

15. J. T. Groves, T. E. Nemo, R. S. Myers. J. Am. Chem. Soc. **1979**, 101, 1032-1033.

16. D. Mansuy, J. F. Bartoli, M. Momenteau, Tetrahedron Lett. **1982**, 23, 2781-2784

17. J. T. Groves, W. J. Kruper, T. E. Nemo, R. S. J. Meyers. J. Mol. Cat. **1980**, 7, 169-170.

18. C. K. Chang, F. J. Ebina. J. Chem. Soc. Chem. Commun. **1981**, 19, 778-779.

19. P. S. Traylor, D. Dolphin, T.G. Tralor. J. Chem. Soc. Chem. Commun. **1984**, 5, 279-280.

20. J. Mario, A. Tolman. Inorg. Chem. **1985**, 24, 4711-4719.

21. W. Nam, I. Kim, Y. C. Kim. J. Chem. Commun. **2001**,14,1262-1263.

22. J. Hee, S. Park, R. Song, W. Nam. Inorg. Chimica Acta. **2003**, 343, 373-376.

23. J. L. Zhang, J. S. Huang. C. M. Che. J. Chem. Eue. **2006**, 14, 3020-3031.

24. Z. Li , C. G. Xia. Tetrahedron Lett. **2003**,44, 2069-2071.

25. J. Collman, H. Tanaka, I. Hembre, I. J. Brauman. J. Am. Chem. Soc. **1990**, 112, 3689-3690.

26. K. M. Kadish, E. V. Caemelbecke. J. Solid State Electrochem. **2003**, 7, 254-258.

27. A. Bewick. G. Edwards, S. John, J. Mellor. J. Chem. Soc. Perkin Trans. **1977**, 1, 1831-1834.

28. J. Gilbert, J. Groves. Inorg. Chem. **1986**, 25, 123-125.

29. C. Horwitz, S. Crager, R. Murray. Inorg. Chem. **1990**, 29, 1006-1011.

30. C.Y. Chen, S. Cheng, Y. Oliver. Electroanal. Chem .**2000**, 487, 51-56.

31. J. Haber, L. Matachowski, K. Pamin, J. Połtowicz. J. Mol. Catal. A. **2000**, 162, 105-109.

32. F. Bedioui, J. Devvynck. Acc. Chem. Res**. 1995**, 28, 30- 36.

33. T. L. Poulos, B. C. Finzel, I. C. Gunsalus, G. C. Wagner, J. Kraut, J. Biol. Chem. **1985**, 260, 16122-16130.

34. K. G. Ravichandran, S. S. Boddupalli, C. A. Hasermann, J. A. Peterson, J. Deisenhofer. Science. **1993**, 261, 731-736.

35. J. H. Dawson. Science. **1988**, 240, 433-439.

36. J. T. Groves. J. Inorg. Biochem. **2006**, 100, 434-447.

37. J. Rittle, M. T. Green. Science. **2010**, 330, 933-937.

38. B. Meunier, S. P. Visser, S. Shaik. Chem. Rev. **2004**, 104, 3947-3980.

39. P. Li, K. Alenezi, S. K. Ibrahim, J. A. Wright, D. L. Hughes, C. J. Pickett. ChemSuschem. **2012**, 5, 2361-2375.

40. D. Dolphin, T. G. Traylor, L. Y. Xie. Acc. Chem. Res. **1997**, 30, 251-259.

41. H. Fujii. J. Am. Chem. Soc. **1993**,115, 4641-4648.

42. T. Higuchi, K. Shimada, N. Maruyama, M. Hirobe. J. Am. Chem. Soc. **1993**, 115, 7551-7552.

43. M. A. Phillippi, H. M. Goff. J. Am. Chem. Soc. **1982**, 104, 6026-6034.

44. W. H. Koppenol, J. F. Liebman. J. Phys. Chem. **1984**, 88, 99-101.

45. J. G. Sharefkin, H. Saltzman. Org. Synth. **1963**, 43, 60-61.

46. T. Al-Salih, D. Phil. Thesis, University of Sussex. **1987.**

47. S. Ibrahim, D.Phil. Thesis, University of Sussex.**1992**.

Chapter 3

3 Electrocatalytic reduction of carbon dioxide

3.1 Introduction

3.1.1 Overview

One of the most significant current debates in the world today is climate change. Carbon dioxide concentrations in the atmosphere have been increasing considerably since the latter half of the 19th century, due to activities during the industrial revolution, with the burning of fossil fuels to release CO_2, seen as a significant contributor to the greenhouse effect [1,2]. However, the natural greenhouse effect (made up by CO_2, H_2O vapour and other gases) is important to life on earth as in its natural proportion, it plays a major role in balancing the earth's temperature by trapping the sun energy which is reflected from the earth's surface, implying that in their absence the temperature of the earth surface would be much lower than it is today [1]. Conversely, an increasing greenhouse effect is predicted to cause an increase in global temperatures, with the increasing levels of CO_2 cited as the main contributing factor. Studies indicate that concentrations of carbon dioxide in the atmosphere have increased from 280 ppm before the industrial revolution, to 380 ppm today. Globally, scientists expect that the surface temperatures will rise from between 0.6 ^0C to 2.5 ^0C within the next fifty years, which may lead to significant and possibly devastating environmental changes in many regions around the world. For instance, sea levels are shown to be rising, due it is believed to the melting of the ice caps, and extreme and temperamental weather conditions are predicted to become more frequent in the coming decades, with suggestions that arable lands could be changed into deserts [3].

Whilst these reasons no doubt make the capture and conversion of CO_2 to more useful products a very attractive target, it represents a grand challenge for chemists due to the thermodynamic stability of the simple carbon dioxide molecule, which renders it relatively unreactive. However, since the second half of the 19th century, CO_2 has been used as a raw material for the synthesis of some important organic compounds in industry, preferred over traditional fossil fuels such as oil, natural gas and coal due to their limited availability. Scheme 3.1 highlights the methods used for the important products utilised in industry, *via* reduction of CO_2 [4,5].
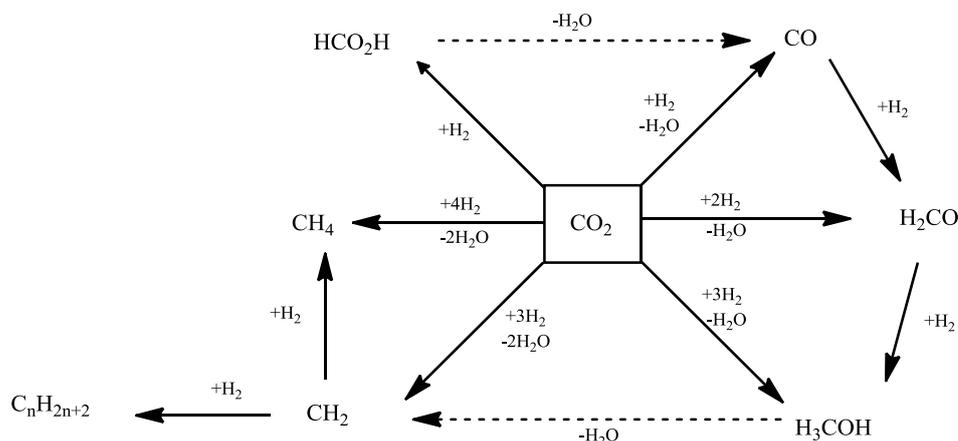
Scheme 3.1 Synthetic pathways for some important industrial products of CO_2 reduction [1]

3.1.2 Properties and geometry of molecular carbon dioxide

In the ground state, carbon dioxide is a linear molecule with a molecular electron count of 16, and although CO_2 is a nonpolar molecule, it contains two polar C-O bonds. Importantly, CO_2 has two possible reaction sites, due to contrasting properties of the carbon atom (an electrophile) and the oxygen atom (a nucleophile) [4].

The properties of molecular carbon dioxide have been investigated by infrared (IR) and nuclear magnetic resonance (NMR) techniques. The C=O symmetric bond in free CO_2 was determined at 1285-1388 cm^{-1} by Raman spectroscopy [4]. Table 3.1 shows some significant physical properties of CO_2 [1, 4].

Table 3.1 physical and spectroscopic properties of CO_2 [1]

Boling point (^{0}C)	-78.5
Bond length (A^0)	1.16
Bond energy (eV)	5.453
Ionization potential (eV)	13.78
Electon afifinty (eV)	-0.6
IR data (cm^{-1})	2300, 1320, 235, 668

One advantage of using CO_2 is that it is non-toxic, which makes it ideal substrate for use in the preparation of novel drugs, food processing, as well as an alternative to toxic substrates used in chemical processing. Another advantage, is that it can easily be stored and transported [6].

However, the maximum solubility of carbon dioxide in chemical solvents is relatively low and strongly depends on the pressure of CO_2 in solution. Solubility levels are shown in table 3.2 [2].

Table 3.2 The solubility of carbon dioxide in selected solvents at 1 atmosphere

Solvent	Concentration of $CO_2(M)$
Water	0.033
Methanol	0.06
Tetrahydrofuran (THF)	0.205 ± 0.008
Acetonitrile (AN)	0.279 ± 0.008
Dimethylformamide (DMF)	0.199 ± 0.006
Dimethylsulphoxide(DMSO)	0.138 ± 0.03

To avoid solubility issues, electroreduction of CO_2 is generally carried out in more miscible non-aqueous solvents, or in aqueous solutions at high pressure.

3.1.3 Interaction of carbon dioxide with transition metal centres

The interaction between CO_2 and metal centres has been studied to identify possible candidates that can catalyse the reduction of carbon dioxide, which may provide new reactions based on coordination between metal centres and CO_2. Early reports in this field showed that CO_2 could bind to Ni centres, through the η^2-C, O bonding mode [7]. Gibson [8] has described the various types of modes of CO_2 bonding to metal centres. The classification of these interaction modes between carbon dioxide and metal centres is shown in Figure 3.1 [1, 4].

$M_1-\overset{\overset{\displaystyle O}{\cdot\cdot}}{C}-O-M_2$

$\mu_2\text{-}\eta^2$

$M_1=C\overset{\displaystyle O}{\underset{\displaystyle O}{\diagup}}M_2$

$\mu_2\text{-}\eta^3$, class (1)

$M_1-C\overset{\displaystyle O}{\underset{\displaystyle O}{\diagup}}M_2$

$\mu_2\text{-}\eta^3$, class (2)

$M_1=C\overset{O-M_2}{\underset{O-M_3}{\diagup}}$

$\mu_3\text{-}\eta^3$

$M_1=C\overset{\overset{\displaystyle M_2}{O}}{\underset{O}{\diagup}}M_3$

$\mu_3\text{-}\eta^4$

$M_2=C\overset{O\diagdown M_3}{\underset{O\diagup M_4}{}}$ with M_1 below

$\mu_4\text{-}\eta^4$

$\mu_4\text{-}\eta^5$
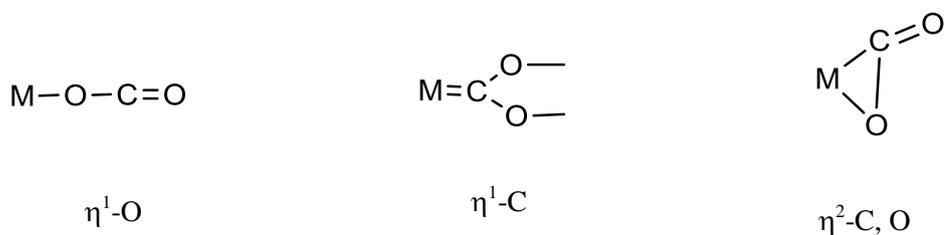
Figure 3.1 Modes of binding for metal-CO_2 complexes
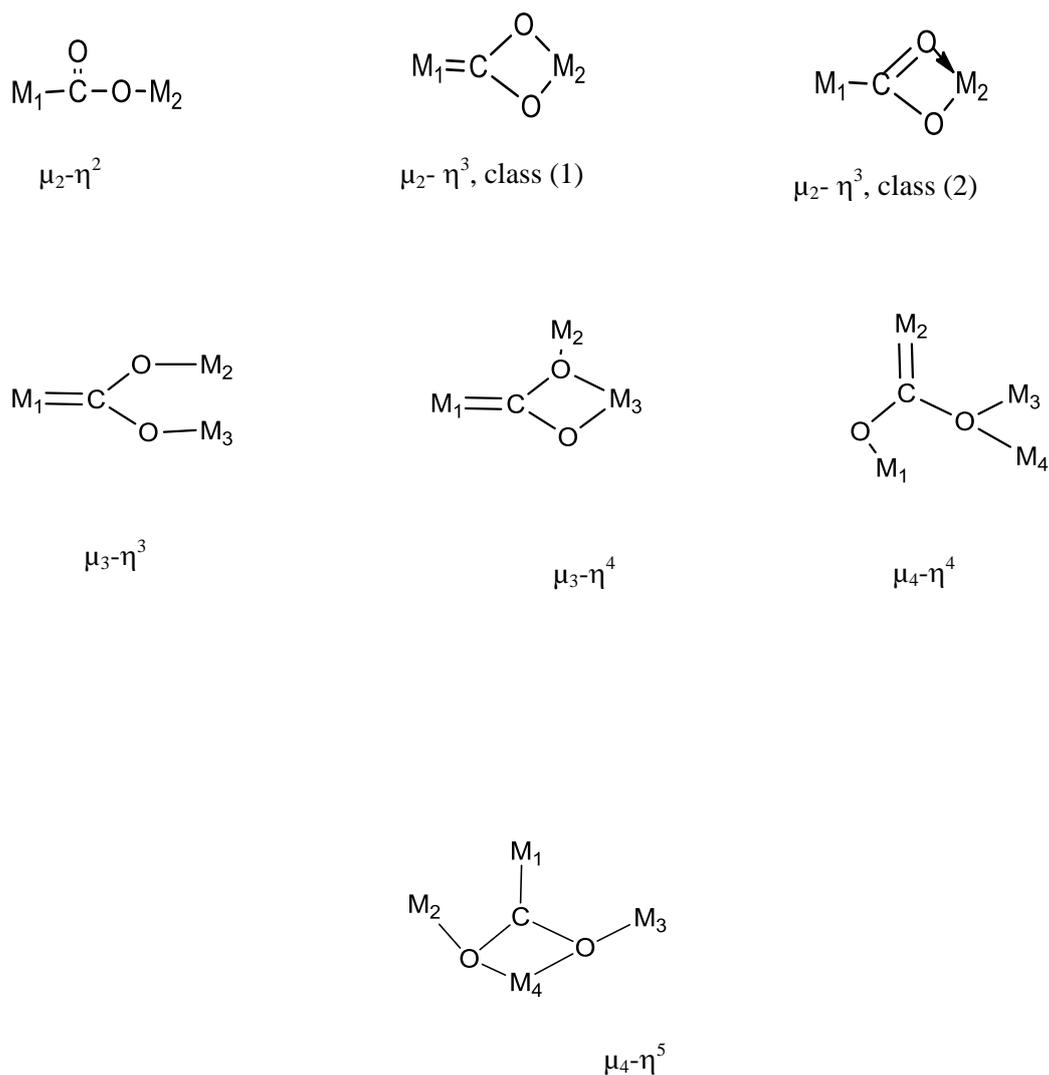
It is clear that the strength of C-O bond(s) decreases upon binding to the metal centre(s), because the length of the bond increases. In Figure 3.1 this is least for the η^1 mode and at the maximum for the $\mu_4\text{-}\eta^5$ mode. The CO_2 can be viewed as progressively activated with respect to the free molecule through this series of binding arrangements.

3.1.4 The electroreduction of carbon dioxide

In nature, carbon compounds and oxygen are generated by natural photosynthesis, driven by sunlight, which utilises carbon dioxide and water as raw materials. Conversely, carbon compounds are converted back to carbon dioxide and water through respiration and combustion by oxidation of carbon compounds. This natural balance between the level of carbon dioxide and oxygen/H_2O in the atmosphere, is essential to the continued success of life on earth. There are various techniques for reducing CO_2 to other substrates, including electrochemical methods, radiochemical methods, thermochemical methods, biochemical methods etc [1]. However the research described in this chapter will focus solely on the electrochemical reduction of CO_2. Electrochemical techniques are widely used by researchers investigating electrocatalytic reduction of CO_2 to useful chemicals or feedstock for fuels; however the inherent stability of CO_2 makes its use as a substrate a formidable challenge [9, 10].

With respect to CO_2 reduction by electrochemical techniques, a proton-coupled multi-electron reaction, which requires less negative potential, is more favourable than the single-electron reaction [11]. The most common reactions of electrochemical CO_2 reduction are summarized in Table 3.3 [11, 12].

Reaction									E^0 / V versus SHE
CO_2	+	$2H^+$	+	$2e^-$	→	CO	+	H_2O	-0.53
CO_2	+	$2H^+$	+	$2e^-$	→	HCO_2H			-0.61
CO_2	+	$4H^+$	+	$4e^-$	→	$HCHO$	+	H_2O	-0.48
CO_2	+	$6H^+$	+	$6e^-$	→	CH_3OH	+	H_2O	-0.38
CO_2	+	$8H^+$	+	$8e^-$	→	CH_4	+	$2H_2O$	-0.24
CO_2			+	e^-	→	$CO_2^{\cdot-}$			-1.9

Table 3.3. All potentials are for aqueous solution at pH 7.0, 25 ^{o}C, 1 atm gas pressure, *versus* standard hydrogen electrode (SHE)

Two significant advantages of using the electrochemical methods for the reduction of carbon dioxide in aqueous solution are that water can function as the proton source, and the electrochemical reactions can be carried out under ambient conditions [13]. Unfortunately, there is also major drawback of carrying out these reactions in aqueous solution, in that the reduction of CO_2 has to compete with the reduction of H^+ to evolve H_2 [2, 14].

The main products from CO_2 reduction under these conditions are formic acid, methanol, hydrocarbons, oxalic acid and carbon monoxide, depending on the conditions of experiments and the material of electrode used. The selectivity of CO_2 products depends on many factors such as [15].

1-Concentration of reactants.

2-Temperature of reaction.

3- Electrode materials.

4-Electrode potentials.

5-Electrolyte solution.

3.1.5 Carbon dioxide reduction on metals and reaction selectivity

The electrolysis of carbon dioxide on metallic electrodes in aqueous or non-aqueous solution has been studied extensively, and indications are that product selectivity depends on the electronic configuration of the metals involved in catalysis, therefore metallic electrodes are grouped into *sp* and *d* types. There are several classification systems that have been used to describe the CO_2 reduction products. Most of these classifications are based on the nature of the main products that are obtained in the electrochemical synthesis [16].

In 1996, Saveant and co-workers [9] reported on the mechanism for the direct electrochemical reduction of carbon dioxide, at an inert electrode such as mercury and in an aprotic solvent such as N,N$^/$-dimethylformamide (DMF). The cyclic voltammetry of CO_2 gives an irreversible wave at -2.21 V *versus* SCE, the temperature on the distribution of products were reported. The CO yield increased with an increase of CO_2 concentration, whilst the yield of oxalate decreases. Similar results are obtained with a decrease of temperature, which also leads to an increase in CO yield and a decrease of the oxalate.

3.1.6 Electrocatalytic CO$_2$ reduction

There is a large volume of published studies that describes the electrocatalytic reduction of CO_2, and generally the reduction of carbon dioxide requires one of two basic types of catalysts, homogenous or heterogeneous catalytic systems. In homogenous catalysis, the molecular catalyst is distributed throughout the solution, which is where the reaction occurs.

Electrocatalytic carbon dioxide reduction has been investigated by several studies, which have sought to overcome two main obstacles. Firstly, the direct electrochemical reduction using metallic electrodes requires large negative potentials, with the required potential for reduction of CO_2 to CO_2^-, a high -2.2 V *versus* (SCE) in N,N'-dimethylformamide (DMF) [9]. Secondly, the distribution of products of direct electrochemical reduction depends on many factors, such as the nature of the electrode, solvent, and CO_2 concentration, leading to a mixture of products. In the presence of a catalyst, CO_2 reduction can be carried out at much more positive potentials which lead to a better selectivity than direct electrochemical reduction on the electrode surface. The process of electrocatalytic reduction of CO_2 depends on the ability of metal complex to associate with CO_2,

and to transfer electrons from electrode to carbon dioxide [17]. A general scheme for an electrocatalytic reduction of CO_2 is shown in Figure 3.2.
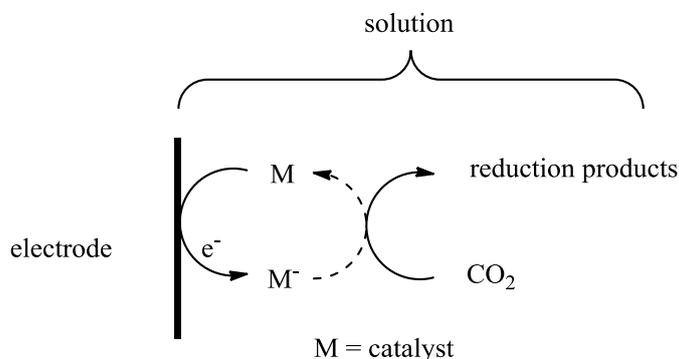

Figure 3.2 General scheme for electrocatalytic reduction of CO_2 [1, 11]

Studies for CO_2 reduction catalysed by transition metals began in the 1970's [18,19,20].

According to a review published by Kubiak and co-workers [18] in 2009, homogeneous catalysts for CO_2 reduction can be divided into three groups, depending on the ligand type:

1- Metal catalysts with bipyridine ligands.

2- Metal catalysts with phosphine ligands.

3- Metal catalysts with macrocyclic ligands

Several groups have reported the electrocatalytic reduction of carbon dioxide with metals bipyridine complexes, such as Re(bipy)(CO)$_3$Cl (bipy = 2,2$^{'}$-bipyridine). This complex was utilised by Lehn and co-workers [21] and reduces CO_2 to CO at -1.5 V *vs.* SCE in a 9:1 DMF:H$_2$O solution. In this study the efficiency of system was reported as 98% , with high selectivity for carbon monoxide.

Tanaka and co-workers [22] found that the bipyridine complexes $[Ru(bipy)(CO)Cl]^+$ and $[Ru(bipy)(CO)_2]^{2+}$ were able to reduce CO_2 to yield CO, H_2 and $HCOO^-$, at a potential of -1.40 V *vs.* SCE in . This study also presented a proposed mechanism for the catalysis associated with CO_2 reduction. Although there are several limitation of this system, such a low TON and selectivity, it did help to solve several questions regarding CO_2 reduction.

In a similar system, $2,2^/$-bipyridine complexes of rhodium and iridium were assayed by the Meyer group for the reduction of CO_2, which was shown to occur at -1.55 V *vs.* SCE. Moreover, it was found that the catalysts could selectively convert carbon dioxide to formate, with no CO detected during any electrolysis experiments. This system showed a low current efficiency (64% for formate, 12% for H_2, formed by degradation of supporting electrolyte) as well as low TON (6.8 to 12.3) [23]. The same group reported that under anhydrous conditions, $[M(bpy)_2(CO)H]^+$ (M = Os,Ru) could reduce CO_2 to give CO as the major product, and that the addition of water was required for the formation of formate [24a].

Mouttet and co-workers reported that the activation of carbon dioxide by cyclic voltammetry and preparative electrolysis on carbon and platinum electrodes modified by electropolymerization of *fac*-[Re $(L)(CO_2)_3Cl$], (L= L_2,L_6,L_7) complexes. In the presence of CO_2 the peak current of Re (1)/Re (0) wave increased in height which illustrated the strong electrocatalytic activity towards CO_2 activation. Preparative electrolysis was carried in acetonitrile electrolyte on modified electrodes yielded higher than 90% carbon monoxide [24b].

The efficiency of the Re(bipy)(CO)$_3$Cl type catalysts for electrocatalytic reduction of CO$_2$ to CO, was improved upon by Kubiak and co-workers by alteration of the groups at the 4 and 4' position of the bipyridine ligand. As well as illustrating a greater current efficiency for the generation CO, the cyclic voltammetry of 4,4'-Bu$_2$bpy complex shows a catalytic reduction wave 3.5 times larger than that of the simple bipyridine complex, in the presence of CO$_2$. The electrolysis of CO$_2$ reduction by this improved Re complex was performed at -1.80 V *vs*. SCE, and it is worth noting that the catalyst maintained catalytic activity post-electrolysis [25].

Due no doubt to its scarcity on earth, groups have attempted to replace rhenium with somewhat more abundant metals for organometallic complexes, such as the Mn(bpy)(CO)$_3$Br used as a catalyst by Deronzier *et al*. to convert CO$_2$ to CO. Electrocatalysis was performed at potential of -1.7 V *versus* Ag/AgCl in acetonitrile. In the absence of CO$_2$ the electrolysis gave [Mn(bpy)(CO)$_3$(MeCN)]$^+$ as a dimer, whilst in the presence of CO$_2$ with 5% water, the second redox wave increases in height, indicative of catalytic electron transfer. Experimentally, CO was selectivity produced during the course of 13 turnovers, and the catalyst was stable for 4 hours, after which time the current decreased and product selectivity diminished [26].

An early report of electrocatalysis of CO$_2$ reduction which does not involve pyridine coligands, nor a precious metal but the simple carbonyl Mo(CO)$_6$ has been reported to give oxalate in a THF electrolyte[27].

Metal catalysts with phosphine ligands have been used for the electrocatalytic reduction of carbon dioxide by a number of research groups, stretching back to

1984 when the Wagenknecht group reported that $Rh(dppe)_2Cl$ [(dppe=1,2-bis(diphenylphosphino) ethane] was capable of reducing CO_2 to the formate anion with small amounts of cyanoacetate, $NCCH_2COO^-$, also formed from the solvent CH_3CN and CO_2. This reduction of CO_2 was performed at -1.55 V *vs* SCE in CH_3CN, with a calculated current efficiency of 42% [28].

A significant development of metal catalyst systems containing phosphine ligands was reported by the Dubois group in 1991, with the isolation of a palladium complex coordinated by polydentate phosphine ligands, $[Pd(triphos)(PR_3)]2[BF_4]$. This was the first type of complex able to catalytically reduce CO_2 to CO in an acidic acetonitrile solution [29].

In 1974, Messhitsuk and co-workers reported for the first time, the use of cobalt and nickel phthalocyanines for the electrocatalysis of CO_2 reduction, and although the TON and determination of products was unclear, it is considered as the first milestone in the understanding of electrocatalytic reduction of CO_2 reduction by transition metal complexes [30].

High current efficiency (98%) and TON (2 to 9 per hour) for CO_2 reduction were reported by Eisenberg and co-workers in 1980, with the use of azomacrocyclic complexes with cobalt and nickel. Electrocatalysis was carried out at a range of potentials (-1.3 V to -1.6 V *versus* SCE) and the products of CO_2 reduction were carbon monoxide and hydrogen [31]. Sauvage and co-workers illustrated that Ni(II)(cyclam) complexes are active electrocatalysts for the reduction of CO_2 to CO, which give high faradic efficiencies of more than 96%, at -0.86 V *versus* SCE. Whilst they are highly stable and selective, they are very sensitive to the pH,
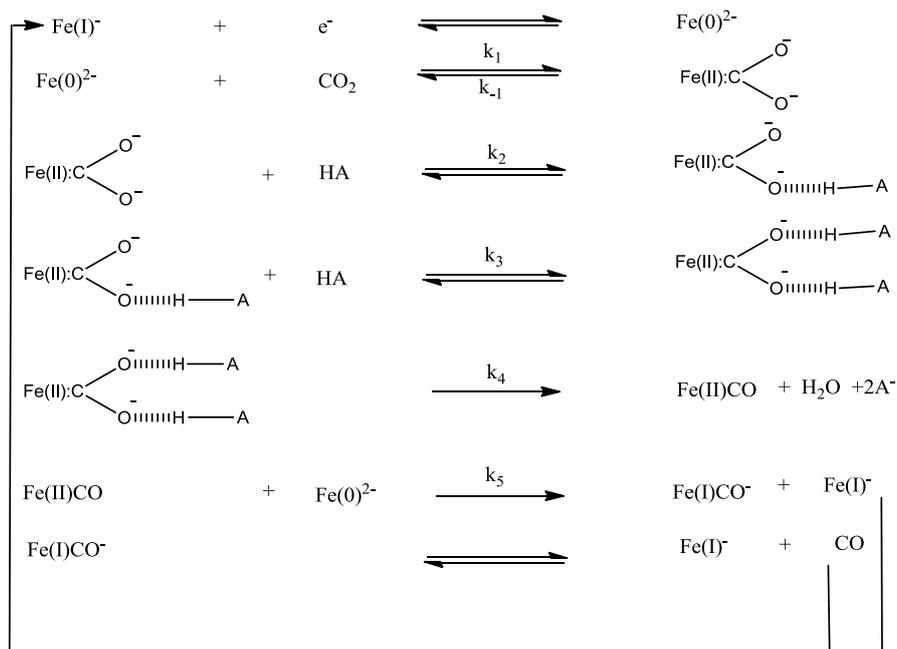
and the selectivity is effected by the anion of the electrolyte, with a fast of rates observed when electrolysis is performed in the presence of KNO_3 or $KClO_4$ [32].

The electrochemical reduction of CO_2 by porphyrin complexes, the subject of this research, is reviewed more extensively below.

3.1.7 Electrocatalytic CO_2 reduction by metal porphyrin complexes

The field of electrocatalytic reduction of CO_2 by metal-porphyrin complexes is popular for many researchers, due in part to the ability of metal-porphyrins to catalyse the reduction of carbon dioxide to carbon monoxide, in both aqueous and non-aqueous solutions. In 1999, Sakata *et al.* [33] employed a metal *meso*-tetraphenylporphyrin (TPP) supported as heterogenous materials on a gas diffusion electrode made of carbon black for the reduction CO_2 in an aqueous electrolyte containing 0.5 $MKHCO_3$. This system showed high activity at both high (20 atm) and low (1 atm) CO_2 pressure. A range of complexes were examined, Co (II), Fe (II), Zn (II), Cu (II), Ni (II), Mg (II), H_2-TPP and Mn(III)(TPP)Cl, in the presence of carbon dioxide. The Co(II), Fe(II) (TPP)Cl species showed high activity for the reduction of CO_2, whilst Zn(II), and Cu(II) (TPP)Cl showed reasonable activity, and Ni(II), Mg(II) (TPP)Cl gave low catalytic activity. The main product was carbon monoxide, with the exception of Cu(II)(TPP), which had selectivity for formation of formic acid, at 22% current efficiency. Under high pressure of CO_2 the potential shifted more positive. It is worth mentioning that the study attributed the production of H_2 to water reduction that occurs at -1.2 V vs. Ag/AgCl.

In 1991, Saveant and co-workers [34] reported on the catalysis of electrochemical reduction of CO_2 by using an iron (0) porphyrin in the presence of cations such as Mg^+. The role the Mg^{2+} ion is that of a hard electrophile that improves the rate of reaction, whilst increasing the stability of catalyst. In the absence of CO_2, the cyclic voltammetry of the porphyrin complex exhibited three reversible waves, assigned to the $Fe^+(III)/Fe(II)$, $Fe(II)/ Fe^- (I)$ and $Fe^-(I)/ Fe^{2-}(0)$. Under 1 atm of CO_2 the $[Fe(TPP)Cl]^{1-/2-}$ couple becomes irreversible and the peak height increase, when magnesium cations are added the current is further increased. The explanation is that Mg^{2+} acts as a Lewis acid. In this study, the electrolysis was carried out at -1.8 V *vs.* SCE and the main reduction product was CO. Later, Saveant and co-workers [17] discovered that the addition of weak Bronsted acids such as 1-propanol, 2-pyrrolidine and CF_3CH_2OH led to a significant improvement in both efficiency and catalyst life time, without any significant formation of H_2. The electrolysis was carried out at -1.7 V *versus* SCE on a mercury electrode in DMF, 0.1 M Et_4NClO_4 at room temperature and 1 atm of CO_2. The distribution of products depended on the synergistic acid, with CF_3CH_2OH favouring production of CO (96 %) with no H_2 or formate, and a TON which increased over time to *ca* 30/h. Use of 1-propanol gives much poorer selectivity, with formation of CO (60 %), formate (35 %), H_2 (4%) and oxalates (1.6 %). Additionally, the effect of water upon catalysis was studied, with addition of 2.8 M containing 1- propanol leading to an increase in CO formation by 20 % (80% total yield), with significant decrease of alternate products. The mechanism of CO_2 reduction in the presence of a catalyst and a Bronsted acid has been proposed and is shown in scheme 3.3.

$Fe(I)^- + e^- \rightleftharpoons Fe(0)^{2-}$

$Fe(0)^{2-} + CO_2 \underset{k_{-1}}{\overset{k_1}{\rightleftharpoons}} Fe(II):C\diagup^{O^-}_{\diagdown O^-}$

$Fe(II):C\diagup^{O^-}_{\diagdown O^-} + HA \overset{k_2}{\rightleftharpoons} Fe(II):C\diagup^{O^-}_{\diagdown O\cdots H\!-\!A}$

$Fe(II):C\diagup^{O^-}_{\diagdown O\cdots H\!-\!A} + HA \overset{k_3}{\rightleftharpoons} Fe(II):C\diagup^{O\cdots H\!-\!A}_{\diagdown O\cdots H\!-\!A}$

$Fe(II):C\diagup^{O\cdots H\!-\!A}_{\diagdown O\cdots H\!-\!A} \overset{k_4}{\longrightarrow} Fe(II)CO + H_2O + 2A^-$

$Fe(II)CO + Fe(0)^{2-} \overset{k_5}{\longrightarrow} Fe(I)CO^- + Fe(I)^-$

$Fe(I)CO^- \rightleftharpoons Fe(I)^- + CO$

Scheme 3.3 The mechanism of CO_2 reduction in the presence of a catalyst and Bronsted acid as proposed by Saveant and coworkers [17]

In 1996, Saveant and co-workers [35] examined the effect that addition of Lewis acid cations such as Mg^{2+}, Ca^{2+}, Ba^{2+}, Li^+, and Na^+, had on the catalysis of CO_2 reduction by Fe(TPP)Cl. Carbon monoxide remained the main product, with formate also formed (30%) in the presence of Mg^{2+}, although it was possible to reduce the amount of formate by instead employing Li^+ (10%).

In a separate study, Saveant and co-workers [36] illustrated that it was possible to increase CO formation from reduction of CO_2 with the introduction of phenolic groups in all ortho and ortho′ positions of the TPP phenyl groups. Preparative scale electrolysis was carried out at -1.4 V *versus* (NHE) resulting in a faradaic yield of 94% for CO formation, along with competing hydrogen formation (6%)

3.1.8 Photoelectrosynthesis of CO from CO_2

Visible light- driven reduction of carbon dioxide affords carbon monoxide as a solar fuel, a key C1 chemical feedstock that provides a pathway for cycling a greenhouse gas [18, 26, 37, 38].

Early work by the Lehn and Geiger groups [37] showed that Re(I) pyridyl complexes are effective electrocatalysts for reduction of CO_2 to CO. The same type of system has been used by Ishitani and co-workers [40] to photocatalyse the reduction of CO_2 to CO in the presence of an amine as a sacrificial electron donor.

More recently, Kubiak and co-workers [26,38] have shown that Re(4,4-Bu$^t_2$bpy)(CO)$_3$Cl catalyses reduction of CO_2 to CO at *p*-type silicon photocathodes when illuminated with visible light. A photo-voltage of *ca*. 600 mV was achieved, facilitating the reduction of CO_2 at potentials of -1.2 V to -1.5 V *versus* SCE. The system reduces CO_2 into CO under illumination, with a current efficiency of 97% during 3 hours of electrolysis.
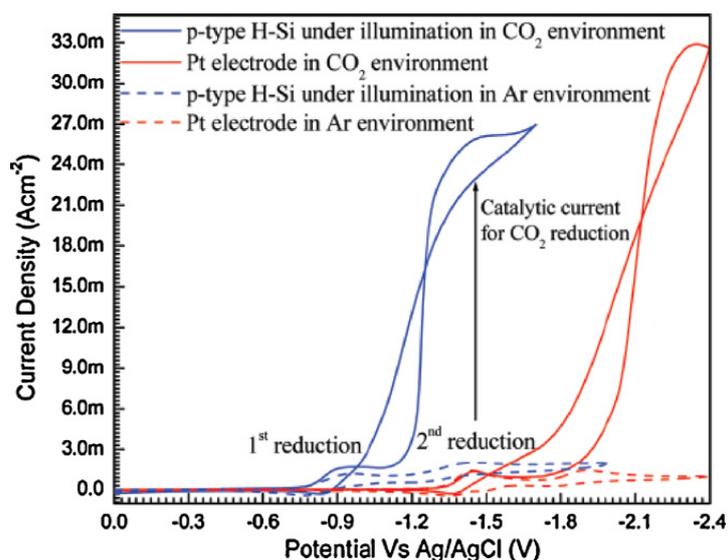
Figure 3.3 Photo-electrocatalytic CO_2 reduction with Re (4,4-*t*Bu$_2$bpy)(CO)$_3$Cl on a *p*-type Si electrode. Reproduced from reference [26]

Under CO_2 and in the presence of water, the Re(4,4'-tBu$_2$bpy)(CO)$_3$Cl catalyses the formation of H_2 and CO with the ratio dependent on the concentration of catalyst. An increase of catalyst leads to an increase of CO, but an increase of water content yields larger amounts of H_2.

However, rhenium is not an earth abundant element and its use in a practical device for photocatalytic or photoelectrocatalytic CO_2 reduction is uneconomical and thus impractical.

3.1.9 Scope of this work

As discussed in section 3.1.1, one of many contemporary and important energy objectives is the economic and efficient conversion of over abundant CO_2, into sources of fuel by means of renewable solar energy. The scope of this chapter is the electrochemical catalysis of carbon dioxide reduction into carbon monoxide by both classical metal porphyrins, and thiolate-containing 'basket-handle' porphyrins at mercury, carbon and illuminated p-type Si electrodes.

The results and discussion sections commence with a description of the basic electrochemistry of the Fe porphyrins at vitreous carbon and dark/illuminated p-type Si electrodes. This is followed by a comparative study of their electrocatalytic and photoelectrocatalytic activity towards CO_2 reduction and a discussion of mechanistic aspects.

3.2 Result and Discussion

3.2.1 Electrocatalysis of CO_2 reduction on inert electrodes: cyclic voltammetry

3.2.1.1 Solvent electrolyte system

The choice of solvent system for all the electrochemical work described below was governed by the need to compare data on mercury and vitreous carbon with that obtained at p-type Si. The epoxy contact to p-type Si is critically important and this is unstable in 100% DMF, the solvent used in earlier basic studies by Saveant and coworkers [17] (see below).

3.2.1.2 Cyclic voltammetry of iron(III) porphyrin complexes under argon

The electrochemistry of the four (new) thiolate Fe(III) porphyrins **Fe-1**, **Fe-2**, **Fe-3** and **Fe-4** together with the known complexes **[Fe(PFTPP)Cl]** and **[Fe(TPP)Cl]**, the structures of which are illustrated in Figure 3.4, were initially studied by cyclic voltammetry.
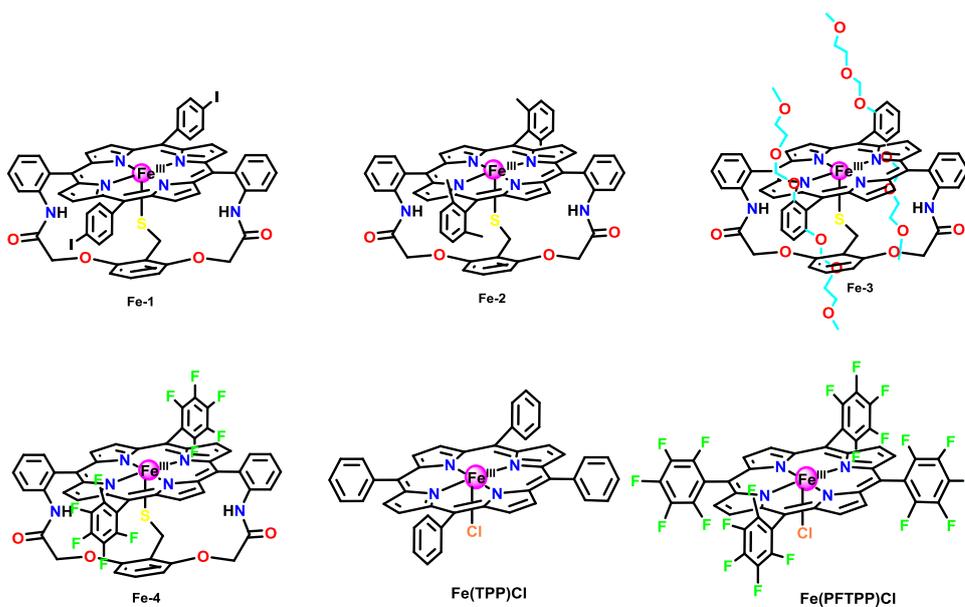
Figure 3.4 Molecular structures of **Fe(TPP)Cl**, **Fe(PFTPP)Cl** and basket-handle iron(III) porphrins together with their abbreviations used in the text

Figure 3.5(a) shows typical cyclic voltammograms for **Fe(TPP)Cl** at vitreous carbon in MeCN-5%DMF(v/v) containing 0.1M [NBu$_4$][BF$_4$]. The cyclic voltammetry exhibits three successive well-defined diffusion controlled reversible one-electron reduction processes (ΔE *ca* 80 mV, i_p^{ox}/i_p^{red} = *ca* 1 at 100 mVs^{-1}) which are formally assigned to the Fe(III)/Fe(II), Fe(II)/Fe(I) and Fe(I)/Fe(0) couples, although the latter may involve porphyrin ring reduction [17].

Figure 3.5 (b) the plot of i_p^{red} for the primary processes *versus* the square root of the scan-rate, $\nu^{1/2}$, which confirms that the process is diffusion controlled. Plots of i_p^{red} *versus* $\nu^{1/2}$ for the Fe(II)/Fe(I) and Fe(I)/(0) couples showed a similar linear dependence. The diffusion coefficient for **Fe(TPP)Cl** was estimated from cyclic voltammetric data as 3.28×10^{-6} cm^{2}s^{-1} using equation 1.10 in Chapter 1.
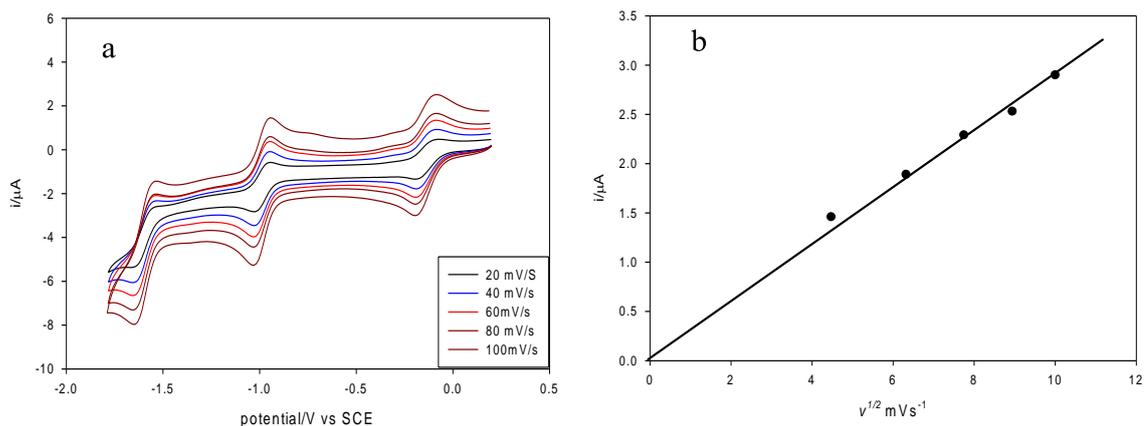
Figure 3.5 (a) Cyclic voltammograms of 0.22 mM **Fe(TPP)Cl** at carbon electrode, at different scan-rates in (MeCN-5%DMF) containing 0.1M [NBu$_4$][BF$_4$]. (b) Plot of i$_p^{red}$ for the Fe(II)/Fe(I) couple versus the square-root of the scan-rate

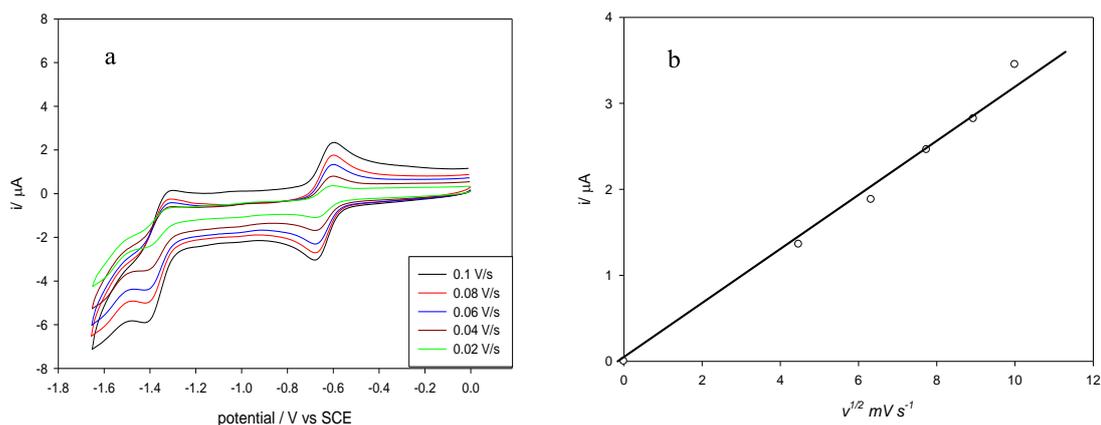**Figure 3.6** (a) Cyclic voltammograms of 0.22 mM **Fe-1** at carbon electrode, at different scan-rates in (MeCN-5%DMF) containing 0.1M [NBu$_4$][BF$_4$]. (b) Plot of i$_p^{red}$ for the Fe(II)/Fe(I) couple versus the square-root of the scan-rate (third reduction at -1.82 V)

Figure 3.6(a) shows the cyclic voltammetry of the thiolate ligated basket handle porphyrin **Fe-1** under argon in MeCN- 5%DMF containing 0.1M [NBu$_4$][BF$_4$]. Three successive reduction steps are observed at potentials E$_{1/2}$= -0.68 , -1.42, and -1.82V *versus* SCE formally corresponding to Fe(III)/Fe(II), Fe(II)/Fe(I) and Fe(I)/Fe(0) processes respectively, the Fe(I)/Fe(0) couple in this system is irreversible. Figure 3.6(a) shows a set of voltammograms recorded at various scan rates for complex **Fe-1** for the primary and secondary process. The primary

110

reduction process is a diffusion controlled reversible one-electron step. Thus: (i) the plot of the peak current $^{I}i_p^{red}$ *versus* $v^{1/2}$ is linear with an intercept close to zero Figure 3.6 (b) (ii) the peak potential separation, $\Delta E = 75$ mV (theoretical separation for a one-electron process is *ca* 60mV at 298K). The diffusion coefficient for **Fe-1** is estimated to be 3.5×10^{-6} cm^2 s^{-1} which is close to that estimated for **Fe(TPP)Cl**. The magnitude of $^{II}i_p^{red}$ for the secondary process is greater than $^{I}i_p^{red}$ ($^{II}i_p^{red}/ {}^{I}i_p^{red}$) ranging from 1.35 at 100 mVs^{-1} to 1.44 at 20 mVs^{-1}. This is consistent with an **ece** process with a chemical step and further electron-transfer taking place at the Fe(II)/Fe(I) level.

The cyclic voltammetry of **Fe-2** is shown in Figure 3.7. The behaviour is similar to that of **Fe-1** insofar as the primary step is a reversible one–electron diffusion controlled processes, the secondary step is partially reversible and the third step is more or less irreversible and gives rise to electroactive products. This general behaviour is observed for all of the basket handle porphyrin complexes, each showing two diffusion-controlled reduction steps with irreversibility of the Fe(I)/Fe(0) couple.
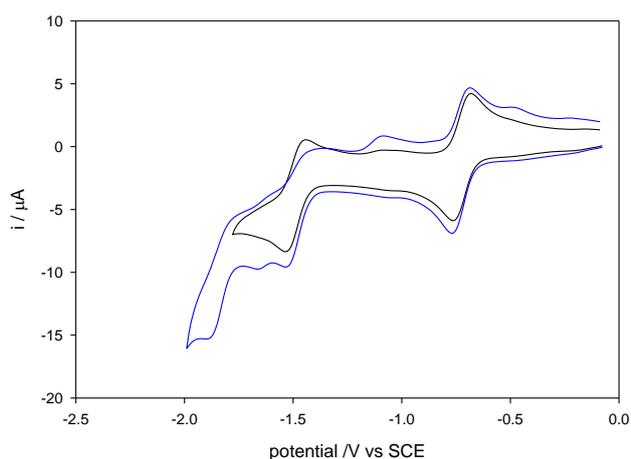

Figure 3.7 Cyclic voltammetry of 0.22 M **Fe-2** at a at a vitreous carbon electrode in MeCN-5% DMF containing 0.1M [NBu$_4$][BF$_4$] , scan rate100mVs^{-1} under Ar

Table 3.4 lists the $E_{1/2}$ data for the three successive reduction steps of all the complexes studied; potentials quoted *versus* SCE and were determined at 100 mVs^{-1}. The overall trend in reduction potentials is as expected; those species possessing electron-withdrawing substituents on the aromatic rings are easier to reduce than are their unsubstituted analogues at corresponding redox levels. For example, the complex **Fe(PFTPP)Cl** which possesses a total of 20 electron-withdrawing fluoro-substituents on the phenyl groups is easier to reduce across all the Fe(III)/Fe(II), Fe(II)/Fe(I) and Fe(I)/Fe(0) redox levels than is its **Fe(TPP)Cl** counterpart. Thus the **Fe(PFTPP)Cl$^{0/1-/2/3-}$** couples occur at potentials which are successively 300, 360 and 400 mV positive of those for the corresponding **Fe(TPP)Cl$^{0/1-/2-/3-}$** couples, Table 3.4.

Table 3.4 Reduction potentials (V versus SCE) in MeCN-5%DMF (v/v) containing 0.1M [NBu$_4$][BF$_4$] at carbon electrode for the porphyrin complexes shown in Figure 3.4

complex	$^1E_{1/2}$	$^2E_{1/2}$	$^3E_{1/2}$
Fe(PFTPP)Cl	0.14	-0.71	-1.20
Fe(TPP)Cl	-0.19	-1.07	-1.60
Fe-1	-0.68	-1.42	-1.82
Fe-2	-0.72	-1.50	-1.92
Fe-3	-0.78	-1.53	-1.97
Fe-4	-0.61	-1.27	-1.46

3.2.1.3 Cyclic voltammetry under CO_2 and in the presence of CF_3CH_2OH.

As discussed above in Section 3.1.7, Saveant and coworkers [17] have shown that the simple iron porphyrin, **Fe (TPP)Cl** in DMF is an efficient and reasonably stable electrocatalyst for CO_2 reduction. Thus at a mercury pool cathode in the presence of CF_3CH_2OH as a proton source, they found conversion to CO with a current efficiency of 95%, high selectivity over H_2 formation, and fast electrode kinetics.

We have examined **Fe(TPP)Cl**, **Fe(PFTPP)Cl** and basket handle thiolate Fe(III) porphyrins as electrocatalysts for reduction of carbon dioxide into carbon monoxide in 95% acetonitrile 5% DMF(v/v) at vitreous carbon in the absence and in the presence of CF_3CH_2OH.

The cyclic voltammetry of the **Fe(TPP)Cl** shows that CO_2 interacts with the reduced catalyst at the Fe(I)/Fe(0) level as evident from the increase in $^{III}i_p$ and the irreversibility under CO_2. The peak current increase is small indicative of slow electrocatalysis [17]. However, addition of a weak acid such as trifluoroethanol results in dramatic increase in the catalytic current, Figure 3.8 (a, b). These observations are fully in accord with those reported earlier by Saveant and coworkers who have attributed the effect of CF_3CH_2OH as being a consequence of the stabilisation of an iron-carbon dioxide adduct by H-bonding [17]. A fuller discussion of the mechanism of electrocatalysis of CO_2 reduction by **Fe(TPP)Cl** at vitreous carbon is given in the context of photoelectrocatalysis at p-type Si in section 3.2.5.
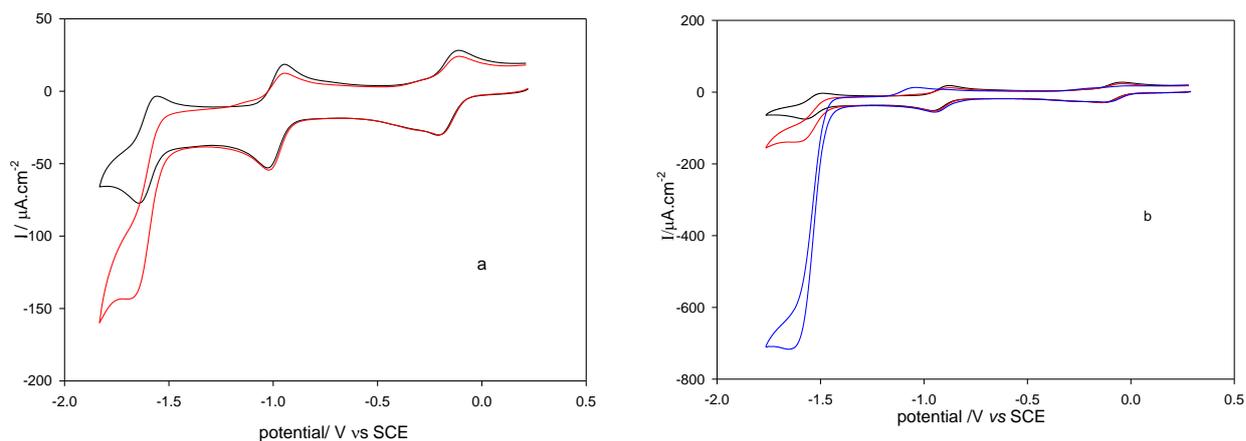
Figure 3.8 Cyclic voltammetry of 0.2 mM **Fe(TPP)Cl** at a vitreous carbon electrode in MeCN-5% DMF containing 0.1M [NBu$_4$][BF$_4$] , scan rate100mVs^{-1} : (a) under Ar and under CO$_2$ at 1 atmosphere; (b) in the presence of 0.032 M CF$_3$CH$_2$OH

The complex **Fe (PFTPP)Cl** shows a very similar behaviour in its cyclic voltammetry under CO$_2$ in the absence and presence of CF$_3$CH$_2$OH to that of the **Fe(TPP)Cl** species, except that the strongly withdrawing fluoro-groups shift the potential for electrocatalysis about 400 mV positive of that for **Fe(TPP)Cl**.

There is a very marked difference in the behaviour of the basket handle thiolate iron porphyrin complexes under CO$_2$. Both **Fe(PFTPP)Cl** and **Fe(TPP)Cl** interact with CO$_2$ at the Fe(0) level, whereas the thiolate complexes appear to interact at the Fe (I) level. This is shown by the cyclic voltammetry of **Fe-1** in Figure 3.9. In the presence of CO$_2$ the primary Fe(III)/Fe(II) couple (I, Figure 3.9) is essentially unaffected by CO$_2$, as is observed for **Fe(TPP)Cl**, showing little or no interaction of the Fe(II) state with the substrate. However, at the Fe(II)/(I) - level there is a marked affect on the voltammetry. The peak is shifted substantially to a more positive potential without a change in the peak height (III, Figure 3.9). This can be explained by fast binding of CO$_2$ to the Fe(I) species, shifting the Nerstian equilibrium to a more positive value. The formation of the Fe^I(CO$_2$) species gives an additional electroactive species which gives rise to a new peak at

E_p = - 1.55V *versus* SCE, (IV, Figure 3.9). This may correspond to the formation of an $Fe^0(CO_2)$ species.

However, some caution is needed in this interpretation. The cyclic voltammogram under CO_2 also shows a broad reduction feature <u>preceeding</u> the Fe(II)/Fe(I) reduction step (II, Figure 3.9). Carbon dioxide may increase the acidity of residual water in the electrolyte which possibly gives rise to the reduction peak II (see below).

The effect on the cyclic voltammetry of **Fe-1** of CF_3CH_2OH under dinitrogen is shown by Figure 3.10. In the presence of the weak acid alone there is a shift in the secondary reduction peak to a more positive value and a new irreversible peak is observed at a more negative potential. The primary oxidation process is relatively unaffected. Peak II observed under CO_2 (Figure 3.9) is absent under these conditions. The two peaks below -1V *versus* SCE in Figure 3.9(b) in the presence of the weak acid are at potentials similar but not identical to those observed under CO_2. Figure 3.11 shows the effect of the presence of CO_2 and CF_3CH_2OH together. Fast electrocatalysis is observed as for the **Fe(TPP)Cl** and **Fe(PFTPP)Cl** complexes and this is observed near -1.6V *versus* SCE. Importantly a *new* well-defined partially reversible one – electron couple is also present at -1.17V *versus* SCE, Figure 3.11, which absent in the presence of either CF_3CH_2OH alone or CO_2 alone. As discussed above, under CO_2 alone the less well-defined peak II is observed, but this not at the same potential for the species in Figure 3.11.
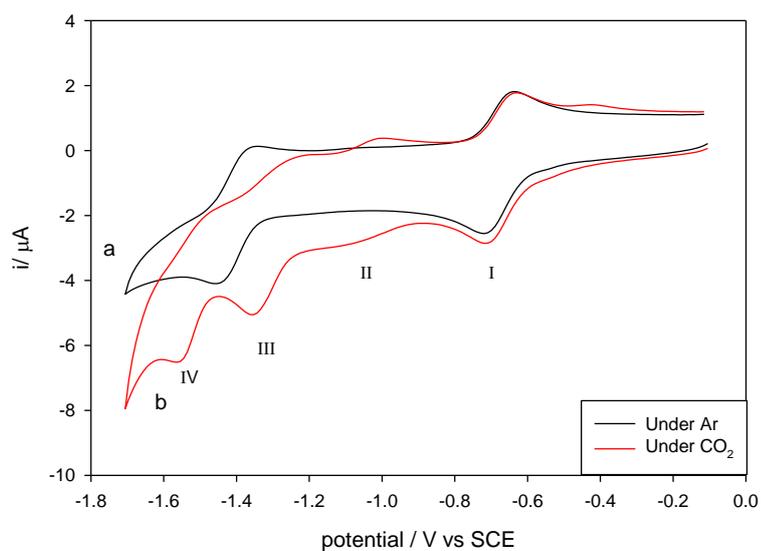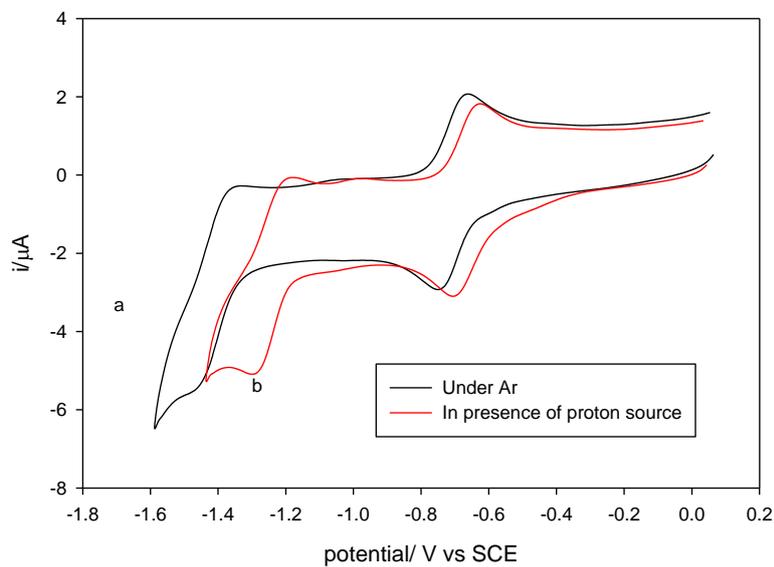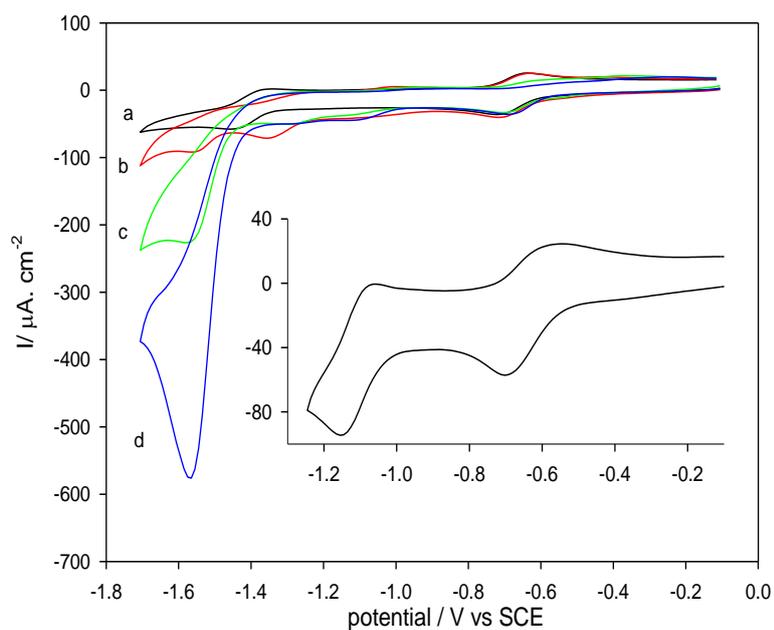
Figure 3.9 Cyclic voltammetry of 0.2 mM **Fe-1** at a vitreous carbon electrode in MeCN-5% DMF containing 0.1M [NBu$_4$][BF$_4$] , scan rate100mVs^{-1} : (a) under Ar ; (b) under CO$_2$ at 1 atmosphere

Figure 3.10 Cyclic voltammetry of 0.2 mM **Fe-1** at a vitreous carbon electrode in MeCN-5% DMF containing 0.1M [NBu$_4$][BF$_4$] , scan rate100mVs^{-1} : (a) under Ar ; (b) in the presence of CF$_3$CH$_2$OH at 0.274M

Figure 3.11 Cyclic voltammetry of 0.2 mM **Fe-1** at a vitreous carbon electrode in MeCN-5% DMF containing 0.1M [NBu$_4$][BF$_4$] , scan rate100mVs^{-1} : (a) under Ar ; (b) under CO$_2$ at 1 atmosphere ; (c) under CO$_2$ at 1 atmosphere in the presence of 0.098 M CF$_3$CH$_2$OH ; (d) under CO$_2$ at 1 atmosphere in the presence of 0.25 M CF$_3$CH$_2$OH. The inset cyclic voltammetric curve was recorded under CO$_2$ in the presence of 0.25 M CF$_3$CH$_2$OH: the range was limited to -0.1 to -1.3V *versus* SCE

Figure 3.12 shows the variation of the peak current as a function of concentration of CF$_3$CH$_2$OH. The current density increases with increasing of [CF$_3$CH$_2$OH] up to about 0.25M, after which the electrocatalysis becomes independent of the acid concentration, indicating protonation is no longer rate-limiting. This is similar to the behaviour of **Fe(TPP)Cl**.
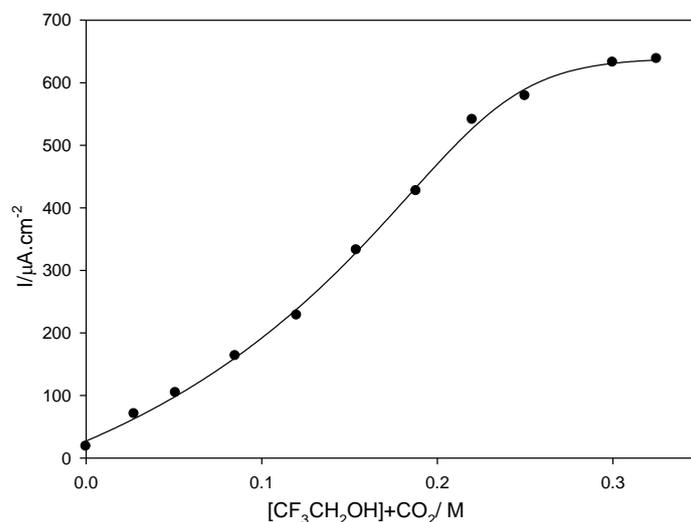
Figure 3.1.2 Effect of the acid concentration of CF_3CH_2OH on the peak current for catalysis by **Fe-1** at scan rate 0.1V/s, at room temperature

The cyclic voltammetry of **Fe-2** is quite similar to that described above for **Fe-1** under the same conditions. Thus Figure 3.13 (a) shows the cyclic voltammetry of **Fe-2** in MeCN-5%DMF containing 0.1M [NBu$_4$][BF$_4$] under argon and CO_2 and Figure 3.13(b) shows the effect of introducing trifluoroethanol which again leads to an electrocatalytic current.
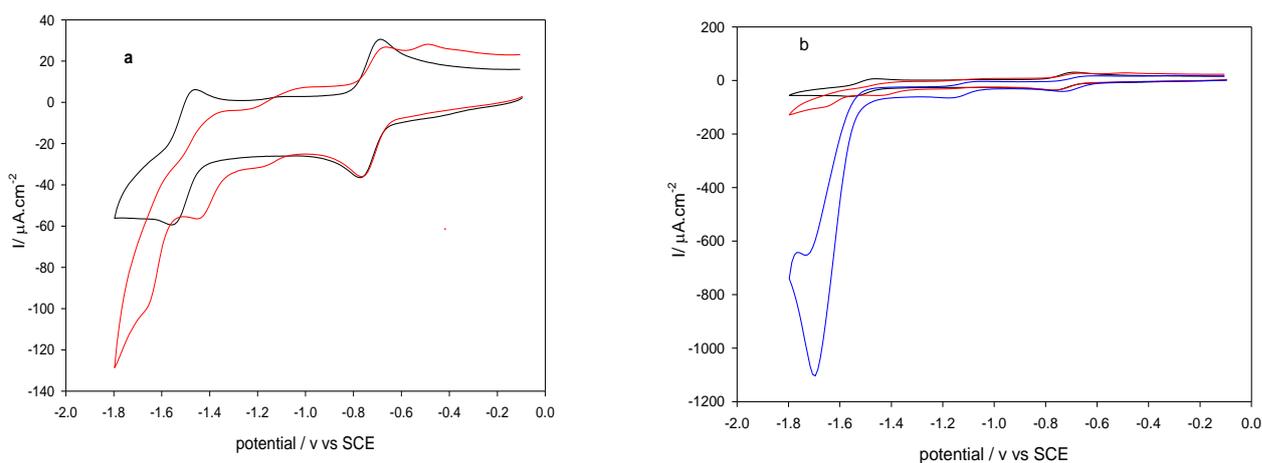
Figure 3.13 Cyclic voltammetry of **Fe-2** (0.2 mM) at a vitreous carbon electrode in MeCN-5%DMF containing 0.1M [NBu$_4$][BF$_4$]; scan rate100mVs^{-1}, (a) under CO_2, (b) in the presence of 0.21 M CF_3CH_2OH

To explore the effect of acid further, we have also examined the behaviour of **Fe-3** under Ar at a vitreous carbon electrode in in MeCN-5%DMF containing 0.1M [NBu$_4$][BF$_4$] in the presence of lutidinium as the acid source. This is a stronger acid than CF$_3$CH$_2$OH. Figure 3.14 show the effect of this proton source on the cyclic voltammetry. All the reduction waves are shifted positive to those observed in the absence of the acid, with major shifts associated with the second and third peaks. Additionally for this system we can show that the effect is fully reversible on addition of the strong base ^{t}BuOK. This behaviour parallels that seen for **Fe-1** in the presence of the weaker acid but the shifts in the potentials are somewhat greater. This can be attributed to electron –transfer coupled to the acid dependent equilibrium as shown in Scheme 3.4.
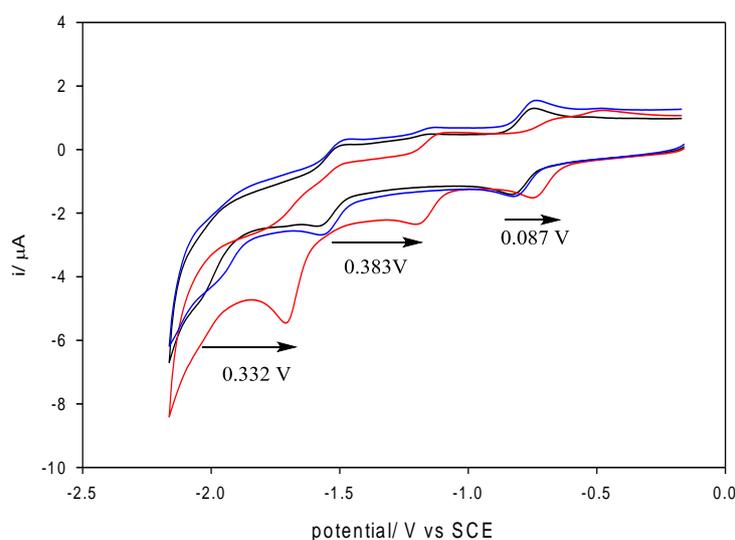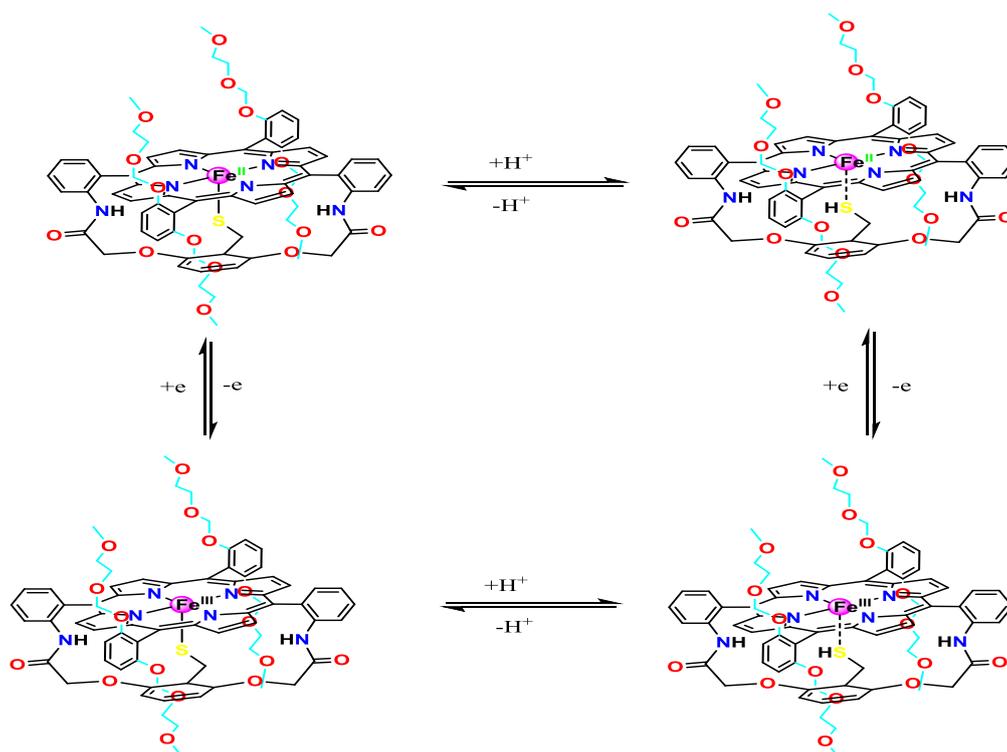

Figure 3.14 Cyclic voltammetry of 0.2 mM **Fe-3** in (MeCN-5%DMF) containing 0.1M [NBu$_4$][BF$_4$], scan rate100 mVs^{-1} at a vitreous carbon electrode under Ar , in the presence of proton source and the presence of potassium *tertiary* butoxide

Scheme 3.4 The behaviour of **Fe-3** under Ar at a vitreous carbon electrode in in MeCN-5%DMF containing 0.1M [NBu$_4$][BF$_4$] in the presence of lutidinium as the acid source

3.2.2. Preparative –scale electrolysis at a mercury pool.

3.2.2.1 Electrosynthesis of CO catalysed by Fe(TPP)Cl

Saveant and co-workers reported that the electrocatalysis of carbon dioxide by **Fe(TPP)Cl** (1 mM) in DMF in the presence of 1.37 M CF$_3$CH$_2$OH gave CO (96 %) with no H$_2$ or formate. The electrolysis was carried out at potential, -1.7 V *vs* SCE for 2 hours [17].

Similarly, we find that bulk scale electrolysis at a Hg-pool cathode under CO$_2$ (*ca* 0.28M [17] gives CO with a current efficiency of *ca* 85% after *ca* 123 turnovers during the course of 2.4 h at -1.7 V *versus* SCE, MeCN-5%DMF (v/v), 0.1M [NBu$_4$][BF$_4$]. Thus using 0.14 mM of catalyst and 0.28 M CF$_3$CH$_2$OH, the charge passed was 20 C and gave 87µmoles of CO which was determined by gas chromatography using a thermal conductivity detector (GC-TCD) A small

amount of hydrogen is formed. The quantity of CO_2 in the saturated solution phase is *ca* 1.4×10^3 μmols (0.27M) in the 11ml gas phase at 1 atmosphere *ca* 5×10^2 μmols is present at the begining of the experiment. The current decayed to an approximate plateau region but after 2h it rapidly declined with time. On the basis of the CO produced less than 5% of the total CO_2 and 15% of the available acid was consumed. The rapid decay of the current is probably indicative of catalyst loss or inhibition of the catalyst by CO. Cyclic voltammetry at the end of electrolysis showed the absence of redox active porphyrin species, suggesting catalyst loss rather than CO inhibition.
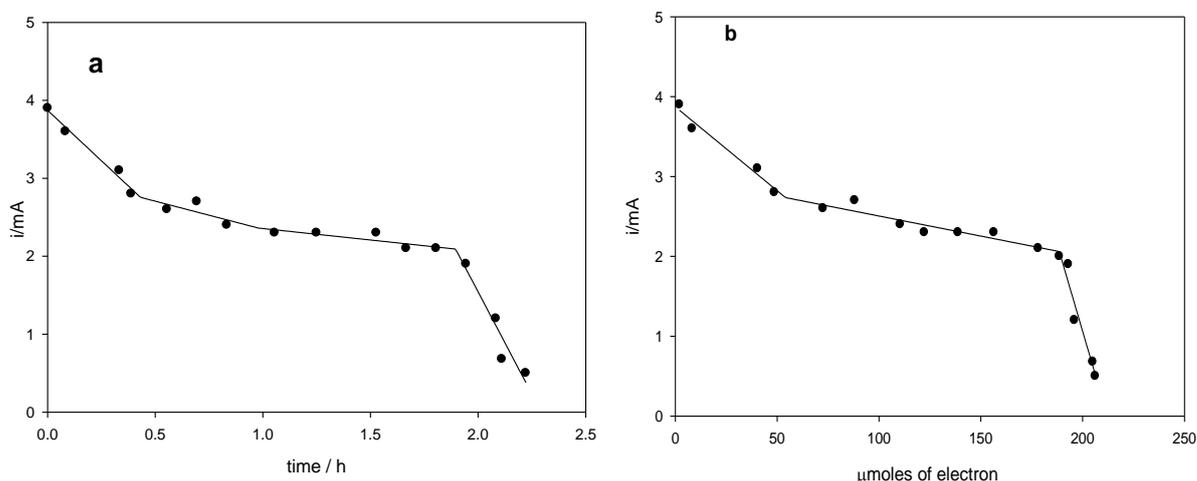
Figure 3.15 (a) Current *versus* electrolysis time , (b) Current *versus* μmoles of electrons for CO_2 reduction in the presence of **Fe(TPP)Cl** . $[CF_3CH_2OH] = 0.275M$ (1375μmol)

3.2.2.2 Electrosynthesis of CO catalysed by Fe(PFTPP)Cl

The electrolysis of a saturated CO_2 solution {mercury pool, -1.30 V *versus* SCE; MeCN-5%DMF (v/v), 0.1M $[NBu_4][BF_4]$; 0.28 mM CF_3CH_2OH} in the presence of **Fe(PFTPP)Cl** (0.11 mM) as the electrocatalyst gave 21μmoles of CO after the passage of 90.5 μmoles of electrons (8.73 C) during the course of 1.8h with a current efficiency of *ca* 46% after 38 turnovers. A small amount of hydrogen is formed with a current efficiency of 1.1%. In a separate experiment where the

concentration **of Fe(PFTPP)Cl** was increased to 0.2 mM there was a small increase in the current efficiency to 53% (36 µmoles CO; charged passed 12.3C). This system is less efficient at producing CO than is **Fe(TPP)Cl**, although the potential is lower. Other products than CO must be formed, possibly oxalate or formate but these have not been determined. Again, although CO_2 is in excess the current decayed at longer times, Figure 3.16, as observed for the **Fe(TPP)Cl** complex,
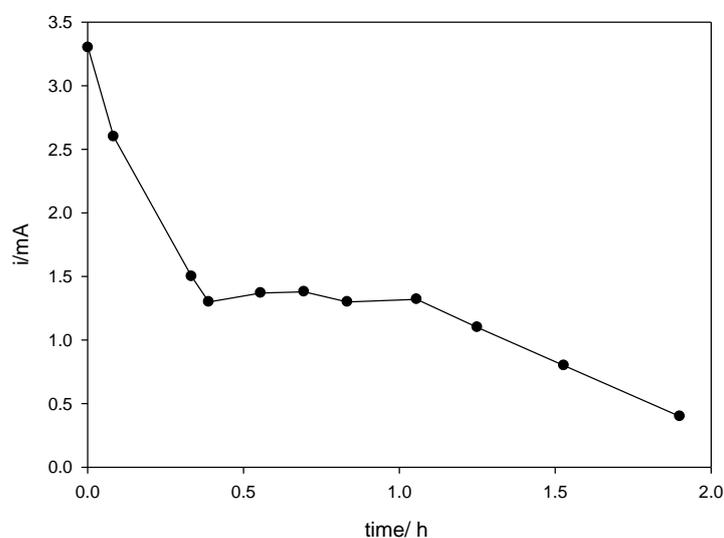

Figure 3.16 Current *versus* electrolysis time for CO_2 reduction in the presence of **Fe(PFTPP)Cl**

3.2.2.3 Electrosynthesis of CO by basket handle thiolate iron (III) porphyrins

Electrocatalytic reduction of carbon dioxide was carried out in 0.1M [Bu$_4$N][BF$_4$]- MeCN+5%DMF at room temperature in the presence of CF$_3$CH$_2$OH on a mercury pool electrode. Based on the cyclic voltammograms of thiolate iron porphyrins, applied potentials for electrolyses of **Fe-1**, **Fe-2**, **Fe-3** an**d Fe-4** under CO$_2$ were set at -1.63V, -1.65 V, -1.68 V, and -1.37 V *versus* SCE respectively. CO was analysed by gas chromatography (GC-TCD) and Table 3.5 summarises the results for the four basket handle porphyrins in terms of charge passed, CO and H$_2$ yields, current efficiency and number of turnovers, T.N.

Table 3.5 Current efficiencies and turnover numbers for electrocatalytic reduction of carbon dioxide catalysed by Fe(III) basket porphyrins

Complex	Potential (SCE)	Number of moles of catalyst /μmole	Time of experiment/h	Charge coulomb/C	Current efficiency CO	T.N CO	μmol of CO	Current efficiency H$_2$	T.N H$_2$
Fe-1	-1.63	0.29	2.2	8.4	79	117	34	0.36	0.53
Fe-2	-1.65	0.22	2.2	5.75	87	130	28.6	0.28	0.31
Fe-3	-1.68	0.28	2	6.34	85.3	99.6	28	3.9	4.7
Fe-4	-1.37	0.25	2	5.45	58.96	66.8	16.7	0.5	0.136

For example**,** the electrochemical reduction of CO$_2$ catalysed by **Fe-1** (0.056 mM) was carried out at a mercury pool cathode {-1.63 V *versus* SCE; MeCN-5%DMF (v/v), 0.1M [NBu$_4$][BF$_4$]; 0.28 mM CF$_3$CH$_2$OH}. At the end of 2.2h the current had decayed to *ca* 5% of the initial current, corresponding to the passage of 87 μmoles of electrons (8.4C) as shown by Table 3.5. As before, the gas phase of the cell was analysed by GC-TCD. The CO yield was 34 μmoles corresponding to a

current efficiency of *ca* 80%. A small amount of H_2 was produced, 0.16 μmoles, with a current efficiency of less than 1%. The current decayed over the period of electrolysis. A plot of current versus charge-passed is shown by Figure 3.17 which again is indicative of loss of the catalyst at longer times.
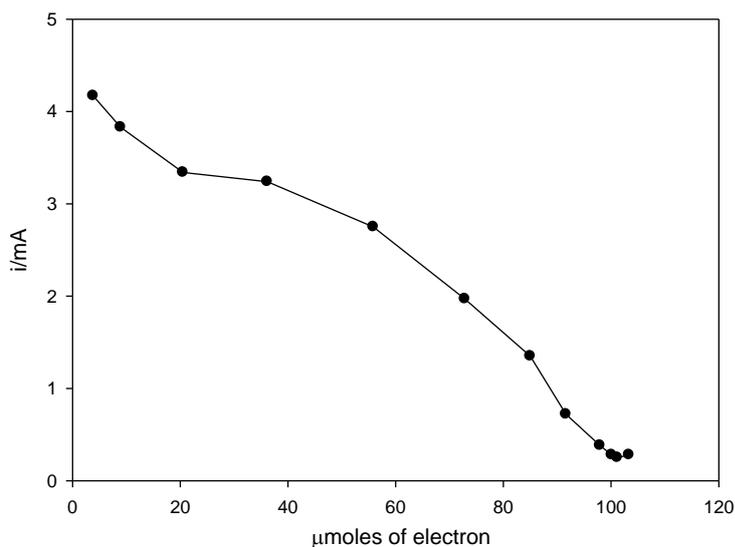

Figure 3.17 The current *versus* μmoles of electrons passed: 0.2mM **Fe-1** in the presence of CO_2 and   0.274 M CF_3CH_2OH in MeCN-5%DMF containing 0.1M [NBu$_4$][BF$_4$]

In a separate experiment the yield of CO was monitored by gas chromatograph as a function of electrolysis time {0.1 mM **Fe-1, -**1.63 V *versus* SCE; MeCN-5%DMF (v/v), 0.1M [NBu$_4$][BF$_4$]; 0.28 mM CF_3CH_2OH}, Figure 3.18 After about 1h the yield does not increase with time corresponding to the low cell current after this period.
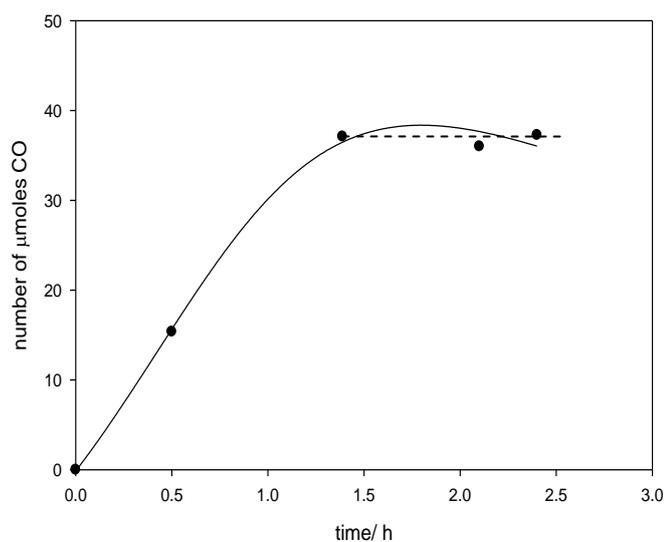
Figure 3.18 CO yield *versus* electrolysis time, 0.1mM **Fe-1**, 0.274 M CF_3CH_2OH and saturated CO_2 (*ca* 0.27M) in a MeCN-5%DMF containing 0.1M [NBu_4][BF_4]

Table 3.6 Data for electrocatalytic reduction of CO_2 by (0.1mM, 0.5μmole) **Fe-1** at mercury pool cathode

Time/h	0.5	1.38	2.1	2.45
Number of μmoles of CO	16.5	40	37.2	40
Current efficiency %	55	80	75	75
T.N	33	80	75	80
Charge passed, C	5.38	8.83	9.8	9.93
μmole of electrons	55.86	91.6	101.3	103

3.2.3 CO₂ reduction at a p-type Si photoelectrode : cyclic voltammetry

3.2.3.1 Cyclic voltammetry of iron porphyrins at p-type Si electrode under Ar

In this work we have examined **Fe(TPP)Cl**, **Fe(PTPP)Cl** and basket handle thiolate Fe(III) porphyrins as catalysts to reduce carbon dioxide into carbon monoxide at p-type Si electrodes in the presence of CF_3CH_2OH in MeCN-5%DMF (v/v) containing 0.1M [NBu_4][BF_4].

125

As briefly mentioned earlier, the stability of the insulating epoxy resin protecting the copper wire/silver epoxide/gallium contact on the p-type Si limited the choice of solvent. The mixed solvent MeCN- 5% DMF(v/v) was a compromise between the poor solubility of the complexes in 100% MeCN and the deterioration of the epoxy resin in 100% DMF

A typical cyclic voltammogram for **Fe(TPP)Cl** at p-type Si electrode (B-doped, Si-H surface termination, 1-10Ω cm^{-1},40-100 Ω cm^{-2}) in the <u>dark</u> is shown Figure 3.19. The potential range is confined to that covering the reduction of the Fe(II)/Fe(I) and Fe(I)/Fe(0) couples because the H-terminated p-type Si is oxidised at potentials positive of about -0.2V *versus* SCE and becomes inactivated. Whereas the Fe(II)/Fe(I) couple shows a reasonable well-defined behaviour and parallels that on vitreous carbon, the Fe(I)/Fe(0) process observed on vitreous carbon becomes irreversible on the p-type Si surface. The reason for this is not known. The structure of the inner reaction layer at the semiconductor may promote halide loss and further electron-transfer to the porphyrin ring. The orientation of **Fe(TPP)Cl** in the inner reaction layer on vitreous carbon and on p-type Si may differ, promoting ring or Fe reduction, traces of water may influence the chemistry on p-type Si more than on vitreous carbon. The response on illuminated p-type Si is dramatically different from that in the dark. When illuminated using a Krüss halogen fibre optic lamp (90 mW cm^{-2}, λmax = 650nm) the primary and secondary reduction processes shift more positive by about 600 mV. Bard and coworkers reported nearly forty years ago the dark reduction of the [Ru(bpy)$_3$]$^{2+/1+}$ system on p-type Si in MeCN and noted the shift in redox response to more positive values upon illumination, the magnitude of the shift in the redox couples was of a similar magnitude, 540 – 600mV [41].

Table 3.7 Reduction potentials (V *versus* SCE) in MeCN-5%DMF (v/v) containing 0.1M [NBu$_4$][BF$_4$] at an illuminated p-type Si electrode

Complex	$^2E_{1/2}$	^3E_p
Fe(PFTPP)Cl	-0.31	-0.83
Fe(TPP)Cl	-0.42	-1.05
Fe-1	-0.53	-1.07
Fe-2	-0.65	-1.17
Fe-3	-0.69	-1.20
Fe-4	-0.42	-0.87

This is evident from Figure 3.19 which shows the cyclic voltammetry of **Fe(TPP)Cl** at p-type Si electrode in the dark and when illuminated. The behaviour of the other complexes **Fe(PFTPP)Cl**, **Fe-1**, **Fe-2**,**Fe-3** and **Fe-4** is similar. The magnitude of the photovoltage as estimated from the difference of E_p^{carbon} and $E_p^{Si, light}$ for the <u>third</u> reversible Fe(I)/Fe(0) reduction steps at vitreous carbon and illuminated p-type Si respectively are listed in Table 3.8 for each of the complexes.

Table 3.8   Fe(I)/Fe(0) photopotentials for the various Fe porphyrin complexes at p-type Si in {MeCN-5%DMF}- 0.1M [NBu$_4$][BF$_4$] determined at 100mV s^{-1}

Complex	$E_p^{carbon} - E_p^{Si,light} / V$	$E_p^{Si,dark} - E_p^{Si,light} / V$
Fe(PFTPP)Cl	0.46	0.48
Fe(TPP)Cl	0.63	0.68
Fe-1	0.83	0.52
Fe-2	0.85	0.56
Fe-3	0.84	0.50
Fe-4	0.85	0.58
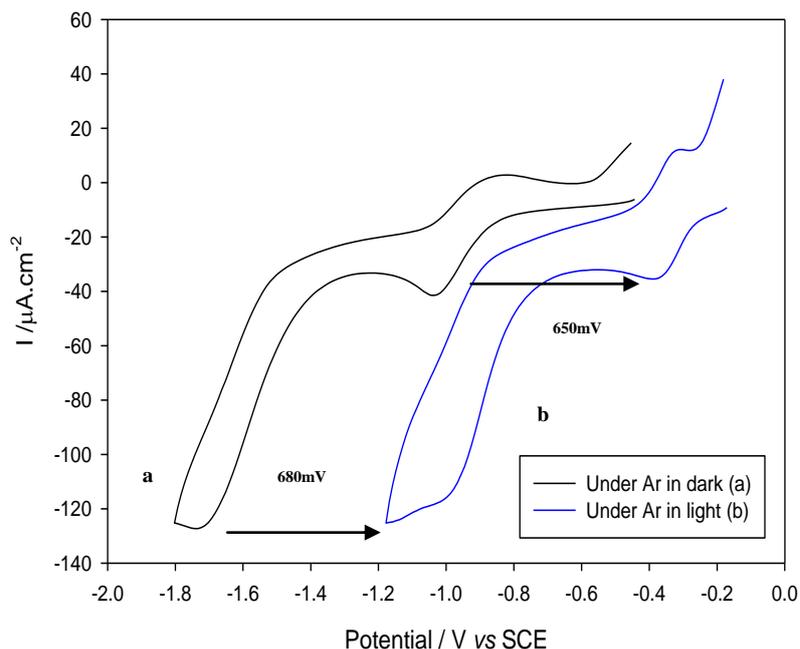
Figure 3.19 Cyclic voltammograms of **Fe(TPP)Cl** at a p-type H-Si electrode in a solvent mixture (MeCN-5%DMF) containing 0.1M [NBu$_4$][BF$_4$] at a scan rate of 100mV·s^{-1}. (a) in the dark; (b) illuminated by a Krüss halogen fibre optic lamp (90mW·cm^{-2}, λ_{max} =650nm)

Figure 3.20 shows a set of voltammograms recorded at various scan rates for **Fe(TPP)Cl** . The second reduction process is a diffusion controlled reversible one-electron step but the third reduction is a quasi- reversible process because the peak current is more than one electron. Figure 3.20 (b) shows the plot of i$_p$^{red} for the primary process *versus* the square root of the scan-rate, $v^{1/2}$. This confirms that the process is diffusion controlled. Plots of i$_p$^{red} *versus* $v^{1/2}$ for the Fe(II)/Fe(I) and Fe(I)/(0) couples showed a similar linear dependence. The diffusion coefficient for **Fe(TPP)Cl** was estimated from the cyclic voltammetric data to be 3.25 x 10^{-6} cm^{2}s^{-1} which is in excellent agreement with that determined on vitreous carbon which was 3.28 x 10^{-6} cm^{2}s^{-1}, as described above. This supports

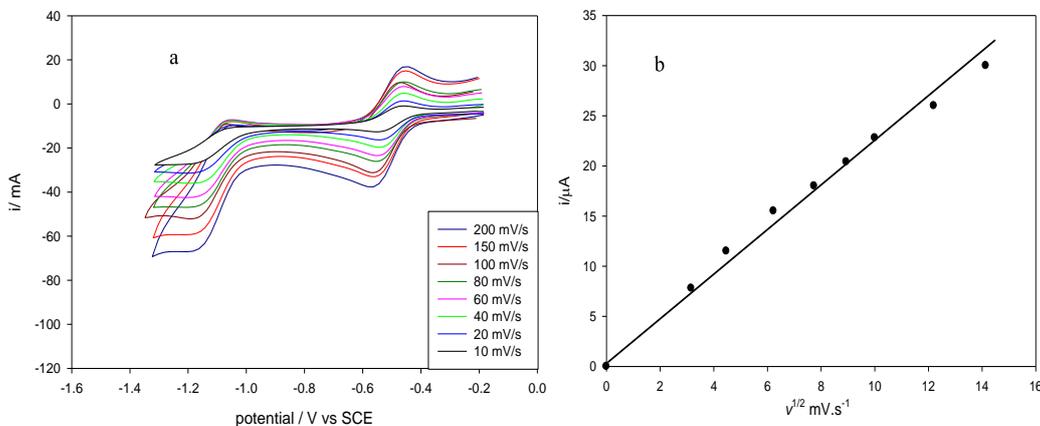the view that the 'electrochemical' area of p-type Si and vitreous carbon are very similar.

Figure 3.20 (a) Cyclic voltammograms of 0.22 mM **Fe(TPP)Cl** at illuminated p-type Si at different scan rates in (MeCN-5%DMF) containing 0.1M [NBu$_4$][BF$_4$] (b) dependence of i$_p^{red}$ for the Fe(II)/Fe(I) couple on the square root of the scan-rate

3.2.3.2 Effect of light intensity on the voltammetric response

Figure 3.21 shows how the cyclic voltammetry of the primary and secondary redox couples respond to the distance of the light source from the p-type Si surface. The photon flux from a point source falls off with the square of the distance. A distance of five times the source diameter is considered as the position at which a source can be approximated to a point source; since the Krüss halogen fibre optic lamp has a cross-section of 0.5 cm we can approximate its behaviour to a point source when it is 2.5 cm from the electrode surface The peak currents are only marginally affected by the decrease in intensity of the light source but there is a dramatic change in the position of the Fe(II)/Fe(I) and Fe(I)/Fe(0) couples as measured by their E$_{1/2}$ values. Figure 3.20 shows how the position of the Fe(II)/Fe(I) and Fe(I)/Fe(0) couples shift with distance. With the light source at 6 cm or less the maximum shift to positive values for the **Fe(TPP)Cl** couples is

observed, that is, the photovoltage is at a maximum. At a distance of 60 cm their is only a small shift in potentials relative to the behaviour at the semi-conductor electrode in the dark and these are close to those observed on vitreous carbon, Figure 3.21 and Table 3.9. Another noticeable feature is that at the lower light intensities the magnitude of peak separations ΔE increases from a minimum of about 100mV at maximum light intensity, 3 cm light source, to 280mV at 60cm light source. A surprising observation is that the increase in ΔE with distance is less for the Fe(I)/Fe(0) couple. The magnitudes of $E_{1/2}$, ΔE for a given distance of the light source are summarised in Table 3.9 for the two photoredox couples.

The observed shifts in $E_{1/2}$ in Figure 3.22 (a) show an approximate linear dependence on distance, d, between the maximum and minimum dark illumination regimes. The intensity of the light, the photon flux is proportional to $1/d^2$ but this does not correlate linearly with the shift in $E_{1/2}$ values. There are several theories which discuss the dependence of potential shifts with light intensity but a detailed consideration of these is beyond the scope of this study [42].
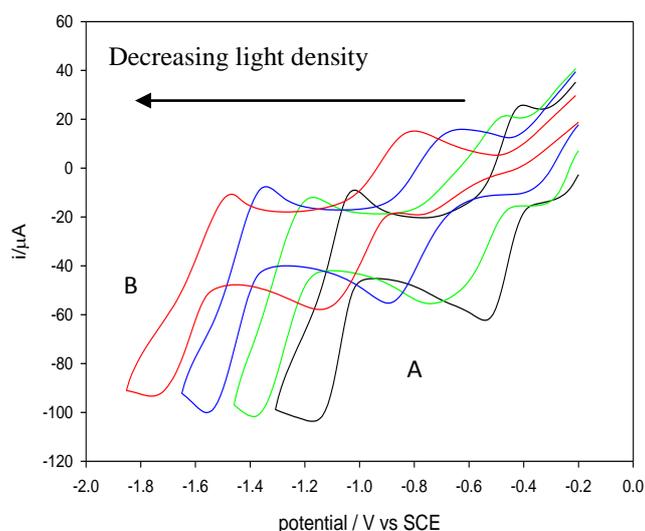
Figure 3.21 The effect of light intensity on the cyclic voltammetry of 0.2 mM **Fe(TPP)Cl** at p-type Si, in (MeCN-5%DMF) containing 0.1M [NBu$_4$][BF$_4$]
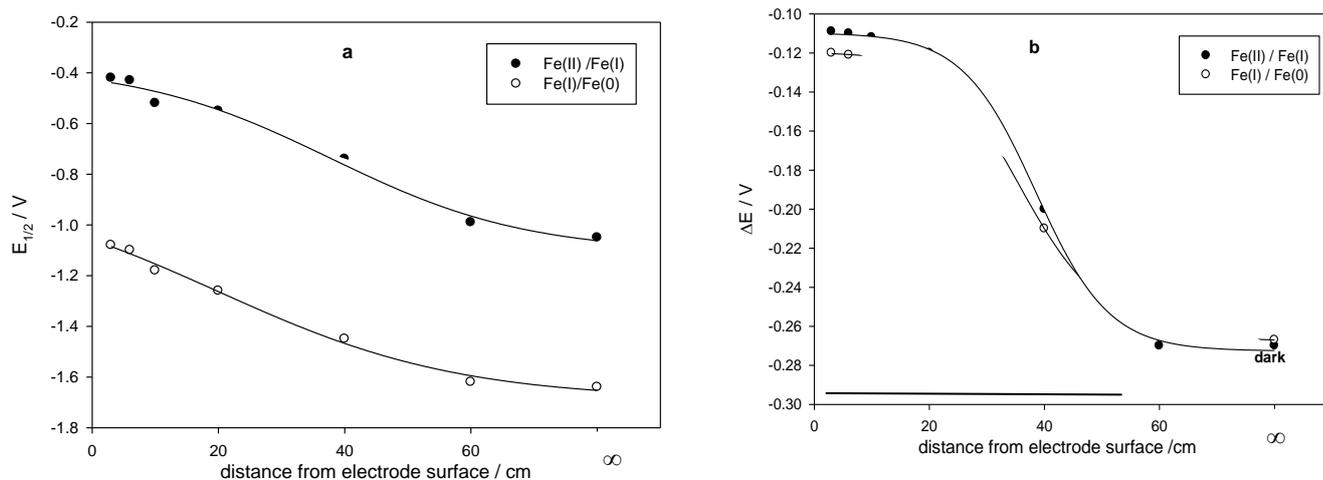
Figure 3.22 Dependence of (a) $E_{1/2}$ and (b) ΔE values on distance of light source from p-type Si electrode

Table 3.9 The magnitudes of $E_{1/2}$ and ΔE for the Fe(II)/(I) and Fe(I)/Fe(0) photoredox couples

distance/ cm	Fe(II)/Fe(I) couple		Fe(I)/Fe(0) couple	
	$E_{1/2}$/ V	ΔE / V	$E_{1/2}$/ V	ΔE / V
6	-0.43	0.1	-1.1	0.12
20	-0.55	0.12	-1.26	0.13
40	-0.74	0.2	-1.45	0.21
60	-0.99	0.28	-1.62	0.26
Dark	-1.05	0.268	-1.64	0.27
Vitreous carbon	-1.07	0.072	-1.65	0.081

Figure 3.23 shows the cyclic voltammetry of 0.1 mM **Fe-1** in MeCN-5%DMF(v/v) containing 0.1M [NBu$_4$][BF$_4$] in the dark (a) at p-type Si (B-doped, Si-H surface termination, 40-100 Ω) and when illuminated (b), using a Krüss halogen fibre optic lamp (90mW cm^2, λmax = 650nm) at the same electrode. In the dark, the successive redox potentials were $E_{1/2}$ = -1.02 V and E_p = -1.58 V *versus* SCE corresponding to Fe(II)/Fe(I) and Fe(I)/Fe(0) . The latter process is not reversible and the peak height indicates it is two electron processes. This may be due to the

nature of the Si-H surface and/ or the effect of solution protons as discussed above. At illuminated p-type Si electrode the potentials of these processes shift more positive at $E_{1/2}$= -0.58 V and E_p= -1.07 V *versus* SCE.
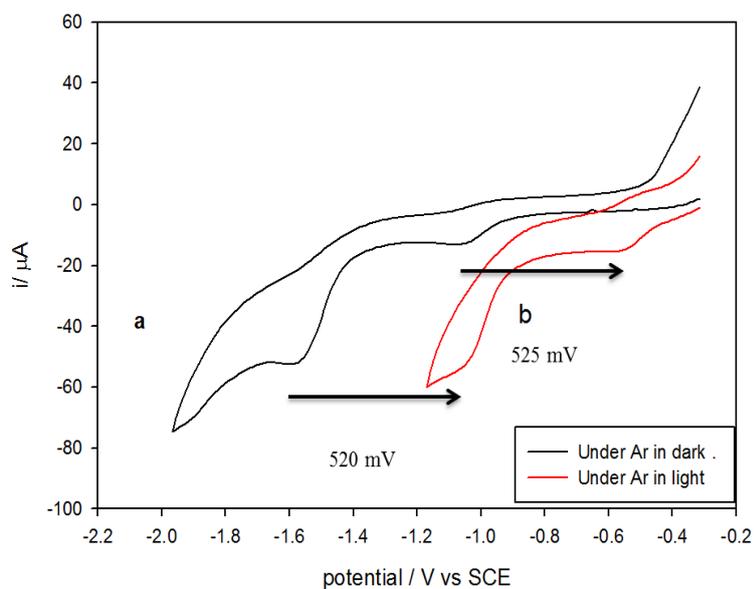

Figure 3.23 The cyclic voltammetry 0.1mM **Fe-1** in (MeCN-5%DMF) containing 0.1M [NBu$_4$][BF$_4$] of 0.1 mM **Fe-1** (a) in the dark under Ar (b) illuminated by light

Figure 3.24 shows the cyclic voltammetry of **Fe(TPP)Cl** in MeCN-5%DMF(v/v) containing 0.1M [NBu$_4$][BF$_4$] in the dark (a) at p-type Si (B-doped, Si-H surface termination, 1-10Ω cm^{-1}) and when illuminated (b), using a Krüss halogen fibre optic lamp (90mW cm^{-2}, λmax = 650nm) at the same electrode under argon. As described above in Section 3.2.3.1, there is a substantial shift of both the primary and secondary reduction processes upon illumination. The effect of replacing argon by CO_2 is also shown in Figure 3.24. There is an enhancement of the current under CO_2 as previously observed for **Fe(TPP)Cl** and at the Fe(I)/Fe(0) level in the dark which has been ascribed to a slow catalytic reduction of the substrate [17], Figure 3.24(c)
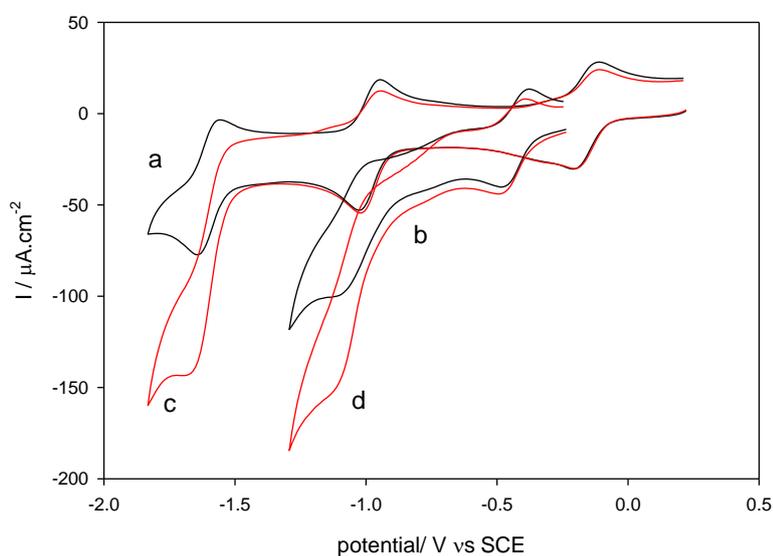
Figure 3.24   Cyclic voltammetry of 0.2 mM **Fe(TTP)Cl** complex in (MeCN-5%DMF) containing 0.1M [NBu$_4$][BF$_4$]   scan rate100mVs^{-1}. Black curves: (a) at a vitreous carbon electrode under Ar (b) at illuminated 1-10 ohm cm^{-1} p-type Si electrode under Ar. Red curves: (c) at a vitreous carbon electrode under CO_2 (d) at an illuminated 1-10 ohm cm^{-1} p-type Si electrode under CO_2
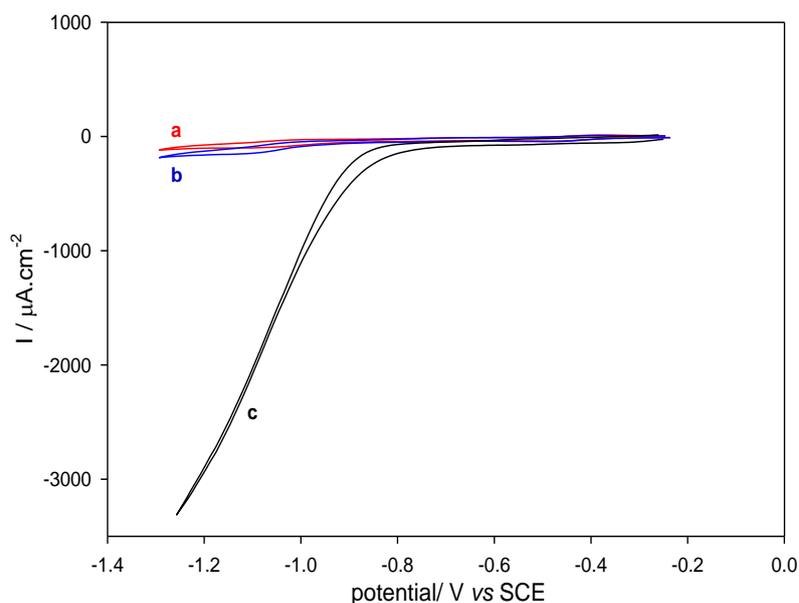
Figure 3.25 Cyclic voltammograms of **Fe(TPP)Cl** at a p-type H-Si electrode illuminated by a Krüss halogen fibre optic lamp (90mW·cm^{-2}, λ_{max} =650nm) in MeCN-5%DMF containing 0.1M [NBu$_4$][BF$_4$] ,scan rate 100mV·s^{-1}. (a) under Ar; (b) in the presence of saturated CO$_2$; (c) in the presence of saturated CO$_2$ and 0.410M CF$_3$CH$_2$OH

As is observed for **Fe(TPP)Cl** at vitreous carbon under CO$_2$, there is a dramatic increase in the electrocatalytic response in the presence of CF$_3$CH$_2$OH. This shown clearly by Figure 3.25 where a catalytic wave is observed near -1.2V *versus* SCE which about 120 times larger than under CO$_2$ alone.

3.2.3.4 Response to chopped light of the Fe (TPP)Cl system under CO$_2$

To unambiguously show the dependence of the electrocatalysis on light experiments using a chopped light source were undertaken. Figure 3.26 shows the potentiodynamic current response of the **Fe(TPP)Cl** under CO$_2$ in the presence of 0.275 M CF$_3$CH$_2$OH to chopped light at a frequency of 2Hz (2 cycles per second). The photocurrent in the illumination periods increases as is expected as the potential is scanned from -0.0 to -1.1 V *versus* SCE at 50 mV s^{-1}, whilst in dark periods across this range the current drops towards zero. Figure 3.27 (a) shows the response from -0.0 to - 1.1 scan rate 50 mVs^{-1} to chopped light at a frequency of

1 Hz. Figure 3.27(b) shows an expanded region of this response in the range −
0.98 and -1.1 V which covers the region where the photoelectrocatalysis is at a
maximum.

In all cases it can be seen that under illumination the current increases to reach
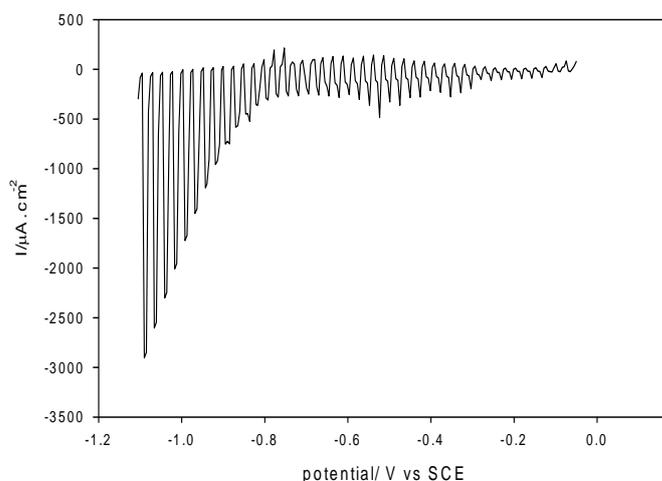*ca* 3000µA.cm^{-2} at -1.15 V *versus* SCE but in dark drops to a value close to zero.

Figure 3.26 Response of **Fe(TPP)Cl** to chopped light at 2Hz under CO_2 in the presence of 0.275
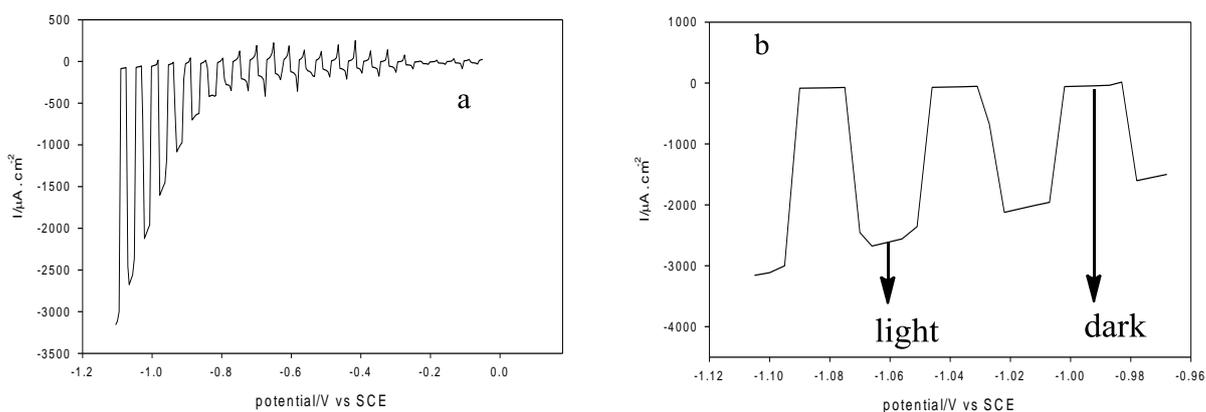M CF_3CH_2OH, scan rate 50 mVs^{-1}

Figure 2.27 Response of **Fe(TPP)Cl** to chopped light at 1Hz under CO_2 in the presence of 0.275
M CF_3CH_2OH, scan rate 50 mVs^{-1}.(a) Response from -0.0 to 1.1V.(b) An expanded region of this
response in the range - 0.98 and -1.1 V versus SCE

Figure 3.28(a) shows the cyclic voltammetry of **Fe-1** in the presence of CO$_2$ in MeCN-5%DMF containing 0.1M [NBu$_4$][BF$_4$].Under CO$_2$ in the absence of weak acid the catalytic current increases slightly but under CO$_2$ and in the presence of the proton source CF$_3$CH$_2$OH there is a dramatic increase in the photocatalytic current which is shown in Figure 3.28(b)
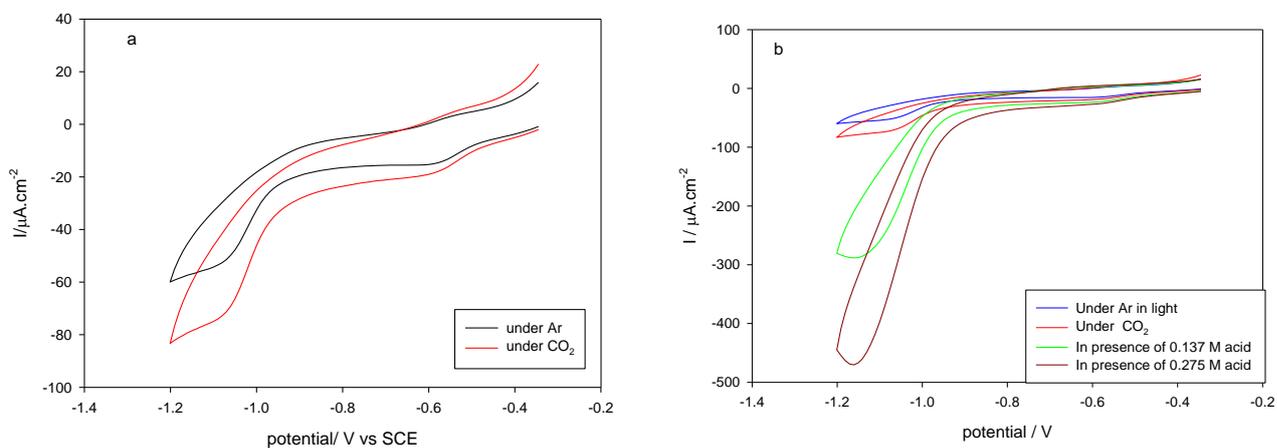
Figure 3.28 Cyclic voltammetry of 0.2mM **Fe-1** complex in (MeCN-5%DMF) containing 0.1M [NBu$_4$][BF$_4$] *versus* SCE: The scan rate is 100mVs^{-1}. (a) Under Ar and CO$_2$ (b) in the presence of CF$_3$CH$_2$OH

The photoelectrochemical behaviour of **Fe-1** is typical of all of the basket-handle porphyrin complexes.

3.2.4 Preparative-Scale Electrolysis at p-type Si electrode

3.2.4.1 Photoelectrosynthesis of CO electrocatalysed by Fe(TPP)Cl

Bulk photoelectrosynthesis on the p-type Si photocathode and examination of the gas phase by gas chromatography established the formation of CO. Production of CO occurred with a current efficiency of 92% after 175 turnovers during the course of 5.75h (-1.1V *versus* SCE, charge passed 36.7C, 175 μmoles CO, 0.2mM catalyst, 0.275 mM CF_3CH_2OH), a small amount of hydrogen was co-produced (current efficiency 0.4%, 0.8 μmoles). The current *versus* charge passed plot was similar to those observed in the dark at a mercury pool, Figure 3.29(a). In a separate experiment we have monitored the yield of CO as a function of electrolysis time, as shown by Figures 3.29(b and c). The cumulative yield of CO increases steadily over about 4h and the rate of CO production falls off towards 6h, Table 3.10. The current efficiency for CO production is essentially sustained over the 6h electrolysis period at *ca* 80%, Figure 3.29(d). As a direct comparison, preparative scale bulk electrolysis at a Hg-pool cathode under CO_2 gives CO with a current efficiency of *ca* 85% (-1.7V *versus* SCE, MeCN-5%DMF (v/v), 0.1M $[NBu_4][BF_4]$, charge passed 20C, yield of CO 87 μmole, 0.14 mM catalyst, 0.28 mM CF_3CH_2OH) after 123 turnovers. H_2 is also formed as a minor product in 0.1% current yield. For completeness, Figures 3.29(e and f) illustrate turnover frequency (T.N/h) and total charge – passed as a function of time.

Table 3.10 Current efficiency and turnover numbers for electrocatalytic reduction of CO_2 by **Fe (TPP)Cl** on the p-type Si photocathode

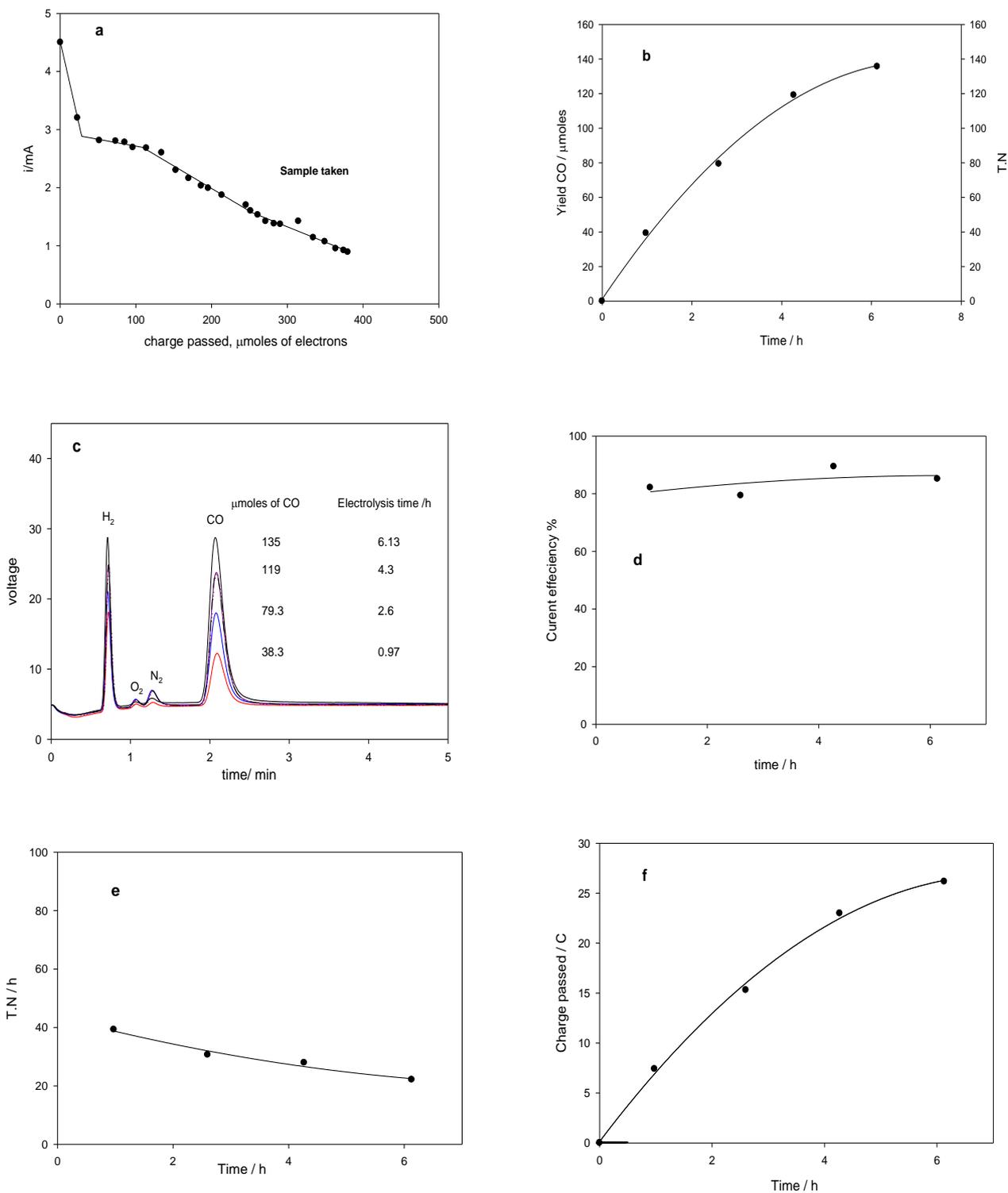| Time/h	0.97	2.6	4.3	6.13
Number of μmoles of CO	38.3	79.3	119	135
Current efficiency %	82	79	89	85
T.N	39	79	119	135
Charge passed, C	7	15	22	26.16
μmole of electrons	72.5	155.5	228	271

Figure 3.29 (a) The current *versus* charge passed, μmole of electrons, (b) CO yield and T.N *versus* electrolysis time; (c) Gas chromatography of monitored the yield of CO as a function of electrolysis time ,(d) current efficiency *versus* electrolysis time. (e) T.N/h versus time, (f) charge passed versus time, . (Photoelectrolysis conditions: 1μmol **Fe(TPP)Cl**, 1.4mmol CF_3CH_2OH and saturated CO_2 (*ca* 0.27M) in a MeCN-5%DMF containing 0.1M [NBu$_4$][BF$_4$] at -1.11 V *vs* SCE on a p-type H-Si electrode under the illumination of a Krüss halogen fibre optic lamp (90mW·cm^{-2}, λ_{max} =650nm),

3.2.4.2 Photoelectrosynthesis of CO by basket handle thiolate iron porphyrins on a p-type Si electrode

Photoelectrosynthesis was carried out in MeCN-5%DMF containing 0.1M [NBu$_4$][BF$_4$] as described for the **Fe(TPP)Cl** complex. Potentials were set at -1.07 V, -1.17 V, -1.2 V, and -0.87 V *versus* SCE for **Fe-1**, **Fe-2**, **Fe-3** and **Fe-4** respectively. Table 3.11 summarises the data for the basket - handle porphyrins and that for **Fe(TPP)Cl** discussed above and **Fe(PFTPP)Cl** are included for comparison.

Table 3.11 Current efficiencies and turnover numbers of electrocatalytic reduction of carbon dioxide catalysed by Fe(III) porphyrins at p-type Si electrode

Complex	Potential / V	Concentration /mM	Duration of experiment/h	Charge coulomb /C	Current efficiency	T.N CO	Yield of CO /µmol	Current efficiency H$_2$	T.N H$_2$	Yield of H$_2$ /µmol
Fe(TPP)	-1.01	0.056	3.8	10.9	72	142	40	5	9	2.6
Fe(PFTPP)	-0.75*	0.058	2.15	3	-	-	-	0.1	0.2	0.058
Fe-1	-1.07	0.055	4.58	8.29	33	53.2	14.3	3.16	5	1.36
Fe-2	-1.17	0.065	4.6	8.54	36	50	16	34.6	47	15.3
Fe-3	-1.2	0.055	2	4.5	40	21	9.25	14.37	7.6	3.35
Fe-4	-0.87	0.055	3.3	3.9	22	15.7	4.36	5.1	3.8	1.04

* The potential of **Fe (PFTPP)** is not negative enough to catalyze CO$_2$ reduction.

As an example, the bulk photoelectrosynthesis of CO on a p-type Si electrode was carried out at -1.07V *versus S*CE in (MeCN-5%DMF) containing 0.1M [NBu$_4$][BF$_4$] at room temperature for 4.6 hours in the presence of **Fe-1** (0.055 mM) and trifluoroethanol (0.27M). The current efficiency for CO production was 33% with a turnover number of 53. The yield of CO was 14 µmoles after 4.6 hours with a charged passed of 8.3 C. H$_2$ also was formed as secondary product in 3.16 % current efficiency.

In a separate experiment, the gas phase was monitored by gas chromatography during the course of electrolysis and confirmed the formation of CO. The conditions were 0.1 mM **Fe-1** in the presence of 0.27 M of CF_3CH_2OH at p-type Si electrode in $0.1M[Bu_4N][BF_4]$-MeCN-5%DMF at -1.07 V for 3.8 hours. The current efficiency for formation of CO over the 3.8 hour period was in ranged from 32- 53 % as the turnover number increased from 2.6 to 22, Figure 3.30 (a),(b). The current efficiency for generation of H_2 was *ca* 3 % and is possibly related to a trace amount of water in solution. Table 3.12 summarises the data for the photoelectrosynthesis of CO catalysed by **Fe-1**
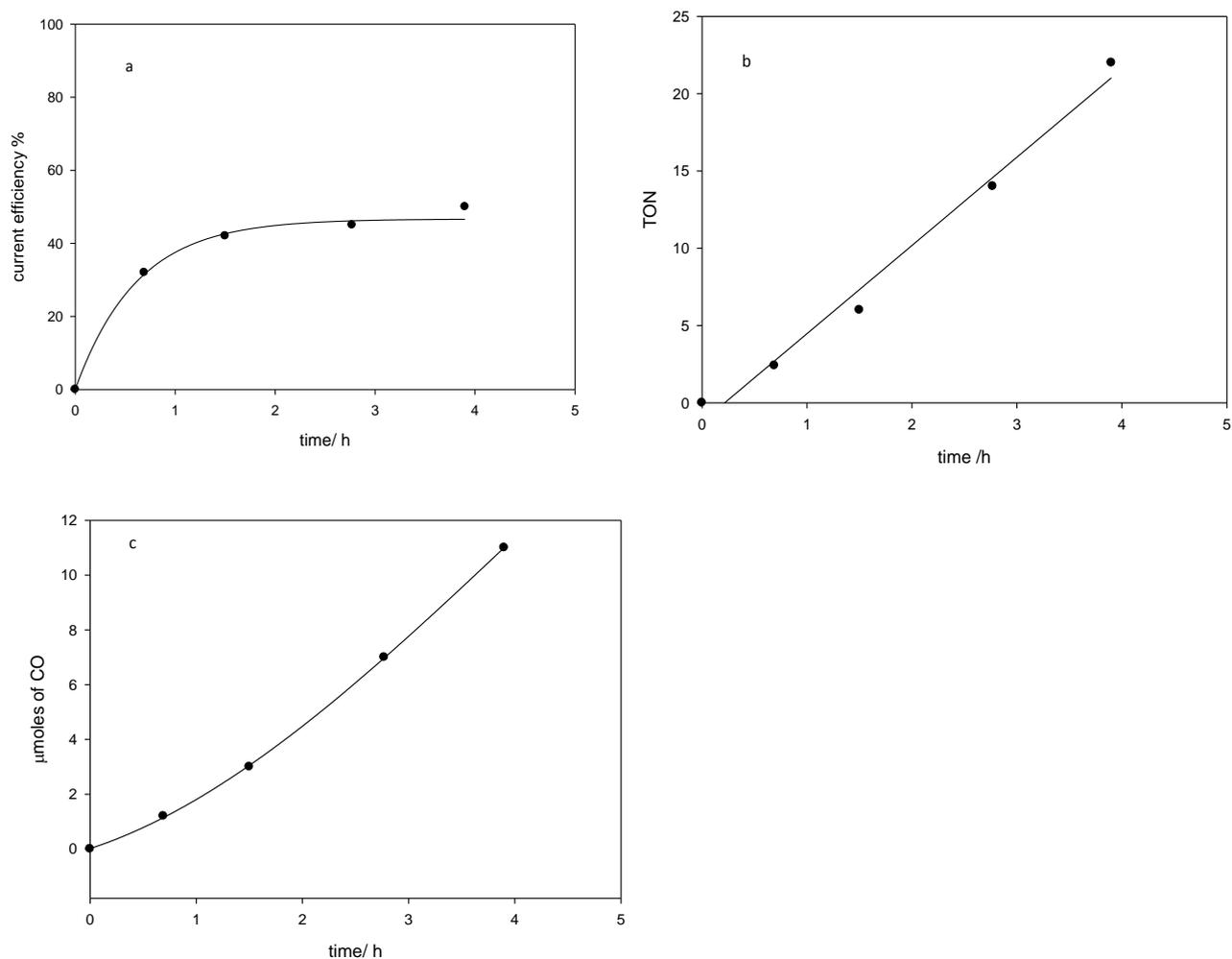

Figure 3.30 (a) Current efficiency *versus* electrolysis. (b) Turnover number *versus* electrolysis time. (c) μmoles of CO *versus* the electrolysis time

Table 3.12 Current efficiency and turnover numbers for electrocatalytic reduction of CO_2 by **Fe-1** on p-type Si electrode

Time/h	0.69	1.5	2.77	3.8
Number of μmoles of CO	1.2	3	7	11
Current efficiency %	32	42	45	53
T.N	2.4	6	14	22
Charge passed, C	0.76	1.36	3.00	3.90
μmole of electrons	7.8	14.1	31	40.4

Under the similar conditions, bulk photoelectrosynthesis of CO in the presence of **Fe-2** on the p-type Si photocathode together with examination of the gas phase by gas chromatography established the formation of CO. Production of CO occurred with a current efficiency of 37% after 50 turnovers during the course of 4.64 h, at -1.17V *versus* SCE. The charge passed was 8.54C, 16.5 μmoles CO, 0.065 mM **Fe-2**, 0.28 mM CF_3CH_2OH), also H_2 is formed with current efficiency 35%.

It is notable that increasing of porphyrin concentration led to an increase in the CO yield and a decrease in the H_2 yield. For example, photoelectrolysis of a 0.1 mM solution of **Fe-2** in the presence of 0.275 M of CF_3CH_2OH increased the current efficiency of CO formation to 52 % whilst reducing that for hydrogen formation to 21% during the course of 5.3h. Data for CO and H_2 current efficiences at different concentrations of **Fe(TPP)Cl** and **Fe-2** are summarised in Figure 3.31.

It can also be seen from Figure 3.31(a) that the addition of water can significantly perturb the ratio of H_2 and CO. This competition between the reduction of H_2O

(protons) and CO_2 was observed previously by Kubiak [38] in a rhenium system. It was qualitatively explained by the heterogenous reduction of protons at the semiconductor surface and homogenous reduction of CO_2 by the molecular catalyst, as illustrated by Scheme 3.5
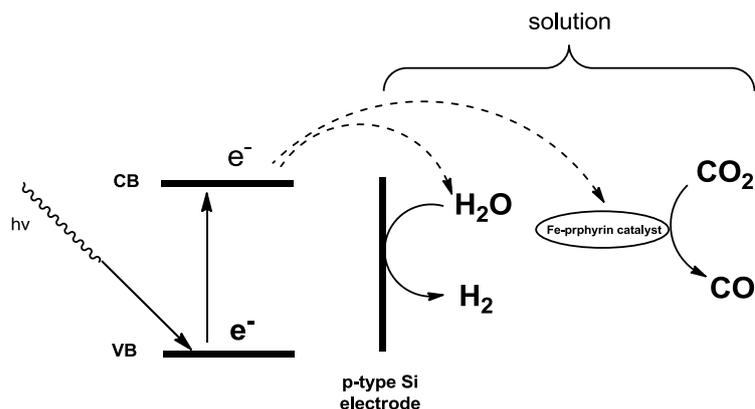
Scheme3.5 Heterogeneous catalysis role of p-type Si for H_2 reduction from H_2O and the Fe-porphyrin role as CO_2 reduction catalysts. Adapted from ref. [38].
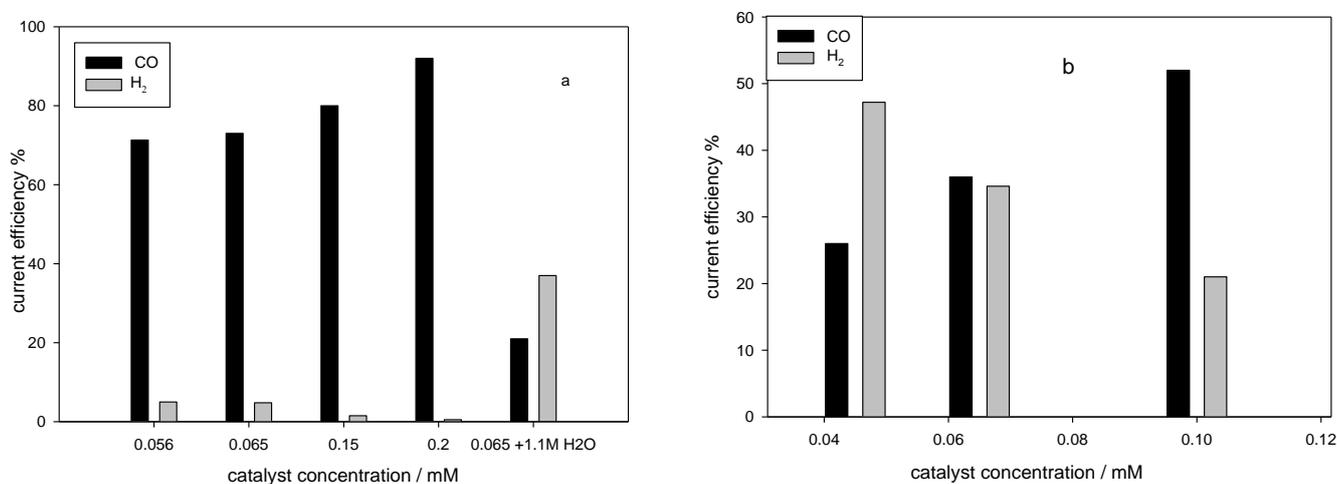

Figure 3.31 Current efficiency of CO nad H_2 formation for different concentrations of catalyst (a)- **Fe(TPP)Cl** ; (b) **Fe-2** complex. Data shown in (a) also includes the effect of added water.

For comparison, the electrosynthesis of CO on a Hg-pool cathode occurs with reasonably high selectivity, *ca* 80% and 85 % for both **Fe-1** and **Fe-2** respectively.

Whereas, the in photoelectrosyntheses the selectivity of CO formation by both **Fe-1** and **Fe-2** were 33 and 37% respectively. This suggests the electrode material plays an important role in determining selectivity.

3.2.5 Mechanistic aspects of the photoelectrocatalysis

The dependence of the photocatalytic current density for CO_2 reduction at -1.2V *versus* SCE on the concentration of the acid is shown by Figures 3.32 and 3.33. The current density tends towards a plateau at $[CF_3CH_2OH] > 0.25M$ which is indicative of an acid independent kinetic regime. Cyclic voltammetry confirms that the photoelectrocatalysis is limited by the turnover of the catalyst rather than by diffusion because the catalytic current is independent of scan-rate: scans run at 20mV s^{-1} and 100mV s^{-1} are essentially superimposable, Figure 3.34. We should note that Fe (TPP)Cl or the basket - handle porphyrins is not adsorbed on the silicon surface. Thus exposing the electrode to a solution of the complex and cycling the potential between -0.24 and -1.2V *versus* SCE followed by washing with electrolyte and transferring it to a fresh electrolyte solution shows no evidence by cyclic voltammetry for surface bound species. The response for the system at vitreous carbon is similar to that at the illuminated p-type Si except that the current density at -1.8 V *versus* SCE is about a factor of two greater than that at p-type Si.
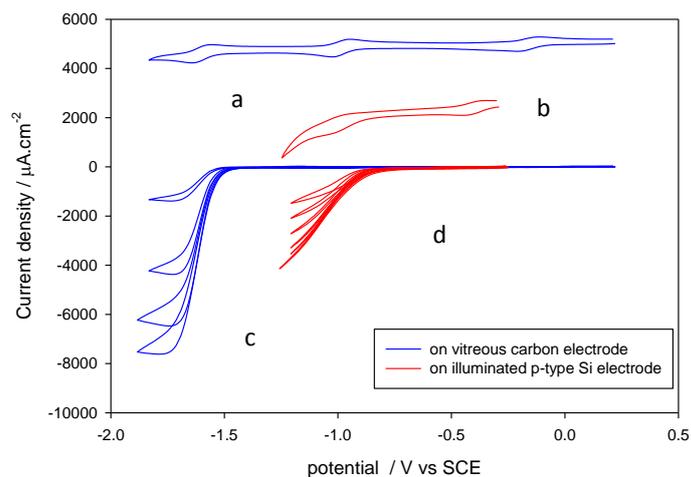
Figure 3.32 Cyclic voltammetry of **Fe(TPP)Cl** (0.22mM) in (MeCN-5%DMF) containing 0.1M [NBu$_4$][BF$_4$], Rt. Scan rate 100 mVs^{-1}. (a) at vitreous carbon electrode under Ar (b) at illuminated p-type Si electrode under Ar (c) at vitreous carbon electrode under 1 atm of CO$_2$ in presence of 0.055M, 0.11M, 0.16M, and 0.22M CF$_3$CH$_2$OH (d) at illuminated p-type Si electrode under same condition as in (c)
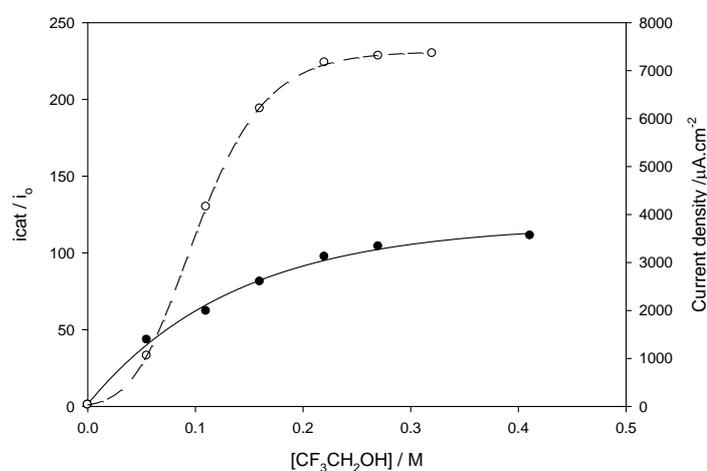

Figure 3.33 Effect of the acid concentration on i$_{cat}$/i$_0$ ratio at a vitreous carbon electrode and at an illuminated p-type H-Si electrode. Solid circles: p-type H-silicon electrode; open circles: vitreous
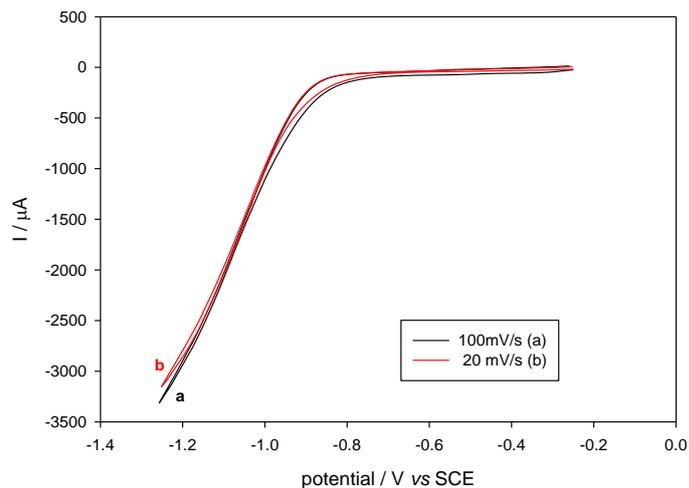
145

Figure 3. 34 Cyclic voltammograms of A at a p-type H-Si electrode illuminated by a Krüss halogen fibre optic lamp (90mW cm^{-2}, λ_{max} =650nm) in a solvent mixture (MeCN-5%DMF) containing 0.1M [NBu$_4$][BF$_4$] in the presence of saturated CO_2 and 0.411 M CF_3CH_2OH : (a) scan rate = 100mV s^{-1}, (b) scan rate = 20mV s^{-1}

The normalised scale i_{cat} / i_0 for the electrocatalysis is also shown in Figure 3.33. where i_{cat} is the measured current in the presence of the acid and CO_2 (saturated) and i_0 is the value of the peak current for the one-electron Fe^{II}/Fe^{I} porphyrin couple measured at the same scan rate, 100mVs^{-1}. Following the approach of Dubois and others [43,44], the rate constant k^{Si}_{obs} at illuminated silicon can be estimated from the i_{cat} / i_0 data using the relationship shown in Equation 3.1, where *F, R* and *T* are the Faraday constant, the gas constant and the temperature respectively, n is the number of electrons involved in the turnover with i_{obs} measured at the potential where the current approaches a plateau at -1.2 V *versus* SCE. The value of k^{Si}_{obs} is equivalent to the turnover frequency (TOF) of the system [43] and is estimated to be 0.24 x 10^4 s^{-1}.

$$k^{Si}_{obs}=0.1992(Fv/RTn^2)(i_{cat}/i_0)^2 \qquad \text{Equation 3. 1.}$$

For comparison, we estimate the turnover frequency on vitreous carbon (independent of light) to be $k^C_{obs} = 1.03 \times 10^4$ s^{-1} as determined from the plateau value of i_{cat} / i_0 at -1.75V, but otherwise under the same conditions.
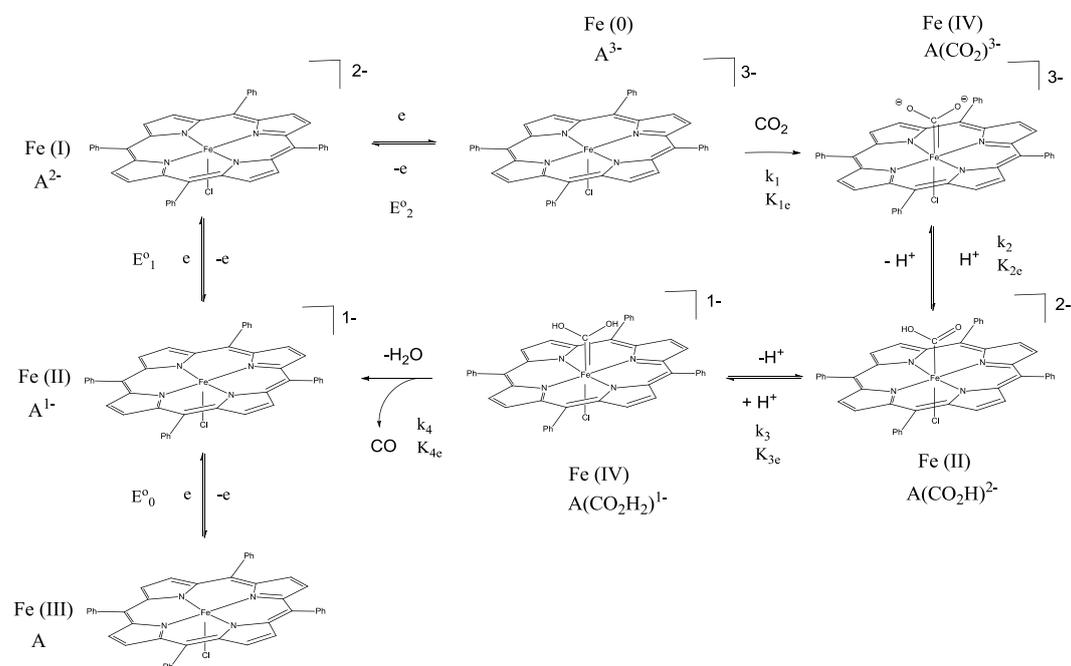
Scheme 3.6 Proposed pathway for photoelectrocatalysis of CO_2 reduction to CO. Values of $E^{o\prime}$s, equilibrium K_n constants and rate constants k_n together with other experimental and fitted parameters used in digital simulations are given below
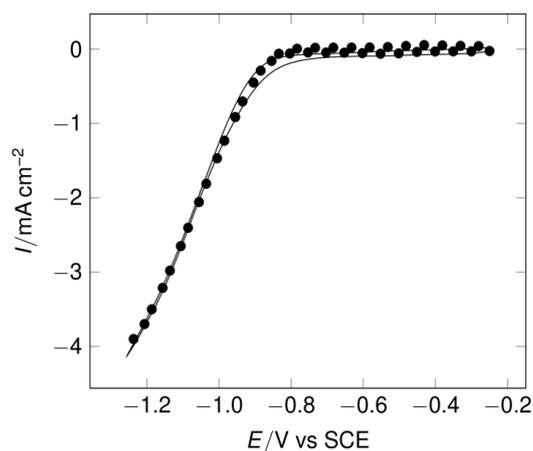

Figure 3.35 Experimental (solid line) and simulated (closed circles) current density versus potential response for **Fe(TPP)Cl** in the presence of $CO_2 = 0.25M$ and $[CF_3CH_2OH] = 0.411M$ at the illuminated p-type Si photocathode

The experimental data was measured at 100mV s^{-1} at 23 $^{\circ}$C. The parameters used in the simulation correspond to those labelled in Scheme 3.6 and are as follows. E^{o}_{1} and E^{o}_{2} = -0.4V and -1.05V *versus* SCE respectively and were experimentally estimated; the diffusion coefficients for all porphyrin species A^{n-} were taken as 3.25 x 10^{-6} cm^{2}s^{-1}, which is the experimentally determined value for the A/A^{1-} couple; small molecule species were assigned diffusion coefficients of 1 x 10^{-5} cm^{2}s^{-1}; the rate constants k_1, k_2 and k_3 were assigned values of 10^8 M^{-1}s^{-1}, 2 x 10^{4}M^{-1}s^{-1} and 2 x 10^4 M^{-1}s^{-1} respectively and that for k_4, the CO generation step, a value of 3.5 x 10^4 s^{-1}. The equilibrium constants K_{1e}, K_{2e} and K_{3e} were each set at a minimal value of 10^3 M^{-1}. Uncompensated resistance was set in the simulation at 60 ohms.

We have modelled the photoelectrocatalytic response by digital simulation of the cyclic voltammetry. This is based upon the mechanism shown in Scheme 3.6 which is a modified version of that proposed by Saveant and coworkers for the electrocatalytic reduction of CO_2 on mercury under similar conditions [17]. Fitting parameters are given above which shows experimental and calculated data for the case where [CF$_3$CH$_2$OH] = 0.411M. The data are in good agreement and consistent with an acid independent rate-limiting step involving the generation of CO from an iron porphyrin intermediate with a first order rate constant k_4 = 3.50 x 10^4 s^{-1} (Scheme 3.6). The calculated turnover frequency of 0.29 x 10^4 s^{-1} is close to that of k_{obs}^{Si} = 0.24 x10^{4}s^{-1} which was experimentally estimated using equation 3.1.
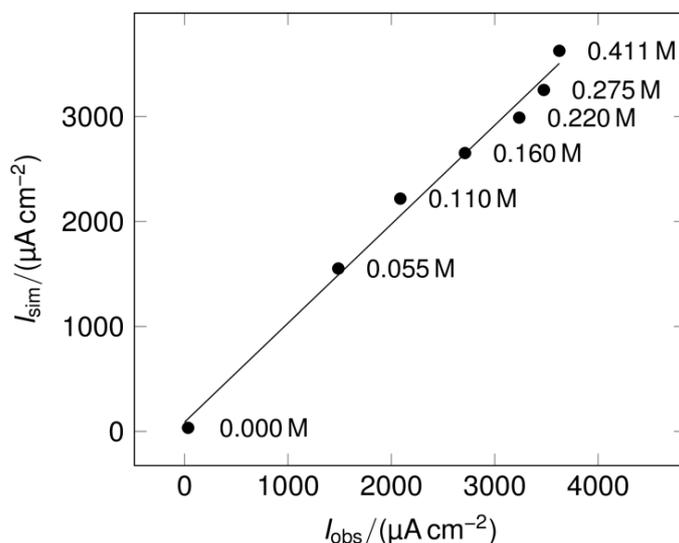
Figure 3.36 Correlation between calculated, I_{sim} , and experimental, I_{obs} , current densities at concentrations of CF_3CH_2OH as labelled in the graph. The simulation is based on the mechanism shown in Scheme 3.6 using the same parameters as given in the text

Figure 3.36 shows the plot of experimental and simulated current densities at -1.2V *versus* SCE for the range of concentrations of $[CF_3CH_2OH]$ employed. The experimental data covers both the acid dependent and acid independent regimes with the theoretical current densities calculated using the same fitting parameters as given above. The agreement is excellent with a correlation coefficient of 0.99 and a slope close to unity, 0.94. This provides further support for the global mechanism proposed in Scheme 3.6.

The kinetics of the electrocatalysis and photoelectrocatalysis of CO_2 reduction by the basket handle porphyrin **Fe-2** was also investigated. Figure 3.37 shows comparative data for the ratio i_{cat} / i_o at a vitreous carbon electrode and at the illuminated p-type Si electrode, *versus* $[CF_3CH_2OH]$. The peak catalytic current, i_{cat} , is that measured at 100 mVs^{-1} and i_o is that for the peak current measured for the primary one-electron reduction step at the same scan-rate. It is noted that at both vitreous carbon and p-type Si electrodes the values of i_{cat} / i_0 become

independent of the acid concentration at *ca* 0.16 M in MeCN-5%DMF containing 0.1M [NBu$_4$][BF$_4$] in the presence of saturated CO_2. In the acid - independent regimes, the magnitude of i_{cat} / i_o for the electrocatalysis on vitreous is about 1.45 times of that on illuminated p-type Si whereas at 0.044M the ratios for i_{cat} / i_0 are comparable. The rate constant (k^{Si}_{cat} 23°C) for the catalysis at illuminated p-type Si is estimated to be $(0.370 \pm 0.1) \times 10^3$ M^{-1}s^{-1} from the magnitude of i_{cat} / i_o in the acid independent regime and that of the corresponding rate constant (k^{C}_{cat}) at vitreous carbon is estimated to be $(0.85 \pm 0.1) \times 10^3$ M^{-1}s^{-1}.
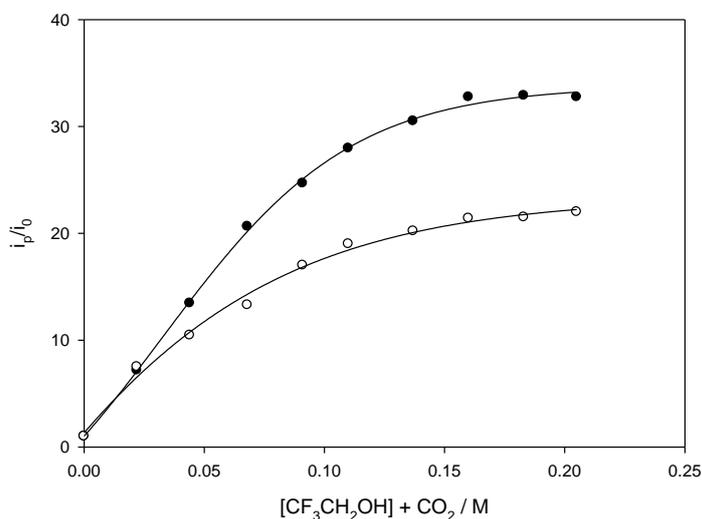

Figure 3.37 Effect of the acid concentration on icat/i$_0$ ratio at a vitreous carbon electrode and an illuminated p-type H-Si electrode. Solid circles: carbon electrode; open circles p-type Si electrode

Table 3.13 summarises $i_{cat/}$ i$_0$ and rate constant data for CO_2 reduction catalysed by the basket - handle porphyrins and those for **Fe(TPP)Cl** and **Fe(PFTPP)Cl** discussed above are included for comparison. From this data it can be seen that **Fe(TPP)Cl** has the highest rate constant for the electrocatalytic reduction on vitreous carbon and that **Fe(PFTPP)Cl** is the slowest electrocatalyst. Included in Table 3.13 are the values of E$_{cat}$ which we have defined as the potential for i_{cat}/2

measured at a concentration of 0.18M CF_3CH_2OH. Figure (3.38)a shows the plot of log k_{cat} for the six complexes *versus* E_{cat}. The overall trend is clear, as E_{cat} becomes more positive the rate constant decreases. The correlation coefficient, R^2, for the linear plot is poor, 0.861. If the analysis is limited to the four basket handle porphyrins a better correlation is observed. A possible explanation for the deviation from linearity for the full set of data is that in the catalytic cycle chloride is lost from the **Fe(TPP)Cl and Fe(PFTPP)Cl** complexes to give square-planar intermediates at which CO_2 can attack at either side. In contrast, the basket handle porphyrin complexes have 'one side' protected from CO_2 attack. Figure (3.38)b illustrates the good linear correlation between log k_{cat} and E_{cat} using corrected $\{k_{cat}/2\}$ values for the simple porphyrins to accommodate this statistical factor, $R^2 = 0.953$.

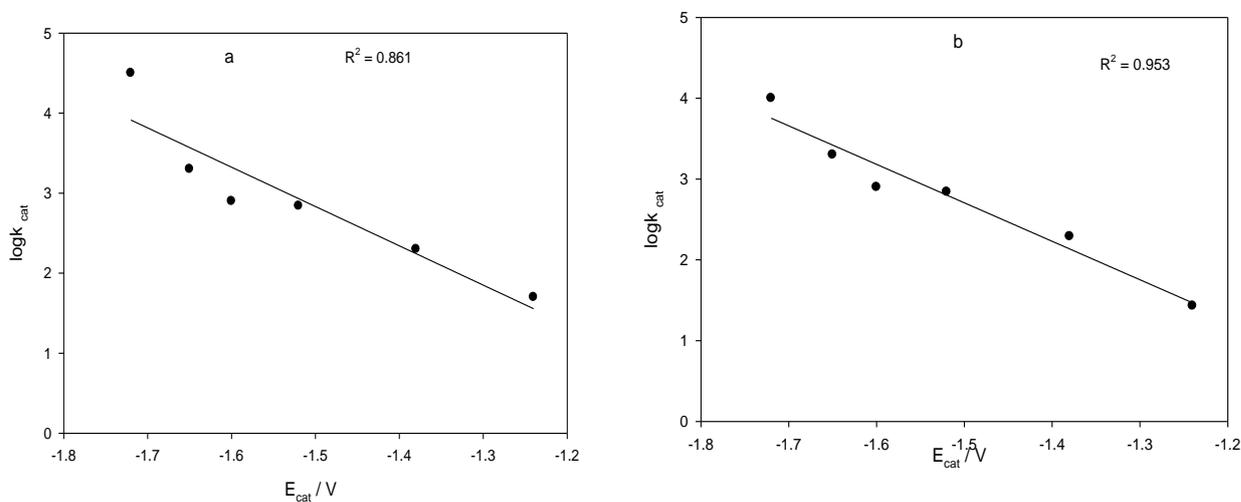**Figure 3.38** shows the plot of log k_{cat} for the six complexes *versus* E_{cat} at vitreous carbon in the presence of saturated CO_2 and 0.18 M CF_3CH_2OH. Plot (a) is for 'uncorrected' k_{cat} data. Plot (b) is that corrected on the assumption that reduced $\{$**Fe(TPP)**$\}$ and $\{$**Fe(PFTPP)**$\}$ species formed by Cl loss may present two equally accessible faces for catalysis whereas the basket handle thiolate complexes present a single face.

The observation that there is an approximate linear free energy relationship (LFER) between log k_{cat} and $-E_{cat}$ for the complexes can be qualitatively interpreted as follows. The more negative the reduction potential then the more reactive is the generated catalytic intermediate likely to be towards the electrophile CO_2. In addition at the more electron-rich centres the bound CO_2 is likely to be more basic and susceptible to protonation.

Table 3.13 also summarises data for the photoelectrocatalysis on p-type Si. The inset in Figure 3.39 shows the plot of k_{cat}^{Si} *versus* k_{cat}^{C}. More revealing in Figure 3.39 is the plot of log k_{cat}^{Si} *versus* log k_{cat}^{C} for all of the complexes, the linear correlation is excellent ($R^2 = 0.9971$) with an intercept close to zero (-0.1189). The empirical relationship from this plot is given in Equation 3.2 which approximates to Equation 3.3 at values of $k_{cat}^{Si} > 20$. The relationship accounts for the change in the ratios k_{cat}^{C}/k_{cat}^{Si} as shown in Table 3.13. The power relationship of Equation 3.3 may explain earlier data on photoelectrocatalysis of hydrogen evolution on p-type Si using certain Mo complexes which indicated comparable rates of catalysis on vitreous carbon and p-type Si [45] because the k_{cat} values were small.

$$\log k_{cat}^{Si} = 0.907\log k_{cat}^{c} - 0.1189 \qquad \text{Equation 3.2}$$

$$k_{cat}^{Si} \approx (k_{cat}^{c})^{0.91} \qquad \text{Equation 33}$$

At the present time we do not have a theoretical interpretation for the empirical relationships given in Equation 3.2 and 3.3. The photoelectrocatalysis rate constants were all determined under saturated illumination conditions at a nominal lamp intensity of 90Wcm^{-2} notably reducing this intensity to 35W cm^{-2} did not

change i_{cat}^{Si}. This may imply that charge-transfer from the conduction band is not rate limiting the catalytic cycle at high values of k_{cat}.
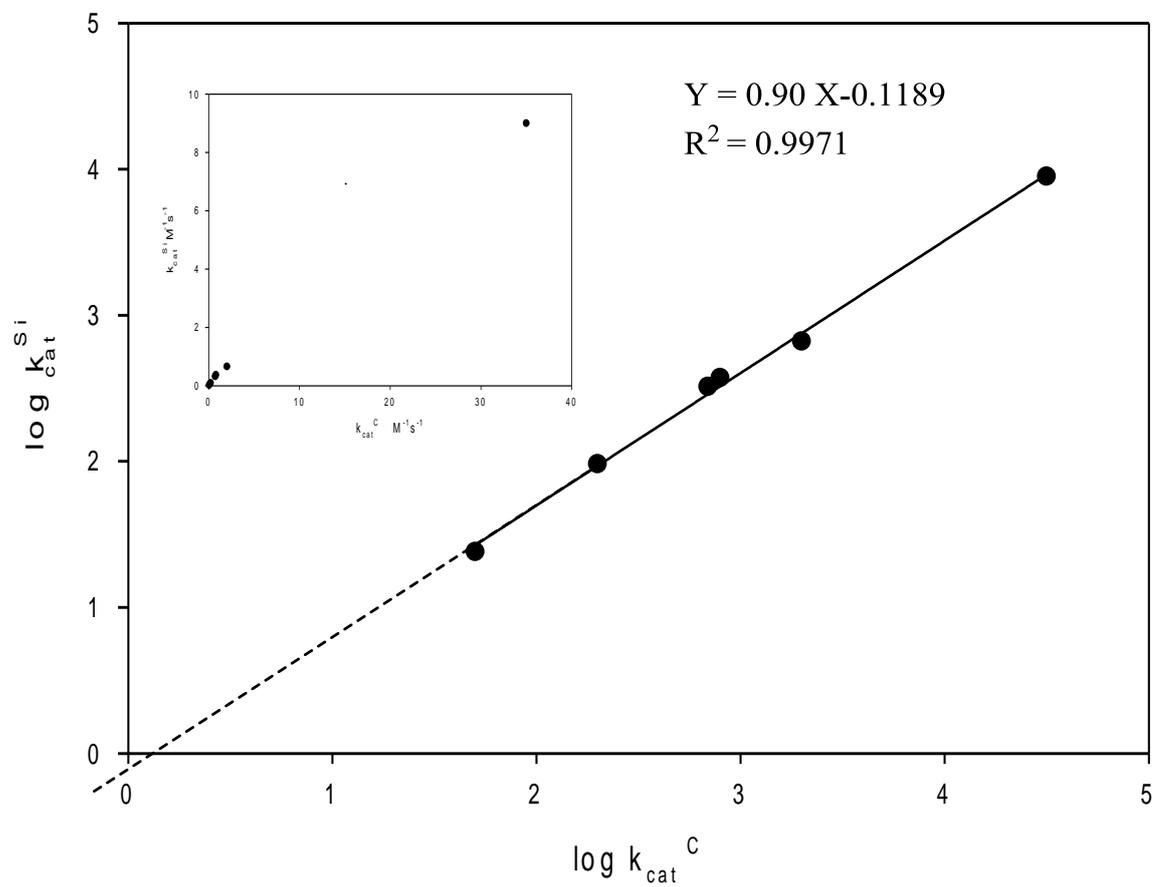

Figure 3.39 Plot of log k_{cat}^{Si} *versus* log k_{cat}^{C} for all of the complexes. The inset shows Plot of k_{cat}^{Si} *versus* k_{cat}^{C}

Table 3.13: Summary of current ratio and rate constant date for the catalytic reduction of CO_2 using the Fe(III) porphyrins complexes.

Complex		Fe(PFPP)Cl	Fe (TPP)Cl	Fe-1	Fe-2	Fe-3	Fe-4
Primary $E_{1/2}$ *versus* SCE		+0.14	- 0.19	- 0.68	- 0.72	- 0.78	- 0.68
E_{cat} at 0.18M acid for $i_{cat}/2$		-1.24	-1.72	-1.52	-1.60	-1.65	-1.38
Carbon electrode	i_p/i_o	8.40	224	31.37	33.06	53.4	16.6
	k_{obs}	13.7	9720	191	212	553	53.4
	k_{cat} $M^{-1}s^{-1}$	0.051×10^3	3.5×10^4	0.71×10^3	0.785×10^3	0.20×10^4	0.198×10^3
p-type Si electrode	i_p/i_o	5.20	112	21.04	22.7	30.2	11.5
	k_{obs}	6.51	2430	85.8	100	177	25.6
	k_{cat} $M^{-1}s^{-1}$	24.1	0.9×10^4	0.32×10^3	0.37×10^3	0.66×10^3	95
$k_{cat}^{C}/ k_{cat}^{Si}$		2.1	4.00	2.22	2.11	3.12	2.08

3.3 Conclusions

A simple iron (III) tetraphenylporphrin electrocatalyst **Fe(TPP)Cl** can enable light assisted reduction of carbon dioxide to carbon monoxide at boron-doped p-type H-terminated silicon photocathodes at a potential *ca* 550mV positive of that at an inert vitreous carbon electrode. The current efficiency at -1.1V *versus* SCE for CO production is *ca* 80-90 % and the photoelectrolysis system is capable of sustaining CO production at a rate of *ca* 30 TN / hr cm^{-2} over a time-scale of 4h . Under saturating photon flux conditions with visible light (90mW cm^{-2}, λ_{max} = 650nm) k_{cat} is *ca* 10^4 M^{-1}s^{-1} which is about 25% of that observed in the dark at vitreous carbon under otherwise the same conditions. We tentatively suggest that the smaller turnover frequency observed for the photoelectrocatalysis by **Fe(TPP)Cl** (k^{Si}_{obs}=0.241 $\times 0^4$ s^{-1}) as compared with that at vitreous carbon in the dark (k^{C}_{obs}=1.03$\times 0^4$ s^{-1}) is also a consequence of the different nature of the interfacial regimes of the two materials.

Considering rate constant data for the complete family of Fe porphyrins, it was found that k_{cat} for CO_2 reduction at vitreous carbon qualitatively correlated with E_{cat}. Thus the more negative the value of E_{cat} the greater was k_{cat}. The linear free energy plot of log k_{cat} versus E_{cat} was modestly linear R^2 = 0.861. If allowance is made for chloride loss from the two classical porphyrins an improved linear fit to the data was observed, R^2 = 0.953.

A comparison of data for the electrocatalysis at vitreous and at p-type Si shows excellent correlation between log k_{cat}^{Si} and log k_{cat}^{C}, R^2 = 0.997. The intercept is relatively small and to a first approximation k_{cat}^{Si} = $(k_{cat}^{C})^{0.91}$. The theoretical basis of this is not understood. However, the H-terminated Si surface is

considered to be hydrophobic whereas that of vitreous carbon has carbonyl, carboxylic, phenolic and other hydroxyphilic surface groups. Enhanced hydrogen-bonding interactions with CF_3CH_2OH may increase its acidity adjacent to the electrode surface at carbon and could explain the modestly faster kinetics on this material. The influence of the protic environment neighbouring or in the outer coordination sphere of a porphyrin catalyst is known to have a dramatic effect on CO_2 reduction kinetics, [39, 40].

The basket handle thiolate iron (III) complexes are all lower in selectivity for the catalysis of the reduction of CO_2 to CO when they are compared with **Fe(TPP)Cl** at p-type Si. For example, photoelectrocatalytic reduction of CO_2 by the complex **Fe-2** gives carbon monoxide and a significant yield of dihydrogen whereas at mercury in the dark the formation of CO dominates. This contrasts markedly with the behaviour of **Fe(TPP)Cl** in so far as the latter gives selectively a high yield of CO in both the photoelectrocatalytic and the dark electrocatalytic systems.

With respect to current efficiency, selectivity and E_{cat}, photocatalysis of CO_2 reduction by **Fe(TPP)Cl** compares favourably with photoelectocatalytic systems at p-type Si which are based on (less abundant) rhenium electrocatalysts [38]. Moreover, the iron porphyrin system operates at a potential *ca* 400mV positive of the Re bipyridyl systems. Illumination with 90mW cm^{-2} visible light from the Krüss lamp sustains a current density of *ca* 4 $mAcm^{-2}$ with a photovoltage gain of *ca* 650 mV with a fill factor of *ca* 50% which corresponds nominally to a photoelectrochemical efficiency of *ca* 1.4 % .

Coupling of homogeneous Fe-porphyrins catalysts for the reduction of CO_2 with heterogeneous H_2O reduction or proton reduction by photocathode p-type Si

electrode was observed. This is similar to work recently described by Kubiak for the Re photoelectrocatalysis. More H_2 production detected at a lower concentration of the catalyst **Fe(TPP)Cl** at p-type Si than at higher concentrations, whereas (dark) electrolysis on Hg under the same conditions as illuminated p-type Si showed very low H_2 production.

3.4 Experimental Section

Chemicals and solvents. The iron porphyrins **Fe(TPP)Cl**, **Fe(PFPP)Cl** and CF_3CH_2OH were purchased from Aldrich and used as received. The basket handle thiolate iron (III) porphyrins were synthesised in our laboratory as previously described [46] .CO_2 gas 99.9% was obtained from BOC Ltd. DMF and MeCN were purified by distillation over calcium hydride.

Single crystal p-type Si electrodes. The single crystal B-doped p-type Si (1-10, 40-100 Ω cm-1, (111) face, thickness 500-550 μm) was supplied by Silicon Materials (Germany). The ohmic contacts were made using Ga-In eutectic and silver epoxy resin by the method of Wrighton et al [47]. These electrodes were converted to the H-terminated form by HF etching. The HF is removed by washing with degassed reagent grade water and acetone then dried in a stream of inert gas. The etched area is scratched and a gallium-indium conductive eutectic is applied. A copper wire is attached and glued in place with conducting silver epoxy and left to dry. The whole back surface is then covered with an insulating. Before using, the p-tpe Si electrode is etched with 40 % HF solution (in ethanol) for 10 mins and then washed with reagent grade water and acetone, the electrode is dried under vacuum and kept under inert gas until it is used.

The light source used during photoelectrochemical measurements was a Krüss KL5125 halogen fibre optic ($\lambda_{max} = 650$ nm; polychromic outputs 90 mW cm^{-2}).

Electrochemical Experiments. All electrochemical measurements were carried out using an Autolab PGSTAT 100N, under strictly anaerobic conditions, as previously described.The electrolyte, [NBu$_4$][BF$_4$] used in all studies was prepared as described in Chapter 2.

Potentials are referenced to SCE using a Ag wire *pseudo-r*eference electrode and ferrocene as an internal standard. This avoids contamination of the electrolyte with water, chloride or other ions.

The working electrodes for cyclic voltammetry experiments were vitreous carbon (area 0.07 cm^2) or p-type Si electrode (0.7-1 cm^2), the counter electrode was a platinum gauze (2cm^2).

Bulk electrolysis experiments were carried out in a three compartment H-type cell. A mercury pool cathode was employed (nominal area 2.5 cm^2) for conventional electrolyses. For photoelectrosynthetic experiments p-type Si electrodes were used (area 0.7-1 cm^2) as for cyclic voltammetry. The total volume of electrolyte solution in the H-type electrochemical cell was *ca* 12 ml, the working electrode compartment was occupied by 5 ml of solvent. The volume of the gas phase ranged from 10-11 cm^3. Reference and secondary electrodes were as for the cyclic voltammetry experiments.

In a typical bulk electrolysis experiment, the iron porphyrin (0.4 -0.75 mg) was dissolved in 0.25 ml dry DMF and stirred under Ar then it was then added to 4.75 ml CH_3CN in the cathode compartment of the electrochemical cell under Ar. Cyclic voltammetric measurements were carried out on this solution under argon at a small vitreous carbon electrode before and after saturating with CO_2 in the presence of 0.275M CF_3CH_2OH to check that the system was functioning and to establish the reduction potential. During the course of electrolysis the current, time and charge – passed were continuously monitored. After 2 to 4 hours the electrolysis was stopped and the gas-phase analysed. A sample of the gas phase (0.5 ml) was extracted with a tight-gas syringe and injected into the gas

chromatograph. This was carried out using a Perkin–Elmer Clarius 500 instrument fitted with a 5Å molecular sieve column (800/100 mesh, 6'x1/8") and thermal conductivity detector (oven temperature 80 ^{0}C ; injection volume , 0.5 ml). Standard calibration were performed the prior to measurments.

A similar procedures were used for the photosynthetic experiments at p-type Si.

3.6 References

1. M. Aulice. B. Viswanthan. Rev. Proc Indian Natn Sci Acad. 2**004**, 3, 407-462.

2. J. Maria. Journal of the University of Chemical Technology and Metalluragy. **2007**, 42, 333-344.

3. S. Roy, O. Varghese, M. Paulose, C. A. Grimes. ACS Nano. **2010**, 4, 1259-1278.

4. M. Aresta, A. Dibenedetto. Dalton Trans. **2007**, 2975-2992.

5. S. Nurhanna, Y. Zhang. Dalton Trans. **2010**, 39, 3347-3357.

6. F. Scholz, C. J. Pickett. Encyclopedia of Electrochemistry .Volume 7a. Wiley - VCH**. 2006**.

7. M. Aresta , C. Nobile, V. Albano, E. Formi, M. Manassero. Chem. Comm. 1975, 15, 636-637.

8. D. Gibson. Chem. Rev. **1996**, 96, 2063-2095

9. A. Gennaro, A. Lsse, M. Severin, E. Vianello, I. Blhugun, M. Saveant. J. Chem. Soc. Faraday Trans. **1996**, 92, 20, 3963-3968.

10. E. Lamy, l. Nadjo, M. Saveant. J. Electroanal. Chem. **1977**, 78, 403.

11. M. Doherty, D. Grills, J. T. Muckerman, D. Polyansky, E. Fujita. Coord. Chem. Rev. **2010**, 254, 2472-2482

12. H.Takedaa, O. Ishitani. Coord. Chem. Rev. **2010**,254, 346-354

13. T. Yamamoto, D. Tryk, K. Hashimoto, A. Fujishima, M. Okawa. J. Electrochem. Soc. **2000**, 147, 3393-3400 .

14. A. Bandi. J. Electrochem. Soc. **1990**, 137, 2157-2160.

15. L.Wenzhen. J. Am. Chem. Soc. **2010**, 1056, 55-76.

16. P. Bequm, G. Pickup. Electrochem. Commun. **2007**, 9, 2525-2528.

17. L. Bhugun, D. Lexa, J-M. Saveant. J. Am. Chem. Soc. **1996**, 118, 1769-1776.

18. E. E. Benson, C. P. Kubiak, A. J. Sathrum, J. M. Smieja. Chem. Soc. Rev. **2009**, 38, 89-99.

19. M. Aresta, C. F. Nobile, V. G. Albano, E. Formi, M. J. Manassero. J. Chem. Soc. Chem. Commun. **1975**, 15,636-637.

20. D. J. Darensbourg, A. Rokicki, M. Y. Darensbourg. J. Am. Chem. Soc.**1981**, 103, 3223-3224.

21. J. Haweeker, J. Lehn, R. Ziessel. J. Chem. Soc. Chem. Commun.**1984**, 6, 328-330.

22. H. Ishida, K. Tanaka, T. Tanaka. Organometallics. **1987**,6 , 181-186.

23. C. M. Bolinger, N. Story, B. P Sullivan, T.J. Meyer. Inorg. Chem.**1988**, 27,4582-4587

24a. M. Burce, E. Megehee, B. P. Sullivan, H. Thorp, T.R. O'Tool, A. Downard T.J. Meyer. Inorg. Chem.**1988**, 7, 238-240.

 24b. S. Cosnier, A. Deronzier, J-C. Moutet, New. J. Chem. **1990**, 45, 381-385.

25. J. M. Smieja, C.P. Kubiak. Inorg. Chem**. 2010**, 49, 9283-9289.

26. C. Windle, R. Perutz. Coord. Chem. Rev. **2012**, 256, 2562- 2570.

27. C. J. Pickett, D. Pletcher. J. Chem. Soc. Dalton Trans. 1976, 749-752

28. S. Sayer, J. H. Wagenknecht. J. Am. Chem. Soc .**1984**, 106, 5367-5368.

29. D. L. DuBois, A. Miedaner, R. C. Haltiwanger. J. Am. Chem. Soc.**1991**, 113, 8753-8764.

30. S. Messhitsuk, M. Ichikawa, K. Tamaru. J. Chem. Soc. Chem. Commun. **1974**,5, 158-159.

31. B. J. Fisher, R. Eisenbrg. J. Am. Chem. Soc. **1980**,102, 7361-7363.

32. M. Beley, J. P. Collin, R. Ruppert, J. P. Sauvage. J. Am. Chem. Soc. **1986**, 108, 7461-7467.

33. N. Sanoyam, M. Kirii, T. Sakata. Electrochem. Commun.**1999**, 1, 213-216.

34. M. Hammouche, D. Lexa, M. Momenteau, J. Saveant. J. Am. Chem. Soc. **1991**,113, 8455-8466.

35. L. Bhugun, D. Lexa, J-M. Saveant. J. Phys. Chem. Soc.**1996**, 100, 19981-19985.

36. C. Costentin, S. Drouet, M. Robert, J-M. Savéant. Chem. Soc. Rev. **2013**, 42, 2423-2436

37. J. Hawecker, J. Lehn, R. Ziessel, Helv. Chim. Acta .**1986**, 69,1990-2012.

38. B. Kumar, J. Smieja, C. Kubiak. J. Phys. Chem. **2010**,114, 14220−14223.

39. I. Bhugun, D. Lexa, J. M. Savéant. J. Am. Chem. Soc. 1**994**, 116, 5015-5016.

40. H. Hori, F. Johnson, K. Koike, O. Ishitani, T. Ibusuki. J. Photochem. Photobio. Chem A, **1996**, 96, 171-174

41. D. Laser, J. Bard. J. Phys. Chem. **1976**, 5, 459- 466.

42. L. M. Peter. Electrochemistry. RSC. London. **1984,** 9, 66-79.

43. T. Liu, D. DuBois, R. Bullock. Nature Chem.**2013**, 5, 228-233.

44. M. Helm, M. Bullock, M. DuBois, D. DuBois. Science. 2011, 18, 11798-11803.

45. L.Webster, S. Ibrahim, J. Wright, C. J. Pickett. Chem. Eur. J. **2012**, 18, 11798-11803.

46. P. Li, K. Alenezi, S. Ibrahim, J. Wright, D. Hughes, C. J. Pickett. ChemSusChem. **2012**, 5, 2361 -2375.

47. R. N. Dominey, N. S. Lewis, J. A. Bruce, D. C. Bookbinder, M. S.Wrighton. J. Am. Chem. Soc. **1982**, 104, 467- 482.

Chapter 4

4 Electrocatalysis of Hydrogen Evolution by [Fe$_4$S$_4$] - Clusters

4.1 Introduction

4.1.1 Overview

This chapter is concerned with exploring electrocatalysis of hydrogen evolution using synthetic {Fe$_4$S$_4$}-clusters. Although, it is known for over forty years, studies of their electrocatalytic properties for hydrogen evolution have been very limited. This is in part because of the acid-lability of the clusters themselves, but also because of problems with adsorption and deposition of heterogenous materials [1]. Nevertheless, clear evidence that in a chemical system reduced clusters can stoichiometrically yield dihydrogen has been provided by the work of Henderson et al [1, 2, 3]. A delineation of the electrocatalytic behaviour of 4Fe4S clusters towards hydrogen evolution is important because this may bear upon hydrogen evolution mechanisms at the FeS sites in the {MoFe$_7$S$_9$}-cluster of nitrogenase and may relate to the possibility that simple clusters were primitive hydrogenases in early evolution before the elaboration of the CN and CO ligated [FeFe]- and [NiFe]-hydrogenases[4,5].

In the following sections a brief review of the occurrence, structure and function of iron sulfur clusters in biology and of their synthetic analogues is provided with a particular focus on the cubane [Fe$_4$S$_4$]-systems, the subject of this study.

4.1.2 Iron sulfur clusters in biological systems

Iron–sulfur centres in proteins are involved in electron transfer as well as catalytic, structural and sensory roles. Since the first iron sulfur clusters were structurally characterised in proteins in the early 1960s [6] studies of the natural proteins and of synthetic iron sulfur cluster chemistry have been research areas of very great activity and have been extensively reviewed [7-12].
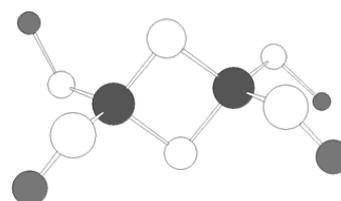
4.1.3 Structures of natural FeS clusters

Iron sulfur centres can be classified into four structural types of site, rubredoxin (Rb) and three different ferredoxin assemblies (Fd), these are illustrated by the structures in   Figure 4.1[13,14].
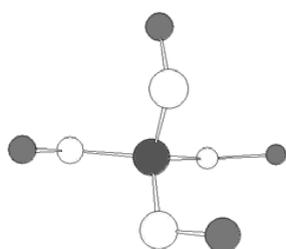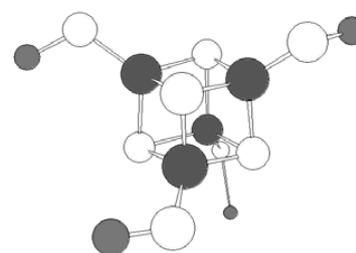

Rubredoxins (Rb) $[Fe_2S_2]$-centres (2-iron ferredoxin)

$[Fe_3S_4]$-centres (3-iron ferredoxin) $[Fe_4S_4]$-centres (4-ironferredoxin)

Figure 4.1 The most common active sites of the known iron sulfur clusters

Where,

sulfur   iron

In the majority of ferredoxins, and in all rubredoxins, the protein ligands are cysteines, which provide four thiolate ligand donors to the iron centres. The $[Fe_2S_2]$, $[Fe_3S_4]$ and $[Fe_4S_4]$ assemblies which are formed by tetrahedrally coordinated iron atoms with bridging sulfides and are most often ligated to the protein through cysteine residues [15-17]. Amongst these, $[Fe_4S_4]$-centres are the most widespread of the iron cluster centres in biological systems. The crystal structure of this type of ferredoxin is described as a distorted cube with alternating Fe and S at the corners and the distances of S-S or Fe-Fe is 3.55 and 2.75Å respectively; four cysteines from the polypeptide chain anchor the cubane to the protein.

4.1.4 Function of Iron Sulfur Clusters

Iron sulfur clusters play a major role in electron transport in biological systems, including respiration, photosynthesis and nitrogen fixation. They may be divided into two types of redox function, inter- and intra-protein electron transport. Inter-protein electron transport involves, for example, the transfer of an electron between a 4Fe4S ferredoxin protein, and its natural partner which may contain the substrate binding and activating centre. Intra-protein electron transport involves transfer of electrons within a protein and this may utilise one or more iron-sulfur centres to relay the electrons to or from the 'outside world' to the catalytic redox

centre. This 'wiring' of an active site is illustrated by the arrangement of iron sulfur clusters in the [FeFe]-hydrogenases, Figure 4.2.
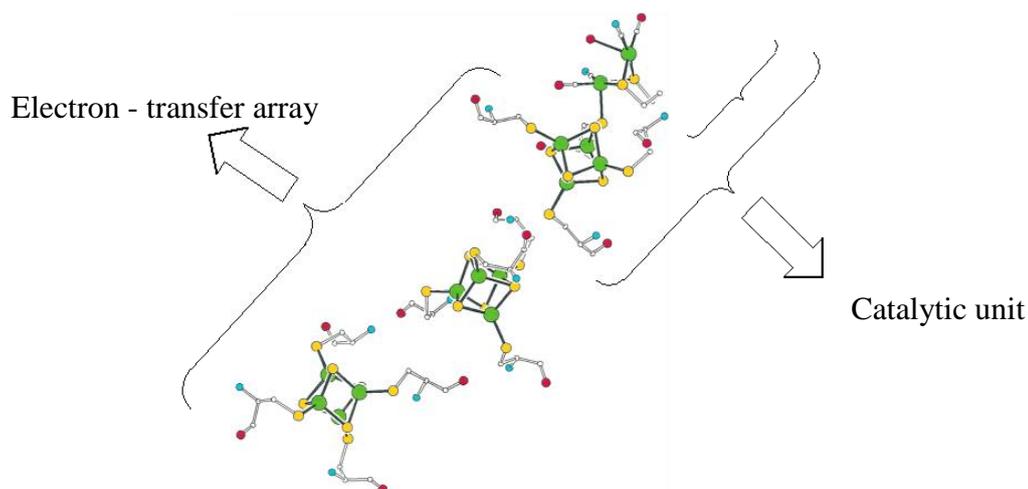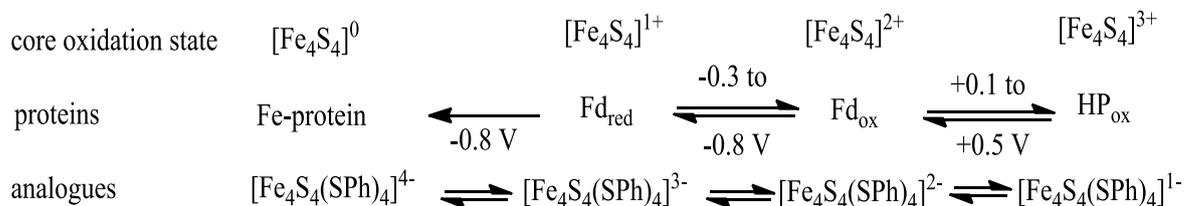

Figure 4.2 Iron sulfur clusters in the [FeFe]-hydrogenases. (X-ray structures : Peters et al 1998,1999 ; Fontecilla-Camps et al 1999) [18]

$[Fe_4S_4]$-centres display four oxidation states which are $[Fe_4S_4]^{3+}$, $[Fe_4S_4]^{2+}$, $[Fe_4S_4]^{+}$ $[Fe_4S_4]^{0}$ [19,20]. Only the first three state are commonly observed in natural systems, although the 'all-ferrous' states $[Fe_4S_4]^{0}$ has been generated by chemical reduction of the Fe-protein of nitrogenase [10].

The cubane ferredoxin proteins can be divided into two subclasses **(i)** <u>low potential</u> electron transfer bacterial ferredoxins (Fd) which operate at the $[Fe_4S_4]^{2+}$ / $[Fe_4S_4]^{+1}$ redox level. In this class the ferredoxins are able to exchange electrons at a low potential (-700 to -300 mV vs. SHE) [21] and **(ii)** <u>high potential</u> iron-sulfur proteins (HiPIP) where the ferredoxins contain a $[Fe_4S_4]^{3+}$/$[Fe_4S_4]^{2+}$ redox couple (+100 to +400 mV vs. SHE). The range of potentials observed for both subclasses indicates a strong dependence on the nature of the protein environment: the cubane centres are evidently sensitive to

electrostatic, hydrogen bonding, steric and other non-covalent interactions, [19, 22, 23].

Scheme 4.1 shows the electron-transfer series for [Fe$_4$S$_4$] centres in proteins and in synthetic analogues [10, 23 , 25].

core oxidation state	[Fe$_4$S$_4$]^0		[Fe$_4$S$_4$]$^{1+}$		[Fe$_4$S$_4$]$^{2+}$		[Fe$_4$S$_4$]$^{3+}$
proteins	Fe-protein	$\xleftarrow{\hspace{1cm}}$ -0.8 V	Fd$_{red}$	$\underset{\text{-0.8 V}}{\overset{\text{-0.3 to}}{\rightleftharpoons}}$	Fd$_{ox}$	$\underset{\text{+0.5 V}}{\overset{\text{+0.1 to}}{\rightleftharpoons}}$	HP$_{ox}$
analogues	[Fe$_4$S$_4$(SPh)$_4$]$^{4-}$	$\rightleftharpoons$	[Fe$_4$S$_4$(SPh)$_4$]$^{3-}$	$\rightleftharpoons$	[Fe$_4$S$_4$(SPh)$_4$]$^{2-}$	$\rightleftharpoons$	[Fe$_4$S$_4$(SPh)$_4$]$^{1-}$

Scheme 4.1 The electron-transfer series of [Fe$_4$S$_4$] of proteins and of analogues [10,23,26] Fd = Ferredoxins and HP = high potential Ferredoxin [potentials vs SHE]

The small molecule transformation by coupled electron and proton –transfer reactions is an important feature of both chemical and biological catalysis. The simplest such reaction is the conversion of H$^+$ to H$_2$ which is performed in nature by hydrogenase and nitrogenase [24]. Fe-S- based clusters are the active sites in both enzymes, and in [FeFe] - hydrogenase this transformation takes place at the H-cluster equation (4.1)

$$2H^+ + 2e^- \leftrightarrow H_2 \qquad\qquad 4.1$$
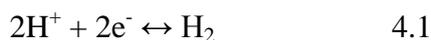
Thus beyond a function as 'simple' electron transport or transfer centres, Fe-S clusters and Fe-S assemblies possessing heterometallic centres provide the active sites of enzymes such as aconitase and nitrogenase. Aconitase is a non-redox enzyme but nitrogenase, a key enzyme of the nitrogen cycle, reduces molecular nitrogen and concommitantly reduces protons to molecular hydrogen. Recent work has provided strong evidence that both N$_2$ reduction and hydrogen generation takes place on FeS sites [27-30].

To understand structure and function of natural iron sulfur systems, both in terms of redox behaviour and catalysis a considerable body of synthetic and mechanistic research has been undertaken in the last 40 or so years. Much of this has been led by the groups of Holm and Coucovanis and their respective coworkers [11, 13,16], particularly structural studies of all classes of FeS assemblies and of those possessing heterometals (*eg* Mo,W, Ni). Henderson has examined protonation reactions of reduced clusters and also the generation of dihydrogen from these [1,2] and others have shown that the isolated cofactor of nitrogenase can support electrocatalysis of hydrogen evolution [31,32] However beyond this, well-defined systems showing electrocatalytic behaviour of FeS assemblies has not been clearly established.

4.1.5 Scope of this work

This chapter focuses on the electrochemical catalysis of proton reduction by the synthetic iron sulfur complex $[Fe_4S_4(SPh)_4]^{2-}$ at vitreous carbon electrode in various solvents in the presence of different acid sources. The work establishes conditions for well defined molecular catalysis of dihydrogen evolution from both electrosynthetic and mechanistic standpoints. Results obtained on vitreous carbon are extended to studies of the photoelectrocatalytic production dihydrogen at illuminated p-type silicon.

4.2 Results and Discussion

4.2.1 Cyclic voltammetry of $[Fe_4S_4(SPh)_4]^{2-}$

The cyclic voltammetry of $[Fe_4S_4(SPh)_4]^{2-}$ in inert non-aqueous electrolytes such as MeCN – 0.2M $[Bu_4N][BF_4]$ or CH_2Cl_2 - 0.2M $[Bu_4N][BF_4]$ is well established [33]. In both solvents there is a diffusion controlled primary reduction step corresponding to the $[Fe_4S_4(SPh)_4]^{2-/3-}$ couple. A second partially reversible reduction at a more negative potential which is observed in the MeCN electrolyte, this is masked in the CH_2Cl_2 electrolyte by reduction of the solvent itself. In CH_2Cl_2 - 0.2M $[Bu_4N][BF_4]$ the primary oxidation step for the $[Fe_4S_4(SPh)_4]^{2-/1-}$ couple is partially reversible whereas in the MeCN electrolyte the oxidation is a multi-electron irreversible process. This is attributable to the nucleophilic MeCN attacking a Fe centre following oxidation. Thus in neither electrolyte is it possible to observe the complete electron – transfer series $[Fe_4S_4(SPh)_4]^{1-/2-/3-/4-}$.

When $[Bu_4N][BF_4]$ is warmed to ca 30°C in toluene an ionic phase separates which has the molar ratio 3 toluene : 1 $[Bu_4N][BF_4]$. This phase is conducting and is capable of dissolving polar and non-polar molecules allowing electrochemistry to be carried out in a medium of low nucleophilicity; importantly it has a wide potential range of ca ±2.5V versus SCE. Thus it has been shown that all members of the $[Fe_4S_4(SPh)_4]^{1-/2-/3-/4-}$ electron-transfer series can be detected by cyclic voltammetry in this medium [34].

Figure 4.3 shows the cyclic voltammetry of the complex $[Fe_4S_4(SPh)_4]^{2-}$ at a vitreous carbon electrode in the toluene- $[Bu_4N][BF_4]$ electrolyte in the reduction regime. Two successive reduction processes at potentials $E_{1/2}$= -0.87V and -1.75V

versus Ag/AgCl corresponding to the reversible $[Fe_4S_4(SPh)_4]^{2-/3-}$ and partially $[Fe_4S_4(SPh)_4]^{3-/4-}$ couples are observed, Equation 4.2.
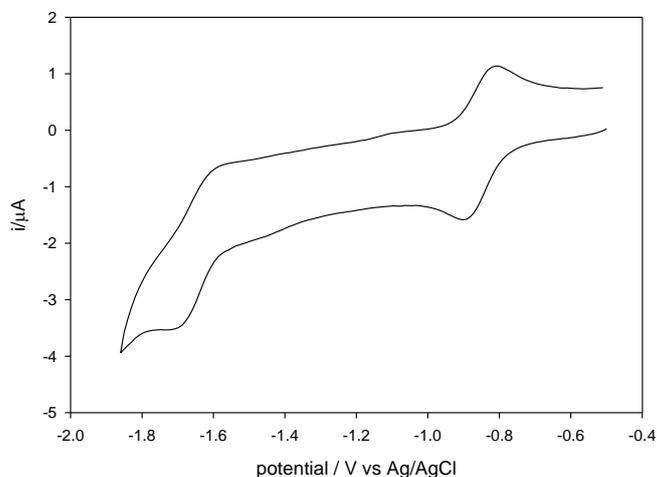
Figure 4.3 Cyclic voltammetry of 0.5 mM $[Fe_4S_4(SPh)_4]^{2-}$ in toluene - $[Bu_4N][BF_4]$; scan rate 100mVs^{-1}, vitreous carbon electrode under Ar at 32°C

$$[Fe_4S_4(SPh)_4]^{2-} \quad \underset{-0.87 \text{ V}}{\overset{e^-}{\rightleftarrows}} \quad [Fe_4S_4(SPh)_4]^{3-} \quad \underset{-1.75 \text{ V}}{\overset{e^-}{\rightleftarrows}} \quad [Fe_4S_4(SPh)_4]^{4-} \qquad 4.2$$
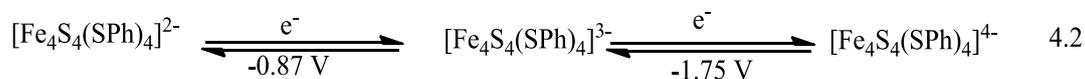
The primary reduction of $[Fe_4S_4(SPh)_4]^{2-/3-}$ is a diffusion controlled reversible one electron step as it is evident from the linear relationship between the peak current and square root of the scan rate Figure 4.4. It is electrocatalysis of proton reduction *via* the generation of $[Fe_4S_4(SPh)_4]^{3-}$ at or near the primary reduction potential of the parent dianion complex with which we are concerned.

173
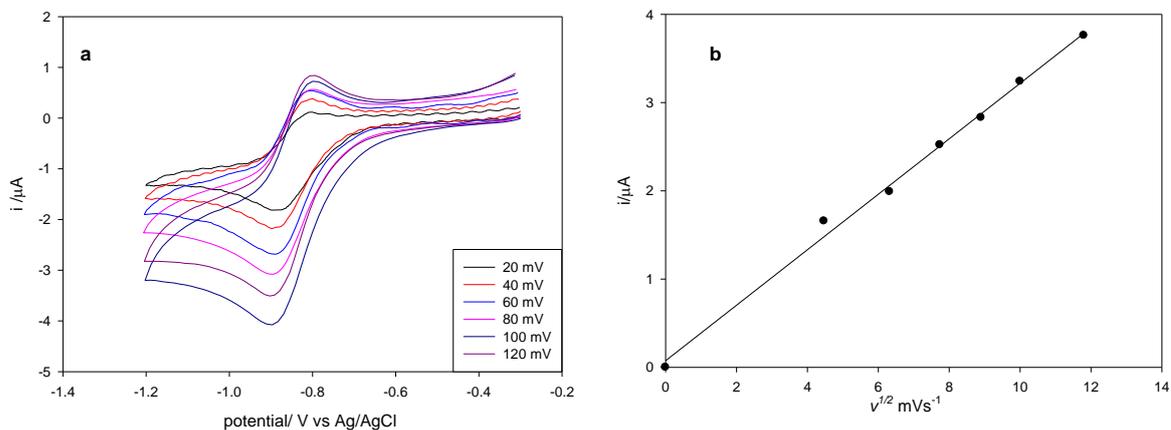
Figure 4.4 (a) Scan rate dependence of the peak current for the primary reduction process (b) linear dependence of the peak current on the square root of the scan-rate showing the process is diffusion controlled.

4.2.2 Electrochemistry of [Fe$_4$S$_4$(SPh)$_4$]$^{2-}$ in the presence of proton source

4.2.2.1 Selection of the acid source

Henderson and co-workers have shown that 2,6 –lutidinium [Hlut$^+$] as the   BF$_4$ salt is a suitable acid for protonation of   [Fe$_4$S$_4$(SPh)$_4$]$^{3-}$ in MeCN. Thus it is a sufficiently strong acid (pKa = 15.4 in MeCN) to protonate the cluster without decomposition [2]. We find that this is the case for the non-nucleophilic toluene electrolyte. Provided concentrations are less than 10 mM, a cluster concentration of 0.5mM is stable on the hours timescale in the toluene electrolyte. In MeCN a black precipitate is formed above about 3-4 mM of the acid. The other criteria is that the acid should reduce directly at a potential considerably negative of that for the electrocatalysis on vitreous carbon. This is the case for [Hlut$^+$] in the toluene and the other electrolytes (see Figure 4.6, below).

4.2.2.2 Selection of the electrolyte

It has been shown in earlier work by Holm and others that electrochemical proton reduction in non-aqueous solvents using $[Fe_4S_4(SPh)_4]^{2-}$ as a catalyst gives low yields of dihydrogen. We find that the cyclic voltammetry of $[Fe_4S_4(SPh)_4]^{2-}$ in MeCN - 0.2M $[Bu_4N][BF_4]$ in the presence of lutidinium (BF_4 salt) as a proton source [2] gives a cyclic voltammetric response consistent with electrocatalysis but preparative scale electrolyses give low yields of dihydrogen and low turnover numbers, with destruction of the catalyst at the end of electrolysis. $[Fe_4S_4(SPh)_4]^{2-}$ in CH_2Cl_2 - 0.2M $[Bu_4N][BF_4]$ again gives a cyclic voltammetric response in the presence of increasing concentrations of $[Hlut^+]$ indicative of electrocatalysis. However, removal of the electrode after cycling in the presence of acid and the cubane catalyst, washing and transfering to fresh electrolyte containing acid gave a current response indicative of the formation of a catalytic film on the electrode surface.

4.2.2.3 Electrocatalysis of proton reduction in the toluene electrolyte

In the presence of proton source the primary reduction wave for $[Fe_4S_4(SPh)_4]^{2-}$ increases in height and becomes irreversible as the concentration of acid increases consistent with electrocatalysis of proton reduction by the $[Fe_4S_4(SPh)_4]^{2-}$ complex, Figure 4.5. Importantly, under the same conditions, direct reduction of 2,6-lutidinium $[Hlut]^+$ on vitreous carbon electrode occurs at E_p = -1.36 V vs Ag/AgCl in $[Bu_4N][BF_4]$-toluene but in the presence of $[Fe_4S_4(SPh)_4]^{2-}$ this is shifted 490 mV more positive at ca -0.87 V vs Ag/AgCl as is evident from Figure 4.6.

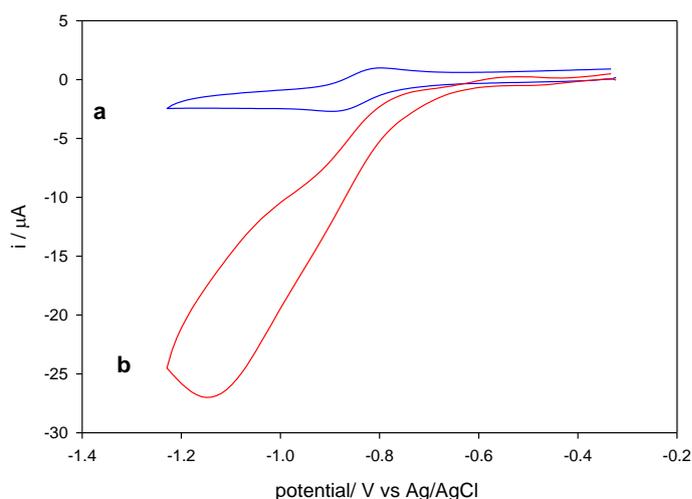**Figure 4.5** Cyclic voltammetry of 0.5 mM $[Fe_4S_4(SPh)_4]^{2-}$ $[Bu_4N][BF_4]$-toluene, scan rate 100mVs^{-1} at a vitreous carbon electrode under Ar (a) In the absence of proton source (b) in the presence of 12 eq $[Hlut]^+$
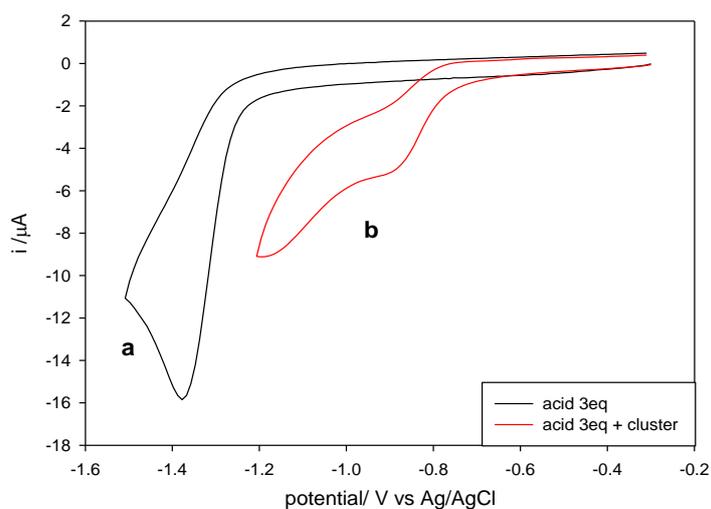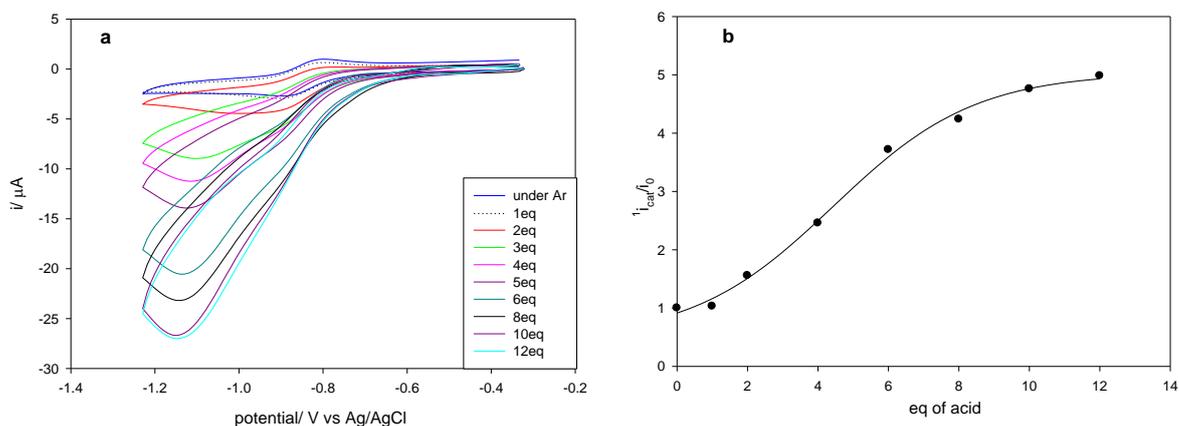

Figure 4.6 (a) Cyclic voltammetry of 1.5 mM $[Hlut]^+$ (b) 0.5 mM $[Fe_4S_4(SPh)_4]^{-2}$ in the presence of 3 eq of $[Hlut]^+$in $[Bu_4N][BF_4]$-toluene, scan rate100mVs^{-1} at a vitreous carbon electrode under Ar

The dependence of the catalytic current for proton reduction at -0.87 V *versus* Ag/AgCl upon the concentration of the acid is shown by Figure 4.7(a). It can be seen that at the lower acid concentrations catalysis is observed close to the primary reduction potential which approaches a maximum current above 8

equivalents of acid. As the concentration of the acid is increased a second catalytic step come into play at a more negative potential and reaches a maximum at about 12 equivalents of the acid. At higher acid concentrations a precipitate is formed as noted above.

It is useful to normalise the peak or plateau catalytic currents by dividing the peak current for the uncatalysed process at the same scan-rate, this simplifies subsequent analysis by eliminating surface area, catalyst concentration and its diffusion coefficient [35]. Figure 4.7 (b) shows a plot of the i^1_{cat} / i_o where i^1_{cat} is the peak current measured at 100mVs^{-1} for the primary catalysis and i_o is the peak current measured for the first one-electron reduction step at the same scan-rate in the absence of the proton source. Figure 4.7 (c) shows the corresponding plot encompassing both the primary and secondary catalytic process i^{total}_{cat} / i_o where i^{total}_{cat} is the total current for both these steps. The net response for the secondary process i^2_{cat} / i_o is shown by Figure 4.7(d). It is evident that the primary electrocatalytic plateau current is about one half of that for the secondary catalytic process. The full analysis of these curves is discussed below in the mechanism section following the sections which establish (i) the formation of dihydrogen in bulk electrolysis experiments and (ii) the inhibition of the electrocatalysis by CO and by thiophenol.
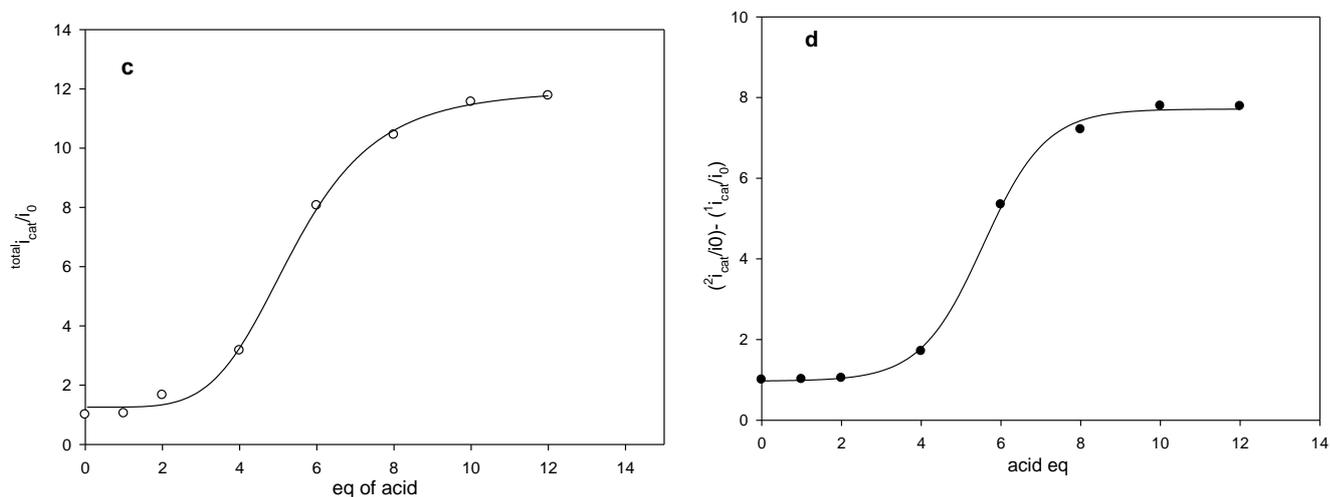
Figure 4.7   (a) Cyclic voltammetry of 0.5 mM [Fe$_4$S$_4$(SPh)$_4$]$^{2-}$ in [Bu4N][BF4]-toluene,   scan rate 100mVs^{-1} at a vitreous carbon electrode under Ar in the presence of increasing concentrations of [Hlut]$^+$ (b) the effect of the acid concentration on i$_{cat}$/i$_0$ ratio for the first process (c) the effect of the acid concentration ratio of i$_{cat}$/i$_0$ for the second process. (d) The net response for the secondary process i$^2_{cat}$ / i$_o$

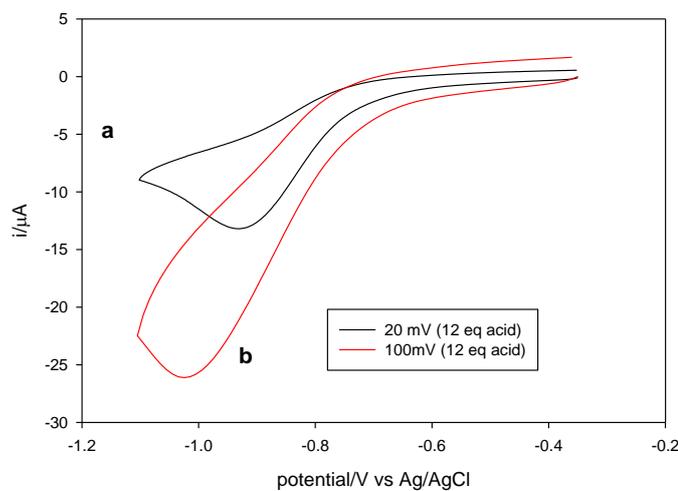The dependence of the catalytic current on the scan-rate is shown by Figure 4.8

Figure 4.8 Cyclic voltammetry of 0.5 mM [Fe$_4$S$_4$(SPh)$_4$]$^{2-}$ in toluene -[Bu4N][BF4], at a vitreous carbon electrode under Ar in the presence 12 equivalents of [Hlut]$^+$ (a) scan rate 20mVs^{-1} , (b) scan rate 100mVs^{-1}

4.2.2.4 Preparative electrocatalysis

Preparative bulk electrolyses were carried out in toluene - $[Bu_4N][BF_4]$ at 32^oC in an H-type cell in the presence of 0.5 mM $[Fe_4S_4(SPh)_4]^{2-}$ (2.51 µmoles) and 12 eq $[Hlut^+]$ at a vitreous carbon cathode of total geometric area 2 cm^2 at an applied potential of -0.95 V *versus* Ag/AgCl. When the current had decayed to *ca* 5% of the initial current, the gas phase of the cell was analysed by gas chromatography using a thermal conductivity detector (GC-TCD). This confirmed the formation of H_2 with a current efficiency of *ca* 65 − 70% (3 experiments). Electrolyses were typically terminated after 6h which allowed *ca* 6 turnovers and gave dihydrogen yields during the course of 5-6 h, H_2 yield was 8.5 − 14 µmoles, Table 4.1. No H_2 was detected when bulk electrolysis was performed in the absence of the catalyst.

Table 4.1 The yield of dihydrogen during the course of 5-6 h for 3 experiments

	Control experiment	*1*	*2*	*3*
Time/h	5	5.5	5.8	6
Acid equivalents	12	9	12	12
Charged passed, C	0.17	3.25	3.6	3.9
Current efficiency %	0	65	64.5	70
Chemical yield % µmoles H_2/µmoles acid	0	75	80	95.6
Yield of H_2 µmoles	0	9.5	12.1	14.3

In a separate experiment under the same conditions as above, the yield of H_2 was monitored by gas chromatography as a function of electrolysis time and of charge passed. Figure 4.9 (a) shows the GC response for dihydrogen measured during the course of electrolysis and Figure 4.9 (b) shows the corresponding plot of the yield

of H_2 as a function of time. It can be seen that the yield of H_2 increased steadily in the first phase of the electrolysis and dropped off in the latter stages as the acid was consumed. The chemical yield of dihydrogen at the end of electrolysis based upon the total acid available was 95.6%, Figure 4.9(b). The current efficiency for H_2 production after the first hour was fairly constant at 68 -71%, Figure 4.9 (c). Figure 4.9 (d) re-casts this data showing the plot of the yield of dihydrogen as a function of charge passed. As expected the plot is essentially linear and the slope corresponds to an average current efficiency for dihydrogen formation of about 73% during the course of electrolysis. This plot takes into account the charge required to generate the tri-anionic cluster. Finally, the plot of current *versus* charge-passed Q, Figure 4.9(e) is essentially linear intercepting the Q-axis at 43 μmole electrons giving an *overall* current efficiency for dihydrogen formation as *ca* 71% after 6 turnovers again allowing for reduction of the catalyst to the tri-anion cluster.

Table 4.2 Current efficiency and turnover numbers for electrocatalytic reduction of protons by $[Fe_4S_4(SPh)_4]$

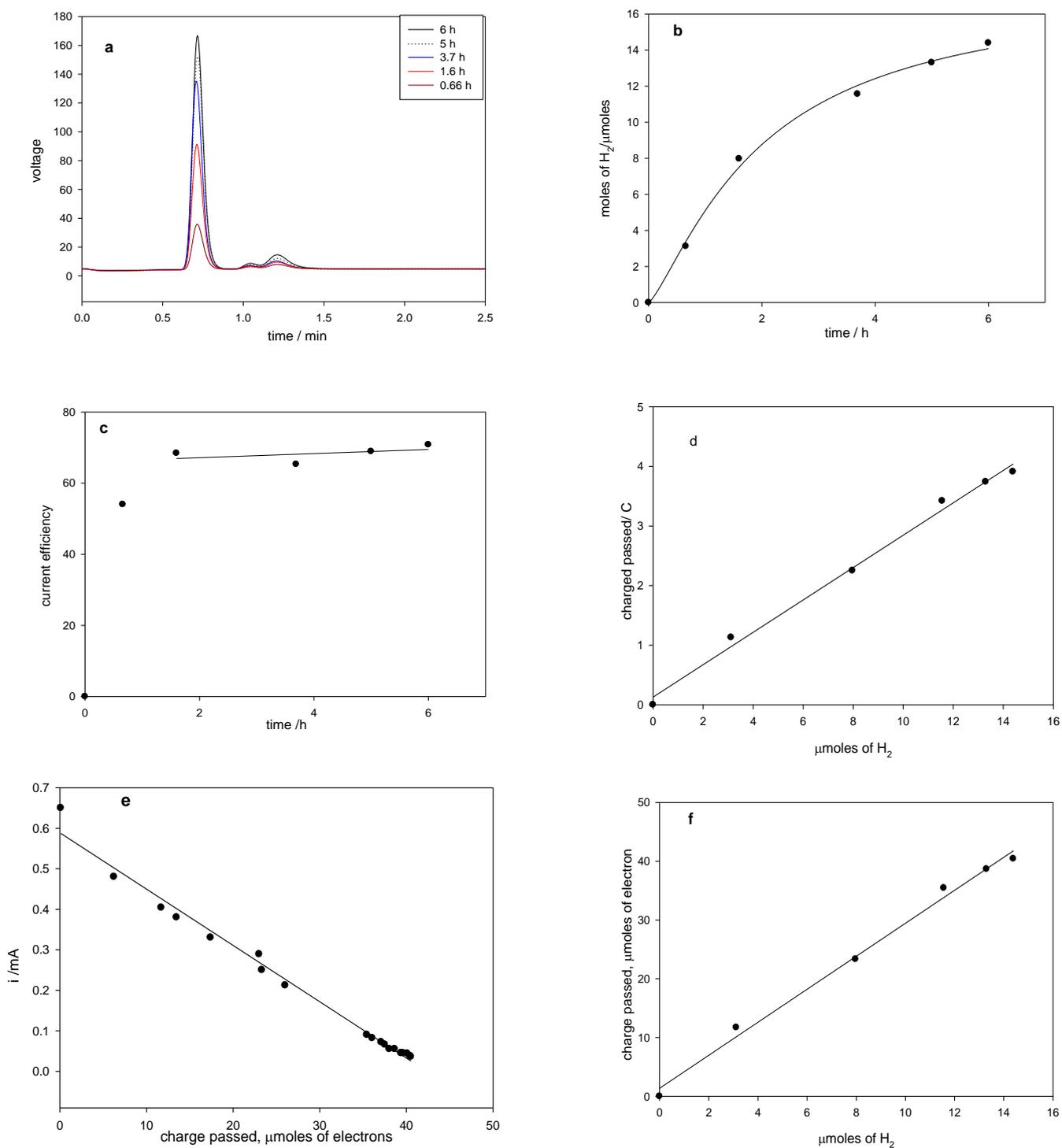| *Time/h*	*0.6*	*1.60*	*3.7*	*5*	*6.1*
Number of μmoles of H_2	3.13	7.97	11.56	13.3	14.33
Current efficiency %	53.3	68.4	65.3	69	70.8
Chemical yield % μmoles H_2/μmoles acid	20.8	53.1	77	88.8	95.6
T.N	1.25	3.2	4.62	5.29	5.69
Charge passed, C	1.31	2.25	3.42	3.73	3.91
μmole of electrons	13.5	23.3	35.4	38.9	40.5

Figure 4.9 (a) Gas chromatography of H_2 production; the major peak(s) at 0.7m is H_2, the minor peaks near 1.1 and 1.2 are dioxygen and dinitrogen which arise from air contamination during sampling by syringe. (b) The yield of H_2 *versus* electrolysis time.(c) The current efficiency *versus* electrolysis time. (d) The yield of dihydrogen as a function of charge passed. (e) The current *versus* charge passed, μmoles of electrons. (f) μmole of H_2 produced *versus* μmole of electrons passed during electrolysis. Conditions: 0.5 mM $[Fe_4S_4(SPh)_4]^{2-}$ in toluene-$[Bu_4N][BF_4]$ in the presence of 12 eq $[Hlut^+]$ at a vitreous carbon electrode held at -0.9 V vs Ag/AgCl under argon.

4.2.2.5 The stability of [Fe₄S₄(SPh)₄]²⁻ during electrolysis

The stability of the iron sulfur cluster catalyst was examined by comparing the cyclic voltammetry before addition of acid and at the end of electrolysis [6 hours] when all the acid had been consumed as shown in Figure 4.10. From the relative peak heights it is evident that about 70% of $[Fe_4S_4(SPh)_4]^{2-}$ was recovered after electrolysis. This is in marked contrast to the behaviour in other solvents. In both MeCN - 0.2M [Bu₄N][BF₄] and CH_2Cl_2 - 0.2M [Bu₄N][BF₄] none of the parent cluster is detected at the end of electrolysis in the presence of the acid.
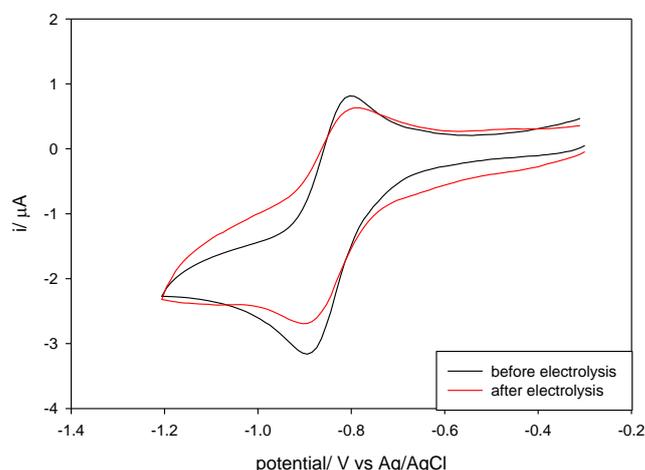

Figure 4.10 Cyclic voltammetry of $[Fe_4S_4(SPh)_4]^{2-}$ before and after electrolysis

4.2.2.6 Effect of carbon monoxide on the catalysis of proton reduction by [Fe₄S₄(SPh)₄]³⁻

The results described in the sections above clearly show that $[Fe_4S_4(SPh)_4]^{2-}$ electrocatalyses electrochemical reduction of protons to dihydrogen under argon. Carbon monoxide is a reversible inhibitor of proton reduction by the hydrogenases and the nitrogenases. In the case of the [FeFe]-hydrogenase CO has been shown to bind to the distal iron of the di-iron subsite whilst it binds to core Fe atoms of the MoFe –cofactor of nitrogenase. Removing the CO restores proton

reduction activity to both types of enzyme. We have therefore examined the effect of the presence of CO on the electrocatalysis of proton reduction by $[Fe_4S_4(SPh)_4]^{2-}$. Figure 4.11 shows the cyclic voltammogram of the iron sulfur cluster under Ar in the absence of acid [curve (a), black] and the presence of 12 equivalents of lutidinium [curve (b), red]. When the system is now saturated with CO at one atmosphere there is a dramatic decrease in the current response [curve (c), green]. Purging the CO from the system with argon restores the catalytic response to essentially that seen before the introduction of CO [curve (d), blue]. In a control experiment in the absence of acid it is found that the reversible one-electron reduction of the cluster under argon is unaffected by the presence of CO at one atmosphere. Thus CO does not bind to either the $[Fe_4S_4(SPh)_4]^{2-}$ or $[Fe_4S_4(SPh)_4]^{3-}$ species to a measurable extent. The effect of CO is not to completely suppress an acid response. The primary reduction step is about twice the height of that in the absence of acid [compare curves (a) and (c)] and is irreversible, the second catalytic step is however effectively eliminated.
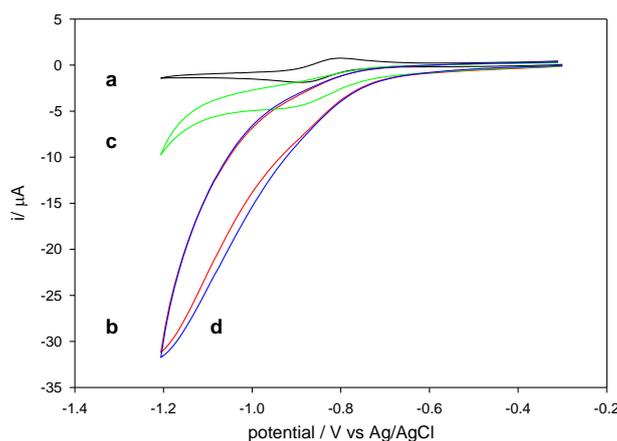

Figure 4.11 The effect of carbon monoxide on the cyclic voltammetry of $[Fe_4S_4(SPh)_4]^{2-}$ in the presence of a proton source: (a), black curve, under argon in absence of acid; (b) red curve, in presence of 12 equivalents of acid; (c) green curve, *after* saturating the solution with CO at 1 atmosphere; (d) blue curve, *after* purging CO saturated solution with argon for 6 minutes

4.3.2.7 Electrocatalysis of proton reduction under Ar and CO

Electrolysis of proton reduction at -0.9V versus Ag/AgCl in 0.5 mM $[Fe_4S_4(SPh)_4]^{2-}$ in the toluene - $[NBu_4][BF_4]$ electrolyte was carried out under Ar and CO in two separate experiments.

Bulk electrolysis at vitreous carbon electrode under Ar in the presence of 12 eq of $[Hlut^+]$ produces H_2 with a current efficiency of *ca* 65% and chemical yield of 77 % after 4.6 turnovers during the course of 3.9 h. The charge passed was 3.48 C and the yield of H_2 was 11.5 μmoles. An electrolysis was performed in the presence of CO saturating the electrolyte, but otherwise under the same experimental conditions as that for the experiment under argon. Over the same electrolysis period the total charge passed (0.66C) was about 20% of that measured under argon. The yield of dihydrogen was less than 2% of that under argon, 0.20 μmoles. The current efficiency of H_2 formation and the chemical yield were 5.8 % and 1.3 %, respectively under CO. Figure 4.12 (a) and (b) show comparative electrolysis data in the presence and absence of carbon monoxide over the whole time-course. After about 0.5h under CO the current reaches a small plateau level following an initial rapid decline. Figure 4.12 (c) shows an expansion of the current – time course in this initial phase and Figure 4.12 (d) shows the corresponding plot of current *versus* charge passed (moles of electrons/moles of cluster) for the system.
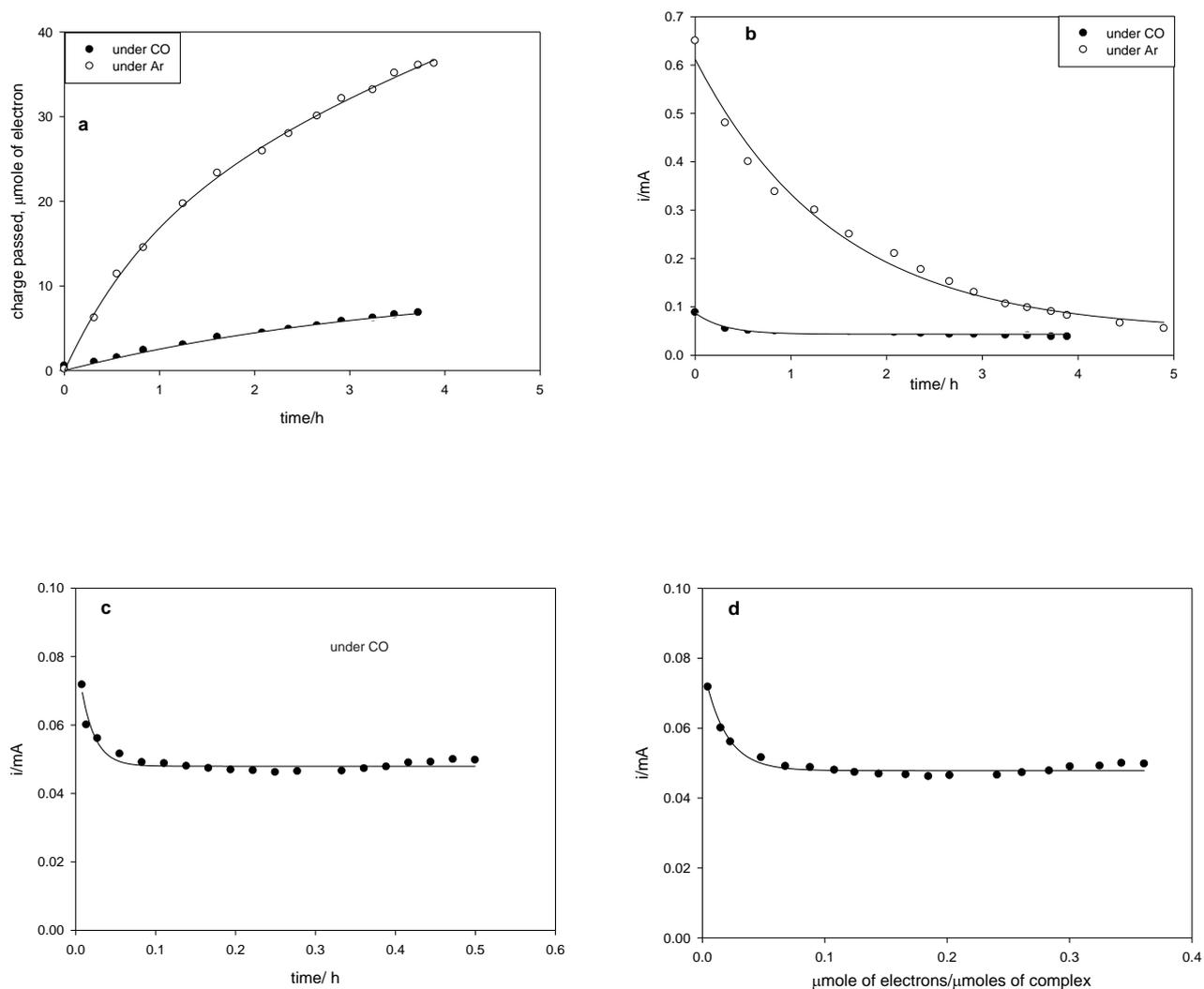
Figure 4.12 (a) Charge passed *versus* electrolysis time, (b) current *versus* electrolysis time , (c) an expansion of the current – time course in this initial phase.(d) the corresponding plot of current *versus* charge passed (moles of electrons/moles of cluster). Electrolysis of 0.5 mM $[Fe_4S_4(SPh)_4]^{2-}$ in $[Bu_4N][BF_4]$-toluene in the presence of 12eq $[Hlut^+]$ on a vitreous carbon electrode ($2cm^2$) under Ar and CO at -0.9 V vs Ag/AgCl.

4.2.2.8 Electrocatalysis in the presence of thiophenol

The reduction of the cluster in the presence of acid may involve the loss of one or more thiophenolate ligands coordinated to Fe during the electrocatalytic process. The effect of free PhSH on the electrochemistry was therefore examined. Thiophenol itself is not sufficiently acidic to engage in electrocatalysis and has no effect on the cyclic voltammetry in the absence of a stronger acid. Figure 4.13 shows the effect of increasing concentrations of PhSH on the electrocatalysis in

the presence of 7 equivalents of 2,6-lutidinium. There is a suppression of the catalytic current for both the primary and secondary steps, with that for the secondary process being shifted to more negative potentials. The reduction in the current at the first catalytic step appears to reach a plateau at about 9 equivalents with a peak current magnitude of about twice that observed for the cluster in the absence of the acid substrate. This effect is similar to that observed for the inhibition by carbon monoxide.
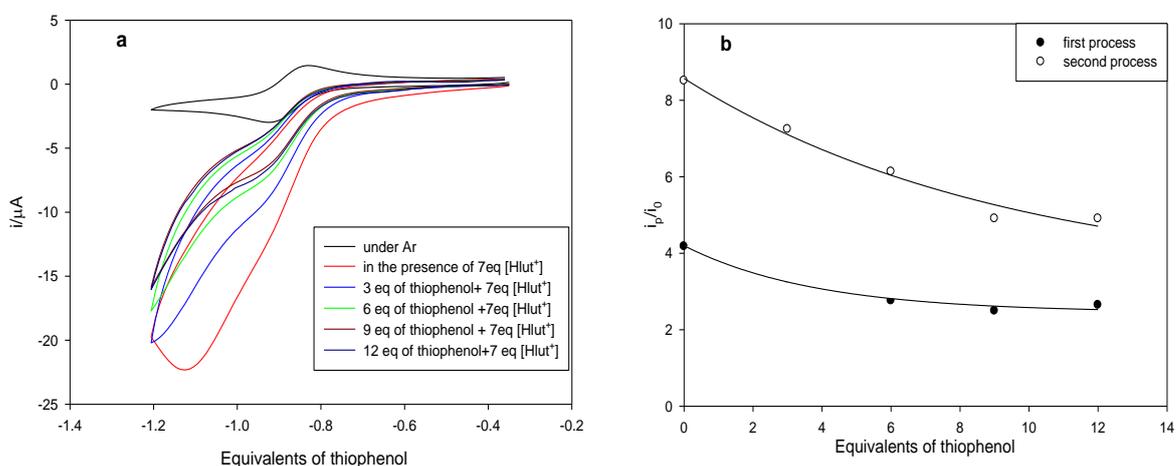

Figure 4.13 (a) The effect of the addition of thiophenol on proton reduction electrocatalysed $[Fe_4S_4(SPh)_4]^{2-}$.(b) The i_{cat}/i_0 ratio at a vitreous carbon electrode(first and second process)

4.2.2.9 Mechanistic aspects of the electrocatalytic proton reduction.

The cyclic voltammetric studies can be interpreted as involving two catalytic cycles for dihydrogen production, a high potential cycle which involves the generation and protonation of the tri-anion, $[Fe_4S_4(SPh)_4]^{3-}$, and a low potential cycle which is suppressed by carbon monoxide and also by PhSH. The inhibitory effect of PhSH suggests that loss of this group as ligand from a protonated species such as $[Fe_4S_4(SPh)_3(PhSH)]^{2-}$ may be involved in the low potential cycle. A

working hypothesis which accommodates the two cycles and the inhibitory effects of CO and PhSH is shown by the mechanism in Scheme 4.2. Further work involving FTIR spectroelectrochemical studies under CO together with DFT calculations are needed to validate or otherwise the Scheme. Here it is noted that Dr Maurizio Bruschi (Milan – Bicocca) has carried out preliminary DFT calculations on $[Fe_4S_4(SPh)_4]^{2-}$ and $[Fe_4S_4(SCH_2Ph)_4]^{2-}$ systems at various levels of electronation and protonation and has identified energetically plausible intermediates with both sideways bound thiol and terminal hydride (Fe-H) moieties, Figure 4.14 , as postulated in Scheme 4.2 [36].
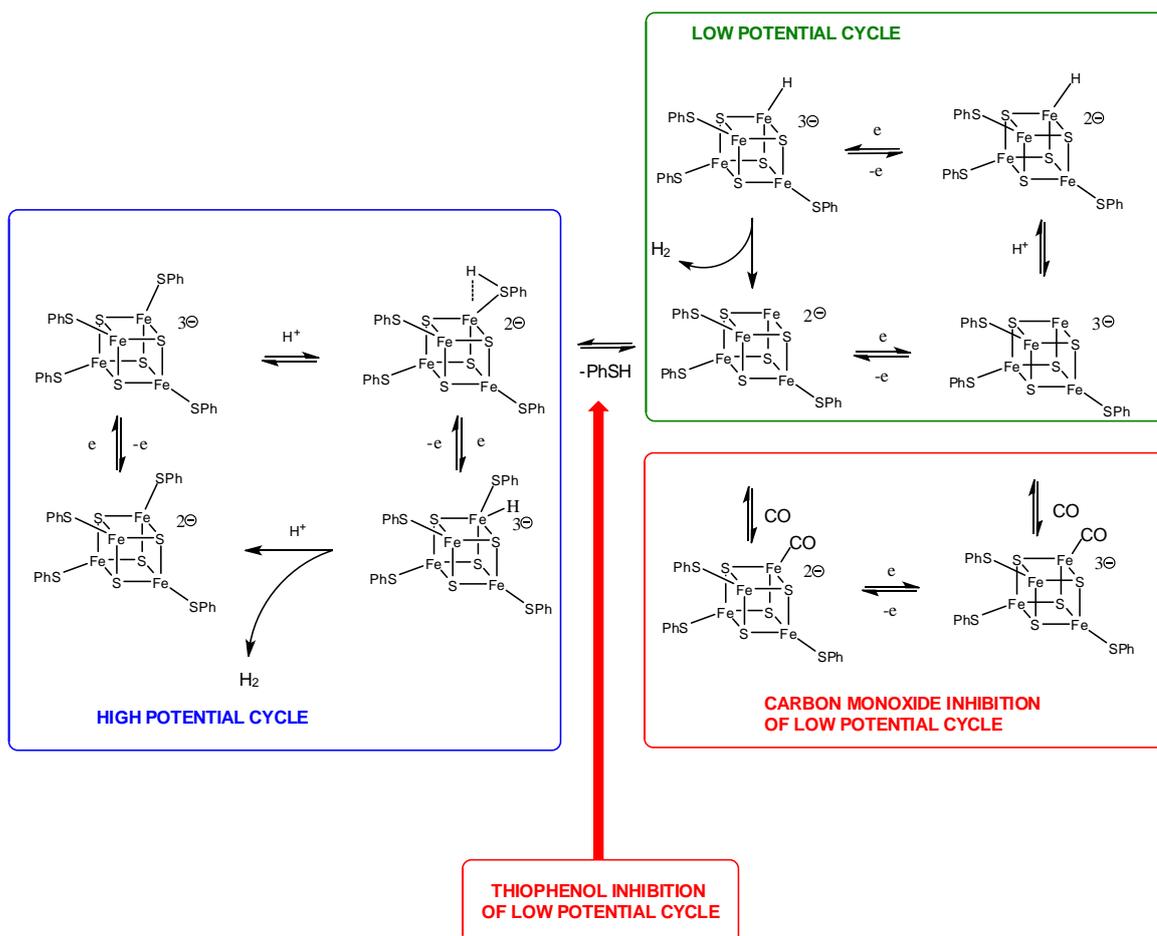
Scheme 4. 2 Postulated mechanism for hydrogen evolution pathways electrocatalysed by $[Fe_4S_4(SPh)_4]^{2-}$ and inhibited by CO and by PhSH.
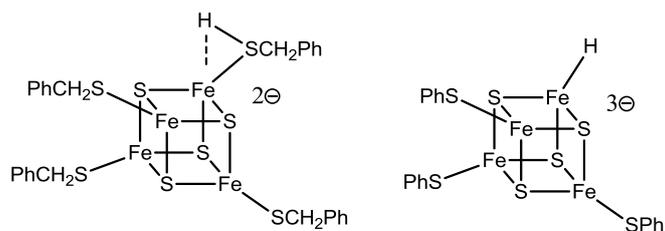
Figure 4.14 : Plausible intermediates suggested by DFT calulations by Dr Maurizio Bruschi (Milan – Bicocca)

However, proposed high and low potential pathways in Scheme 4.2 differ from the mechanism of stoichiometric evolution of dihydrogen from the reduced cluster $[Fe_4S_4(SPh)_4]^{3-}$ as proposed from a detailed kinetic analysis by Henderson and coworkers [1,2]. In their stopped-flow study, protonation at μ^3-S core sulfur atoms and thiolate occurs with the parent tri-anion providing an additional electron (rather than an electrode) for the stoichiometric formation of dihydrogen, Scheme 4.3. It was concluded that $[Fe_4S_4(SPh)_4]^{3-}$ can bind a maximum of three protons with the extent of protonation dependent on the pKa of the proton source. For $[NHEt_3]^+$ (pKa= 18.46 in MeCN) the dominant species was suggested to be neutral $[Fe_4S_3(SH)(SPh)_3(SHPh)]^-$, whereas with $[Hlut^+]$ (pKa = 14.1 in MeCN) triple protonation occurs to give $[Fe_4S_2(SH)_2(SPh)_3(SHPh)]$. GC analysis showed that a reasonable amount of H_2 is produced only under conditions where $[Fe_4S_2(SH)_2(SPh)_3(SHPh)]$ is formed and this enables an 82% yield of dihydrogen to be attained. The mechanism of the hydrogen evolution step remains unknown.
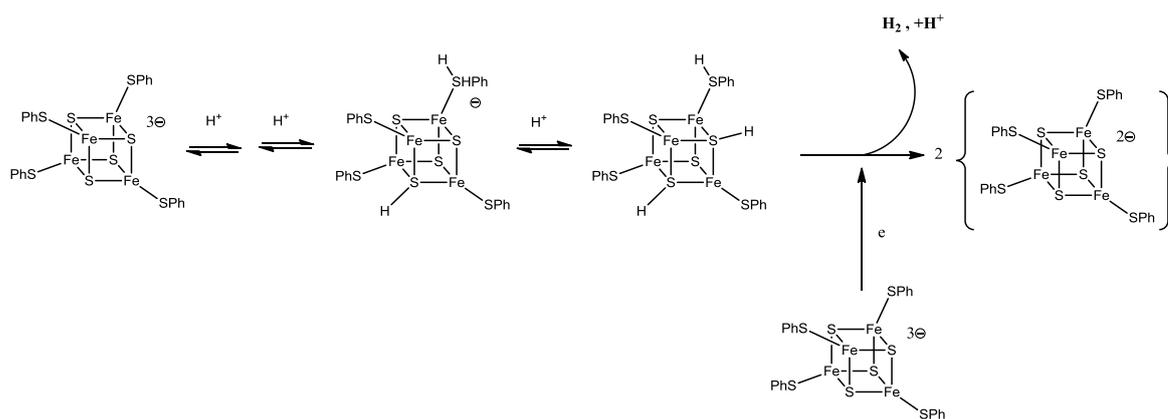
Scheme 4.3: Henderson mechanism of stoichiometric release of dihydrogen release. Adapted from refs [1, 2].

4.2.3 Electrochemistry of iron sulfur cluster at p-type Si under Ar

The photoelectrocatalytic reduction of proton by $[Fe_4S_4(SPh)_4]^{2-}$ in toluene electrolyte at illuminated p-type Si semiconducting electrodes was examined by cyclic voltammetry and bulk electrolysis. The cyclic voltammetry of iron sulfur cluster under Ar in the absence of a proton source in toluene-$[Bu_4N][BF_4]$ at 40-100Ω cm^{-1} p-type Si B-doped is shown in Figure 4.15. In dark the primary reduction wave takes place at $E_{1/2}$= -0.88 V *vs* Ag/AgCl , similar to that potential reduction found at vitreous carbon electrode. Whilst under illumination using a Krüss halogen fibre optic lamp (90mW cm^{-2}, λmax = 650nm) a photovolage of 400 mV was observed at $E_{1/2}$= -0.47 V *vs* Ag/AgCl.

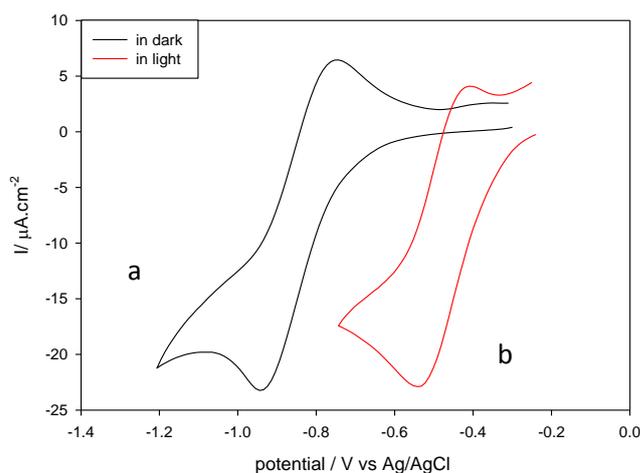**Figure 4.15** Cyclic voltammograms of $[Fe_4S_4(SPh)_4]^{2-}$ at a p-type H-Si electrode in toluene-$[NBu_4][BF_4]$,scan rate $100mV \cdot s^{-1}$. (a) In the dark; (b) illuminated by a Krüss halogen fibre optic lamp ($90mW \cdot cm^2$, $\lambda_{max} = 650nm$)

Figure 4.16(a) shows the various scan rates for $[Fe_4S_4(SPh)_4]^{2-}$ at p-type Si electrode, the primary reduction of $[Fe_4S_4(SPh)_4]^{2-}$ involves an electrochemically reversible one-electron transfer which occurs at $E_{1/2} = -0.47$ V vs Ag/Ag. The plot of peak current ${}^{I}i_p^{red}$ $versus$ $v^{1/2}$ is linear which is consistent with diffusion controlled reversible one electron step Figure 4.16(b).
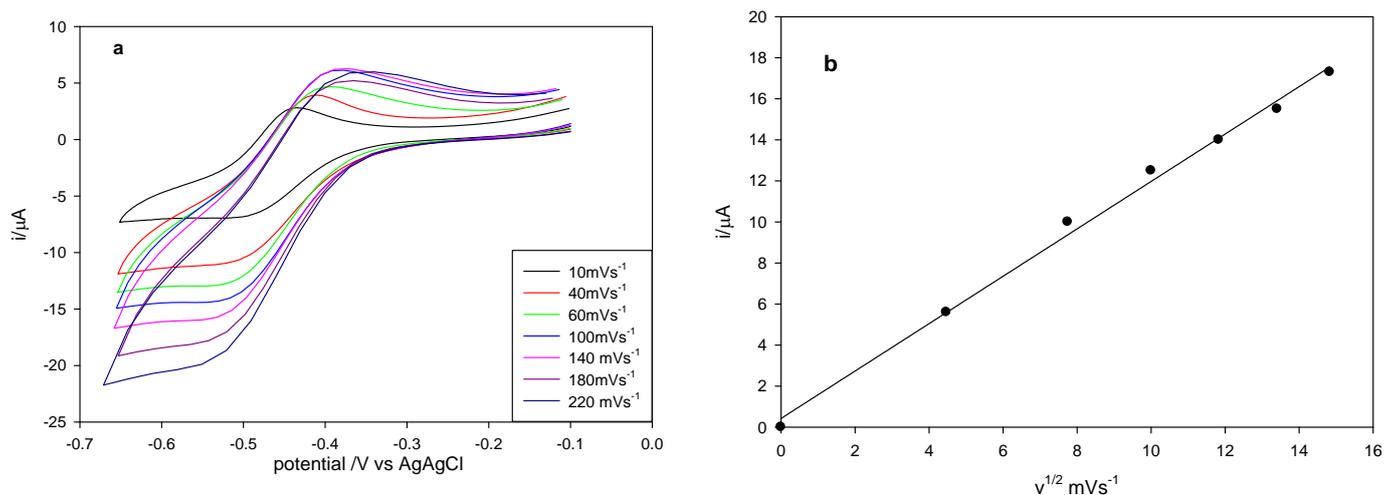

Figure 4.16 (a) Cyclic voltammograms of 0.5mM $[Fe_4S_4(SPh)_4]^{2-}$ at p-type Si electrode (first reduction) at different scan rates in toluene-$[Bu_4N][BF_4]$. (b) Plot of i_p^{red} versus $v^{1/2}$

4.2.3.1 The dependence of the catalytic current for proton reduction at p-type Si electrode on the concentration of the acid

The dependence of the catalytic current for proton reduction at p-type Si electrode at -0.5V versus Ag/AgCl upon the concentration of [Hlut$^+$] is shown in Figure 4.17(a). It is noted that there is no significant increase in peak current with addition of 1 and 2 eq of [Hlut$^+$] which may be just related to protonation of complex, but the catalytic current, i_{cat}, increases with high [Hlut$^+$] concentration. The peak current, i_0, was measured for the primary one-electron reduction step at the same scan-rate in the absence of proton source. In this experiment we have shown the effect of 5 eq [Hlut$^+$] and the values of i_{cat}/i_o become independent of the acid concentration at *ca* 10 eq in the toluene electrolyte, Figures 4.17(b).
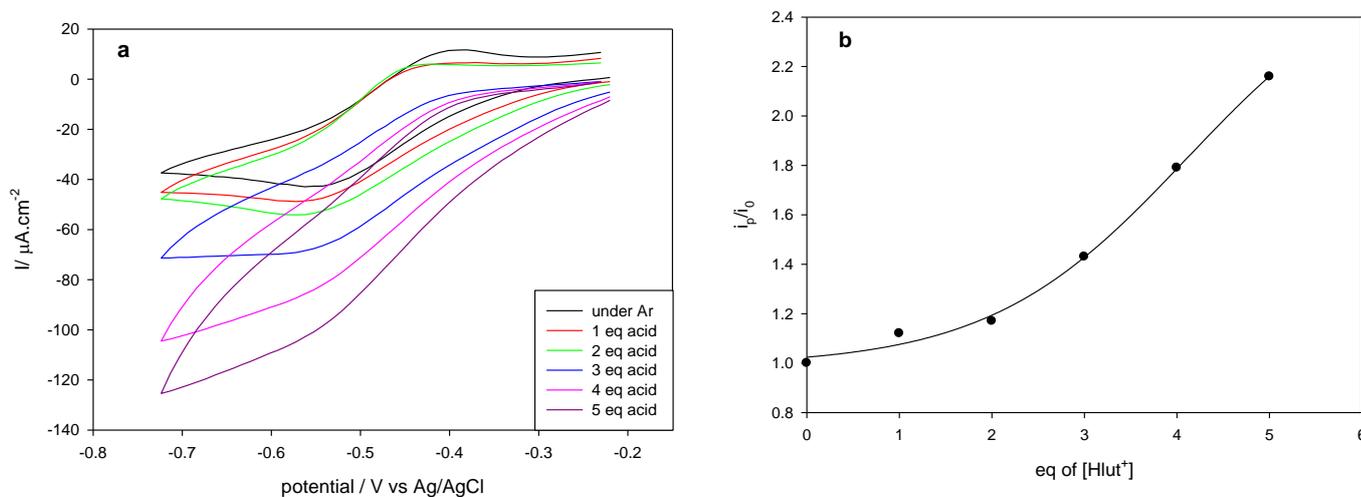

Figure 4.17 (a) Cyclic voltammograms of [Fe$_4$S$_4$(SPh)$_4$]$^{2-}$ in the presence of various concentration of [Hlut$^+$] at a p-type H-Si electrode illuminated by a Krüss halogen fibre optic lamp (90mW·cm^{-2}, λ_{max} =650nm) toluene-[NBu$_4$][BF$_4$] at a scan rate of 100mV·s^{-1}. (b) The variation of i_{cat}/i_0 *versus* concentration of [Hlut$^+$]

4.2.3.2 Potentiodynamic current response to chopped light

Figure 4.18 shows the potentiodynamic current response to chopper light which is confirming that the proton reduction catalysis by iron sulfur cluster was driven by light. It is shown that the peak current increases to ca 250µA.cm^{-2} at -0.5 V under

the illumination, but in dark the current is close to zero. The chopper light experiement for $[Fe_4S_4(SPh)_4]^{2-}$ was carried out in the presence of 12 eq $[Hlut^+]$, scan rate $50mVs^{-1}$, chopper 2 HZ.

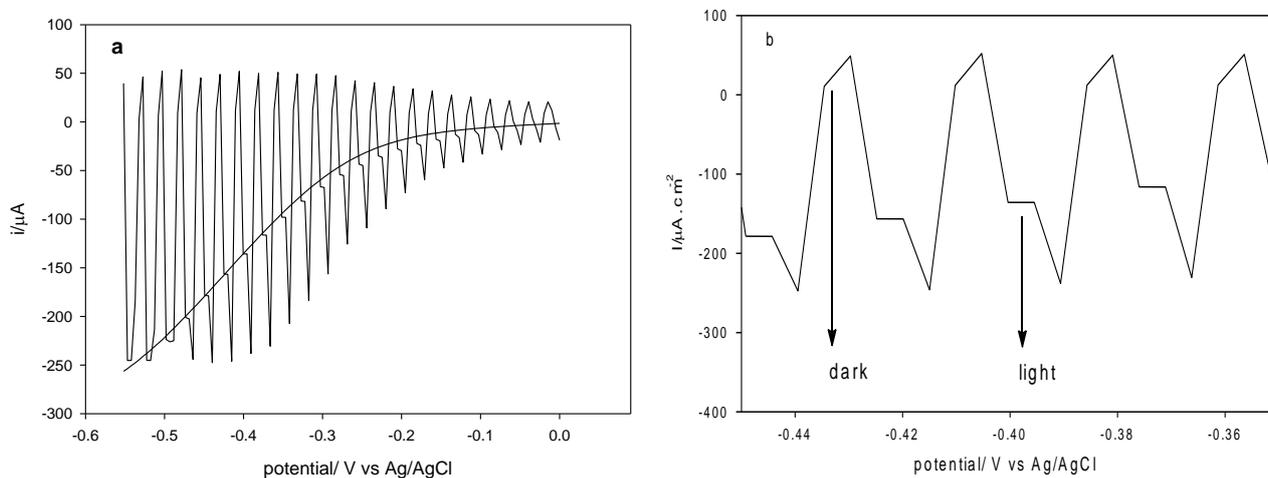**Figure 4.18** Response of $[Fe_4S_4(SPh)_4]^{2-}$ to chopped light at 2Hz the presence of 12 eq $[Hlut^+]$, scan rate 50 mVs^{-1}. (a) Response from -0.0 to- 0.6 V. (b) An expanded region of this response in the range - 0.3 to -0.5 V *versus* Ag/AgCl

4.2.3.3 Preparative Scale Electrolysis

The photoelectrocatalysis of proton reduction on a p-type Si electrode was performed in $[Bu_4N][BF_4]$-toluene at room temperature for 6 hours in the presence of 5 mM $[Fe_4S_4(SPh)_4]^{2-}$ and 12eq $[Hlut^+]$ at -0.58 V vs Ag/AgCl. GC of the gas phase confirm the formation of H_2 Figure 4.19(a). The yield of H_2 was 6.05 μmoles monitored as a function of electrolysis time over about 6 hours and a charge pass of 1.8 C, Figure 4.19(b). The current efficiency to reduce proton into H_2 after 6 hours was 72 % but the chemical yield was *ca* 42 % with a turnover number of 2.5, this was because the electrolysis time was not enough for the 12eq of proton to be consumed, Figure 4.19(c). Figure 4.19(d) shows the plot of current

versus charge passed is essentially linear and intercepts the Q-axis at 25 μmole electrons. This corresponds to an *overall* current efficiency for dihydrogen formation as *ca* 72% after 6 h. All the results of electrolysis at p-type Si electrode are summarised in Table 4.3.

Table 4.3 Current efficiencies and turnover numbers for proton reduction catalysed by 5mM $[Fe_4S_4(SPh)_4]^{2-}$

Time/h	0.69	1.69	3.75	6
Number of μmoles of H_2	0.48	2.53	4.24	6.05
Current efficiency %	40.4	73	70	72.1
Chemical yield % μmoles H_2/ μmoles of acid	4.7	11.2	25.6	41.3
T.N	0.2	1.03	1.73	2.5
Charge passed, C	0.23	0.67	1.19	1.6
μmole of electrons	2.38	6.95	12.33	16.58
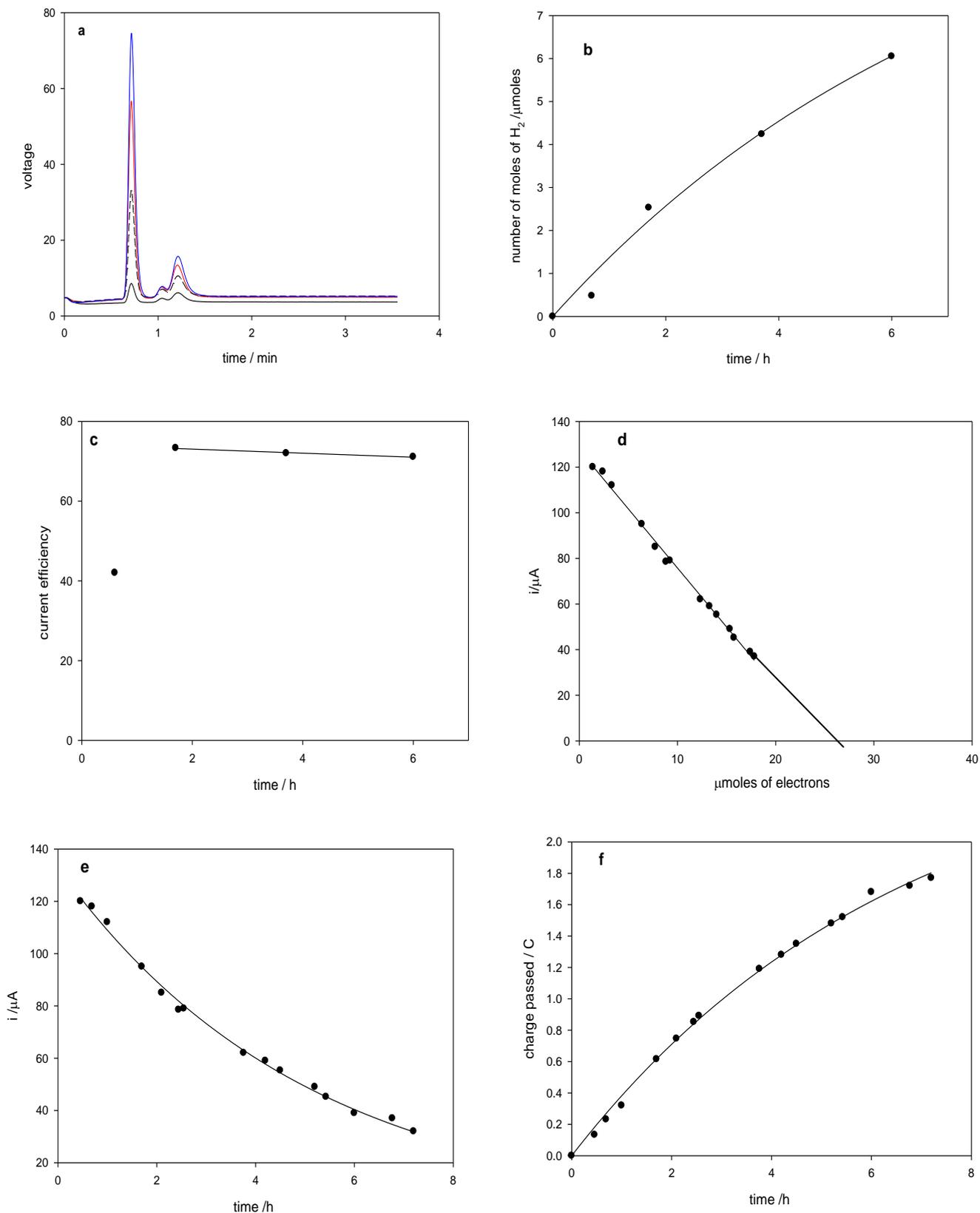
Figure 4.19 (a) Gas chromatography of H$_2$ produced during course of electrolysis (b) The yield of H$_2$ *versus* electrolysis time.(c) Current efficiency *versus* electrolysis time. (d) Current *versus* charge passed, μmole of electrons. (e) Current *versus* electrolysis time. (f) Charge passed *versus* electrolysis time. Coditions: 0.5 mM [Fe$_4$S$_4$(SPh)$_4$]$^{2-}$ in toluene-[Bu$_4$N][BF$_4$] in the presence of 12 eq [Hlut$^+$] at a p-type Si electrode at -0.58V *vs* Ag/AgCl under argon.

194

4.2.4 Calculation of k_{cat} at carbon electrode and p-type Si electrode

Figure 4.20 Effect of [Hlu$^+$] on i_{cat}/i_0 ratio at a vitreous carbon electrode. (a) Open circles: vitreous carbon electrode; solid circles: p-type H-silicon electrode for the <u>first reduction</u> process. (b) Open circles: vitreous carbon electrode, <u>second reduction</u> process; for comparison, solid circles: p-type H-silicon electrode for the <u>*first reduction*</u> process as shown in (a).
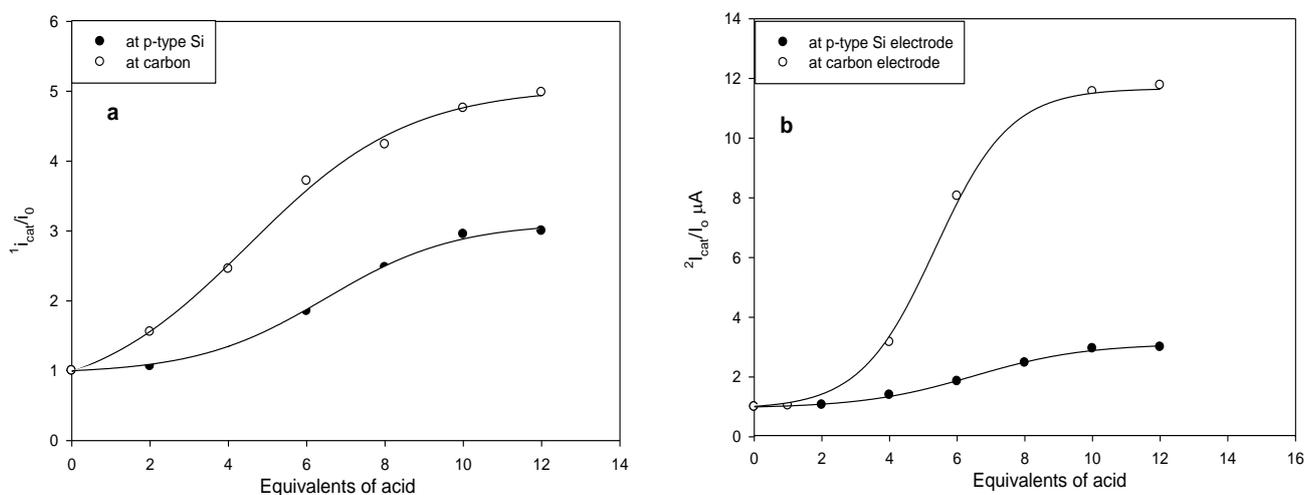
Figure 4.20 shows comparative data for the ratio i_{cat} / i_o at a vitreous carbon electrode and at the illuminated p-type Si electrode, *versus* [Hlu$^+$]. The peak catalytic current, i_{cat}, is that measured at 100mVs^{-1} in presence of acid and i_o is that for the peak current measured for first wave reduction (one-electron) before addition of acid at the same scan-rate. It is apparent that at both vitreous carbon and p-type Si electrodes the values of i_{cat} / i_o become independent of the acid concentration at 4 mM , ca 10 equivalents in the toluene electrolyte . It is noted that the magnitude of i_{cat} / i_o for the electrocatalysis on vitreous is about 2.6 times of that on illuminated p-type Si. The rate constants ($k^C_{cat,}$ 306 K) at vitreous carbon are 17.56 s^{-1} and 102.5 s^{-1} for the first and second processes respectively, whereas the rate constant (k^{Si}_{cat}, 306 K) for the single step catalysis at illuminated p-type Si is 6.8 s^{-1}.

4.3 Conclusions

This chapter has shown that $[Fe_4S_4(SPh)_4]^{2-}$ electrocatalyses the reduction of protons to dihydrogen at a vitreous carbon electrode in the electrolyte toluene-$[Bu_4N][BF_4]$ at 33 ^{0}C. Two reduction pathways are suggested. The first is a high potential process (E_{cat} = -0.87 V *versus* Ag/AgCl; $[Hlu^+]$ = 6 mM) which has a rate constant, $^1k^C_{cat}$ = 17.56 s^{-1} (33°C) under conditions where protonation is not rate limiting. The second pathway is faster $^2k^C_{cat}$ = 102.5 s^{-1} (33°C) but occurs at a lower potential (E_{cat} = -1.1 V *versus* Ag/AgCl). The electrocatalysis is strongly inhibited by CO and by PhSH. CO entirely suppresses the secondary process but does not totally eliminate the high potential electrocatalysis; the effect of PhSH on the two steps is similar.

The electrocatalytic reduction of protons to dihydrogen can be assisted by light at a p-type Si photocathode. The primary catalysis is associated with a photovoltage of ca 490 mV under saturated illumination conditions. It is associated with an acid-independent rate constant $^1k^{Si}_{cat}$ of 6.8 s^{-1} which is smaller than that at vitreous carbon under similar conditions. The second catalytic pathway at the p-type Si cannot be resolved because on this material background reduction of the free acid occurs.

The current efficiency for proton reduction on a bulk scale for both vitreous carbon and p-type Si were the same within experimental error, *ca* 70%, but the chemical yield at vitreous carbon electrode was higher than at a p-type Si electrode *ca* 96, 41.3 % respectively with low turnovers.

4.4 Experimental Section

4.4.1 General considerations

All manipulations were carried out under an atmosphere of an inert gas N_2 or Ar. The iron sulfur cluster $[Fe_4S_4(SPh)_4][Bu_4N]_2$ was prepared according to the literature method [37]. Gas chromatography and electrochemical measurements including a description of cells, was described in the previous chapter. The toluene electrolyte was prepared by warming $[Bu_4N][BF_4]$ to 30 -35°C in toluene, a lower ionic phase separates which has the molar ratio 3 toluene : 1 $[Bu_4N][BF_4]$ and in which the cyclic voltammetric and electrolyses were performed at 33 ^{o}C.

4.4.2 Cyclic voltammetry experiments

$[Fe_4S_4(SPh)_4][Et_4N]_2$ (3.2 mg, 2.51 µmoles) was dissolved under argon in the toluene electrolyte contained in the working electrode compartment of the cell. Cyclic voltammograms were recorded at a vitreous carbon electrode (0.072 cm^2) under argon in the absence and in the presence of a proton source, $[Hlut^+]$, 1-12 equivalents. Similar experiments were undertaken at 40-100Ω cm^{-1} p-type Si B-doped (0.9-1cm^2). The light source used during photoelectrochemical measurements was a Krüss KL5125 halogen fibre optic (λ_{max} = 650 nm; polychromic outputs 90 mW cm^{-2}). Similar conditions were used in the experiments performed in the presence of CO.

4.4.3 Bulk Electrolyses

Bulk electrolysis experiments were performed under argon at either a vitreous carbon electrode (-0.9V *vs* Ag/AgCl) or at illuminated p-type Si electrode (-0.58V *vs* Ag/AgCl) with the catholyte stirred at a steady rate. At the end of electrolysis the cyclic voltammetry of the catholyte solution was recorded. H_2 produced by electrolysis was measured by sampling the gas space above the catholyte in a closed system. Samples were taken by gas tight syringe normally 0.5 ml and determined by GC (thermal conductivity detector) using the column and conditions described in Chapter 3. Similar electrolysis experiments were performed under an atmosphere of the inhibitor carbon monoxide.

Background control experiments were performed as follows. Electrolysis was performed under the same conditions as for electrocatalysis, but in the *absence* of the iron sulfur cluster. No hydrogen was detected at a vitreous carbon electrode after electrolysis for 6 hours at -0.9 V *versus* Ag/AgCl. A negligible amount of hydrogen was formed in case of p-type Si electrode after 6 hours electrolysis at -0.58V *versus* Ag/AgCl.

4.3 References

1. R. Henderson. Coord. Chem. Rev. **2005**, 249, 1841-1856.

2. B. Garrett, R. Henderson. Dalton Trans**, 2010**, 39, 4586-4592.

3. R. Henderson, K. E. Oglieve. J. Chem. Soc. Dalton Trans. **1999**, 3927-3934.

4. D. Evans, C. J. Pickett. Chem. Soc. Rev, **2003**, 32, 268-275

5. F. Osterloh, C. Achim, R. H. Holm. Inorg. Chem. **2001**, 40, 224-232

6. W. Lovenberg, B. B. Buchanan, J. C. Rabinowitz. J. Biol. Chem. **1963**, 238, 3899-3913.

7. H. Beinert, M. C. Kennedy, C. D. Stout. Chem. Rev. **1996**, 96, 2335-2373.

8. H. Beinert, R. H. Holm, E. Munck. Science. **1997**, 277, 653-659.

9. H. Beinert. J. Biol. Inorg. Chem. **2000**, 5, 2-15

10. P. Venkateswara, R. H. Holm. Chem. Rev. **2004**, 104, 527-559.

11. R. Gary, R. Dukes, R. H. Holm. J. Am. Chem. Soc. **1975**, 5, 528-533.

12. T. Yamamura, G. Christou, R. H. Holm. J. Inorg. Chem. **1983**, 22, 939-949.

13. C. Tard, D.Phil. Thesis, University of East Anglia. **2005**.

14. D. Johnson, R. Dean, A. Smith, M. Johnson. Ann. Rev. Bio.chem. **2005**. 74. 247-81.

15. L. Zheng, D. Dean. J. Biol. Chem. **1994**, 269, 18723-18726.

16. H. Beinert. J. FASEB. **1990**, 4, 2483-2491

17. D. Rees. Ann. Rev. Bio. Chem. **2002**, 71, 221-246.

18. Y. Nicolet, C. Piras, P. Legrand, C. Hatchikian, J. Fontecilla-Camps. Structure. **1999**, 7, 1-11.

19. W. Sweeney. Ann. Rev. Biochem. **1980.** 49,139-1361.

20. S. Bian, J. Cowan. Coord. Chem. Rev. **1999**, 190, 1049-1066.

21. T. Rouault, R. Klausner. Trends. Biochem Sci .**1996** , 5, 174-177

22. B. Guigliarelli, A. Magalon, M. Asso, P. Bertrand, C. Frixon, G. Giordano, F. Blasco. Biochemistry. **1996,** 35, 4828-4836

23. J. Hudson, K. Heffron, V. Kotlyar. Y. Sher, E. Maklashina, G. Cecchini, F. Armstrong. J. Am. Chem. Soc. **2005**, 127, 6979-6989.

24. G. Christou, R. V. Hageman, R. H. Holm. J.Am. Chem. Soc. **1980**, 102, 7601-7603.

25. T. Sullivan , M. Millar. J. Am. Chem. Soc. 1**985**, 107, 4096-4097.

26. R. H. Holm, P. Kennepohl, E. I. Solomon. Chem. Rev. **1996**, 96, 2239-2314

27. B. K. Burgess. Chem. Rev. **1990,** 90, 1377 -1406.

28. B. K. Burgess, D. J. Lowe. Chem. Rev. **1996**, 96, 2983-3012.

29. J. W. Peters, M. H. Stowell, S. M. Soltis, M. G Finnegan, M. K Johnson, D. C Rees. Biochem. **1997**, 36, 1181-1187.

30. S. M. Mayer, D. M. Lawson, C. A. Gormal, S. M. Roe, B. E. Smith. J. Mol. Biol. **1999**, 292, 871-891.

31. K. L. C. Grönberg, R. A. Henderson, S. K. Ibrahim, T. Le Gall, C. J. Pickett. Coord. Chem. Rev. **1999,**185, 669-687

32. T.Le Gall, S. K. Ibrahim, C. A. Gormal, B. E. Smith, C. J. Pickett. Chem. Commun**. 1999**, 773-774.

33. C. Goh, B. M. Segal, J. Huang, J. R. Long, R. H. Holm. J. Am. Chem. Soc. 1**996**, 118, 11844-11853.

34. C. J. Pickett. J. Chem. Soc. Chem. Comm. **1985**, 323-326

35. B. E. Smith, M. C. Durrant, S. A. Fairhurst, C. A. Gormal, T. Liu, D. DuBois, R. Bullock. Nature Chem.**2013**, 5, 228-233.

36. [M. Bruschi, *personal communication*]

37. B. V. Pamphilis, B. A. Averill, T. Herskovitz, L. Que jnr, R. H. Holm. J. Am. Chem. Soc. **1974**, 96, 4159.

Chapter 5

5. *Summary and possible future work*

5.1 *Alkane oxidation by iron porphyrin complexes*

- The catalysis of hydrocarbon oxidation to alcohols or epoxide by a series of new basket-handle thiolate Fe (III) porphyrins has been investigated and their activities have been benchmarked against iron tetraphenylporphyrin and its tetrapentafluorophenyl analogue.

- It has been shown that adamantane oxidation and cyclooctene epoxidation can be driven anodically at a vitreous carbon cathode in the first detailed study which has established current yields.

5.2 *Alkane oxidation by iron porphyrin complexes: possible future work*

- A pathway for the anodic oxidation of hydrocarbons has been suggested but further studies are needed to evaluate the role of hydroxy intermediates and metal or porphyrin centred radicals.

- It would be interesting to explore the possibility of driving the electrochemical oxidation of alkanes at a photoanode. The potentials for the electrochemical oxidation in the presence of the porphyrin catalysts are very positive +1.2 to +1.6 V *versus* SCE, this might be substantially lowered by photoassisting the oxidation at a semiconductor.

5.3 Electrocatalysis of carbon dioxide reduction to carbon monoxide

- The reduction of CO_2 on carbon or mercury electrode catalysed by various iron porphyrin complexes, has been explored by electrochemical methods. Certain basket handle thiolate porphyrins have been shown to be capable of high efficiency and selectivity in the electrocatalytic reduction of CO_2 to CO.

- A key part of the electrocatalysis by basket handle porphyrins is the de-coordination of the anchored thiolate ligand in the presence of a proton source and this distinguishes their electrochemical behaviour from classical Fe porphyrins.

- It has been shown for the first time that carbon dioxide reduction to carbon monoxide can be driven at a visible light illuminated p-type Si photocathode using **Fe(TPP)Cl** and certain other iron porphyrin electrocatalysts in the presence of a proton source at a potential ca 500 - 600mV positive of that required for carbon and Hg electrodes.

- **Fe(TPP)Cl** electrocatalyses the selective photoreduction of CO_2 to CO at illuminated p-type silicon photocathode with current efficiency of 93%, but the basket handle thiolate iron (III) complexes are all lower in selectivity for the catalysis of the reduction of CO_2 to CO, producing more H_2 probably by heterogenous reduction of protons at the p-type Si.

- Fe-porphyrin photoelectrocatalysis of CO_2 reduction has certain advantages over a recently reported Re system in that; (i) it employs an abundant metal, Fe *vs* Re and (ii) the photoelectrocatalysis with **Fe(TPP)Cl** takes place at a photopotential that is more positive by

about 100mV.

5.4 Electrocatalysis of carbon dioxide reduction to carbon monoxide: possible future work

- The electrocatalysis and photoelectrocatalysis work on the Fe porphyrin systems could possibly be extened to studies of Co analogues which may show different a distribution of CO and H_2 products. In addittion there is scope for further modification of the porphyrin framework to enhance electrocatalytic activity as has been shown by Saveant and coworkers with the introduction of phenolate substitents [1].

- Some explanation for the differences between k_{cat} values measured on vitreous carbon and on illuminated p-type Si remain have been provided but further mechanistic work in this area would be advantageous.

5 5 Electrocatalysis of proton reduction by iron-sulfur clusters

- It has been shown that $[Fe_4S_4(SPh)_4]^{2-}$ electrocatalyses the reduction of protons to dihydrogen at a vitreous carbon electrode in the electrolyte 3toluene:1$[Bu_4N][BF_4]$. This may have some bearing on early biotic proton/hydrogen metabolism where simple ferredoxins might have function as primitive hydrogenases. It is particularly interesting that CO inhibits dihydrogen formation as is observed with conventional [FeFe] hydrogenases.

- The electrocatalytic reduction of protons to dihydrogen can be assisted by light at a p-type Si photocathode with a photovoltage of *ca* 400 mV under saturated illumination conditions. The photoelectrocataysis on p-type Si is slower but can be sustained over several hours.

- An overall mechanistic scheme has been proposed for proton reduction by the iron-sulfur cluster which involves two dihydrogen evolving pathways.

5.6 *Electrocatalysis of proton reduction by iron-sulfur clusters: possible future work*

- The cluster $[Fe_4S_4(SPh)_4]^{2-}$ has four potential Fe sites at which chemistry involving protons and inhibitors can take place. Studies of 'site differentiated' clusters which possess 3Fe cubane atoms tightly chelated by a tripodal ligand leaving a single Fe site at which chemistry can take place may aid in understanding the electrocatalytic mechanism and in spectrocopic characterisation of CO inhibited intermediates.

- Preliminary DFT studies of proton interactions with $[Fe_4S_4(SPh)_4]^{2-}$ clusters are very promising and suggest the formation of hydridic Fe-H bonds and FeHSPh semi-bridging hydrides. Further studies by the Milan-Bicocca group are in progress and will undoubtedly illuminate the electrocatalytic chemistry.

5.7 Reference

1. C. Costentin, S. Drouet, M. Robert, J-M. Saveant. Science. **2012**, 90, 90-94.

Publication from this work

1- P. Li, K. Alenezi, S. K. Ibrahim, J. A. Wright, D. L. Hughes, C. J. Pickett. ChemSusChem. **2012**, 5, 2361-2375

2- K. Alenezi, S. K. Ibrahim, P. Li, C. J. Pickett.J. Chem. Eur . **2013**, 19, 13522 -13527